Oscar Camara Ender Konukoglu
Mihaela Pop Kawal Rhode
Maxime Sermesant Alistair Young (Eds.)

Statistical Atlases and Computational Models of the Heart

Imaging and Modelling Challenges

LNCS 7085

Second International Workshop, STACOM 2011
Held in Conjunction with MICCAI 2011
Toronto, ON, Canada, September 2011, Revised Selected Papers

Springer

Lecture Notes in Computer Science 7085

Commenced Publication in 1973
Founding and Former Series Editors:
Gerhard Goos, Juris Hartmanis, and Jan van Leeuwen

Oscar Camara Ender Konukoglu
Mihaela Pop Kawal Rhode
Maxime Sermesant Alistair Young (Eds.)

Statistical Atlases and Computational Models of the Heart

Imaging and Modelling Challenges

Second International Workshop, STACOM 2011
Held in Conjunction with MICCAI 2011
Toronto, ON, Canada, September 22, 2011
Revised Selected Papers

Springer

Volume Editors

Oscar Camara
University of Pompeu Fabra, Plaça de la Mercè 10-12, 08002 Barcelona, Spain
E-mail: oscar.camara@upf.edu

Ender Konukoglu
Microsoft Research, 7 J J Thomson Avenue, Cambridge CB3 0FB, UK
E-mail: enderk@microsoft.com

Mihaela Pop
University of Toronto, 610 University Avenue, Toronto, ON, M5G 2M9, Canada
E-mail: mihaela.pop@utoronto.ca

Kawal Rhode
King's College, St. Thomas' Hospital, Lambeth Wing, London SE1 7EH, UK
E-mail: kawal.rhode@kcl.ac.uk

Maxime Sermesant
Inria Sophia Antipolis - Méditerranée
2004 Route des Lucioles - BP 93, 06902 Sophia Antipolis Cedex, France
E-mail: maxime.sermesant@inria.fr

Alistair Young
University of Auckland, 85 Park Road, Auckland 1023, New Zealand
E-mail: a.young@auckland.ac.nz

ISSN 0302-9743 e-ISSN 1611-3349
ISBN 978-3-642-28325-3 e-ISBN 978-3-642-28326-0
DOI 10.1007/978-3-642-28326-0
Springer Heidelberg Dordrecht London New York

Library of Congress Control Number: 2012930995

CR Subject Classification (1998): J.3, H.4, H.5.2, H.1.2, H.5.1

LNCS Sublibrary: SL 6 – Image Processing, Computer Vision, Pattern Recognition, and Graphics

Typesetting: Camera-ready by author, data conversion by Scientific Publishing Services, Chennai, India

Printed on acid-free paper

Springer is part of Springer Science+Business Media (www.springer.com)

Preface

This year's edition of STACOM was held in conjunction with the MICCAI conference (Toronto, Canada), and followed last year's workshop, STACOM 2010 (held in 2010, Beijing, China), with the same goal of organizing an international event that provides a forum for the discussion of the latest developments in the areas of statistical atlases and computational imaging and modelling of the heart. This broad aim included: cardiac mapping, image processing, atlas construction, statistical modelling of cardiac function across different patient populations, cardiac computational physiology, model personalization, ontological schemata for data and results, atlas-based functional analysis, integrated functional and structural analyses, as well as the clinical applicability of these methods. STACOM 2011 again attracted participants from around the world, with 28 papers accepted and published by Springer in this volume of *Lecture Notes in Computer Science*. Besides regular contributions on state-of–the-art cardiac image analysis techniques, atlases and computational models that integrate data from large-scale databases of heart shape, function and physiology, additional efforts of this year's STACOM workshop focused on imaging and modelling challenges.

The integration of cardiac models in pre-clinical and clinical platforms is important for understanding disease, evaluating treatment, and planning intervention. However, significant clinical translation of these tools is constrained by the lack of complete and rigorous technical and clinical validation, as well as benchmarking of the developed tools. To validate the models, available ground-truth data capturing generic knowledge on healthy and pathological hearts are required. Several efforts are now established to provide Web-accessible structural and functional experimental datasets for clinical, research and educational purposes. We believe that these approaches will only be effectively developed through collaboration across the full research scope of the cardiac imaging and modelling communities. Last year's STACOM workshop was complemented with the CESC 2010 challenge, where a complete dataset containing cardiac geometry and fiber orientations from diffusion-tensor MRI as well as epicardial transmembrane potentials from optical mapping (acquired at Sunnybrook Research Institute, University of Toronto) was provided in advance for the analysis of different strategies for the personalization of electrophysiological models. This resulted in a joint journal publication including all CESC 2010 participants, and was recently published in *Progress in Biophysics and Molecular Biology* (Camara *et al*, 2011).

STACOM 2011 was enhanced by the organization of three different challenges for participants to test their computational tools on given data: an Electrophysiology (EP) Simulation Challenge (organized by the Sunnybrook Research Institute - University of Toronto, and Inria - France), a Cardiac Motion Analysis Challenge (organized by Kings College London and Universitat Pompeu Fabra,

Barcelona) and a Cardiac Segmentation Challenge (organized by the University of Auckland); each challenge is briefly described here.

The Electrophysiology (EP) Simulation Challenge was organized with the aim to better understand structural and electrical functional properties of healthy and infarcted hearts using a fusion of EP and (MRI) data obtained in a preclinical animal model. Specifically, two datasets (acquired at Sunnybrook Research Institute, Toronto) obtained in healthy and infarcted porcine hearts were made available to the challengers in order to validate their computer models. These datasets included in vivo EP data (i.e., electro-anatomical voltage and isochronal maps acquired with the CARTO-XP system, Biosense Webster) and corresponding high-resolution ex vivo 3D diffusion-weighted MRI scans (from which the anatomy, infarct extent and fiber direction were extracted). However, this year's EP simulation challenge did not aim to compare the results among challengers, but was rather focused on different applications and modelling approaches using the EP-MRI data provided. Three research groups participated in the challenge, from the following institutions: Inria - Asclepios Project (France), Rochester Institute of Technology (USA) and Sunnybrook Research Institute (Toronto, Canada). Each group presented a different application to 3D MR image-based cardiac computer modelling using one or both EP-MRI datasets. These applications concerned forward and/or inverse theoretical problems that apply to computational electrophysiology, and aimed to either validate simple or complex mathematical models, to optimize the model's parameterization from EP measures or to detect non-invasively the infarct scar. A collate journal paper summarizing all these EP simulation challenge results is under preparation.

Many forms of cardiac pathology affect the pattern of motion of the myocardium. Analysis of this motion can be useful for diagnosis, treatment planning, treatment guidance and treatment follow-up. Echocardiography (echo) and MRI are the imaging modalities of choice for studying myocardial motion, but quantitative analysis can be very time-consuming and prone to inter- and intra-observer variability. The recent development of several semi- and fully-automatic motion analysis algorithms has the potential to make a significant clinical impact in the field of cardiology. The benchmarking of these methods in terms of accuracy and robustness is necessary in order to make the approaches feasible for widespread clinical translation. This was the motivation for the First Cardiac Motion Analysis Challenge (cMAC) that took place as part of the MICCAI 2011 conference. State-of-the-art imaging acquisition methods were employed to acquire four-dimensional (4D) echo and MRI data of a left ventricular phantom (at the University of Ulm, Germany) and 15 healthy volunteers (at King's College London, UK). These data were made available to participants in order to quantify the deformation fields and subsequently compare the results with manual ground truth annotations. Four international research groups took part in the challenge: Fraunhofer MEVIS, Bremen, Germany; Imperial College London/University College London, UK; Universitat Pompeu Fabra, Barcelona, Spain; and Inria—Asclepios Project, France. Each participant quantified deformation fields from either or both of the echo and MRI data. The protocols

for the data acquisition and the methodologies and results from each of the participants are presented within this volume. Quantitative comparison with the ground truth and a comparison between participants will be the subject of a future journal publication. The longevity of the availability of the data has been assured by making the data available through the Cardiac Atlas Project (www.cardiacatlas.org) so that researchers can use the data for future benchmarking.

The 2011 Left Ventricular Segmentation Challenge was organized to allow researchers to test their segmentation algorithms on a large dataset. In total, there were 200 cases of cardiac MRI data consisting of patients with myocardial infarction from the DETERMINE cohort, made available for this challenge from the Cardiac Atlas Project database. Half of the data were randomly selected for testing and the remaining ones were set for the challenge. A set of ground truth-labeled images, manually and carefully drawn by experts, was provided in the test set to the participants. The objective of this challenge was rather uncommon compared with previous segmentation challenges. This challenge was held as a collaborative effort between peers to produce better ground truth images of the myocardium. As such, there was no 'winner' and the results were presented without ranks. The Expectation-Maximization-based STAPLE method was applied to estimate the ground truth images from all the participants. Five automated segmentation methods and two sets of expert contours participated in this challenge. A collation study of this segmentation challenge is presented in these proceedings.

We hope that the results obtained by the three challenges, together with the regular paper contributions, will act to accelerate progress in the important areas of heart function and structure analysis.

September 2011

Oscar Camara
Ender Konukoglu
Mihaela Pop
Kawal Rhode
Maxime Sermesant
Alistair Young

Organization

We would like to thank the Program Committee, the additional reviewers, and all participants for their time and effort, as well as our sponsors: Ontario Consortium for Imaging in Cardiovascular Therapeutics (Canada), Siemens AG (Siemens Corporate Research, Princeton NJ, USA) and Scimedia/BrainVision (Japan and USA).

Chairs

Oscar Camara	Universitat Pompeu Fabra, Spain
Ender Konukoglu	Microsoft Research, UK
Mihaela Pop	University of Toronto, Canada
Kawal Rhode	King's College London, UK
Maxime Sermesant	Inria, France
Alistair Young	University of Auckland, New Zealand

Program Committee

Leon Axel	New York University, USA
Nicholas Ayache	Inria, France
Antonio Criminisi	Microsoft, UK
Hervé Delingette	Inria, France
Alejandro Frangi	Universitat Pompeu Fabra, Spain
Peter Hunter	University of Auckland, New Zealand
Tommaso Mansi	Siemens Corporate Research, USA
Perry Radau	Sunnybrook Health Sciences Centre, Canada
Reza Razavi	King's College London, UK
Nic Smith	King's College London, UK
Graham Wright	University of Toronto, Canada

Challenges—Organizing Teams

Segmentation Challenge: Alistair Young, Avan Suinesiaputra
Motion Challenge: Kawal Rhode, Mathieu de Craene, Catalina Tobon-Gomez
EP Simulation Challenge: Mihaela Pop, Graham Wright, Maxime Sermesant

Additional Referees

Constantine Butakoff
Ruben Cardenes
Mathieu de Craene
Daniel Ennis
Pau Medrano-Gracia
Yingliang Ma
Wenzhe Shi
Xiahai Zhuang
Bjoern Menze
Kilian Pohl
Brett R. Cowan
Jean-Marc Peyrat
Stéphanie Marchesseau
Kristin McLeod
Ben Glocker
Maria J. Ledesma-Carbayo
Bart Bijnens

Sponsoring Institutions

The STACOM 2011 workshop was sponsored by the Ontario Consortium for Imaging in Cardiovascular Therapeutics (Ontario, Canada), Siemens AG (Siemens Corporate Research, Princeton NJ, USA) and Scimedia/BrainVision (Japan and USA) and was endorsed by SCMR (Society for Cardiovascular Magnetic Resonance, USA).

Table of Contents

EP Simulation Challenge

Motion Tracking Challenge

Segmentation Challenge

Regular Papers

EP Challenge - STACOM'11: Forward Approaches to Computational Electrophysiology Using MRI-Based Models and In-Vivo CARTO Mapping in Swine Hearts

Mihaela Pop[1], Maxime Sermesant[2], Tommaso Mansi[3], Eugene Crystal[1], Sudip Ghate[1], Jatin Relan[2], Charles Pierre[4], Yves Coudiere[5], Jennifer Barry[1], Ilan Lashevsky[1], Beiping Qiang[1], Elliot R. McVeigh[6], Nicholas Ayache[2], and Graham A. Wright[1]

[1] Sunnybrook Research Institute, University of Toronto, Canada
[2] INRIA - Asclepios Project, Sophia-Antipolis, France
[3] Siemens Corporate Research, Princeton, NJ, USA
[4] University of Pau, France
[5] Inst. Mathematiques de Bordeaux, France
[6] Johns Hopkins University, Baltimore, USA
mihaela.pop@utoronto.ca, gawright@sri.utoronto.ca

Abstract. Our broad aim is to integrate experimental measurements (electro-cardiographic and MR) and cardiac computer models, for a better understanding of transmural wave propagation in individual hearts. In this paper, we first describe the acquisition and processing of the data provided to the EP simulation challenge organized at STACOM'11. The measurements were obtained in two swine hearts (i.e., one healthy and one with chronic infarction) and comprise in-vivo electro-anatomical CARTO maps (e.g., surfacic endo-/epicardial depolarization maps and bipolar voltage maps recorded in sinus rhythm), and high-resolution ex-vivo diffusion-weighted DW-MR images (voxel size < $1mm^3$). We briefly detail how we built anisotropic 3D MRI-based models for these two hearts, with fiber directions obtained using DW-MRI methods (which also allowed for infarct identification). We then focus on applications in cardiac modelling concerning propagation of depolarization wave, by employing forward mathematical approaches. Specifically, we present simulation results for the depolarization wave using a fast, macroscopic monodomain formalism (i.e., the two-variable Aliev-Panfilov model) and comparisons with measured depolarization times. We also include simulations obtained using the healthy heart and a simple Eikonal model, as well as a complex bidomain model. The results demonstrate small differences between computed isochrones using these computer models; specifically, we calculated a mean error ± S.D. of 2.8 ± 1.67 ms between Aliev-Panfilov and Eikonal models, and 6.1 ± 3.9 ms between Alie-Panfilov and bidomain models, respectively.

Keywords: electrophysiology, 3D computer modelling, cardiac DW-MRI.

1 Introduction

Abnormal rhythms (arrhythmias) are often associated with abnormal propagation of electrical wave in hearts with structural disease and are a major cause (>85%) of

O. Camara et al. (Eds.): STACOM 2011, LNCS 7085, pp. 1–13, 2012.

sudden cardiac death [1]. Currently, chronic infarct areas are identified during the electrophysiology (EP) study using for instance the CARTO-XP electro-anatomical system (Biosense, Diamond, USA). This system is limited to surfacic endocardial and/or epicardial maps obtained invasively via catheters inserted into the heart cavities, under fluoroscopy. However, many patients are hemodynamically unstable and therefore the scar mapping is done only during the sinus rhythm; only very established clinical centers map the patients under pacing conditions. Thus, there is a strong clinical motivation to supplement the electrophysiology measurements with non-invasive information, like 3D anatomy and accurate scar delineation. Should this information is known, image-based predictive computer models could be integrated in treatment planning platforms and help the clinician improve therapy through identification of strategies most appropriate to the individual patient [2]. Hence, an important task is to find the location, extent and transmurality of the scar in post-infarction patients. Clinically, this is done non-invasively with contrast-enhanced (c-e) MRI methods; however, identification of infarcted areas suffers from partial volume effects due to the slice thickness (~ 8 mm) [3]. Other methods, like non-contrast MR could be exploited, particularly those that allow extraction of fiber directions. For instance, using diffusion-weighted DW-MRI methods, it was demonstrated in ex-vivo formalin-fixed porcine hearts studies that scars correspond with the regions of increased apparent diffusion coefficient (ADC) [4]. Similar findings were observed in-vivo, in patients with prior myocardial infarct, but these MR scans are in general of poor resolution because motion artifacts significantly affect in-vivo imaging [5].

In addition to standard clinical evaluations using EP studies and MR imaging, computer modelling has been extensively used in cardiac electrophysiology to predict the heart's electrical activity [6,7]. Recent progress has demonstrated that image-based computer models can be integrated in treatment planning platforms [2]. However, prior to integration into routine clinical applications, such predictive models have to be validated/calibrated using experimental techniques selected to reflect EP phenomena at spatio-temporal scales similar to those in simulations. Importantly, these cardiac computer models need to account for myocardial tissue anisotropy; here the fiber directions are obtained via ex-vivo DW-MRI or atlases. Other groups focused to construct image-based models from normal and pathologic large animal hearts, with size relevant to human hearts. Some applications concerned simulations of virtual cases of arrhythmias using complex computer models built from noisy fractional anisotropy maps of dog hearts; although the results were encouraging, the studies lacked experimental validation [8]. Our group combined simplified 3D MRI-based computer models with electrophysiology measures from optical fluorescence imaging, to validate the propagation and characteristics of action potential, as well as to customize several model parameters in large healthy hearts, ex-vivo [9, 10]. However, our final aim is to characterize post-infarction chronic scars using realistic in-vivo EP measures augmented with accurate 3D information from high-resolution ex-vivo MRI imaging, and also to complement this knowledge with insights from theoretical modeling. The first step in achieving this goal is the development of a pre-clinical large-heart model that could characterize cardiac electrical and structural function with sufficient information, at least at a macroscopic level. This should allow

us to perform accurate validation and parameterization of computer models on a heart-basis, as well as to test various mathematical approaches of different degree of complexity, and test the utility and performance of associated computer models.

We believe that the development of experimental datasets and sharing data and results within the community, will advance us toward this goal by addressing the advantages and limitations of different mathematical models. One step forward in this direction was already taken for the last year's EP simulation challenge at STACOM-CESC'10, where the participants have tested and/or calibrated their computer models using experimental datasets published in [9, 10]. These datasets comprised ex-vivo optical fluorescence images (isochronal maps of depolarization and repolarization phase) fused with ex-vivo DW-MR images of healthy swine hearts. A review paper [11] included the results from all challenge participants, focusing on consistency and main complementarities between various modelling approaches proposed by these research groups.

The next logical step is to advance such efforts towards the applications concerning in-vivo EP measurements. This current challenge paper describes first in detail the data acquisition and processing for the EP simulation challenge organized at STACOM'11, where we provided the challengers with experimental datasets (in-vivo EP and ex-vivo MRI) obtained in healthy and chronically infarcted swine hearts. We then present applications in computational electrophysiology using the two 3D MRI-based heart models (healthy and pathologic) and forward (direct) mathematical approaches. Specifically, we include simulation results for the depolarization wave using a simple macroscopic, monodomain formalism (i.e., the two-variable Aliev-Panfilov model), as well as qualitative and quantitative comparisons with the measurements. We investigate if, for applications concerning only computations of the electrical wave propagation, this two-variable model is sufficient, and, for this, include comparisons between simulation results obtained with Aliev-Panfilov model, and simulation results obtained using other formalisms: the simplest model (i.e., Eikonal model) and a complex model (i.e., bidomain model).

2 EP-CARTO and DW-MRI Data Acquisition and Processing

We describe below the experimental steps following the order in which they were performed. We first completed the in-vivo EP studies. We then explanted the hearts and used DW-MRI to measure the myocardial fiber directions and delineate the infarct. These MR images were further used to build 3D heart computer models.

2.1 In-Vivo Electrophysiology Study and Ex-Vivo MRI Study

For the EP simulation challenge organized at STACOM'11, we included two cases in which the in-vivo EP study was performed in accordance to the animal protocol in a pre-clinical swine model approved by Sunnybrook Research Institute (Toronto, Canada). All electrophysiology maps described in this paper were recorded in sinus rhythm with the CARTO-XP electro-anatomical mapping system (Biosense,

Diamond, USA). Specifically, the EP studies were performed in: a healthy swine, and a swine that had a 5-week old chronic infarct. For the pathologic case, the infarction was generated by occluding the left circumflex artery (LCX) for 90'-min with a balloon catheter; this was followed by the retraction of the balloon, reperfusion of the LCX-territory and scar healing.

Figure 1 shows representative images taken during an in-vivo EP study in the infarcted heart. Fig 1a shows the EP catheter inserted into the cavity of LV of LCX-infarct heart, under fluoroscopy guidance. Figure 1b shows the location of each recorded point on a raw mesh reconstructed with the CARTO-XP analysis software. Figure 1c shows the reconstructed isochronal map of the LV-epicardium (isochrones 5 ms apart) with latest activation time points in blue and the earliest points in red. For each recorded point, the following information was stored: precise geometrical location (via the X, Y, Z coordinates), unipolar values, bipolar voltage values, early activation times (EAT), late activation times (LAT). From these recordings, isochronal maps of the depolarization phase can be constructed and displayed, or exported to other software tools for further analysis.

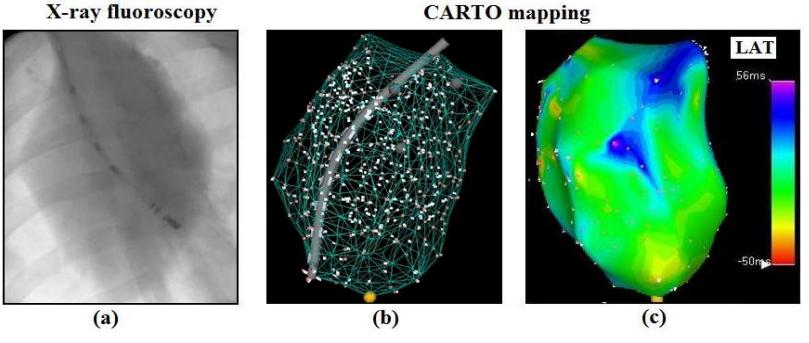

Fig. 1. The in-vivo EP study in the LCX-infarct heart: (a) recording EP catheter viewed under X-ray fluoroscopy, during its guidance into LV cavity for LV-endocardial mapping; (b) anatomical positions of the LV-endocardial CARTO points and associated mesh; and (c) reconstructed LV endocardial isochronal map (with the isochrones of depolarization times shown 5 ms apart)

At the completion of the EP studies, the hearts were explanted, gently preserved in formalin, and imaged using a 1.5Tesla SignaExcite GE MR scanner for anatomy, myocardial fiber directions previously described in [9, 12], and scar delineation. For these two hearts we used the following MR parameters: TE = 32 ms, TR = 700 ms, NEX=1, *b*-value ~ 700 (for healthy heart) and ~500 (for LCX-infarct heart), 7 directions for diffusion gradients, FOV/matrix = 10 cm, 256x256 acquisition matrix (yielding a 0.5 mm x 0.5 mm in plane spatial resolution), and an approximately 1.5 - 1.8mm slice thickness.

Figure 2a shows the in-vivo electro-anatomical voltage maps (EAVM) calculated from bipolar maps recorded in the LCX-infarct heart on the LV-endocardium and epicardium. To delineate the scar in these CARTO bipolar voltage maps, we used

clinical cut-off threshold voltage values < 1.5 mV; note that this threshold included dense infarct scar and peri-infarct areas (found at the border zone between dense scar and healthy myocardium). Figure 2b shows a 2D ex-vivo long-axis DW-MR image through this heart; elevated values of apparent diffusion coefficient (ADC-MRI) in the infarct areas are observable in the LCX territory. Very good correspondence was observed between the location and extent of the infarct area identified in both EP-CARTO maps and DW-MR images.

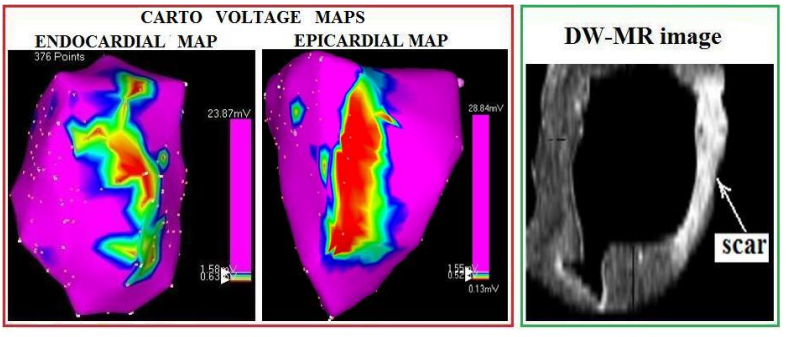

Fig. 2. Scar identification and characterization for the LCX-infarcted heart: (a) scar delineated in the endocardial EAVM (left) and epicardial EAVM (right) from bipolar maps; and b) a 2D long-axis view in an MR image with the scar delineated by the elevated (i.e., bright) ADC values compared to the values in remote, healthy tissue

2.2 Fiber Directions from DW-MRI and Histological Evaluation of the Scar

For both hearts, fiber directions for their corresponding anisotropic models were estimated from the first Eigen vectors, using reconstructed diffusion tensor images. Figure 3 shows the reconstructed fiber directions for both hearts.

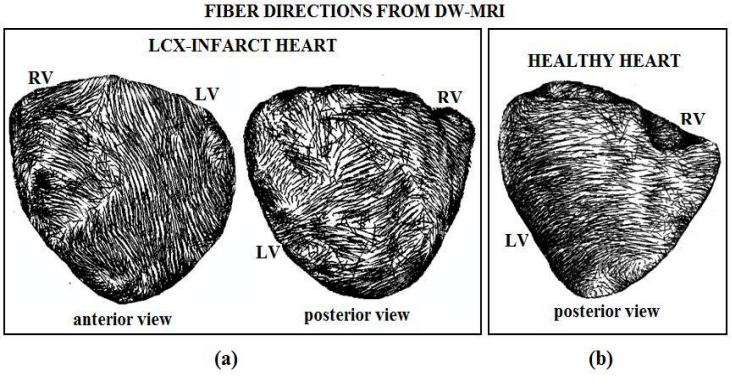

Fig. 3. Fiber directions from DW-MRI in the: (a) LCX-infarct heart; and (b) healthy heart

Histopathological analysis using Picrosirius Red stain in the LCX-infarct heart demonstrated dense collagen deposition, replacement of dead myocytes by fibrosis and severe alteration in myocardial tissue architecture in the infarct area. Figure 4 shows a 2D short-axial image through the 3D DW-MRI volume, that matched the corresponding histological samples taken from the scarred tissue and from a remote healthy area in the LV-endocardium of the LCX-infarcted heart. The stained slide was then scanned at a 5-micron resolution, using an Aperio-ImageScope system and saved as multi-resolution digital image.

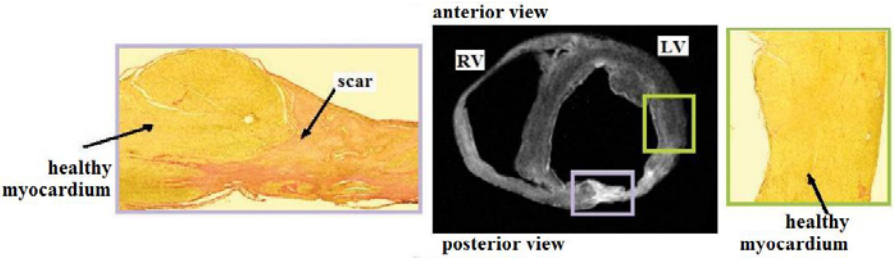

Fig. 4. Chronic infarct scar identified in the DW-MRI image and corresponding histological slide using Picrosirius Red stain that demonstrated collagen deposition (in red), with fibrosis in the infarct area replacing dead myocytes

For the construction of the 3D heart models, the anatomy of each heart was extracted from the un-weighted images (i.e., b=0) and then used to generate masks and volumetric meshes for the mathematical model; fiber directions were also integrated in these meshes. For the LCX-infarct heart, the 3D apparent diffusion coefficient (ADC) maps were further used to segment this heart into two zones: healthy tissue and infarct area (note that the latter is electrically inert and does not propagate electrical wave).

3 Forward Problems Applied to Computational Electrophysiology

3.1 A Simple Macroscopic Two-Variable Modelling Approach

We used the macroscopic Aliev-Panfilov model, which is based on reaction-diffusion type of equations, and has a monodomain approach (i.e., the intra- and extracellular spaces are collapsed into each other and represented by "bulk" tissue properties) as described in [13]. The term $-kV(V-a)(V-1)$ controls the fast processes (initiation and upstroke of action potential, AP) via the threshold parameter a, while r, determines the dynamics of the repolarization phase. In the system of equations (1)-(2) we solve for the AP, here noted V. We use Finite Element Methods, with an explicit Euler time integration scheme, as implemented in [14].

$$\frac{\partial V}{\partial t} = \nabla \cdot (D \nabla V) - kV(V-a)(V-1) - rV \tag{1}$$

$$\frac{\partial r}{\partial t} = -(\varepsilon + \frac{\mu_1 r}{\mu_2 + V})(kV(V-a-1) + r) \tag{2}$$

This simple two-variable model accounts for heart anisotropy via the diffusion tensor D (which depends on tissue 'bulk' conductivity, d). The anisotropy ratio is set to 0.25 for a wave propagating twice as fast along the fibers. The values for model's input parameters were assigned as in [15]; d was set to zero in the infarct scar (i.e., the electrical wave does not propagate through this scar zone).

The 3D-heart model (anatomy and scar) of the LCX-infarct heart is shown in Fig 5a. The simulation results for this heart were achieved as follows: the normal sinus rhythm was simulated by applying a square pulse of 5 ms seconds and maximum amplitude (i.e., V = 1, since the output has normalized values for AP). In the absence of realistic Purkinje fibers integrated in the model, this stimulus was

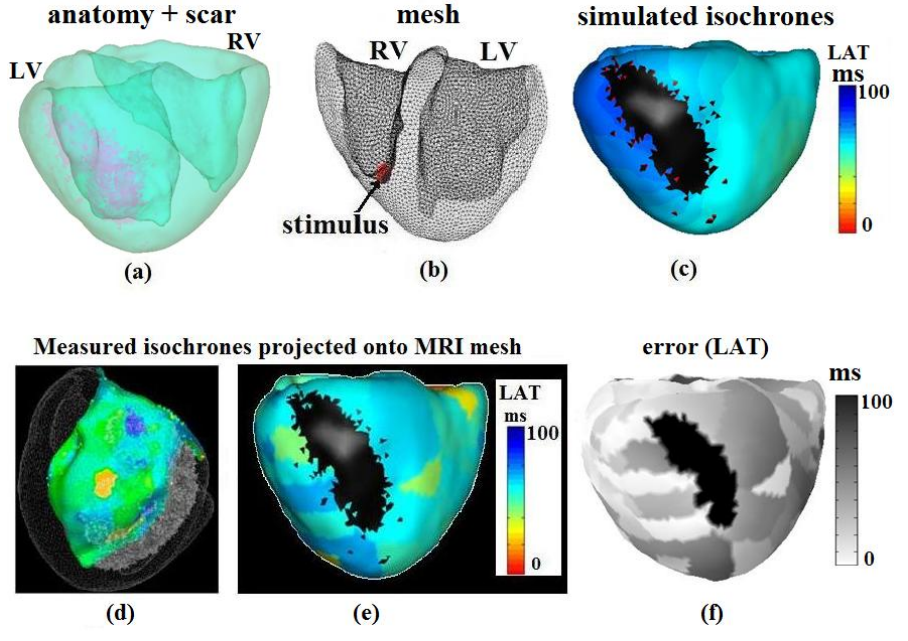

Fig. 5. Results obtained using the image-based model built for the LCX-infarct heart: (a) the 3D MRI-based heart model; (b) the location where the stimulus was applied at the apex of the RV-endocardium; (c) simulated isochrones of depolarization phase represented by LAT times (ms), displayed in a lateral-view. Corresponding experimental isochronal maps projected onto: (d) LV-endocardium, (e) epicardium; and (f) absolute error between the measured depolarization times on the epicardium and corresponding map of simulated depolarization times (ms).

applied on the endocardium (at the apex) to mimic a normal activation wave, with an apex-to-base propagation. Note that in the CARTO-endocardial maps we identified a conduction block on the septum of left ventricle with an LBBB morphology, which was mimicked by applying the stimulus only at the RV-apex (see red dot in Fig. 5b). Figure 5c shows the simulated depolarization map (lateral-posterior view of the epicardium, with scar in black), with early depolarization times in red and late activation times in blue. Figures 5d and 5e show the experimental endocardial and epicardial isochronal maps (in a lateral-posterior view) projected onto the mesh, whereas Fig. 5f shows the error in activation times (i.e., absolute difference between measured and simulated depolarization times).

Figure 6 shows a good correspondence between experimental and simulated isochronal maps of depolarization times, for the healthy heart. Experimental isochrones are represented from the RV-endocardium (Fig 6a), for LV-endocardium (Fig 6b), as well the epicardial maps (Fig 6c), all maps have early depolarization times in red, and latest activation times, LAT, in blue. The black points in Fig 6d (cross-section view through the heart) represent the locations where the stimuli (square pulse, $V = 1$) were applied in the 3D MRI-based computer model (selected on the endocardium of RV and LV); these points closely reproduced the locations of early activation points determined from experimental endocardial maps. The resulting epicardial breakthrough, had similar pattern and timing in experiment and simulations.

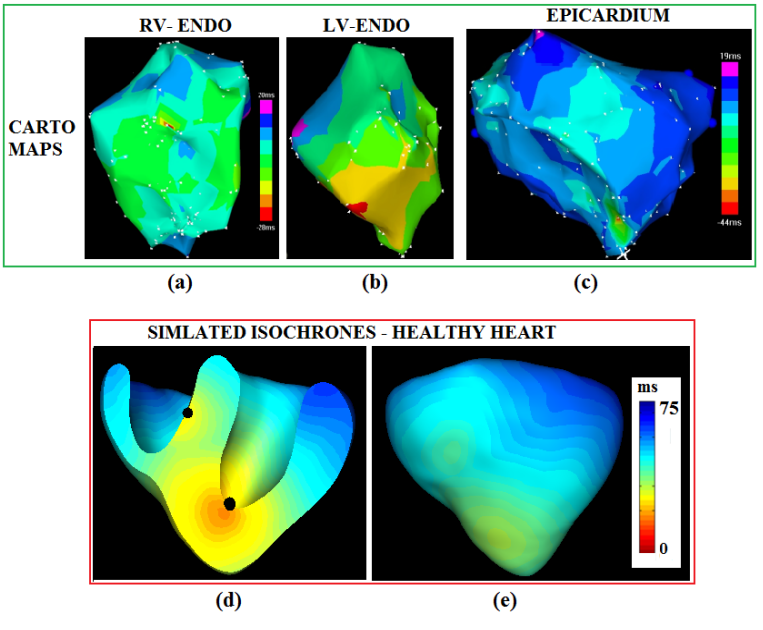

Fig. 6. Experimental (a-c) and simulation (d-e) results obtained in the healthy heart

For the Aliev-Panfilov model, when using time steps of $5x10^{-5}$s, the simulation time of 0.8s of the heart cycle on a mesh of approximately 190,000 elements (with an average element size of approximately 1.2 mm), is about 40 min on an Intel ® Core™ 2 duo CPU, T5550 @1.83GHz, with 4 GB of RAM.

3.2 Other Mathematical Models and Computation Results of Forward Problems

We further investigated the feasibility of applying other mathematical approaches to the forward problem, in order to compute the wave propagation. For this, we selected two other well-established models: one simpler than the A-P model (i.e., the Eikonal model) and the other one more complex (i.e., the bidomain model).

The Eikonal model is the simplest and fastest mathematical model used in cardiac electrophysiology [16]; thus, is attractive to clinical applications [2]. It computes only the wave front propagation (i.e., the depolarization phase Td of the electrical wave) based on the anisotropic Eikonal equation (3):

$$v^2\left(\nabla T_d^t D \nabla T_d\right)=1 \tag{3}$$

Where the v is the local speed of the wave and D is the diffusion tensor. In the fiber orientation coordinates, D = diag(1, ρ, ρ), where ρ is the anisotropy ratio between conduction velocity (i.e., speed of wave) in transverse and longitudinal directions.

The bidomain model offers the most complete description of electrical behaviour of myocardium. It explicitly accounts for the current flow in the two spaces (extra-/intercellular) through non-linear PDEs (4) and (5):

$$A_m(C_m(\partial_t V_m + I_{ion}(V_m,y,c)-I_{stim}(x,t)) = div(G_i \nabla(V_m+\phi_e)) \tag{4}$$

$$div((G_i+G_e)\nabla\phi_e) + div(G_i \nabla Vm)) =0 \tag{5}$$

where V_m is the transmembrane potential, c is ion concentration (/specie), A_m is the cellular surface to volume ratio, Cm is membrane capacitance, G is the conductance of a space extra- or intracellular. The system models these spaces from an electro-static point of view; thus, these equations need to be coupled via a non-linear model that describes the current flow from one space into the other. In this paper, for the computation of this current, we use the model proposed by Tusscher-Noble-Noble-Panfilov described in [17]. For the numerical method and algorithm, the equations are discretized using the P1 Lagrange FEM, and a first order implicit/explicit time-stepping strategy. The evolution of V_m and ϕ_e is solved implicitly using the optimal pre-conditioner defined in [18]. For the boundary conditions of the system (4)-(5), we use the following constraints: $G_i \nabla(V_m+\phi_e)\cdot n = 0$ and $G_e \nabla\phi_e \cdot n = 0$.

Figure 7 shows a comparison of the depolarization times obtained using the three models. For each model, the results are shown in: top-view (Figs 7a, 7d and 7g), longitudinal/transmural cross-section view (Figs 7b, 7e and 7h), and anterior view, respectively (Figs 7c, 7f and 7i). A good agreement between the LATs was observed, along with very small notable differences in the pattern of activation times and epicardial breakthrough. Note that, for these particular set of simulations, in all three

models, we started the excitation at the RV-apex and LV-apex on the endocardium. For the A-P and Eikonal models we used an anisotropy ratio of 0.25. For A-P, most parameters were set as in [15] except for $d = 2$ (to tune a speed of wave that resulted in ventricles depolarization within ~92 ms); for the Eikonal model we set a speed of 65 cm/s (along the fiber). For the bidomain model, we used the following conductivities (mS/cm) for the longitudinal & transverse directions, and for the intra-/extracellular spaces: $G_i(l) = 1.741$; $G_i(t) = 0.193$; $G_e(t) = 1.970$ and $G_e(l) = 3.906$. Other membrane characteristics were set to $C_m = 1$ mF/cm^2 and $A_m = 250$ cm^{-1}; an external current of 52 μA/cm^2 was applied to start the depolarization and a time step of 1x10^{-4}s was used to solve explicitly the equations for ion concentrations. The time required to compute 0.2 s of heart cycle using the bidomain model was ~70 min, and less than 1 min for the Eikonal model.

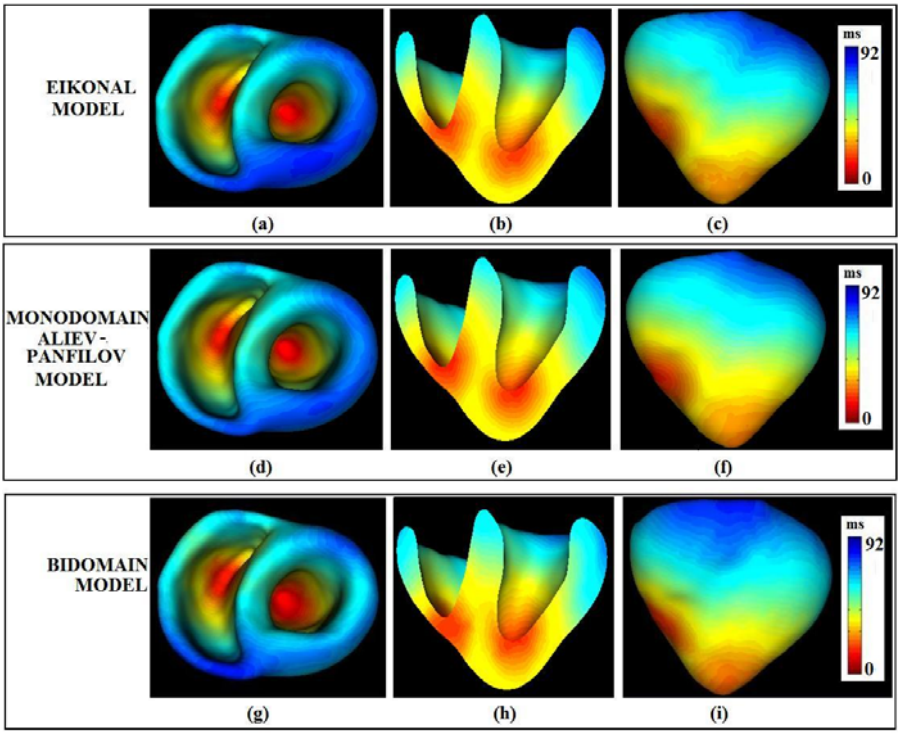

Fig. 7. Comparison between the simulated isochronal maps obtained using: (a-c) the Eikonal model, (d-f) the Aliev-Panfilov model; and (g-i) the Bidomain model (see more details in the text)

The errors between simulated depolarization times obtained using the models are shown in Fig 8. Specifically, for the comparison between Aliev-Panfilov model and Eikonal model, we computed a mean error ± S.D of 2.76 ± 1.67 ms (calculated over all vertices in the mesh) with an RMS error 7.4 ms. For the comparison between Aliev-Panfilov and bidomain model, we obtained a mean error 6.1 ± 3.9 ms, and a 12.96 ms RMS error.

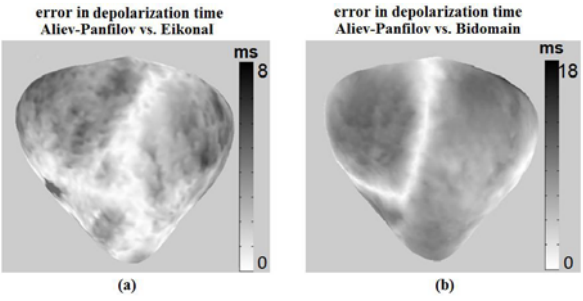

Fig. 8. Absolute difference between computed depolarization times (ms): (a) Aliev-Panfilov vs. Eikonal model; and (b) Aliev-Panfilov vs. Bidomain model

4 Discussion

Advances leading to improved disease management and therapy planning, as well as outcomes assessment, would have immediate impact on the quality of life in patients with prior myocardial infarction. Integration of EP measures with image-based models is useful because it can help us understand a realistic 3D transmural propagation of the cardiac excitation wave. Thus, current research efforts are focused on improving non-invasive imaging methods, and on developing image-based predictive computer models using forward [8, 9, 11, 20] and inverse problems [2, 10, 19] designed to customize such models. With this respect, sharing experimental data, as well as comparing modelling results between research groups are important milestones; the EP simulation challenge (at STACOM'10 and STACOM'11) represents an excellent joined effort toward achieving this goal.

In this paper, we described in detail several steps undertaken in the development of a pre-clinical framework that integrates experimental in-vivo CARTO data and high-resolution ex-vivo DW-MRI data from the two swine hearts (healthy and with chronic infarction), given to the STACOM'11 participants. The DW-MRI data allowed us to delineate the scar, as well as to determine the fiber directions, which is important to consider for a correct representation of tissue anisotropy. For the modelling part, we presented forward approaches to cardiac modelling and computed only the propagation of depolarization wave. Further, isochronal maps depolarization times were calculated, and then compared with measured depolarization times recorded by EP-CARTO. Our simulation results suggest that the two-variable Aliev-Panfilov model can give a good representation of the wave propagation. In a first approximation, the conductivity parameter d, which tunes the conduction velocity and, consequently, the depolarization times was tuned using a "trial and error" approach. This adjustment of d minimized the errors between simulations and experiments, and resulted in a good correspondence with respect to associated activation patterns and isochronal maps. We acknowledge that a more accurate tuning of model parameters could be performed by: i) partitioning the heart in smaller (AHA) zones, ii) analyzing the infarct heterogeneities (i.e., classify the infarct in scar and border zone), and iii) optimizing the parameters adjustment as per the methods proposed in [10, 19].

Fast predictive models that require short computation times are desirable, particularly for models aiming to be integrated into clinical platforms. Applications of cardiac image-based computer models, limitations, validation, parameterization, as well as accuracy and associated errors between predictions and measurements, are all important. As a preliminary test, for the healthy heart, we included simulations obtained using the simplest model (Eikonal) and a complex model (Bidomain); our results demonstrated small differences between the computed activation pattern and depolarization maps using these three models. In the future, we will design specific tests to demonstrate when simplified models fail to produce satisfactory results, and thus complex models should be used (in particular for modelling the pathologic cases).

To conclude, evaluation of 3D image-based computer models performance and utility, as well as customization using in-vivo EP measurements will help us to use such models correctly, and to properly target them for different applications.

Acknowledgement. This work was financially supported in part by a grant from the Canadian Institutes of Health Research (MOP93531).

References

1. Stevenson, W.G.: Ventricular scars and VT tachycardia. Trans. Am. Clin. Assoc. 120, 403–412 (2009)
2. Chinchapatnam, P., Rhode, K.S., Ginks, M., Rinaldi, C.A., Lambiase, P., Razavi, R., Arridge, S., Sermesant, M.: Model-Based imaging of cardiac apparent conductivity and local conduction velocity for planning of therapy. IEEE Trans. Med. Imaging 27(11), 1631–1642 (2008)
3. Bello, D., Fieno, D.S., Kim, R.J., et al.: Infarct morphology identifies patients with substrate for sustained ventricular tachycardia. J. Am. College of Cardiology 45(7), 1104–1110 (2005)
4. Wu, E.X., Wu, Y., Tang, H., Wang, J., Yang, J., Ng, M., et al.: MR-DT imaging study of post infarct myocardium; structural remodeling in a porcine model. Magn. Res. Med. 58(4), 687–695 (2007)
5. Wu, M.T., Tseng, W.Y., Su, M.Y., Chiou, K.R., Reese, T.G., Yang, C.F.: DT-MRI mapping of fiber architecture remodeling in human myocardium after infarction. Circulation 114, 1036–1045 (2006)
6. Clayton, R.H., Panfilov, A.V.: A guide to modelling cardiac electrical activity in anatomically detailed ventricles. Progress in Biophysics & Molecular Biology – Review 96(1-3), 19–43 (2008)
7. Hunter, P.J., Crampin, E.J., Nielsen, P.M.: Bioinformatics, multi-scale modeling and the IUPS Physiome project. Brief Bioinform. 9(4), 333–343 (2008)
8. Vadakkumpadan, F., Rantner, L., Tice, B., Boyle, P., Prassl, A., Vigmond, E., Plank, G., Trayanova, N.: Image-based models of cardiac structure with applications in arrhythmia and defibrillation studies. J. Electrocardiology 42(2), 15 (2009)
9. Pop, M., Sermesant, M., Lepiller, D., Truong, M., McVeigh, E.R., Crystal, E., Dick, A.J., Delingette, H., Ayache, N., Wright, G.A.: Fusion of optical imaging and MRI for the evaluation and adjustment of macroscopic models of cardiac electrophysiology: a feasibility study. Medical Image Analysis 13(2), 370–380 (2009)

10. Relan, J., Pop, M., Delingette, H., Wright, G.A., Ayache, N., Sermesant, M.: Personalisation of a cardiac electrophysiology model using optical mapping and MRI for prediction of changes with pacing. IEEE Trans. Biomed. Eng. (January 20, 2011) (in press)
11. Camara, O., Sermesant, M., Lamata, P., Wang, L., Pop, M., Relan, J., De Craene, M., Delingette, H., Liu, H., Niederer, S., Plank, G., Pashaei, A., Romero, D., Sebastian, R., Wong, K.C.L., Zhang, H., Ayache, N., Frangi, A.F., Shi, P., Smith, N.P., Wright, G.A.: Inter-model consistency and complement-tarity: learning from ex-vivo imaging and electrophysiological data towards an integrated understanding of cardiac physiology. Prog. Biophys. Molec. Biol. (in press, 2011)
12. Helm, P., Tseng, H.J., Younes, L., McVeigh, E.R., Winslow, R.L.: Ex-vivo 3D diffusion tensor imaging and quantification of cardiac laminar structure. Magn. Res. Med. 54, 850–859 (2005)
13. Aliev, R., Panfilov, A.V.: A simple two variables model of cardiac excitation. Chaos, Soliton and Fractals 7(3), 293–301 (1996)
14. Sermesant, M., Delingette, H., Ayache, N.: An electromechanical model of the heart for image analysis and simulations. IEEE Transaction in Medical Imaging 25(5), 612–625 (2006)
15. Nash, M.P., Panfilov, A.V.: Electromechanical model of excitable tissue to study reentrant cardiac arrhythmias. Prog. Biophys. Molec. Biol. 85, 501–522 (2004)
16. Keener, J.P., Sneeyd, J.: Mathematical physiology. Springer, Heidelberg (1998)
17. Ten Tusscher, K.H., Noble, D., Noble, P.J., Panfilov, A.V.: A model for human ventricular tissue. Am. J. Physiol. Heart Circ. Physiol. 286(4) (2004)
18. Pierre, C.: Preconditioning in bidomain model with almost linear complexity. Journal of Computational Physics (in press, 2011)
19. Konukoglu, E., Relan, J., Cilingir, U., Menze, B., Chinchapatnam, P., Jadidi, A., Cochet, H., Hocini, M., Delingette, H., Jais, P., Haissaguerre, M., Ayache, N., Sermesant, M.: Efficient probabilistic model personalization integrating uncertainty on data and parameters: applications to Eikonal-Difusion models in cardiac electrophysiology. Prog. Biophys. Molec. Biol. (in press, 2011)
20. Pop, M., Sermesant, M., Mansi, T., Crystal, E., Ghate, S., Peyrat, J.-M., Lashevsky, I., Qiang, B., McVeigh, E.R., Ayache, N., Wright, G.A.: Correspondence between simple 3D MRI-based computer models and in-vivo EP measurements in swine with chronic infarctions. IEEE Trans. Biomed. Eng. 58(12) (2011)

Personalisation of a 3D Ventricular Electrophysiological Model, Using Endocardial and Epicardial Contact Mapping and MRI

Jatin Relan, Maxime Sermesant*, Hervé Delingette, and Nicholas Ayache

Inria, Asclepios Project, Sophia Antipolis, France
maxime.sermesant@inria.fr

Abstract. Personalisation, i.e. parameter estimation of a cardiac ElectroPhysiology (EP) model is needed to build patient-specific models, which could then be used to understand and predict the complex dynamics involved in patient's pathology. In this paper, we present an EP model personalisation approach applied to an infarcted porcine heart, using contact mapping data and Diffusion Tensor MRI. The contact mapping data was gathered during normal sinus rhythm, on the ventricles *in-vivo*, endocardially as well as epicardially, using a CARTO mapping system. The Diffusion Tensor MRI was then obtained *ex-vivo*, in order to have the true cardiac fibre orientations, for the infarcted heart. Both datasets were then used to build and personalise the 3D ventricular electrophysiological model, with the proposed personalisation approach. Secondly, the effect of using only endocardial mapping or epicardial mapping measurements, on the personalised EP model was also tested.

1 Introduction

Modelling of the cardiac electrophysiology has been an important research interest for the last decades, but in order to translate this work into clinical applications, there is an important need for personalisation of such models, i.e. estimation of the model parameters which best fit the simulation to the clinical data. Cardiac model personalisation is required to develop predictive models that can be used to improve therapy planning and guidance.

There is a large variety of cardiac electrophysiology models for myocyte action potential developed at cellular and sub-cellular scales [1,2,3]. Cardiac tissue and whole-heart electrophysiological computations of these models are based on the principles of reaction-diffusion systems [1]. According to the reaction term computation, these models can be broadly categorised as Biophysical Models (BM), Phenomenological Models (PM) and Generic Models (GM). BM [2,3] model ionic currents and are the most complete and complex but are less suitable for parameter estimation from clinical data due to a high computational cost and to the lack of observability of their parameters. PM [4] are based on PDEs and are of intermediate complexity level and less computationally expensive. GM [5,6] represent simplified action potentials and are the least complex. Simple Eikonal

* Corresponding author.

O. Camara et al. (Eds.): STACOM 2011, LNCS 7085, pp. 14–22, 2012.

Models (EM) [7] model the action potential propagation in the cardiac tissue without modelling the action potential itself. They can be very fast to compute [8], but less reliable in arrhythmia predictions due to the complexity of both the refractoriness and the curvature of the wavefront.

In this paper, we present a coupled personalisation framework (EK-MS), which is fast and combines the benefits of an Eikonal (EK) model with those of a simplified biophysical model, the Mitchell-Schaeffer (MS) model. The fast 3D EK model is used to estimate the tissue conductivity parameter over the ventricles from the contact mapping of endocardial & epicardial surface potentials, using an adaptive iterative algorithm. This is then used to set the conductivity parameter of the 3D MS model, which could be then used for reliable arrhythmia predictions.

In the past years, authors have focused on the personalisation of the PM and MS model on 3D volumes [9,10] using optical and MR data. Recently, we have proposed the coupled personalisation approach (EK-MS), with an application to a patient with infarction, using non-contact mapping and 3D MRI [11]. The contributions of this paper are: 1) Application of the EK-MS personalisation approach to an infarcted porcine heart, using contact mapping data and DT-MRI, and 2) Study of the effect of using either endocardial only or epicardial only measurements, on the EP model personalisation.

2 3D Electrophysiology Model with Chronic Infarction

The models used in the EK-MS personalisation approach are simple Eikonal (EK) model and a simplified biophysical model, the Mitchell-Schaeffer (MS) model.

The EK model simulates the propagation of the depolarization wave in quiescent tissue, ignoring repolarisation phase. The EK model is governed by eikonal-diffusion (ED) equation and is based on anisotropic Fast Marching Method (FMM). More detailed analysis can be found in [8]. The non-linear EK model equation is solved using a fixed point iterative method combined with a very fast eikonal solver, on the bi-ventricular geometry, as explained in [7].

The MS model [12] is a 2-variable simplified biophysical model derived from the 3-variable Fenton Karma (FK) ionic model [13]. It models the transmembrane potential as the sum of a passive diffusive current and several active reactive currents including a sodium ion (influx) current and a potassium ion (outflux) current. Unlike FK model, it does not model the Calcium ion current. More detailed analysis can be found in [12]. The MS model is modelled as reaction diffusion equations and is spatially integrated using a linear tetrahedral mesh of the bi-ventricular myocardium, taking into account the fiber orientation as well, and is temporally integrated using a semi-implicit time integration scheme (MCNAB) [14].

In this paper, we focus only on conductivity estimation, thus chronic scars are modelled with low conductivity in the ischemic zones. While the gray zones (the regions around scars) had conductivity estimated from the data, as shown later.

However, we had shown the approach of modelling chronic scars along with APD heterogeneity in [11].

3 Contact Mapping and MR Dataset Processing

In this paper, we performed the adjustments on an infarcted porcine heart. The acquired data consists of contact mapping data gathered on the ventricles *in-vivo* during normal sinus rhythm, endocardially as well as epicardially, using a CARTO mapping system, and a Diffusion Tensor MRI (DT-MRI) representing geometry and fiber orientation *ex-vivo*.

The 3D mapping system (CARTO) localizes the extracellular potentials at points in 3D space and on a 3D ventricular geometry acquired by connecting all those points, during the interventional procedure, using invasive catheters. The measurement of extracellular potentials could be unipolar or bipolar (Fig 2(b)). The mapping system then extracts the local activation times (LAT) for the contact points in 3D space and produces a local activation map on the 3D ventricular geometry, representing the action potential wave propagation pattern, as shown in Fig 2(a).

The DT-MRI is used to reconstruct the cardiac fibers using the principal eigenvector of the diffusion tensor. It is also used to create the 3D ventricular model, as shown in Fig 1.

The 3D ventricular geometry acquired using CARTO is then registered to the 3D ventricular model. The measurement contact points of the CARTO, are then projected on to the 3D ventricular geometry using closest points projections (Fig 2(c & d)). Finally, the LATs measured at those points is then interpolated on the endocardial and epicardial surface, to have a rough guess on the action potential wave propagation, as shown in Fig 3.

The interpolated epicardial and endocardial LAT maps on the 3D ventricular model, are then used as input for EP model personalisation. In order to penalise the point projection and interpolation errors, we use the projection distance of the points and the interpolated projection distance maps (Fig 4) as a spatial penalising factor in the conductivity estimation procedure, as explained later.

4 Building Personalised Electrophysiological Model

4.1 Coupled Personalisation Approach (EK-MS)

Cardiac tissue conductivity is a crucial feature for the detection of conduction pathologies. The Apparent Conductivity (AC) of the tissue can be measured by a parameter d in the EK model [8]. For computational affordability reasons, we use the simplest EK model for fast tissue conductivity estimation, with an adaptive iterative algorithm based on gradient free optimisation, as explained in details in [8,11]. For reliable pathological predictions with chronic scars, we couple the personalised parameters of the EK model to a relatively more complicated biophysical MS model. The coupling procedure is explained in details in [11].

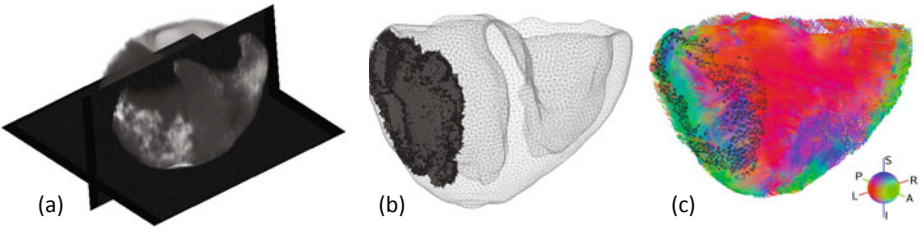

Fig. 1. (a) Volume rendering of DT-MRI to visualize scars (bright in intensity), (b) 3D ventricular model constructed from DT-MRI, with labelled scar zones (black), (c) cardiac fiber construction from DT-MRI, showing the fiber disorientation in and around scars (black contour)

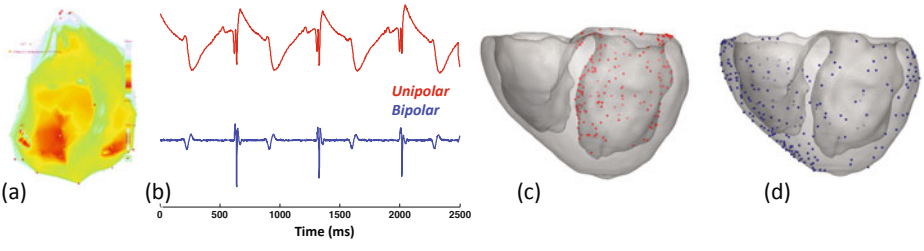

Fig. 2. (a) LAT map constructed on a 3D ventricular geometry using CARTO mapping system, (b) Unipolar & bipolar extracellular potentials measured using invasive catheters, (c & d) measurement contact points (red - endocardial & blue - epicardial) gathered in 3D space using CARTO, registered and then projected on the endocardial (c) & epicardial (d) surface respectively, of the 3D ventricular model

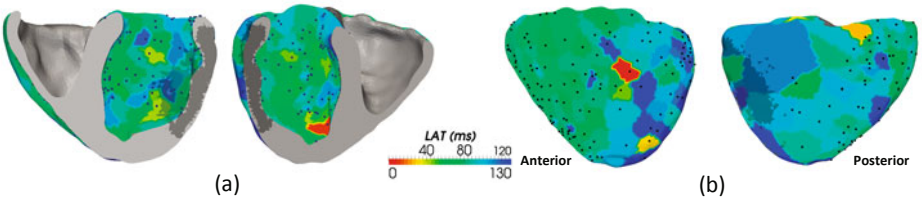

Fig. 3. LAT maps construction from linear interpolation of the measurement contact points (black) for (a) endocardial and (b) epicardial surfaces of the 3D ventricular model

The input to the algorithm are the linearly interpolated LAT maps on the surface of the ventricular model (Fig 3). The cost function for each zone to minimise, is adapted here, and is given as

$$J(d_{zone}) = \sum_{\forall i \in S \cap zone} \left(PenaltyFactor_i * \left(LAT_i - DT_i^{sim}\left(d_{zone}\right)\right)\right)^2 \quad (1)$$

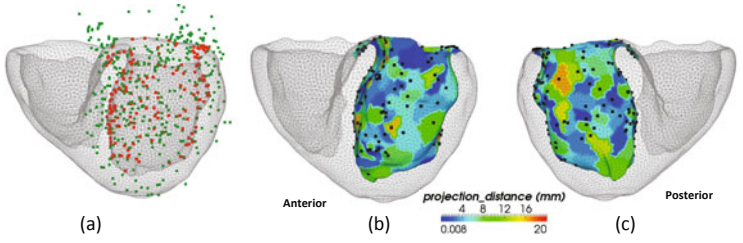

Fig. 4. Projection distance calculated and interpolated from the contact points (black), on to the endocardial surface

with vertex i in zone, belonging to the surface S having measures, DT^{sim} are the simulated depolarisation times from the EK model, and $PenaltyFactor$ is computed from the normalisation of interpolated projection distance maps (Fig 4(b & c)), with 1.0 representing lowest distance and $8.14e^{-9}$ representing the farthest distance.

4.2 Application

In order to assess the influence of mapping (endocardial and epicardial) details on the model personalisation, we tested model personalisation with various configurations as follows.

With Endocardial and Epicardial Mapping. In the state of the art in clinics, simultaneous endocardial and epicardial mappings are the finest amount of acquisition details possible for capturing the action potential wave propagation dynamics during normal sinus rhythm. Thus we use the apparent conductivity estimated using this mapping data, as the closest approximation of the true tissue conductivity distribution, with the proposed personalisation approach. The mean error on activation times, after model personalisation was 15.93 ms. Fig 5(a & b) shows the activation isochrones after personalisation, and Fig 6(a & b) shows the AC distribution, along with the residual activation time error after optimisation.

With Endocardial Mapping. Now we use only the endocardial mapping, to estimate the AC distribution. The mean error on activation times, after personalisation was 15.26 ms. Fig 5(e) shows matching of the LV endocardial isochrones with Fig 5(a) and data (Fig 3(a)), but has a large misfit of the epicardial isochrones (Fig 5(f) compared against Fig 5(b) and Fig 3(b)). Thus the reproducibility of the isochrones on the epicardial side is highly prone to errors. This is confirmed by the large prediction errors on the epicardial surface, as shown in Fig 7(c).

With Epicardial Mapping. Here we use the epicardial mapping, to estimate the AC distribution. The mean error on activation times, after personalisation was 9.59 ms. Fig 5(c & d) shows good matching of the LV endocardial isochrones, as well as epicardial isochrones with Fig 5(a & b) and data (Fig 3(a & b)). Thus epicardial mapping could be sufficient enough to reproduce the true wave propagation dynamics, as compared to endocardial mapping data. This is confirmed by the low prediction errors on the endocardial surface, as shown in Fig 7(b).

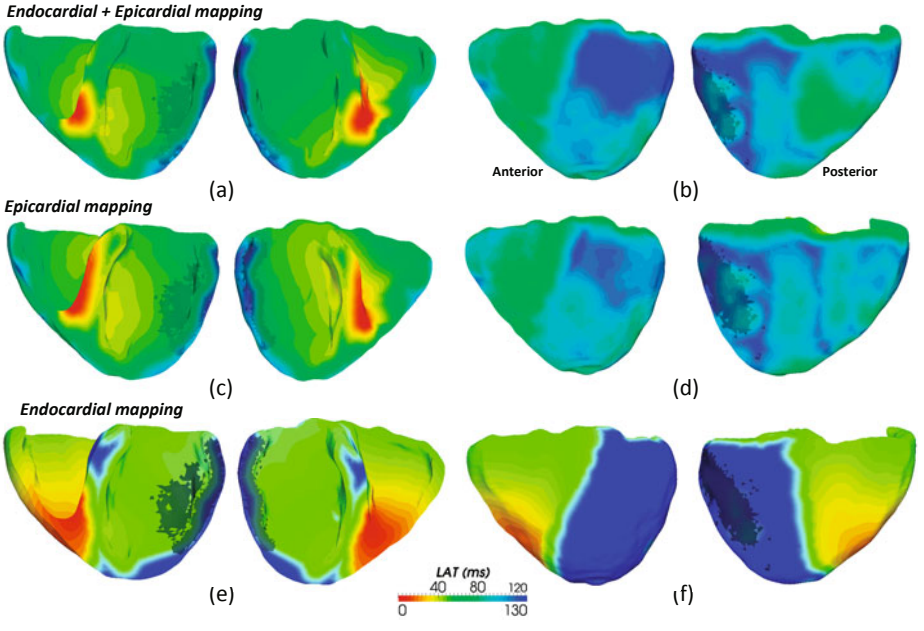

Fig. 5. Volumetric activation times after personalisation using endocardial & epicardial mapping (top row), only epicardial mapping (middle row) and only endocardial mapping (bottom row)

5 Conclusion

In this work, we have shown the application of a proposed coupled personalisation framework to the contact mapping data of an infarcted porcine heart. The cardiac fibre orientations estimated from DT-MRI were incorporated inside the model personalisation for a more accurate tissue conductivity estimation. We also tested the influence of mapping details on the model personalisation algorithm. We found that personalisation using epicardial mapping gave a conductivity estimation closest to the one obtained with personalisation using both endocardial and epicardial mapping, and also showed a low prediction error. On the other hand, the personalisation with endocardial mapping had an important

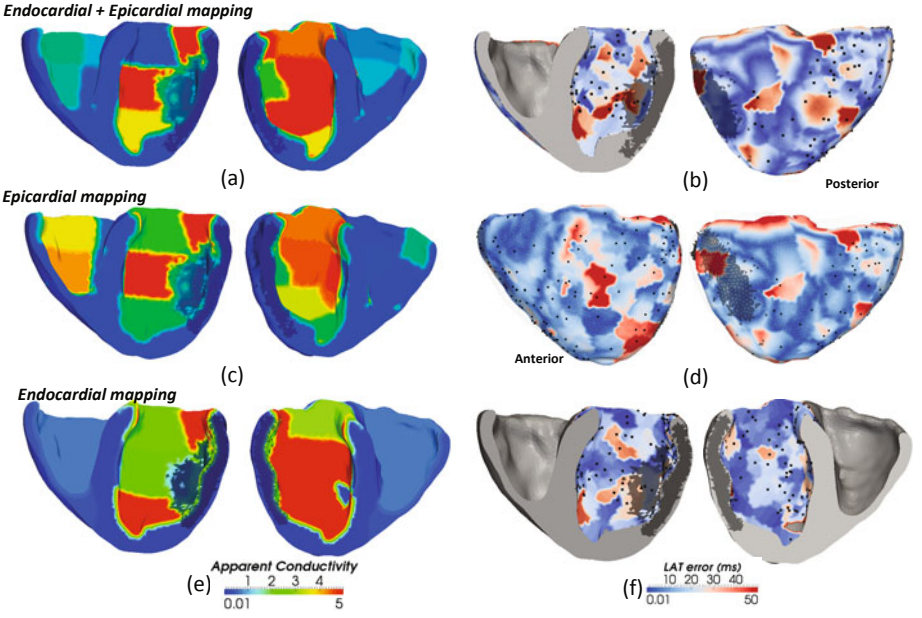

Fig. 6. The first two columns show estimated AC distributions and last two columns show residual error after personalisation, for various configurations explained

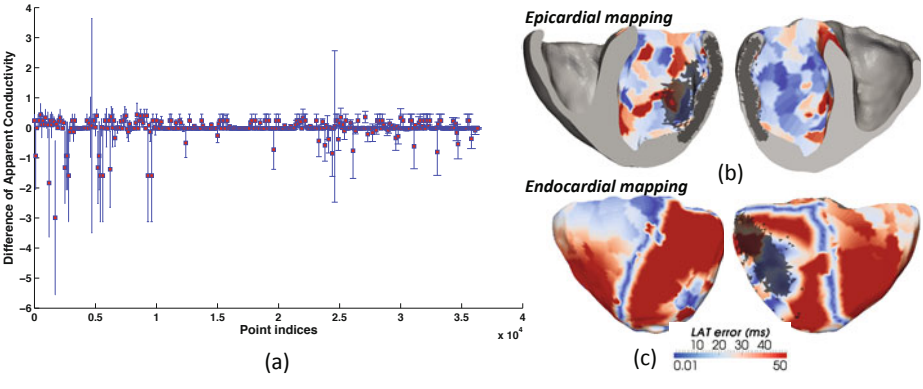

Fig. 7. Graph: mean and standard deviation of the difference of AC values estimated for the 3 configurations. Zero mean with low standard deviation shows good agreement between the AC values for a given data point. Other figures show the prediction error on the endocardial side, for personalisation with epicardial mapping (b) and on the epicardial side, for personalisation with endocardial mapping.

deviation from the estimated distribution obtained with both endocardial & epicardial mapping. It also had an important prediction error on the epicardial surface. Thus, within this experimental setting, epicardial mapping proved to

be a sufficient acquisition to reproduce a tissue conductivity distribution, closer to the one estimated using both endocardial and epicardial mapping. This was also the case when the personalisation was done on similar data from a clinical case [15]. Such finding has to be tested on other configurations, for different healthy and pathological cases.

Acknowledgements. The research leading to these results was partially funded by the the euHeart project (FP7/2007-2013 under grant agreement n 224495). We thank Dr. Mihaela Pop and Dr. Graham Wright both of Sunnybrook Research Institute, (Toronto - Canada) for providing the EP-CARTO and DT-MRI data, and to Dr. Thomas Mansi (Siemens Corporate Research, Princeton, NJ, USA) for the mesh generation and fibre extraction for the infarct heart, and to Dr. Maxime Sermesant (INRIA, Asclepios project - Sophia Antitpolis France) for mesh generation and fibre extraction for the normal heart".

References

1. Fenton, F.H., Cherry, E.M.: Models of cardiac cell. Scholarpedia 3(8), 1868 (2008)
2. Noble, D., Varghese, A., Kohl, P., Noble, P.: Improved guinea-pig ventricular cell model incorporating a diadic space, IKr and IKs, and length-and tension-dependent processes. The Canadian Journal of Cardiology 14(1), 123 (1998)
3. Ten Tusscher, K., Noble, D., Noble, P., Panfilov, A.: A model for human ventricular tissue. American Journal of Physiology-Heart and Circulatory Physiology 286(4), H1573 (2004)
4. Bueno-Orovio, A., Cherry, E., Fenton, F.: Minimal model for human ventricular action potentials in tissue. Journal of Theoretical Biology 253(3), 544–560 (2008)
5. Fitzhugh, R.: Impulses and physiological states in theoretical models of nerve membrane. Biophysical Journal 1(6), 445–466 (1961)
6. Aliev, R.R., Panfilov, A.V.: A simple two-variable model of cardiac excitation. Chaos, Solitons & Fractals 7(3), 293–301 (1996)
7. Sermesant, M., Konukoğlu, E., Delingette, H., Coudière, Y., Chinchapatnam, P., Rhode, K., Razavi, R., Ayache, N.: An Anisotropic Multi-front Fast Marching Method for Real-Time Simulation of Cardiac Electrophysiology. In: Sachse, F.B., Seemann, G. (eds.) FIHM 2007. LNCS, vol. 4466, pp. 160–169. Springer, Heidelberg (2007)
8. Chinchapatnam, P., Rhode, K., Ginks, M., Rinaldi, C., Lambiase, P., Razavi, R., Arridge, S., Sermesant, M.: Model-based imaging of cardiac apparent conductivity and local conduction velocity for diagnosis and planning of therapy. IEEE Transactions on Medical Imaging 27(11), 1631–1642 (2008)
9. Lepiller, D., Sermesant, M., Pop, M., Delingette, H., Wright, G., Ayache, N.: Cardiac Electrophysiology Model Adjustment Using the Fusion of MR and Optical Imaging. In: Metaxas, D., Axel, L., Fichtinger, G., Székely, G. (eds.) MICCAI 2008, Part I. LNCS, vol. 5241, pp. 678–685. Springer, Heidelberg (2008)
10. Relan, J., Pop, M., Delingette, H., Wright, G., Ayache, N., Sermesant, M.: Personalisation of a cardiac electrophysiology model using optical mapping and mri for prediction of changes with pacing. IEEE Transactions on Biomedical Engineering (2011)

11. Relan, J., Chinchapatnam, P., Sermesant, M., Rhode, K., Ginks, M., Delingette, H., Rinaldi, C., Razavi, R., Ayache, N.: Coupled personalization of cardiac electrophysiology models for prediction of ischaemic ventricular tachycardia. Interface Focus 1(3), 396 (2011)
12. Mitchell, C., Schaeffer, D.: A two-current model for the dynamics of cardiac membrane. Bulletin of Mathematical Biology 65(5), 767–793 (2003)
13. Fenton, F., Karma, A.: Vortex dynamics in three-dimensional continuous myocardium with fiber rotation: filament instability and fibrillation. Chaos 8(1), 20–47 (1998)
14. Relan, J., Sermesant, M., Delingette, H., Pop, M., Wright, G., Ayache, N.: Quantitative comparison of two cardiac electrophysiology models using personalisation to optical and mr data. In: IEEE International Symposium on Biomedical Imaging: From Nano to Macro, ISBI 2009, pp. 1027–1030. IEEE (2009)
15. Konukoglu, E., Relan, J., Cilingir, U., Menze, B., Chinchapatnam, P., Jadidi, A., Cochet, H., Hocini, M., Delingette, H., Jaïs, P., Haïssaguerre, M., Ayache, N., Sermesant, M.: Efficient probabilistic model personalization integrating uncertainty on data and parameters: Application to eikonal-diffusion models in cardiac electrophysiology. Progress in Biophysics and Molecular Biology (accepted, 2011)

Transmural Electrophysiologic and Scar Imaging on Porcine Heart with Chronic Infarction

Linwei Wang[1], Fady Dawoud[2], Ken C.L. Wong[3], Heye Zhang[4], Huafeng Liu[5], Albert C. Lardo[2], and Pengcheng Shi[1]

[1] Computational Biomedicine Laboratory
Rochester Institute of Technology, Rochester, NY, USA
[2] School of Medicine, Johns Hopkins University, Baltimore, MD, USA
[3] Asclepios Research Project, INRIA, Sophia-Antipolis, France
[4] Chinese University of Hong Kong, Hong Kong
[5] Zhejiang University, Hangzhou, China

Abstract. Myocardial scar is the most common substrate for malignant arrhythmia and cardiac arrest. Radiofrequency ablation, as one of the emerging mainstream therapies, is subject to limited success rate because of the inadequate assessment of scar substrates that currently relies on electrophysiologic (EP) map acquired on endocardial and occasionally epicardial surfaces. As myocardial scar is often complex with shapes varying with the depth of the myocardium, endocardial and epicardial maps may differ substantially, and may fail to identify mid-wall fibrosis that exist in $\sim$ 30% of patients with nonischemic cardiomyopathy. Alternatively, noninvasive and transmural scar delineation by current imaging techniques does not always show electrically altered functional substrates. Participating in CESC'11, we presented a new application of the previously developed method of transmural EP imaging, where epicardial unipolar electrograms acquired by CARTO together with MRI-derived ventricular anatomical data of a porcine heart with chronicle myocardial infarction were used for computing the transmural EP dynamics and subsequently classifying conduction blocks of the porcine heart. Validation was performed versus CARTO electroanatomic maps on the epicardium and endocardium, as well as DW-MRI enhanced anatomical scars. This allowed detailed examinations of the reported method in computing transmural EP anomalies using only surface data and without any condition-specific knowledge *a priori*, which could not be achieved with either current EP mapping or medical imaging techniques alone.

Keywords: Transmural electrophysiology, scar delineation, myocardial infarction, electroanatomic mapping, DW-MRI.

1 Introduction

Myocardial scar is the most common substrate for ventricular arrhythmia such as tachycardia (VT), which could result in hemodynamic collapse with syncope or sudden death if sustained [6]. For the management of ventricular arrhythmia,

O. Camara et al. (Eds.): STACOM 2011, LNCS 7085, pp. 23–32, 2012.

radiofrequency catheter ablation has emerged to be a mainstream therapy. The current state of the art for VT ablation relies on the electroanatomic maps acquired during electrophysiologic (EP) mapping, performed by moving the mapping catheter from site to site on the endocardial and occasionally epicardial surfaces. The commonly-used surface voltage map acquired during sinus rhythm represent scars as low-voltage ($\leq 1.5mV$) regions [6]. More precisely, activation map of VT provides a surface view of re-entrant circuits for localization of ablation targets, though VT mapping can be very difficult because it requires the VT to be inducible in EP laboratory and hemodynamically tolerated for some period of time [9]. Besides being time consuming and technical challenging, the invasive point-to-point EP mapping is confined to heart surfaces with limited measurement sites. As myocardial scar is often complex with shapes varying with the depth of the myocardium, endocardial and epicardial maps may differ substantially, and may fail to identify mid-wall fibrosis that exist in $\sim 30\%$ of patients with nonischemic cardiomyopathy [7]. Alternatively, high-resolution delay contrast enhanced imaging [3] can be used to characterize myocardial necrosis in the transmural dimension. Nevertheless, tomographic imaging detects only anatomical scars but not electrically-altered functional conduction abnormality.

Computational EP imaging was motivated to achieve the strengths of both techniques, namely, to reconstruct subject-specific EP dynamics deep into the myocardium in a noninvasive manner, from which both structural and functional electrically-altered anomalies can be delineated. Participating in the 2011 Electrophysiology Simulation Challenge (CESC'11), we presented a new application of the previously described computational method of transmural EP imaging [11,12] in a porcine heart with chronic infarction. This method was originally developed to combine body-surface electrocardiographic signals and image-derived anatomic data to *noninvasively* produce subject-specific EP activity deep into the myocardium [11], and to further delineate electroanatomic substrates from the abnormal spatiotemporal EP features [12]. Adapted to the CESC'11 dataset, this study investigated the performance of the method in using epicardial CARTO measurements for inferring transmural information. Validation was carried out versus a comprehensive dataset including transmural DW-MRI scar delineation and CARTO electroanatomic maps on both the epi- and endocardium. It allowed a detailed investigation of the presented method in mapping transmural and electrical-altered anomalies, which could not be achieved by either the current EP mapping or tomographic imaging techniques alone. The new application of using only epicardial maps to compute transmural and endocardial information might also be of interest in clinical EP study for circumventing the need of introducing a catheter inside the high pressure LV chamber.

2 Methods

2.1 Experimental Setup and Data Processing

The experiment was performed on the data set (*in-vivo* EP measurements and 3D *ex-vivo* MRI of the ventricles) obtained in a porcine heart with chronic

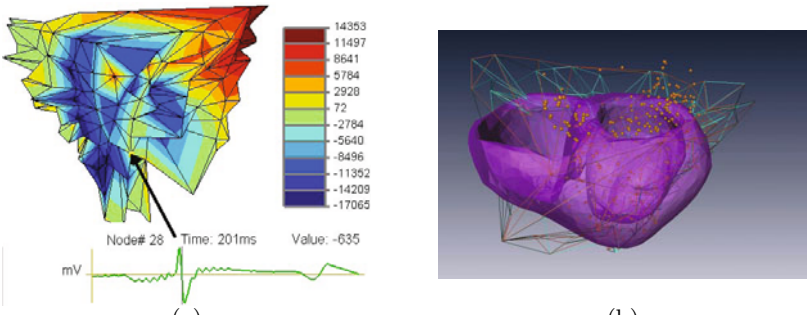

Fig. 1. (a) Snapshot of unipolar potential map on CARTO epicardial geometry, reconstructed from 341 CARTO measurement sites. (b) Alignment of CARTO endocardial (yellow spheres) and epicardial (line mesh) surfaces with image-derived ventricular model (transparent purple).

infarction (approximately 5-6 weeks old), provided through STACOM'11 EP Challenge. The *in-vivo* electroanatomic unipolar voltage maps on the epicardium and the image-derived anatomical data were used as input to the proposed method of transmural EP imaging, and the electroanatomic unipolar voltage maps on the endocardium and 3D DW-MR scar delineation were used for validation of the computed transmural and endocardial EP and scar outcome.

More specifically, two types of input data were prepared for the study. The anatomic data of the ventricles, including the 3D geometry and fiber structure, were generated from 3D DW-MR images acquired *ex-vivo* with $< 1mm^3$ voxel size on a 1.5T GE Signa-Excite scanner. A finite-element mesh of the ventricles (with 190181 elements and 36384 vertices) was made available through CESC'11. For algorithmic and computational feasibility of the presented inverse method, a meshfree model with 2084 nodes and associated fiber structure was generated from the provided mesh to represent the same ventricles at the macroscopic scale with much lower spatial resolution.

Epicardial unipolar electrograms acquired by CARTO-XP systems (Biosense Webster, Inc., Diamond Bar, CA) were used as the input electrical signals (Fig 1 (a)) to the algorithm. Spatial registration was performed manually between the CARTO epicardial surface and the image-derived ventricular model (Fig 1 (b)). After alignment, the epicardial CARTO points were projected to the closest points on a *pericardial* surface dilated from the epicardium of the image-derived ventricular model so that it encloses the entire ventricles (Fig 2 (a)). Since the epicardial electrograms were acquired point-by-point over multiple beats, temporal alignment of these signals was done based on the best matching QRS complexes in body surface lead III. Out of 341 epicardial CARTO points, 87 had cross correlation $\geq 90\%$ and were selected as input signals. Fig 2 (b) illustrates the locations of the 87 input unipolar potential signals after being projected to the closest points on the pericardial surface, where the color of the nodes encodes the distance between the original CARTO points and the projected pericardial points. Note that the input signals reside mainly on the

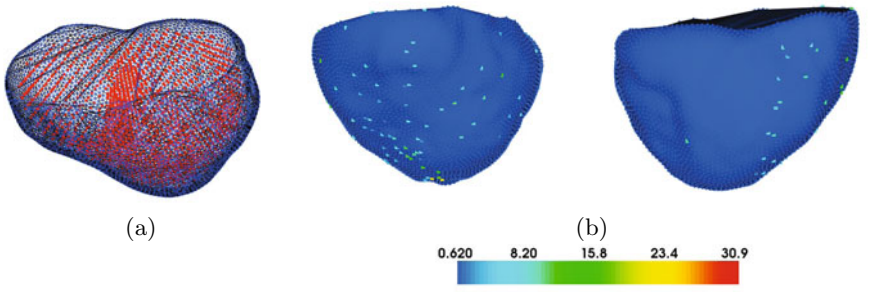

Fig. 2. (a) Illustration of the *pericardial* surface (blue wired mesh) dilated from the image-derived ventricular epicardium and encloses the mesh-free model of the ventricles (red points) . (b) Locations of the input unipolar signals projected to the closest points on the pericardium from CARTO surface; the color encodes the projection distance.

free wall of the right ventricle, and the projection error is $8.39 \pm 5.90mm$ with the minimum distance $0.62mm$ and maximum distance $30.94mm$. This introduces extra errors into the input data for the subsequent transmural EP imaging.

2.2 Transmural EP and Scar Imaging

The previously described method of transmural EP and scar imaging [11,12] is briefly reviewed in the following for background knowledge. This method was originally motivated to tackle the severely ill-posed inverse problem to infer transmural EP dynamics from body-surface electrocardiographic data. To constrain the otherwise non-unique inverse solution of transmural TMP dynamics, a simple two-variable, phenomenological model of transmembrane potential (TMP) dynamics (*Aliev-Panfilov* model) [1] was adopted. While this dimensionless macroscopic model substantially simplifies the EP biophysics, models with higher levels of complexity might aggravate the issue of identifiability given that the observational data represent the organ-level collective EP behavior of the whole heart. To mimic real-world applications where *a priori* knowledge of specific conditions is hardly available, no patient-specific knowledge was incorporated in this model except image-derived anatomic information of the ventricles. Therefore, electrical stimuli used to initialize the model were applied on the experimentally-established locations of regular earliest ventricular excitation [4], and model parameters were all fixed at literature values [1]. Relation between transmural TMP and extracellular potential on any surface enclosing the ventricles is described by quasi-static electromagnetic theory [8] and numerically modeled as a linear mapping model [10]. Instead of the body-surface, here the observation surface was moved to a pericardial surface enclosing the ventricles.

Estimation of subject-specific transmural TMP dynamics is formulated into *maximum a posteriori* probabilistic estimation to take into account the uncertainty that exist in the generic models and the input data (electrical data and anatomic data). After transforming the physiological models into a stochastic

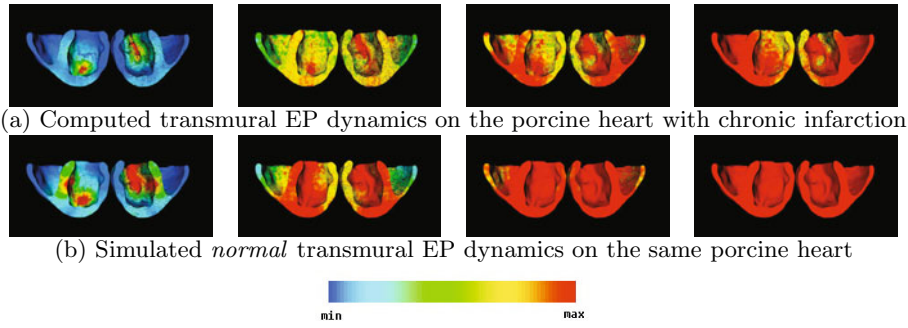

(a) Computed transmural EP dynamics on the porcine heart with chronic infarction

(b) Simulated *normal* transmural EP dynamics on the same porcine heart

Fig. 3. Comparison of computed transmural EP dynamics versus simulation with *Aliev-Panfilov* model assuming normal conditions. Color encodes the amplitude of transmembrane potential and black contours represent isopotential lines. Compared to the fast, simultaneous activation of both ventricles expected in a healthy heart (b), the output of condition-specific transmural EP dynamics shows conduction delay and latest activation in the inferior-lateral wall of the LV.

state space system, TMP estimation was carried out based on the unscented Kalman filter [5] to accommodate the nonlinearity and high dimensionality of this problem. Model and data errors are assumed to be zero-mean Gaussian noises with predefined covariance matrices. After obtaining the estimates of personalized transmural TMP dynamics, two primary EP features, activation time (AT) and action potential duration (APD), are extracted and their deviances from normal conditions are equally weighted to generate a new feature that characterizes electrical conduction abnormality. K-means clustering is applied on this feature to eventually discriminate between healthy and electrophysiologically-altered tissues. For more details refer to [11,12].

3 Results and Discussions

Fig 3 (b) shows the constraints for transmural EP imaging, namely the generic EP dynamics with electrical stimuli applied on regular first-excited LV and RV endocardial sites [4]. Fig 3 (a) shows the transmural EP activation computed under this constraint, where evident delay is exhibited particularly in inferior-lateral LV. In addition to the conduction block located at inferior-lateral LV, the reconstructed pattern also resembles the pattern of left bundle branch block (LBBB) where sequential right ventricle to left ventricle activation (Fig 3 (a)) replaces the simultaneous ventricular activation (Fig 3 (b)).

The computed transmural EP dynamics was investigated at 3 levels. First, pericardial electrograms and epicardial activation pattern generated from the output were compared to epicardial CARTO data. Second, transmural conduction block detected by the method was validated with anatomical scar delineated from DW-MRI. Note that DW-MRI only provides information regarding anatomical scars, while the presented method detects electrically-altered

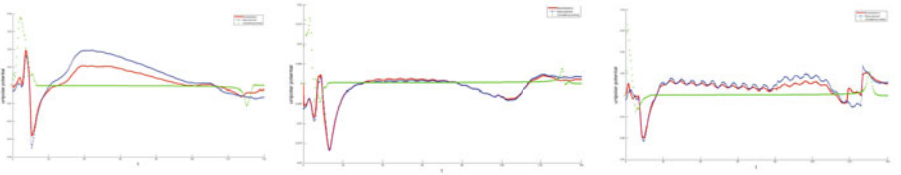

(a) CARTO pts ♯87 (b) CARTO pts ♯194 (c) CARTO pts ♯265

Fig. 4. Examples of unipolar electrograms produced by the transmural EP dynamics on three different CARTO measurement sites. Red solid: estimation results. Blue dot-dash: measurements. Green dot: simulation of normal conditions.

substrates that might relate to either structural or functional anomalies. Third, endocardial electrical activation was compared to CARTO maps acquired from the LV endocardium. Note that currently no transmural electrical data is available and validation on endocardial data is the next best available option. Registration between the LV endocardial surface obtained by CARTO and the MR-derived ventricular mesh was carried out manually taking into consideration the general shape of the chamber and the location of DW-MRI enhanced scar.

Epicardial Validation: First, we investigated the electrical signals produced on the pericardium and epicardium by the computed transmural EP. Fig 4 shows the examples of pericardial electrograms produced by the transmural EP dynamics, in comparison to the input measurements acquired by CARTO. For reference, the pericardial electrograms produced by simulated *normal* EP dynamics are also displayed. These simulated electrograms (green dotted line) correspond to the generic knowledge provided to the algorithm, which differ substantially from the CARTO measurements (blue dotted-dashed line). The algorithm was able to assimilate the condition-specific information from the measurement, correct the erroneous prior knowledge and produce the results close to the measurement taking into account measurement noises. The averaged relative root mean squared error (RRMES) and correlation coefficient (CC) between the 87 estimated and measured electrograms are 0.49 ± 0.27 and 0.83 ± 0.17, respectively, indicating that the computed output resembles the measurements closely pattern-wise but might involve larger amplitude difference on some locations.

To activation time measured on 223 epicardial CARTO points were then projected to the closest points on the image-derived ventricular epicardium. The distance between the CARTO points and the projected epicardial points is $6.68 \pm 5.54mm$, ranging between $0.37mm$ and $33.60mm$. Fig 5 compares the computed epicardial activation maps with CARTO activation maps at anterolateral and inferolateral views of LV epicardium. The consistence of septal to lateral activation and late lateral LV activation is visually apparent. Two types of quantitative errors were calculated: the difference between the computed and measured activation time is $6.51 \pm 7.08ms$ on the 223 projected points; the difference between the computed activation time on the entire epicardial surface (5028 points) and that linearly interpolated from the CARTO measurement is

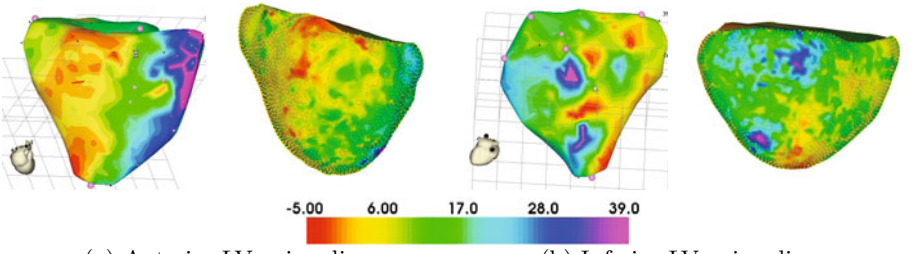

(a) Anterior LV epicardium (b) Inferior LV epicardium

Fig. 5. Comparison of epicardial activation maps computed from the presented method (right) and acquired from CARTO systems (left) at anterior and inferior views of LV. The color encodes the value of activation time in milliseconds.

$8.91 \pm 8.16ms$. Note that in CARTO activation mapping, scar points were assigned activation times although it might be not showing much activity.

Transmural Validation: Second, we analyzed the computed transmural EP features. Fig 6 (a) and (b) shows the transmural maps of activation time (AT) and action potential duration (APD) extracted from the computed EP dynamics. Note that if EP signals were only mapped or computed on heart surfaces, no EP information would be available along the transmural dimension of the heart wall as shown in Fig 6. On one hand, late activation and shortened action potential duration of the computed EP were highlighted in inferior-lateral LV, consistent with the location of infarct delineated from DW-MRI. On the other hand, late activation and shortened APD also exhibit on a small area of middle-anterior LV and septum, where no structural scars have been detected in DW-MRI.

Fig 7 (a) illustrates the transmural view of EP substrates detected by the algorithm, which is further displayed in Fig 7 (b) in meshfree points superimposed with the scar mass delineated from DW-MRI. As shown, the presented algorithm detected two major conduction blocks in the LV according to the features of delayed AT and shortened APD. One cluster of detected electroanatomic substrates resides in lateral-inferior LV (yellow meshfree points), primarily overlapping with the DW-MRI enhanced anatomical scar (light blue, red highlights the overlapping) and extending to the adjacent areas. This is consistent with the findings in [2] regarding the correlations between anatomically and electrically defined substrates. The other cluster of detected conduction block (green) corresponds to septal wall where no structural scar is enhanced in the DW-MRI. This corresponds to the LBBB-like transmural EP pattern and might indicate a functional conduction delay at septum. However this can not be confirmed with available data. In terms of AHA 17-segment division of LV, the DW-MRI enhanced anatomical scars reside in inferior-lateral segments $11, 5, 10, 6, 16, 15, 12, 4$ in descending order of percentage. The presented method clustered the electrically-altered substrates at 4 septal segments $2, 3, 8, 9$ that indicate septal functional block, the inferior-lateral segments $4, 5, 11, 6, 16$, $10, 15$ that has

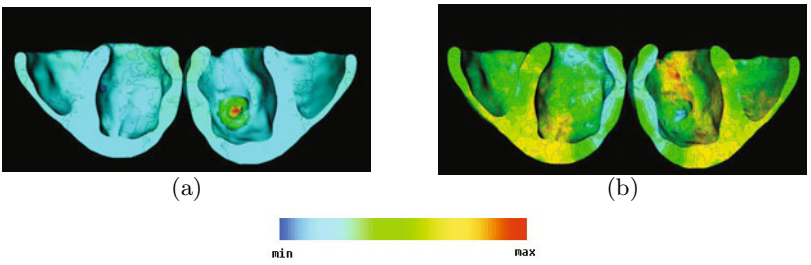

Fig. 6. (a) Computed transmural activation map. (b) Computed transmural map of action potential duration. The color encodes values of activation time and action potential duration, respectively.

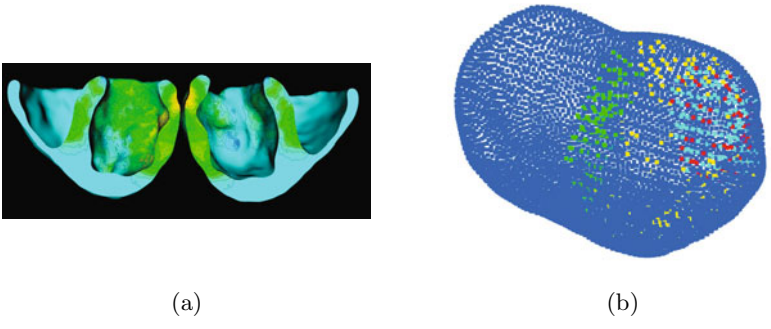

Fig. 7. (a) Detected conduction blocks. The color bar is the same as Fig 6 and encodes the feature value for detecting block. (b) Detected conduction blocks (yellow and green) represented by meshfree points, superimposed with DW-MRI enhanced anatomical scar (light blue); red highlights the overlapping.

anatomical scars, and a small percentage at anterior segments $1, 3$ that explains the difference between anatomical scar and electrical dysfuntions.

Endocardial Validation: Finally, we compared the endocardial activation maps of left ventricles to those acquired from CARTO systems. The activation time measured on 208 LV endocardial CARTO points were projected to the closest points on the image-derived endocardium of LV. The distance between the CARTO points and the projected endocardial points is $4.91 \pm 3.58mm$, ranging between $0.06mm$ and $22.16mm$. Fig 8 compares the computed endocardial activation maps with CARTO activation maps at inferiolateral views of the endocardium, both of which show similar activation from apex to base and from septal to lateral where areas latest to activation reside on inferolateral base wall. The difference between the computed and measured activation time is $10.22 \pm 8.22ms$ on the 208 projected points; the difference between the computed activation time on the entire endocardial surface (2357 points) and that linearly interpolated from the CARTO measurement is $9.68 \pm 7.51ms$.

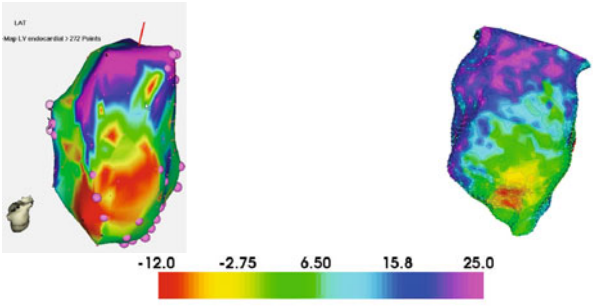

Fig. 8. Comparison of inferiolateral LV endocardial activation maps computed from the presented method (b) and acquired from CARTO systems (a)

Discussions: This study presented a new application of the previously-described transmural EP imaging method to compute transmural and endocardial EP dynamics from measured epicardium or pericardial signals. Without any *a priori* subject-specific knowledge other than anatomical data, the computed endocardial EP dynamics agree qualitatively and quantitatively well with electroanatomic maps and the detected transmural EP substrate is consistent with DW-MRI data. Furthermore, the computed transmural EP dynamics indicates a functional septal block that can not be detected in DW-MRI while the LBBB-like EP pattern agrees well with the CARTO maps. This demonstrated that the presented method was able to use generic EP knowledge and limited electrical measurements to reconstruct transmural EP abnormalities that might be of important diagnostic values and that can not be detected by either EP mapping or medical imaging techniques alone. It also indicates a potential application of this method in EP study to potentially circumvent some of the complications of introducing a catheter inside the high pressure LV chamber.

Experimental validation of transmural EP imaging faces many challenges and difficulties caused by the errors introduced in the data acquisition and processing procedure. First, the CARTO surface and image-derived ventricular model were created in different spaces and needed to be properly aligned. Second, the projection of CARTO points to the pericardium that serves the observation surface introduced extra errors into the input signals. Third, the validation was further complicated by the errors generated in the projection of CARTO points and the interpolation from hundreds of CARTO measurements to the entire epicardial or endocardial surfaces with thousands of nodes. Furthermore, the validation using data from point-by-point mapping requires care in data recording and processing because of the beat-beat variability and occasional preventricular complexes (PVC's) especially when mapping the endocardium. Rejecting epicardial electrograms from dissimilar lead III beats was a reasonable way to overcome variability of activation over different beats.

Because of these experimental challenges, a promising alternative of validation could be performed on computer-simulated testbed, where complex ionic models

can be used to simulate and mimic various sinus-rhythm or pacing conditions as realistically as possible. The proposed transmural EP imaging, constrained by macroscopic phenomenological EP model, can then be performed on these simulated and noise-corrupted datasets and be validated with the simulated ground truth of transmural EP and scar details.

Acknowledgements. We thank Dr. Mihaela Pop and Dr. Graham Wright (Sunnybrook Research Institute, Toronto, Canada) for providing the EP-CARTO and DT-MRI data, and to Dr. Thomas Mansi (Siemens Corporate Research, Princeton, NJ, USA) for the mesh generation and fiber extraction for the infarct heart, and to Dr. Maxime Sermesant (INRIA, Asclepios project, Sophia Antitpolis, France) for mesh generation and fiber extraction for the normal heart.

References

1. Aliev, R.R., Panfilov, A.V.: A simple two-variable model of cardiac excitation. Chaos, Solitions & Fractals 7(3), 293–301 (1996)
2. Ashikaga, H., Mickelsen, S.R., Ennis, D.B., et al.: Electromechanical analysis of infarct border zone in chronic myocardial infarction. American Journal of Physiology - Heart and Circulatory Physiology 289, H1099–H1105 (2005)
3. Ashikaga, H., Sasano, T., Dong, J., et al.: Magnetic resonance-based anatomical analysis of scar-related ventricular tachycardia. implications for catheter ablation. Circulation 101, 939–947 (2007)
4. Durrer, D., van Dam, R.T., Freud, G.E., Janse, M.J., Meijler, F.L., Arzbaecher, R.C.: Total excitation of the isolated human heart. Circulation 41, 899–912 (1970)
5. Julier, S.: The scaled unscented transform. International Journal for Numerical Methods in Engineering 47, 1445–1462 (2000)
6. Nazarian, S.: CMR for mapping the missing dimension in ventricular ablation. Journal of the American College of Cardiology: Cardiovascular Imaging 3(3), 286–288 (2000)
7. Nazarian, S., Bluemke, D.A., Lardo, A.C., et al.: Magnetic resonance assessment of the substrate for inducible ventricular tachycardia in nonischemic cardiomyopathy. Circulation 112, 2821–2825 (2005)
8. Plonsey, R.: Bioelectric phenonmena. McGraw Hill, New York (1969)
9. Stevenson, W.G., Delacretaz, E.: Strategies for catheter ablation of scar-related ventricular tachycardia. Current Cardiology Reports 2, 537–544 (2000)
10. Wang, L., Zhang, H., Wong, K., Liu, H., Shi, P.: Electrocardiographic simulation on personalized heart-torso structures using coupled meshfree-BEM platform. International Journal of Functional Informatics and Personalized Medicine 2(2), 175–200 (2009)
11. Wang, L., Zhang, H., Wong, K., Liu, H., Shi, P.: Physiological-model-constrained noninvasive reconstruction of volumetric myocardial transmembrane potentials. IEEE Transactions on Biomedical Engineering 5(2), 296–315 (2010)
12. Wang, L., Zhang, H., Wong, K., Liu, H., Shi, P.: Noninvasive computational imaging of cardiac electrophysiology for 3-d infarct. IEEE Transactions on Biomedical Engineering 58(4), 1033–1043 (2011)

A Multimodal Database for the 1^{st} Cardiac Motion Analysis Challenge

Catalina Tobon-Gomez[1,2], Mathieu De Craene[1,2], Annette Dahl[3], Stam Kapetanakis[3], Gerry Carr-White[3], Anja Lutz[4], Volker Rasche[4], Patrick Etyngier[5], Sebastian Kozerke[3], Tobias Schaeffter[3], Chiara Riccobene[1,2], Yves Martelli[1,2], Oscar Camara[1,2], Alejandro F. Frangi[1,2,⋆⋆], and Kawal S. Rhode[3,⋆⋆]

[1] Center for Computational Imaging & Simulation Technologies in Biomedicine (CISTIB), Universitat Pompeu Fabra (UPF), Barcelona, Spain[⋆]
[2] Networking Biomedical Research Center on Bioengineering, Biomaterials and Nanomedicine (CIBER-BBN), Barcelona, Spain
[3] Division of Imaging Sciences & Biomedical Engineering, King's College London, London, United Kingdom[⋆⋆]
[4] Department of Internal Medicine II - Cardiology, University of Ulm, Ulm, Germany
[5] Medisys Research Lab, Philips Healthcare, Suresnes, France

Abstract. This paper describes the acquisition of the multimodal database used in the *1^{st} Cardiac Motion Analysis Challenge*. The database includes magnetic resonance (MR) and 3D ultrasound (3DUS) datasets from a dynamic phantom and 15 datasets from healthy volunteers. The MR acquisition included cine steady state free precession (SSFP), whole-heart turbo field echo (TFE), and 4D tagged MR (tMR) sequences. From the SSFP images, the end diastolic anatomy was extracted using a deformable model of the left ventricle (LV). The LV model was mapped to the tMR coordinates using DICOM information. From the LV model, 12 landmarks were generated (4 walls at 3 ventricular levels). These landmarks were manually tracked in the tMR data over the whole cardiac cycle by two observes using an in-house application with 4D visualization capabilities. Finally, the LV model was registered to the 3DUS coordinates using a point based similarity transform. Four institutions responded to the challenge by providing motion estimates for the data. Preliminary results are presented for one of the volunteer data sets.

1 The Challenge

Despite the fast development of analysis tools in medical imaging, their translation to the clinical environment is limited. One of the main limitations for

[⋆] This work has been funded by the Spanish Ministry of Innovation and Science under the CICYT programme (TIN2009-14536-C02-01), and the European Commission Seventh Framework Programme (FP7/2007-2013) under the euHeart project (FP7-ICT-2007-2-224495).

[⋆⋆] A.F. Frangi and K.S. Rhode share senior coauthorship.

O. Camara et al. (Eds.): STACOM 2011, LNCS 7085, pp. 33–44, 2012.

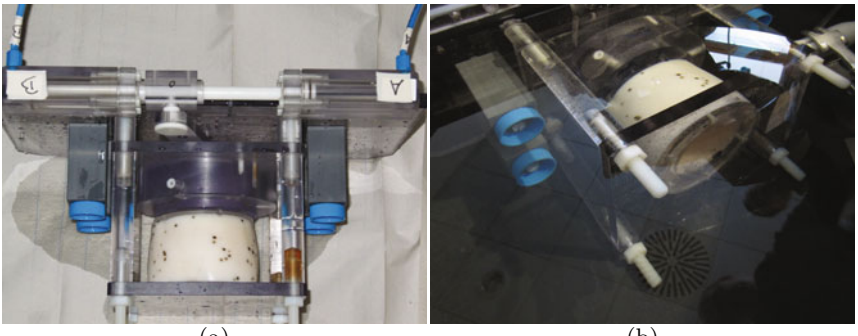

(a) (b)

Fig. 1. The phantom: (a) placed inside the actuator and (b) immersed in water for echocardiography acquisition

algorithms to be adopted in the clinical arena is the lack of proper validation strategies. Even for algorithms with extensive in-house validation, a comparison with *state-of-the-art* techniques is difficult due to differences on the evaluated datasets (i.e. type of patients, number of cardiac phases, image quality, image resolution).

Since 2007, some workshops within the Medical Image Computing and Computer Assisted Intervention (MICCAI) conference have provided a unique opportunity to evaluate algorithms from multiple research groups. In the context of a *challenge*, the workshop organizers provide datasets to test the algorithms. Several researchers process the datasets with their algorithms and submit their results to be evaluated in a unified manner. For an updated list of relevant challenges, please visit `http://www.grand-challenge.org/`.

This paper describes the acquisition of the multimodal database used in the 1^{st} *Cardiac Motion Analysis Challenge* (cMAC). The objective of this challenge was to evaluate the accuracy and reproducibility of different motion analysis algorithms. Each participant quantified myocardial motion in the left ventricle from cine and/or tagged Magnetic Resonance (MR) and/or 3D ultrasound (3DUS) modalities. Four institutions responded to the challenge and preliminary results are presented for one volunteer data set.

2 The Data

The database includes a dynamic phantom [1] and 15 healthy volunteers. In both cases, MR and 3DUS images were obtained.

– **The phantom:** the phantom was constructed with polyvinyl alcohol (PVA, Lenticats, GeniaLab, Braunschweig, Germany). This material offers mechanical durability, variable stiffness and good MR imaging properties. The phantom was placed in an MR-compatible air-pressured actuator (see Fig. 1-a).

The actuator compresses and rotates the PVA according to a preset heart rate (in our case $60bpm$). For the 3DUS acquisition, the phantom was inserted in a container filled with water to improve echogenicity conditions (see Fig. 1-b). The phantom actuator was synchronized with the MR scanner and echocardiography system by sending a $10mVpp$ electrocardiography (ECG) waveform to the optically decoupled standard ECG monitoring unit. The datasets were acquired at the Department of Internal Medicine II - Cardiology, University of Ulm, Germany.

– **The volunteers:** fifteen healthy volunteers without clinical history of cardiac disease were recruited (3 female, aged 28 ± 5 years). Demographics and body surface area measurements are summarized in Table 1. The MR and 3DUS acquisitions were obtained within 3.5 ± 3.3 days of each other. The data was acquired at the Division of Imaging Sciences and Biomedical Engineering, King's College London, United Kingdom.

2.1 Ultrasound Acquisition

The ultrasound datasets were acquired from the apical view using a iE33 3D echocardiography system (Philips Healthcare, Best, The Netherlands). Full-volume mode was used in which several smaller imaging sectors are combined to form a large composite volume with each smaller sector acquired in a single heart cycle. The cardiologist was free to adjust the image processing settings to improve the quality of the images. After acquiring several volumes the cardiologist selected the best quality dataset to be uploaded for the challenge.

2.2 MR Acquisition

The MR datasets were acquired using a 3T Philips Achieva System (Philips Healthcare, Best, The Netherlands). The MR acquisition included three types of sequences (see Fig. 2 and Fig. 3):

– **Cine Steady State Free Precession (SSFP) sequences:** images were scanned with an SSFP sequence in multiple views (TR/TE=2.9/1.5ms, flip angle=40°, cardiac phases=30). All images were acquired during breath-holds of approximately 15 seconds and were gated to the vector ECG. Details on spatial and temporal resolution of the datasets are summarized in Table 1.
– **Whole-heart Turbo Field Echo (TFE) sequence:** the whole heart TFE sequence acquires an isotropic non-angulated volume (TR/TE=5.2/2.5ms, flip angle=20°, cardiac phases=1) [2]. Images were acquired during free breathing with respiratory gating and at end-diastole with ECG gating. Details on spatial and temporal resolution of the datasets are summarized in Table 1.
– **4D tagged Magnetic Resonance sequence (tMR):** this sequence is obtained with three sequential breath-hold acquisitions in each orthogonal

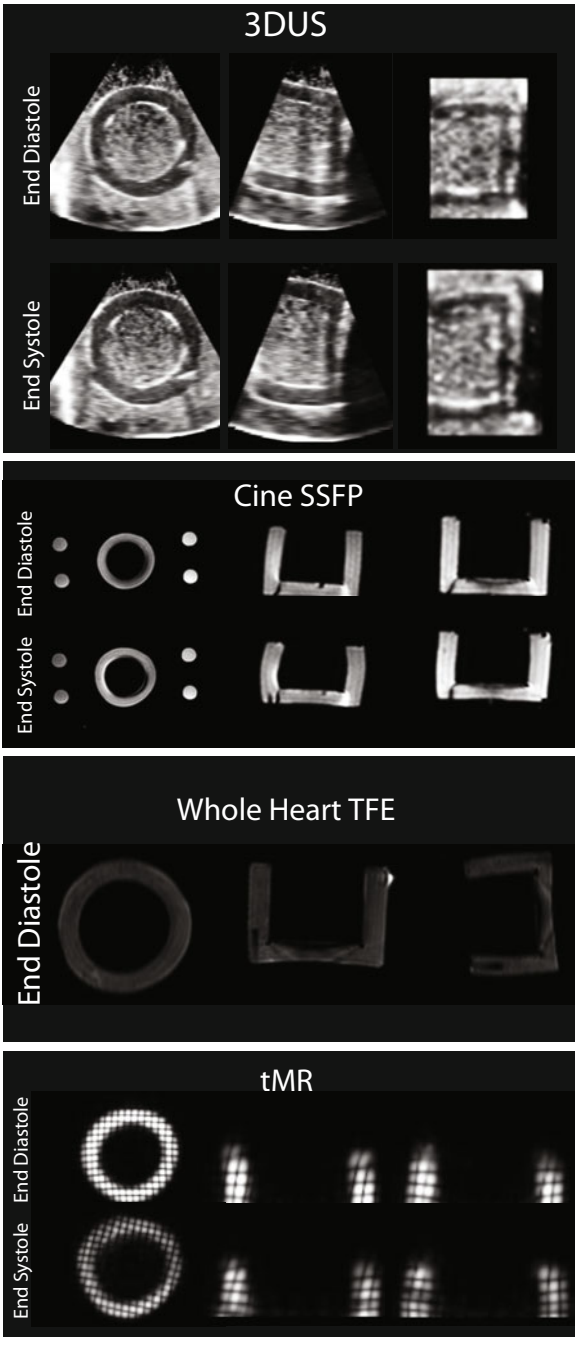

Fig. 2. Example images of the dynamic phantom. 3DUS= 3D ultrasound; SSFP= Steady State Free Precession; TFE= Turbo Field Echo; tMR= 4D tagged Magnetic Resonance.

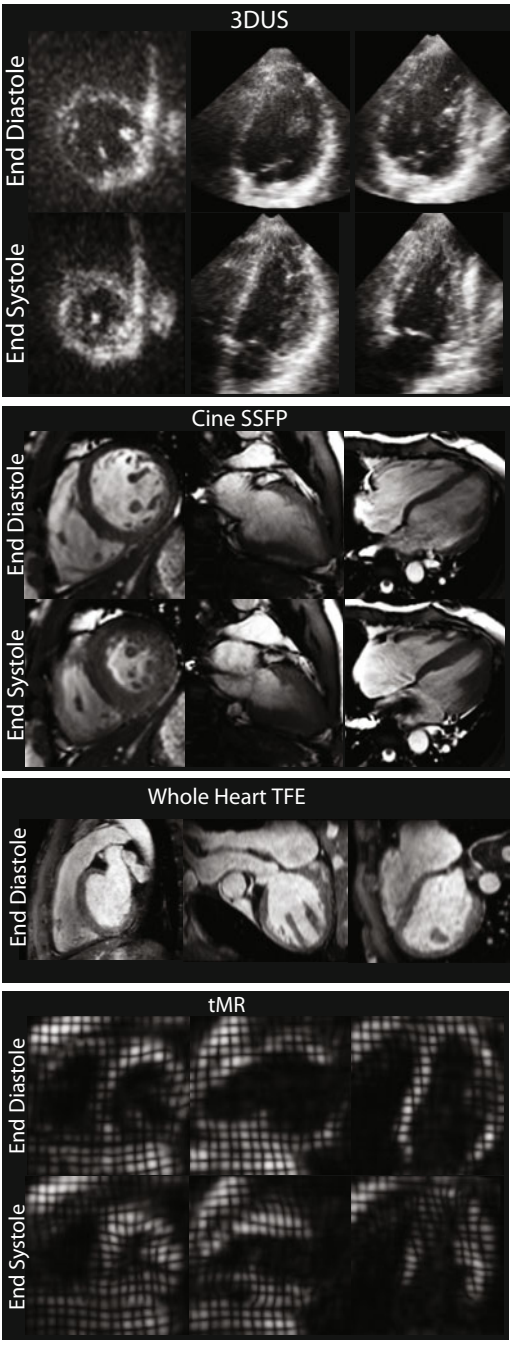

Fig. 3. Example images of a volunteer. 3DUS= 3D ultrasound; SSFP= Steady State Free Precession; TFE= Turbo Field Echo; tMR= 4D tagged Magnetic Resonance.

Table 1. Dataset description: demographics, temporal and spatial resolution

	Age	G	BSA	3DUS			4ch SSFP			2ch SSFP			sAX SSFP				WH TFE				tMR		
				pixel	thk	ph	pixel	thk	ph	pixel	thk	ph	sl	pixel	thk	ph	sl	pixel	thk	sl	pixel	thk	ph
	yr		m^2	*mm*	*mm*		*mm*	*mm*		*mm*	*mm*			*mm*	*mm*			*mm*	*mm*		*mm*	*mm*	
phantom	*n.a.*	*n.a.*	*n.a.*	1.35	0.96	19	1.20	8	30	1.20	8	30	9	1.20	8	30	70	0.75	1.6	68	1.01	1.01	23
V1	28	M	1.73	0.66	0.58	14	1.19	8	30	1.19	8	30	14	1.25	8	30	95	0.75	1.5	111	0.96	0.96	23
V2	30	F	1.55	0.66	0.58	16	1.13	8	30	1.25	8	30	11	1.25	8	30	80	0.75	1.6	111	0.96	0.96	29
V3	29	F	1.63	0.82	0.72	11	1.25	8	30	1.25	8	30	14	1.25	8	30	90	0.75	1.5	111	0.96	0.96	26
V4	36	M	1.84	0.77	0.68	15	1.25	8	30	1.25	8	30	14	1.25	8	30	94	0.75	1.6	111	0.96	0.96	23
V5	34	M	1.92	0.82	0.72	14	1.13	8	30	1.25	8	30	14	1.25	8	30	94	0.75	1.6	111	0.96	0.96	23
V6	32	M	1.99	0.82	0.72	17	1.13	8	30	1.15	8	30	14	1.15	8	30	100	0.75	1.6	111	0.96	0.96	31
V7	27	M	2.13	0.82	0.72	14	1.13	8	30	1.15	8	30	16	1.15	8	30	100	0.75	1.6	111	0.96	0.96	31
V8	29	M	1.78	0.82	0.72	14	1.13	8	30	1.25	8	30	14	1.25	8	30	94	0.75	1.6	111	0.96	0.96	30
V9	22	M	1.84	0.82	0.72	13	1.13	8	30	1.25	8	30	14	1.25	8	30	80	0.75	1.6	111	0.96	0.96	27
V10	22	M	1.88	0.82	0.72	15	1.13	8	30	1.25	8	30	14	1.15	8	30	100	0.75	1.6	111	0.96	0.96	32
V11	30	M	1.94	0.82	0.72	13	1.13	8	30	1.25	8	30	14	1.25	8	30	80	0.75	1.6	111	0.96	0.96	24
V12	31	M	1.78	0.77	0.58	24	1.13	8	30	1.25	8	30	14	1.15	8	30	90	0.75	1.5	111	0.96	0.96	38
V13	24	F	1.61	0.96	0.72	18	1.13	8	30	1.25	8	30	14	1.15	8	30	75	0.75	1.6	111	0.96	0.96	29
V14	20	M	1.65	0.96	0.72	13	1.13	8	30	1.16	8	30	12	1.25	8	30	90	0.75	1.6	111	0.96	0.96	21
V15	20	M	2.06	0.82	0.72	13	1.13	8	30	1.16	8	30	14	1.25	8	30	90	0.75	1.6	111	0.96	0.96	25

G= gender; BSA= body surface area; 3DUS= 3D ultrasound; 4ch= four-chamber; 2ch= two-chamber; sAX= short-axis; WH= whole heart; yr= years; pixel= in-plane pixel size; thk= slice thickness; ph= cardiac phases; sl= slices.

direction (TR/TE =7.0/3.2ms, flip angle=19-25°, tag distance=7mm) [3]. Images were acquired with reduced field-of-view enclosing the left ventricle (108×108×108 mm^3). Depending on the heart rate of the volunteer, 23-38 time frames were acquired (see Table 1). A respiratory navigator was used to compensate for any respiratory miss-alignment during the three sequential acquisitions.

2.3 Distribution

All the data were provided in anonymized DICOM format following HIPAA regulations. The imaging data were provided without any pre-processing after reconstruction. DICOM images were sorted by modality, sequence and time frames. The original tMR images in three orthogonal directions were fused in a grid-tagged volume sequence. The volumetric tMR datasets were converted to VTK and NIFTI formats. The 3DUS datasets were also converted to VTK. All format conversions were performed with GIMIAS v1.3.0 [4].

3 The Evaluation

3.1 Ground Truth

– **tMR:** In order to generate the ground truth from the tMR datasets, we incorporated anatomical information from the SSFP images. Firstly, the end diastolic frame of the tMR datasets was selected. The short-axis SSFP dataset with the closest trigger time was selected. Secondly, the left ventricular (LV) cavity was segmented from the selected short-axis dataset by manually deforming a left ventricular model [5]. Thirdly, the manually segmented mesh was registered to the coordinates of the tMR data using DICOM header information (see Fig. 4).

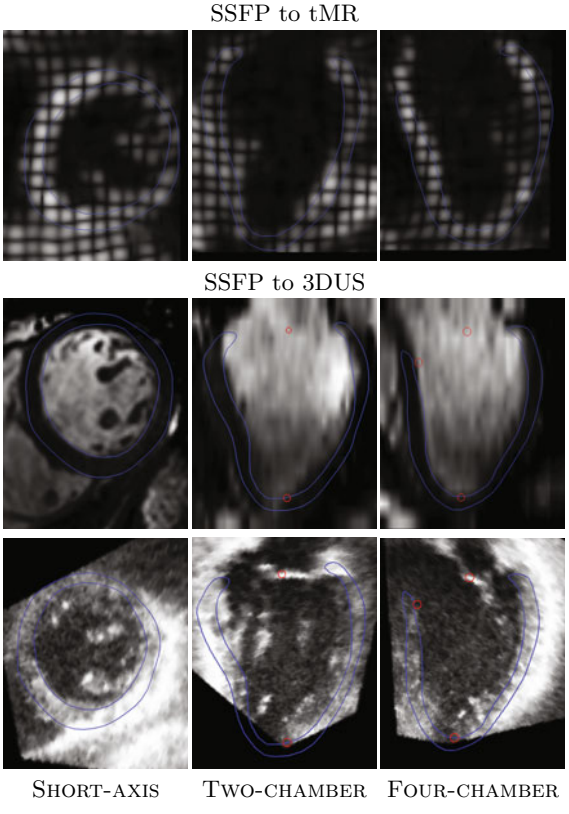

Fig. 4. A segmentation is obtained from the short-axis SSFP dataset (middle). The LV model is registered to tMR coordinates using DICOM header information (top) and to 3DUS coordinates using a point based similarity transform (bottom). The landmarks are displayed as red circles (middle-bottom).

From the manually segmented mesh, one landmark per wall (anterior, lateral, posterior, septal) per ventricular level (basal, midventricular, apical) were computed, totalling 12 landmarks per subject (see Fig. 6). These landmarks were used as initialization points for two observers to do the manual tracking. In order to achieve real 4D tracking of the landmark, the process was done one landmark at a time. Each landmark was positioned on the closest tag intersection from the 3 orthogonal directions. The landmark was propagated to the next time frame and manually displaced to follow the tag marks. This process was repeated until the landmark was tracked over the whole cardiac cycle (see Fig. 5). The manually tracked landmarks will be used to evaluate accuracy of methodologies applied in the challenge. Visualization, segmentation and tracking was performed with GIMIAS v1.3.0 [4].

– **3DUS:** LV model extracted from the end diastolic SSFP dataset was registered to 3DUS coordinates. Firstly, three orthogonal visualization planes were selected to match MR acquisition planes (short-axis, four-chamber,

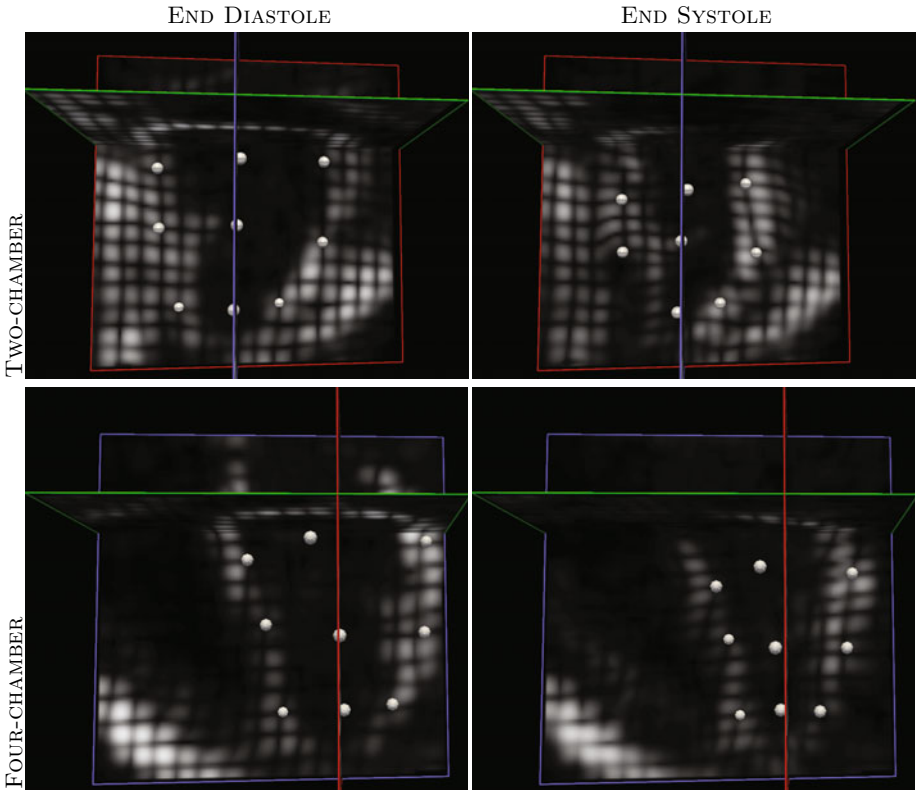

Fig. 5. Results of manual landmark tracking: note the in-out-of-plane motion of the landmarks due to our 4D tracking strategy

two-chamber). Secondly, three anatomical landmarks were marked on the four-chamber view: start of the inter-ventricular septum at basal level, centroid of the mitral valve and endocardial apex. Thirdly, with the corresponding landmarks on the MR datasets, a point based similarity transform was performed (see Fig. 4). The resulting transformation will be used to map the ground-truth landmarks to 3DUS coordinates.

3.2 3DUS Quality Assessment

Even in healthy volunteers, either due to obesity or small rib separation, acoustic windows for US acquisition may be suboptimal. Therefore, the datasets were graded according to their diagnostic quality. The datasets were assessed by consensus of two expert cardiologists four weeks after the last recruitment. To avoid bias, datasets were renamed with a randomized ID. The assessment was performed at global and regional level. For regional evaluation, each myocardial

Table 2. Quality assessment of 3DUS datasets

	Basal						Midventricular						Apical				Overall
	A	AL	IL	I	IS	AS	A	AL	IL	I	IS	AS	A	L	I	S	
V1	2	2	2	2	2	2	2	2	2	2	2	2	1	2	2	1	3
V2	1	1	2	2	2	1	0	1	1	1	2	1	0	1	1	1	1
V3	1	1	2	2	2	1	1	2	2	2	2	1	0	2	1	1	2
V4	1	1	2	2	2	1	0	1	2	2	2	2	0	1	1	1	2
V5	1	1	1	2	2	1	2	1	1	2	2	2	1	2	1	2	2
V6	1	1	2	1	1	1	1	1	1	1	1	2	0	1	0	2	1
V7	0	1	2	2	2	0	0	1	2	2	1	0	0	1	1	2	0
V8	1	1	2	2	1	2	0	1	1	2	1	1	1	1	1	1	1
V9	0	1	1	2	2	0	1	2	2	2	2	0	1	1	0	1	1
V10	1	1	2	2	2	2	1	1	1	2	2	2	1	0	1	1	2
V11	1	1	2	2	1	1	1	1	2	2	2	1	1	2	1	2	2
V12	1	2	2	2	2	2	1	2	2	2	2	1	1	1	2	2	2
V13	1	1	2	2	2	1	1	1	2	2	2	2	1	2	2	1	2
V14	1	2	2	2	2	0	1	2	2	2	2	0	1	2	1	1	1
V15	1	1	1	1	2	1	1	1	2	2	2	1	0	0	1	1	2

3DUS= 3D ultrasound; A= anterior; L= lateral; I= inferior; S= septal.
Segmental scores: 0= unusable; 1= suboptimal; 2= optimal.
Overall scores: 0= unusable; 1= usable; 2= average; 3= excellent.

AHA segment was graded. Table 2 summarizes the results. The quality gradings will be correlated with the accuracy of methodologies applied in the challenge.

4 Results

4.1 Response to the Challenge

The call for challengers raised interest from 13 worldwide groups, all of which successfully downloaded the data. After 3 official withdrawals, we obtained 4 final submission to the challenge from the following groups (by order of submission): Fraunhofer MEVIS, Bremen, Germany; Imperial College London, UK; Universitat Pompeu Fabra, Barcelona, Spain; INRIA-Asclepios project (Sophia-Antipolis), France. Details on their methodology can be found in the workshop proceedings: *Statistical Atlases and Computational Models of the Heart: Imaging and Modelling Challenges (STACOM)*. All the groups processed the tMR data, while the 3DUS was processed only by INRIA and MEVIS. Table 3 summarizes the data processed by each challenger.

Table 3. Response to the challenge

Institute	Acronym	Phantom			Volunteers		
		MRI		3DUS	MRI		3DUS
		tMR	SSFP		tMR	SSFP	
Fraunhofer MEVIS	MEVIS	✓		✓	✓		✓
Imperial College London	ICL				✓	✓	
Universitat Pompeu Fabra	UPF	✓			✓		
INRIA-Asclepios project	INRIA	✓	✓	✓	✓	✓	✓

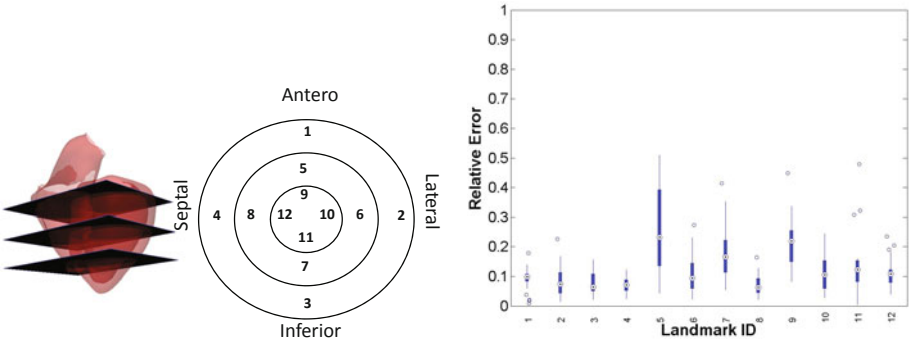

Fig. 6. (left) Diagram representing the 12 landmarks used for manual tracking: one landmark per wall (anterior, lateral, posterior, septal) per ventricular level (basal, mid-ventricular, apical). (right) Box-plot of inter-observer variability for V2, were relative error was calculated with Eq 1.

4.2 Inter-observer Variability

In order to provide initial feedback to the challengers during the workshop meeting, we selected an average quality dataset (V2) to test all the deformation fields. After obtaining the ground truth as described in Sec. 3, we calculated the inter-observer variability for this dataset. To get a better idea of the magnitude of the differences between observers, we calculated the relative error as:

$$R_{error} = \frac{distance(Lmk_i^{obs1}, Lmk_i^{obs2})}{maxDisplacement(Lmk_i)} \quad (1)$$

where i is each landmark, $distance(a, b)$ is the euclidian distance between points a and b, and $maxDisplacement$ is the maximum displacement of each landmark i across the cardiac cycle. Fig. 6 shows a box-plot of the inter-observer variability observed on dataset V2.

4.3 Qualitative and Quantitative Results

To visualize the results obtained by each challenger, we applied the deformation fields to the manually segmented mesh of V2. All challengers obtained a physiologically consistent result: systolic contraction (10-11 frames), isovolumetric contraction (2-3 frames), early relaxation (7-8 frames), diastasis (3-4 frames) and late relaxation due to atrial contraction (4 frames).

The methodology of MEVIS obtained good longitudinal and radial deformation (Fig. 7). We can also observe local inaccuracies on the antero-lateral wall, most likely due to a loss of signal on the dataset. Incidentally, this region also presented high inter-observer error. Quantitatively this translated into low average errors with a few outliers (Fig. 8).

The methodology of ICL generated a smooth mesh with good radial deformations (Fig. 7). This is most likely due to the inclusion of SSFP information

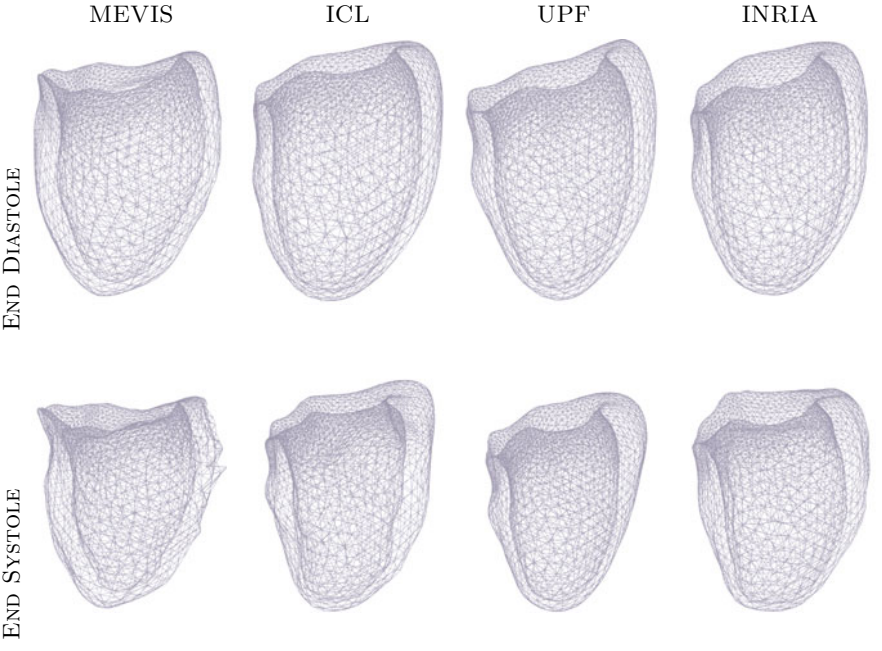

Fig. 7. Visual results for each challenger at end diastole and end systole

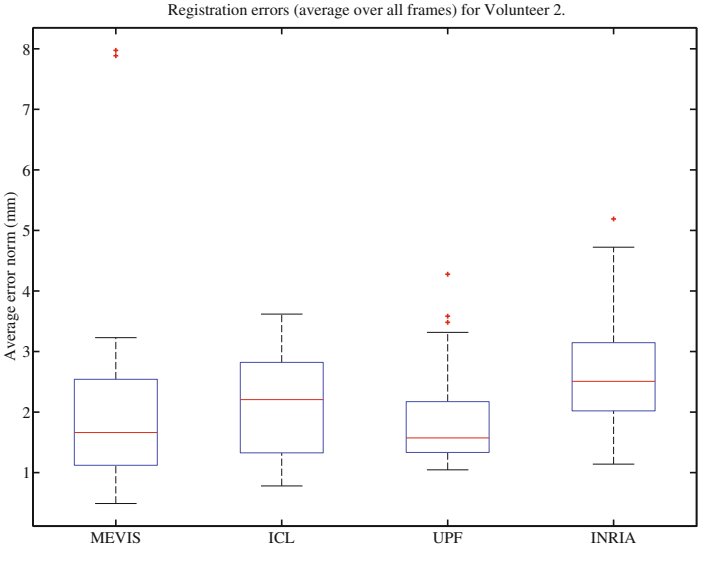

Fig. 8. Box-plots of registration errors for each challenger on the dataset of V2

in the methodology. However, the longitudinal deformation was underestimated with respect to the ones of MEVIS and UPF. During the workshop, it was suggested to increase the weight of the tMR information to better retrieve the longitudinal deformation. In Fig. 8, we can observe that the methodology is very consistent over the cardiac cycle, represented by the lack of outliers in the box-plot.

The methodology of UPF generated a smooth mesh with good longitudinal deformation. However, the radial deformation was relatively less than the one obtained by all other participants (Fig. 7). This is most likely due to an over-smoothing effect of the methodology. Similarly to MEVIS, we observed the presence of outliers in the antero-lateral wall (Fig. 8).

The methodology of INRIA generated a smooth mesh. The radial deformation was larger than the one obtained by UPF, yet slightly lower than the ones obtained by MEVIS and ICL. The longitudinal deformation was comparable to the one obtained by ICL.

5 Outlook

First of all, the organizers would like to thank challenge participants for their contribution. The analysis presented in this manuscript is based on initial results on a single dataset. Therefore, no final conclusions should be drawn from these results. Once we establish the ground-truth for all volunteers and phantom, we will perform a full quantitative analysis of the results and submit a collaborative paper to a relevant journal. Our aim is to combine the deformation fields provided by the challengers with a STAPLE-like approach [6]. Finally, efforts are underway to make the datasets available via the Cardiac Atlas Project [7].

References

1. Manzke, R., Lutz, A., Schenderlein, M., Bornstedt, A., Chan, R.C., Dietmeyer, K., Rasche, V.: A new PVA-based dynamic cardiac phantom for evaluation of functional MR imaging methods at 3T. In: ISMRM Proceedings (2010)
2. Uribe, S., Muthurangu, V., Boubertakh, R., Schaeffter, T., Razavi, R., Hill, D.L., Hansen, M.S.: Whole-heart cine MRI using real-time respiratory self-gating. Magn. Res. Med. 57(3), 606–613 (2007)
3. Rutz, A.K., Ryf, S., Plein, S., Boesiger, P., Kozerke, S.: Accelerated whole-heart 3D CSPAMM for myocardial motion quantification. Magn. Res. Med. 59(4), 755–763 (2008)
4. GIMIAS v1.3.0: Center for Computational Image and Simulation Technologies in Biomedicine, Universitat Pompeu Fabra (2011), http://www.gimias.org
5. Ordas, S., Oubel, E., Leta, R., Carreras, F., Frangi, A.F.: A statistical shape model of the whole heart and its application to model-based segmentation. In: SPIE Medical Imaging: Physiology, Function, and Structure from Medical Images, vol. 6511, p. 65111K (2007)
6. Warfield, S.K., Zou, K.H., Wells, W.M.: Simultaneous truth and performance level estimation (staple): an algorithm for the validation of image segmentation. IEEE Trans. Med. Imaging 23(7), 903–921 (2004)
7. The Cardiac Atlas Project, http://www.cardiacatlas.org/

Automatic Cardiac Motion Tracking Using Both Untagged and 3D Tagged MR Images

Haiyan Wang[1], Wenzhe Shi[1], Xiahai Zhuang[2], Simon Duckett[3], KaiPin Tung[1], Philip Edwards[1], Reza Razavi[3], Sebastien Ourselin[2], and Daniel Rueckert[1]

[1] Biomedical Image Analysis Group, Imperial College London
[2] Center for Medical Image Computing, University College London
[3] The Rayne Institute, Kings College London

Abstract. We present a fully automatic framework for cardiac motion tracking based on non-rigid image registration for the analysis of myocardial motion using both untagged and 3D tagged MR images. We detect and track anatomical landmarks in the heart and combine this with intensity-based motion tracking to allow accurately model cardiac motion while significantly reduce the computational complexity. A collaborative similarity measure simultaneously computed in three LA views is employed to register a sequence of images taken during the cardiac cycle to a reference image taken at end-diastole. We then integrate a valve plane tracker into the framework which uses short-axis and long-axis untagged MR images as well as 3D tagged images to estimate a fully four-dimensional motion field of the left ventricle.

1 Introduction

In this paper, we make two contributions: First, we propose a fully automatic approach to identify and track important cardiac landmarks throughout the cardiac cycle. In particular we use a machine learning approach to detect landmarks such as the valve plane simultaneously in three LA views and then track the motion throughout the cardiac cycle. The second contribution is the combination of complementary information from tagged and ungagged MR images using a spatially adaptive weighting and a valve plane constraint to build an accurate and realistic cardiac motion analysis framework.

2 Spatial and Temporal Correction

The analysis of cardiac motion information from different MR images requires a common spatial and temporal reference space. However, there are three major difficulties: (i) the presence of tags in 3D tagged images obscuring the anatomy, (ii) differences in position caused by respiratory and patient motion within sequences and across sequences and (iii) variable temporal resolution of the different image sequences. Camara et al. [1] presented a registration algorithm to correct the spatial misalignment between SSFP MR image sequences and

O. Camara et al. (Eds.): STACOM 2011, LNCS 7085, pp. 45–54, 2012.

CSPAMM MR image sequences, but temporal misalignment is not included. We extend this framework for the combination of information derived from untagged and 3D tagged MR image sequences which accounts for spatial misalignment as well as differences in temporal resolution.

2.1 Temporal Alignment

Each frame of a MR image sequence contains a DICOM meta-tag describing the trigger time. We define T^s and T^e as the trigger time of the first and last phase respectively and N as number of frames. Hence each image sequence, e.g. short-axis (SA), horizontal long axis (HLA), vertical long axis (VLA), 3-chamber (3CH) untagged and 3D tagged images has such a pair of trigger times. We define T^s_{ref} and T^e_{ref} as the maximum value of the trigger times respectively and N_{ref} as minimum value of the number of frames in each sequence. The common temporal resolution is then defined as $\Delta t = (T^e_{ref} - T^s_{ref})/N_{ref}$. All image sequences are resampled to this common temporal resolution using nearest neighbour interpolation.

2.2 Spatial Alignment

The 3D tagged MR images are free from respiratory motion artifacts since respiratory navigators are used during the acquisition. They contain complete 3D motion information with isotropic sampling in all 3 directions. Thus, it provides an ideal common spatial coordinate system. The only difficulty is the presence of tags in the image that obscure the anatomical information which is needed to align to the untagged MR images.

Removal of Tags from 3D Tagged MR. Several techniques for tag removal exist [6,7,1], yet none of these provided satisfactory results due to the fact that the 3D tagged MR images used here are dominated by tag patterns and show little of the underlying anatomy. However, one can easily extract the low frequency band by applying a FFT, band-pass filtering and inverse FFT. We have performed this naive but effective approach for tag removal and then averaged the three 3D detagged MR images to generate the 3D pseudo-anatomical image. We then align the untagged MR images to the 3D pseudo-anatomical image using registration by normalized mutual information [10].

Spatial Registration. Images from multiple cardiac MR image sequences may be misaligned due to patient motion and different breath-hold positions during acquisition. For short-axis untagged MR images this misalignment can also occur between slices [1,2] as Figure 1 demonstrates. To correct these artifacts, we extract the middle phase in the reference temporal resolution from both the SA and LA untagged MR images. We then register all available SA and LA untagged MR image sequences to the 3D pseudo-anatomical MR image using rigid registration. In contrast to the work in [2] the transformation is modeled as

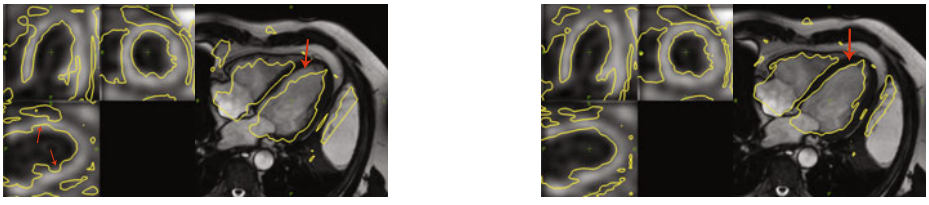

(a) (b)

Fig. 1. This figure shows the 3D tagged pseudo-anatomical image overlaid with isolines from the SA and LA images: (a) before alignment and (b) after alignment. Misalignments are pointed out by red arrows.

a 3D rigid transformation rather than a 2D rigid transformation. The resulting transformation of each slice in the middle phase is then applied to the same slice in all other phases of the untagged MR image data.

3 Comprehensive Motion Tracking

During the cardiac cycle, the left ventricle undergoes a number of different deformations including circumferential, radial and longitudinal motion. While the 3D tagged MR images provide good information about all aspects of the motion, the SA images may provide more information of radial motion and the LA images may provide some extra information about the radial and longitudinal motion.

Consider a material point in the myocardium at a position $\mathbf{p} = (x, y, z)^T$ at time $t_0 = 0$ that moves to another position $\mathbf{p}' = (x', y', z')^T$ at time $t_i = i\Delta t$ where Δt is the time interval between two consecutive phases and i corresponds to the time frame. The goal of the motion tracking is to find the transformation $\mathbf{T}$ for all time phases i such that $\mathbf{T}(\mathbf{p}, t_i) = \mathbf{p}'$. In this work we represent $\mathbf{T}$ using a series of free-form deformations [8] as described in [3].

The estimation of the deformation field $\mathbf{T}$ proceeds in a sequence of registration steps. Using the spatial and temporal alignment described in section 2, all image sequences have been mapped into a common spatial and temporal coordinate system. We label the myocardium of the left ventricle at the end diastolic (ED) phase of the untagged MR images using an automatic segmentation tool[9]. The segmentation tool propagate an probabilistic atlas to unseen image using affine, LARM [13] and non-rigid registration [8], and using the propagated atlas to constrain the MCEM [9] segmentation.

In addition, a gradient detector is used to highlight the epicardial and endocardial contours on untagged MR images. The information from both segmentation and the gradient-detector is combined into a spatially varying weighting function which moderates the influence of the tagged and untagged images on the motion tracking. We then register the images taken at time t_1 to the reference image at time t_0 and obtain a transformation representing the motion of the myocardium at time t_1 [8]. We use the resulting transformation as an input for the next time

frame and continue this process until all the time frames in the sequence are registered to the first phase[3].

3.1 Weighted Similarity Measure

To exploit the complementary nature of the tagged and untagged MR images we have developed a spatially adaptive weighting function that accounts for the different types of information available: The 3D tagged images characterise well the motion inside the myocardium while untagged SA and LA images characterize the motion well at the epi- and endocardial borders of the myocardium. Outside of the myocardium there is no useful information for cardiac motion tracking apart from papillary muscles. Thus, we would like to generate a weighting function that is zero outside the myocardial region, that maximizes the weighting of the tagged images within the myocardium and increases the influence of the untagged images at the myocardial border. The spatial weights for the tagged and untagged images are generated for the reference image used for the registration.

The weighting for the untagged images, $W^u(\mathbf{p})$, is generated by multiplication the gradient of the segmentation with the gradient of the image intensity. Higher weighting indicates possible presents of myocardial edge which is critical to estimation of radial motion. Let L denote the segmentation of the short-axis MR image I. This segmentation assigns a label $\Lambda = \{L_{bg}, L_{myo}, L_{blood}\}$ to every voxel. The probability for myocardium $P(\mathbf{p}, L_{myo})$ can be derived from myocardium segmentation's intensity distribution by applying a Gaussian model. Furthermore assume that ∇I_σ denotes the gradient of image I after convolution with a Gaussian kernel G with standard deviation σ. The weights for the untagged MR image are defined as

$$W^u(\mathbf{p}) = \frac{||\nabla I_\sigma(\mathbf{p})||||\nabla P_\sigma(\mathbf{p}, L_{myo})||}{\max\left(||\nabla I_\sigma(\mathbf{p})||\right)\max\left(||\nabla P_\sigma(\mathbf{p}, L_{myo})||\right)} \tag{1}$$

where $||\nabla I_\sigma(\mathbf{p})||$ and $||\nabla P_\sigma(\mathbf{p}, L_{myo})||$ are the gradient of intensity and the gradient of myocardium probability at location $\mathbf{p}$ after convolution with a Gaussian kernel G with standard deviation $\sigma = 10mm$ respectively.

The weights for the 3D tagged image are defined as

$$W^t(\mathbf{p}) = \begin{cases} 1 - W^u(\mathbf{p}) & \text{if } L(\mathbf{p}) = L_{myo} \\ 0 & \text{otherwise} \end{cases} \tag{2}$$

Given a weight map, we define the similarity between two images I_A, I_B as the weighted normalized cross-correlation between the image intensities:

$$S(I_A; I_B; W, \mathbf{T}) = \frac{\sum W(\mathbf{p})(I_A(\mathbf{p}) - \mu_A)(I_B(\mathbf{T}(\mathbf{p})) - \mu_B)}{\sqrt{\sum W^2(\mathbf{p})(I_A(\mathbf{p}) - \mu_A)^2(I_B(\mathbf{T}(\mathbf{p})) - \mu_B)^2}} \tag{3}$$

For simultaneous registration of the untagged and 3D tagged images, the correlation is computed separately across tagged images and untagged images and combined into a single similarity measure:

$$C_s = \{\sum_{s\in T} |\Omega_s| \left[S(I_{t_0}^{t,s}, I_{t_i}^{t,s}, W^{t,s}, \mathbf{T})\right] + \sum_{s\in U} |\Omega_s| \left[S(I_{t_0}^{u,s}, I_{t_i}^{u,s}, W^{u,s}, \mathbf{T})\right]\} / \sum_{s\in U,T} |\Omega_s| \quad (4)$$

Here $|\Omega_s|$ denote the sum of weights in the image. Note, that the similarity measure takes into account that different images have usually a different number of voxels and therefore the correlation must be weighted accordingly.

4 Detection and Tracking of Cardiac Landmarks

We propose a fully automatic approach to localise and track landmarks of the heart in LA views to provide essential information for myocardial motion tracking and segmentation. This approach is illustrated in Figure 2 for detection of the mitral valve points heart across three LA views. A-priori knowledge about the position of the landmarks is obtained based on a statistical analysis of the location of landmarks. We use an approach akin to the marginal space learning proposed in [12] to identify regions which are likely to contain the landmarks of interest and then apply machine learning based landmark detector to voxels within this region. Landmarks such as the valve annulus are tracked simultaneously in three LA views using template matching.

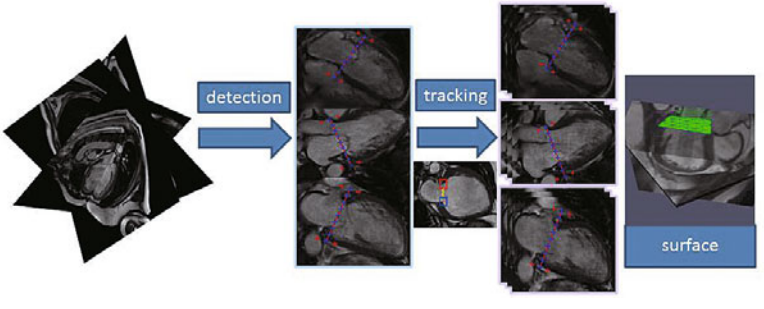

Fig. 2. This figure shows the work flow of valve plane tracking

4.1 Valve Annulus Modelling and Detection

During the cardiac cycle, the mitral valve annulus undergoes mostly longitudinal motion along with a number of other types of deformations including circumferential and radial motion. In a LV view, the valve plane can be modelled by a

line between two valve points in each LA view. However, due the large variations in cardiac anatomy across subjects, its position, orientation and appearance can differ significantly across subjects. Lu et al. [5] presented a joint context method for landmark detection, but only one LA view was considered hence generated relatively large errors. For any machine learning based approach, a meaningful feature set which can distinguish the object from other anatomical structures efficiently is crucial for the success of the detector. In this work a set of Haar-like features [11] as well as steerable features [12] are used.

In addition, a-priori knowledge about the position of the valve points can be exploited. As illustrated in Figure 3a, the line of the intersection between the top stack of the SA view and VLA, and the line of the intersection between HLA and VLA intersect at point O. This point O is usually approximately half way from the valve annulus to apex and therefore can be used to roughly anchor the valve plane. A bounding box can be generated relative to the point O indicating the likely location of the valve plane. A Gaussian mixture model is applied to classify the voxels in the LA images into air, soft tissue or blood. Only those voxels labelled as soft tissue are considered as candidate valve points. For each candidate valve point $\mathbf{p}_i$ its normalised distance to the border of the bounding box can be used to model the likelihood for a valve point at this location. In addition, the SA view is usually planned at 90° relative to the LA of the left ventricle that intersects the apex and the centre of the mitral valve plane. Therefore, the orientation of the LA can be derived from the intersection line of SA and any LA view. Ideally, if a point $\mathbf{p}_i$ is a valve plane point, then a second valve point $\mathbf{q}_i$ should be present in the direction perpendicular to the LA direction. Thus, the valve plane can be found by detecting a pair of points $\{\mathbf{p}_i, \mathbf{q}_i\}$ and no dedicated feature extraction is needed for orientation estimation, thus reducing the computational complexity significantly. However, in practice due the fact that the valve annulus deforms and scan planes may not be planned in the ideal orientation, the correct orientation of the valve plane may sometimes differ by a small angle θ . We therefore test every point $\mathbf{p}_i$ with every point in the neighbourhood of $\mathbf{q}_j$ so that the set of candidate valve-planes points becomes $\{\mathbf{p}_i, \mathbf{q}_j | \forall i; j = i + k\}$.

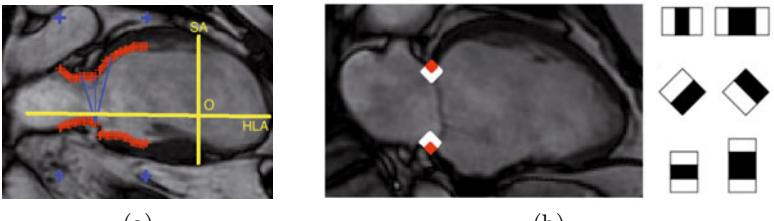

(a) (b)

Fig. 3. Automatic detection of valve points. (a) An example shows a bounding box (4 blue points) for the valve plane containing the possible candidate point pairs and. (b) some of the Haar-like features used for detection.

4.2 Simultaneous Valve Plane Detection in Multiple Views

Most clinical cardiac MR acquistions include multiple LA views such as VLA, HLA and 3CH views. All three views can provide useful complementary information. We therefore construct three different detectors for the three LA views to detect a pair of valve points in VLA and HLA views, as well as the valve point in the bottom border in 3CH (the valve point in the upper border in 3CH varies too much across samples due to larger variability in the acquisition of 3CH views, and hence is not used as landmark). Two layers of Adaboost [11] are cascaded for each detector to avoid the training to be biased by negative samples, which are 10 times more likely than positive samples. As different features sets are used for the two layers, the hypotheses from the first layer are maintained to be combined with the result from the last layer.

4.3 Valve Plane Motion Tracking

As described above (section 4.1), it is reasonable to make the assumption that the valve annulus mainly undergoes deformation in the long-axis direction during the cardiac cycle and accompanied shrinking and expanding perpendicular to the long-axis. To track the motion of the valve annulus we conduct template tracking based 2D collaborative tracking simultaneously on three LA views. To perform template tracking we define two regions encompassing the valve end points in each LA view and use cross-correlation to track these two valve end points location in the next time frame. In total six regions are tracked simultaneously in three LA view.

4.4 Constrained Myocardial Motion Tracking Using Tagged and Untagged MR Images

The valve plane is an important landmark for accurate cardiac motion estimation but is not clearly visible in untagged SA images and tagged SA images. From the LA views, we have tracked the valve annulus using the collabrative tracker described in section 4.3 and construct a valve plane surface V_t for each time frame using Delaunay triangulation.

To estimate the motion within the myocardium, a weighted similarity measure described in section 3 is used. The constructed valve surface V is applied as one of the constraints in non-rigid image registration to correlate the myocardial motion to the tracked valve plane in form of a penalty term:

$$C_v = -\frac{\sum_{p \in V_{t_0}} D(\mathbf{T}(p), V_{t_i})}{|V_{t_0}|} \tag{5}$$

where V_{t_i} denotes the valve plane surface at time t_i and D is the surface distance operator (symmetric closest points).

5 Results

We collected three LA views and SA sequences from each of the 50 patients. For valve annulus detection, 40 sets of images are randomly chosen for learning and 10 sets are used for testing. The collaborative tracker is then applied on the 10 test cases. The accuracy of the motion tracking is computed as the Euclidean distance between the detected valve points and points manually marked in each time frame for 10 cases in the test set, which is reported in Figure 4. The relative large error from patient 2 is due to the fact that patient 2 is actually a healthy volunteer, hence its feature set is very different from that of the most samples from the training set (38 patients plus 2 volunteers).

A transformed synthetic tagging grid is often used to access the accuracy of tag tracking in addition to numerical result. Figure 5 shows a deformed grid at the end systolic phase (subject v4). A full movie has been submitted to the challenge data base. A realistic estimation of cardiac motion should include radial,

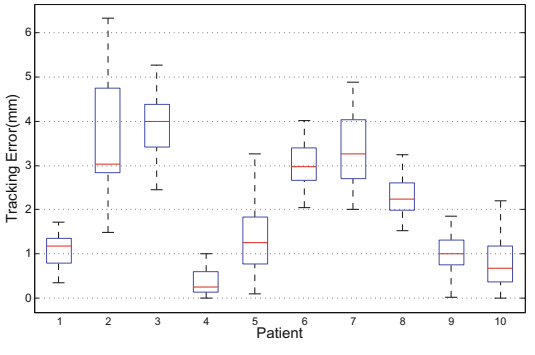

Fig. 4. Automatice motion tracking results. Tracking errors are estimated as distances between tracked valve positions and ground truth positions for 10 patients through the cardiac cycle. The edges of the blue box are $25th$ and $75th$ percentiles.

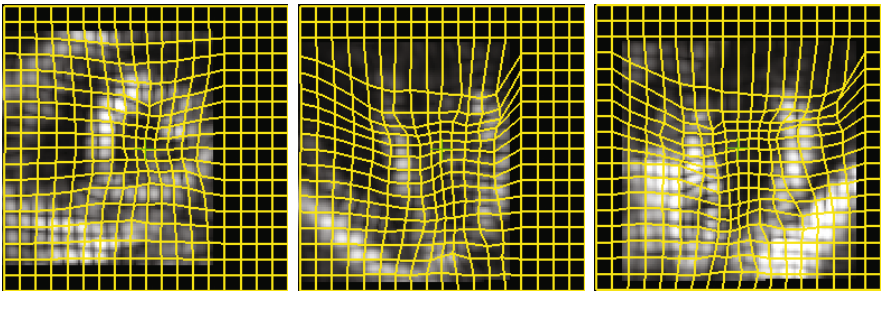

Fig. 5. This figure shows a synthetic grid propagated to end systolic phase and overlaid with 3D tagged image of subject v4

circumferential and longitudinal motion. An accurate tracking of the endocardial and epicardial boundaries on short-axis MR images indicates good radial motion estimation. Similarly, the accurate tracking of the endocardial and epicardial boundaries on the long-axis MR images indicates good longitudinal motion estimation. An example of the motion in different direction from subject v4 is shown in Figure 6.

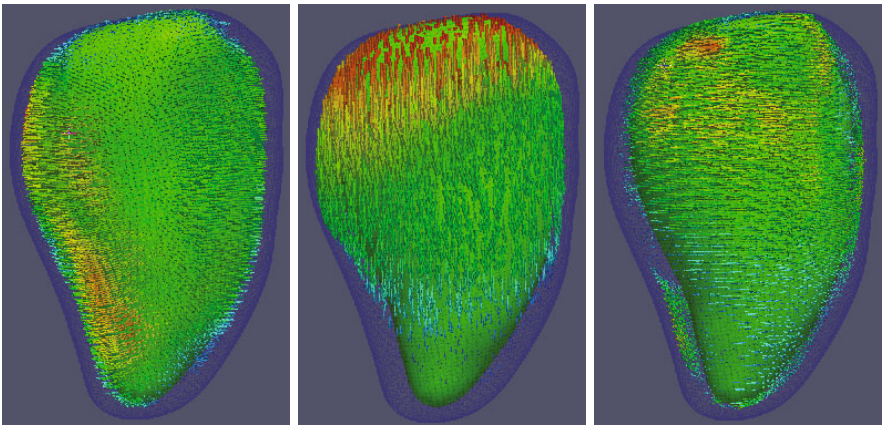

Fig. 6. This figure shows respectively radial longitudinal and circumferential motion at end systolic phase and myocardial segmentation of subject v4

6 Conclusion and Future Work

In this paper we have presented a fully automatic approach to identify and track a sparse set of landmarks throughout the cardiac cycle and conduct cardiac motion tracking using both 3D tagged as well as untagged image sequences from short-axis and long-axis views simultaneously. The key advantage of the proposed method is the simultaneous use of complementary motion information contained in the tagged and untagged images. By combining complementary information using a spatially adaptive weighting and valve plane constraint, we have successfully build an accurate and realistic cardiac motion analysis framework. Future work will investigate continuous transformation model in the temporal direction to avoid temporal alignment and small errors introduced by [4]. We will also work on the automatic detection and tracking of a larger number of generic cardiac landmarks. This will enable better hybrid sparse and dense motion tracking with a view to improve speed and accuracy of the motion tracking.

Acknowledgements. This work was funded in part by EPSRC grant EP/H019847/1.

References

1. Camara, O., Oubel, E., Piella, G., Balocco, S., De Craene, M., Frangi, A.: Multi-sequence Registration of Cine, Tagged and Delay-Enhancement MRI with Shift Correction and Steerable Pyramid-Based Detagging. In: Ayache, N., Delingette, H., Sermesant, M. (eds.) FIMH 2009. LNCS, vol. 5528, pp. 330–338. Springer, Heidelberg (2009)
2. Chandler, A., Pinder, R., Netsch, T., Schnabel, J., Hawkes, D., Hill, D., Razavi, R.: Correction of misaligned slices in multi-slice MR cardiac examinations by using slice-to-volume registration. In: 3rd IEEE International Symposium on Biomedical Imaging: Nano to Macro, pp. 474–477. IEEE (2006)
3. Chandrashekara, R., Mohiaddin, R., Rueckert, D.: Analysis of 3-D myocardial motion in tagged MR images using nonrigid image registration. IEEE Tansactions on Medical Imaging, 1245–1250 (2004)
4. De Craene, M., Piella, G., Duchateau, N., Silva, E., Doltra, A., Gao, H., D'hooge, J., Camara, O., Brugada, J., Sitges, M., Frangi, A.F.: Temporal Diffeomorphic Free-Form Deformation for Strain Quantification in 3D-US Images. In: Jiang, T., Navab, N., Pluim, J.P.W., Viergever, M.A. (eds.) MICCAI 2010. LNCS, vol. 6362, pp. 1–8. Springer, Heidelberg (2010)
5. Lu, X., Georgescu, B., Jolly, M., Guehring, J., Young, A., Cowan, B., Littmann, A., Comaniciu, D.: Cardiac Anchoring in MRI through Context Modeling. In: Jiang, T., Navab, N., Pluim, J.P.W., Viergever, M.A. (eds.) MICCAI 2010, Part I. LNCS, vol. 6361, pp. 383–390. Springer, Heidelberg (2010)
6. Manglik, T., Axel, L., Pai, W., Kim, D., Dugal, P., Montillo, A., Qian, Z.: Use of bandpass Gabor filters for enhancing blood-myocardium contrast and filling-in tags in tagged MR images, p. 1793 (2004)
7. Qian, T., Huang, R., Metaxas, D., Axel, L.: A novel tag removal technique for tagged cardiac MRI and its applications. In: 4th IEEE International Symposium on Biomedical Imaging: From Nano to Macro, ISBI 2007, pp. 364–367. IEEE (2007)
8. Rueckert, D., Sonoda, L., Hayes, C., Hill, D., Leach, M., Hawkes, D.: Nonrigid registration using free-form deformations: Application to breast MR images. IEEE Transactions on Medical Imaging, 712–721 (1999)
9. Shi, W., Zhuang, X., Wang, H., Duckett, S., Oregan, D., Edwards, P., Ourselin, S., Rueckert, D.: Automatic Segmentation of Different Pathologies from Cardiac Cine MRI using Registration and Multiple Component EM Estimation. In: Metaxas, D.N., Axel, L. (eds.) FIMH 2011. LNCS, vol. 6666, pp. 163–170. Springer, Heidelberg (2011)
10. Studholme, C., Hill, D., Hawkes, D., et al.: An overlap invariant entropy measure of 3D medical image alignment. Pattern Recognition 32(1), 71–86 (1999)
11. Viola, P., Jones, M.: Robust real-time object detection. International Journal of Computer Vision 57(2), 137–154 (2002)
12. Zheng, Y., Barbu, A., Georgescu, B., Scheuering, M., Comaniciu, D.: Four-chamber heart modeling and automatic segmentation for 3-D cardiac CT volumes using marginal space learning and steerable features. IEEE Transactions on Medical Imaging, 1668–1681 (2008)
13. Zhuang, X., Rhode, K., Razavi, R., Hawkes, D.J., Ourselin, S.: A Registration-Based Propagation Framework for Automatic Whole Heart Segmentation of Cardiac MRI. IEEE Transactions on Medical Imaging, 1612–1625 (2010)

An Incompressible Log-Domain Demons Algorithm for Tracking Heart Tissue

Kristin McLeod[1], Adityo Prakosa[1], Tommaso Mansi[2], Maxime Sermesant[1], and Xavier Pennec[1]

[1] INRIA Méditerranée, Asclepios Project, Sophia Antipolis, France
[2] Siemens Corporate Research, Image Analytics and Informatics, Princeton, NJ, U.S.A.

Abstract. We describe an application of the previously proposed iLogDemons algorithm to the STACOM motion-tracking challenge data. The iLogDemons algorithm is a consistent and efficient framework for tracking left-ventricle heart tissue using an elastic incompressible non-linear registration algorithm based on the LogDemons algorithm. This method has shown promising results when applied to previous data-sets. Along with having the advantages of the LogDemons algorithm such as computing deformations that are invertible with smooth inverse, the method has the added advantage of allowing physiological constraints to be added to the deformation model. The registration is entirely performed in the log-domain with the incompressibility constraint strongly ensured and applied directly in the demons minimisation space. Strong incompressibility is ensured by constraining the stationary velocity fields that parameterise the transformations to be divergence-free in the myocardium. The method is applied to a data-set of 15 volunteers and one phantom, each with echocardiography, cine-MR and tagged-MR images. We are able to obtain reasonable results for each modality and good results for echocardiography images with respect to quality of the registration and computed strain curves.

1 Methodology

1.1 Cardiac Motion Tracking Using Physiological Constraints

Tracking cardiac motion from 3D images is a difficult task due to the complex movement of the myocardium through the cardiac cycle. The left ventricular (LV) movement includes a contraction of the ventricle with a longitudinal motion towards the apex as well as a twisting motion from the base of the ventricle in the circumferential direction. Common methods for motion tracking using non-rigid registration are able to capture the dilation of the ventricle, however capturing the twisting motion is a difficult task. The incompressible log-domain demons algorithm described in [1] (iLogDemons for short) aims to tackle this problem by imposing physiological constraints (such as incompressibility and elasticity in the myocardium) in the previously proposed log-domain demons algorithm (LogDemons) [2]. For the purpose of this work we don't provide here a state of the art on cardiac motion tracking algorithms, but rather refer the reader to [1]

O. Camara et al. (Eds.): STACOM 2011, LNCS 7085, pp. 55–67, 2012.

and references therein. We apply the iLogDemons method to a 3D data-set of 15 volunteers and one phantom with echocardiography, cine-MR and tagged-MR image sequences. The method is described here in brief, for a more thorough and descriptive analysis see [1].

1.2 Review of the Log-Domain Demons Algorithm

The iLogDemons algorithm is an extension of the LogDemons algorithm [2]. The LogDemons algorithm estimates a dense non-linear transformation ϕ that best aligns a template image T to a reference image R. The transformation ϕ is parameterised by stationary velocity fields $\mathbf{v}$ through the exponential map $\phi = \exp(\mathbf{v})$ [3]. The images R and T are registered by minimising in the space of velocities (the log-domain) the energy functional: $\varepsilon(\mathbf{v}, \mathbf{v}_c) = 1/\sigma_i^2 \parallel R - T \circ \exp(\mathbf{v}_c) \parallel^2_{L_2} + 1/\sigma_x^2 \parallel \log(\exp(-\mathbf{v}) \circ \exp(\mathbf{v}_c)) \parallel^2_{L_2} + 1/\sigma_d^2 \parallel \nabla \mathbf{v} \parallel^2$, where σ_i^2 relates to the noise in the images and σ_d^2 controls the regularisation strength. The velocity field $\mathbf{v}$ parameterises the transformation ϕ, and $\mathbf{v}_c$ parameterises an intermediate transformation $\phi_c = \exp(\mathbf{v}_c)$ that models the *correspondences* between the voxels of the two images. During the *optimisation step*, $\varepsilon(\mathbf{v}, \mathbf{v}_c)$ is minimised with respect to $\mathbf{v}_c$. Under the diffeomorphic update rule $\phi_c \leftarrow \phi \circ \exp(\delta\mathbf{v})$, the optimal update velocity writes $\delta\mathbf{v}(\mathbf{x}) = (R(\mathbf{x}) - T \circ \phi(\mathbf{x}))/(\parallel (J(\mathbf{x}) \parallel^2 + \sigma_i/\sigma(\mathbf{x}))J(\mathbf{x})$. In this equation, $J(\mathbf{x})$ is the symmetric gradient $J(\mathbf{x}) = (\nabla R(\mathbf{x}) + \nabla(T \circ \phi)(\mathbf{x}))/2$. The correspondence velocity $\mathbf{v}_c$ is then updated using the first order approximation of the Baker-Campbell-Hausdorff (BCH) formula $\mathbf{v}_c = Z(\mathbf{v}, \delta\mathbf{v}) = \mathbf{v} + \delta\mathbf{v} + 1/2[\mathbf{v}, \delta\mathbf{v}] + 1/12[\mathbf{v}, [\mathbf{v}, \delta\mathbf{v}]] + O(\parallel \delta\mathbf{v} \parallel^2)$, where the Lie bracket $[\cdot, \cdot]$ is defined by $[\mathbf{v}, \delta\mathbf{v}] = (\nabla\mathbf{v})\delta\mathbf{v} - (\nabla\delta\mathbf{v})\mathbf{v}$. Finally, the *regularisation step* estimates the optimal regularised transformation ϕ by minimising $\varepsilon(\mathbf{v}, \mathbf{v}_c)$ with respect to $\mathbf{v}$, which is approximated by smoothing the correspondence velocity $\mathbf{v}_c$ with a Gaussian kernel G_σ.

1.3 Modeling Elasticity in the Myocardium

In order to incorporate an elastic regularizer into the LogDemons framework, a consistent mathematical formulation of the LogDemons regularisation is required. In [1] a closed-form expression of the demons Gaussian regulariser $\varepsilon_{reg}(\mathbf{v}) = 1/\sigma_x^2 \parallel \log(\exp(-\mathbf{v}) \circ \exp(\mathbf{v}_c)) \parallel^2_{L_2} + 1/\sigma_d^2 \parallel \nabla\mathbf{v} \parallel^2$ is given by linearising the first term using the BCH formula and replacing the second term with the infinite sum Tikhonov regulariser. We could then replace the Gaussian regularizer by an elastic-like one, in a consistent way. The proposed elastic regularizer amounts to filtering the correspondence velocities by the elastic-like kernel:

$$\mathbf{v} = \left(G_\sigma Id + \frac{\sigma^2 \kappa}{1 + \kappa} HG_\sigma \right) \star \mathbf{v}_c = G_{\sigma,\kappa} \star \mathbf{v}_c \tag{1}$$

where $\sigma^2 = 2/\sigma_d^2$, HG_σ is the Hessian of the Gaussian kernel G_σ and $G_{\sigma,\kappa}$ is the elastic-like vector filter. In this formulation, $\kappa > 0$ penalises the global compressibility, and setting $\kappa = 0$ gives the Gaussian filter used in the LogDemons algorithm.

1.4 Incorporating Strong Incompressibility in the Myocardium

Incorporating incompressibility into the LogDemons consists in constraining the velocity fields $\mathbf{v}$ to be divergence-free. Demons optimisation step is not modified, as it optimises $\mathbf{v}_c$ only, but demons regularisation energy is now optimised under the divergence-free constraint, which amounts to minimising the Lagrange function:

$$P(\mathbf{v},p) = \frac{1}{\sigma_x^2} \parallel \mathbf{v}_c - \mathbf{v} \parallel_{L_2}^2 + \int_\Omega \sum_{k=1}^{+\infty} \frac{Q_{el}^k(\mathbf{v})}{\sigma_x^2 \sigma_d^{2k}} - \frac{2}{\sigma_x^2} \int_\Omega p \nabla \cdot \mathbf{v}. \tag{2}$$

where Q_{el}^k is the k^{th} order isotropic differential quadratic form (IDQF) of a vector field $\mathbf{v}$ defined by $Q_{el}^k(\mathbf{v}) = \alpha_k \delta_{i_1 \ldots i_k} \mathbf{v}_{i_{k+1}} \delta_{i_1 \ldots i_k} \mathbf{v}_{i_{k+1}} + \beta_k \delta_{i_1 \ldots i_k} \mathbf{v}_{i_{k+1}} \delta_{i_2 \ldots i_k} \mathbf{v}_{i_1}$. In this equation, the Lagrange multiplier p is a scalar function of the Sobolev space $H_0^1(\Omega)$ that vanishes at infinity. The second term is the elastic-like regularizer that leads to the filter previously mentioned. We refer the reader to [1] for details.

Optima of (2) are found by solving $\delta_{\mathbf{v}} P(\mathbf{v},p) = 0$:

$$\mathbf{v} + \sum_{k=1}^{\infty} \frac{(-1)^k}{\sigma_d^{2k}} (\alpha_k \Delta^k \mathbf{v} + \beta_k \Delta^{k-1} \nabla \nabla^T \mathbf{v}) = \mathbf{v}_c - \nabla p \tag{3}$$

with $p = 0$ at the domain boundaries $\delta\Omega$. The divergence of (3) under the optimal condition $\nabla \cdot v = 0$ yields the Poisson equation $\Delta p = \nabla \cdot \mathbf{v}_c$ with 0-Dirichlet boundary conditions, which can be solved independently of $\mathbf{v}$ to get p. The right hand side of (3) is thus the L_2 projection of $\mathbf{v}_c$ onto the space of divergence-free vector fields. Computationally, the divergence-free constraint on the velocity fields is enforced by smoothing the velocity field then projecting onto the space of divergence-free velocity fields. This is theoretically the same as projecting onto the space of divergence-free velocity fields then smoothing the results since convolution and derivatives commute (up to issues at the boundary).

Algorithm 1 summarises the main steps of the method. Implementation of this algorithm is described in the following section. A more thorough description of the derivations of the previous equations can be found in [1].

Algorithm 1. iLogDemons: Incompressible Elastic LogDemons Registration

Require: Stationary velocity field $\mathbf{v}^0$. Usually $\mathbf{v}^0 = \mathbf{0}$ i.e. $\phi^0 = Id$.

1: **loop** {*over n until convergence*}
2: Compute the update velocity: $\delta\mathbf{v}^n$ (see [1]).
3: Fluid-like regularisation: $\delta\mathbf{v}^n \leftarrow G_{\sigma_f} \star \delta\mathbf{v}^n$, G_{σ_f} is a Gaussian kernel.
4: Update the correspondence velocity: $\mathbf{v}^n \leftarrow Z(\mathbf{v}^{n-1}, \delta\mathbf{v}^n)$ (see [2]).
5: Elastic-like regularisation: $\mathbf{v}^n \leftarrow G_{\sigma,\kappa} \star \mathbf{v}^n$ (see [1]).
6: Solve: $\Delta p = \nabla \cdot \mathbf{v}^n$ with 0-Dirichlet boundary conditions.
7: Project the velocity field: $\mathbf{v}^n \leftarrow \mathbf{v}^n - \nabla p$.
8: Update the warped image $T \circ \phi^n = T \circ \exp(\mathbf{v}^n)$.
9: **return** $\mathbf{v}$, $\phi = \exp(\mathbf{v})$ and $\phi^{-1} = \exp(-\mathbf{v})$.

2 Implementation

The algorithm has been implemented using ITK and the open source implementation of the LogDemons algorithm [4]. The Poisson equation (which is solved at the incompressible domain) is discretised on the image grid using finite difference schemes [5] as the incompressible domain Γ may be of irregular shape. Image gradients are computed with periodic boundary conditions over the entire image domain [4] and the Gaussian filters are implemented with ITK recursive filters.

Despite the additional constraints, the complexity of the algorithm remains reasonable with respect to the LogDemons algorithm. Demons update velocity is computed at each voxel. The elastic-like filter is computed using Gaussian convolutions, therefore no significant overhead is added to the original Gaussian filtering. The complexity of the divergence-free projector directly depends on the number of voxels of the incompressible domain Γ.

The algorithm requires computing i) the divergence of the velocity field, ii) the gradient of the pressure field p, and iii) solving a linear system with $n \times n$ elements, where n is the number of voxels of the incompressible domain. The divergence and gradient operators are linear in the number of voxels. The Poisson Equation is solved at each iteration using iterative solvers like GMRES [6].

The codes are written in C++ and require as input the fixed image file and moving image file, as well as optional input of the mask image file, and registration parameters. The parameters used in the registration are summarized in the table below. These values were chosen based on tests performed on similar data-sets that concluded that the key parameter of interest is σ, which defines the weight of the Gaussian smoothing of the velocity field (in mm). The original voxel size of the images are$0.67 \times 0.68 \times 0.58$ for echocardiography, $1.25 \times 1.25 \times 8$ for cine-MR and $0.96 \times 0.96 \times 0.96$ for tagged-MR. The choice of σ is generally based on the voxel size to be around 1-2 times the largest original voxel size. Given the large difference in voxel size for cine-MR σ was a trade-off between the largest and smallest voxel size. More levels were used for the echocardiography sequences to speed up convergence of the simulation. This could also be done for the cine-MR sequences but was not considered necessary in this case. For the tagged-MR sequences, increasing the number of multi-resolution levels can remove the tags from under-sampling.

3 Image Pre-processing

In order to apply the algorithm to the different data types, some pre-processing is needed to prepare the data. The method is defined in a way such that the user can give as input a region (which we define as a binary image with value 1 in the incompressible region and value 0 outside) where the incompressibility constraint is imposed. This region is defined at one time-frame only (end diastole). If no input is given the entire image is constrained to be incompressible, otherwise the user can turn off the incompressibility constraint (giving the standard

Input parameters:	**Echo**	**Cine**	**Tag**
Multi-resolution levels (frame-by-frame registration)	3	2	2
Multi-resolution levels (refinement step)	2	1	1
Number of iterations / level	100	100	100
Sigma (update field) in *mm*	0.5	0.5	0.5
Kappa (update field) in *mm*	0	0	0
Sigma (stationary velocity field) in *mm*	0.5	2	2
Kappa (stationary velocity field) in *mm*	1	1	1
Incompressibility update field (0-Disable,1-Enable)	0	0	0
Incompressibility velocity field (0-Disable,1-Enable)	1	1	1

LogDemons algorithm). Therefore, in order to use the iLogDemons algorithm, we need to define the region where we impose the incompressibility constraint by delineating the left ventricle myocardium using image segmentation tools (since in this case we are interested in the deformation of the left ventricle). Note that for the cine-MR sequences we segmented also the right ventricle since it is clearly visible in all the images and provides added information to the registration.

Myocardium Segmentation to Define the Incompressible Region. For each image sequence we used an interactive 3D segmentation tool that builds a 3D mask image and mesh. Control points are added by the user to define the inside, outside, and border of the region, from which a 3D mesh is constructed using an implicit variational surfaces approach. The tool is included within the CardioViz3D software package available for download[1]. For further details on the tool see [7]. We segmented the LV endocardium and the LV epicardium and then applied arithmetic tools to obtain the LV myocardium image. We then dilate the resulting mask to ensure that the full myocardium is covered and to avoid possible boundary effects. The incompressibility domain is shown in yellow for each of the the imaging modalities (see Fig. 1). A screenshot of the segmentation tool is shown in Fig. 2.

Isotropic Resampling. The cine-MR images have anisotropic voxel sizes. To correct for this, we re-sampled the voxels to be isotropic in all directions. Isotropic voxel size improves the registration since the transformation is defined on a grid with enough resolution to avoid "aliasing" effects (as is true for any demons algorithm). The echocardiography and tagged-MR image sequences had already isotropic voxels.

Contrast Enhancement. To enhance the image contrast we clamped the tails of the grey-level histogram to exclude the 1st and 99th quantiles. The grey level intensities were then normalized for each slice using a fixed scale. This was done for each image in the sequence independently. An example of the before and after image is shown in Fig 3. This processing also reduced the effects of tag fading, thus further improving registration results.

[1] http://www-sop.inria.fr/asclepios/software/CardioViz3D/

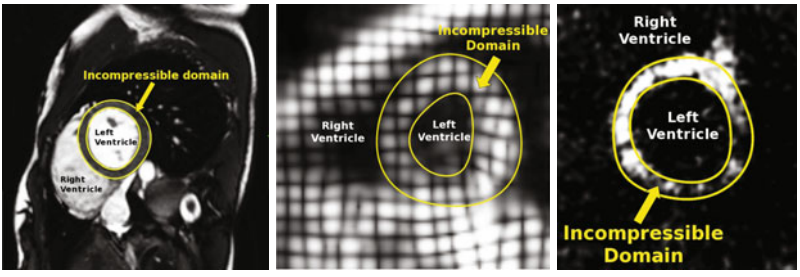

Fig. 1. The incompressibility domain shown on a cine-MR image (left), tagged-MR image (center) and echocardiography image (right). This domain defines where the incompressibility constraint is enforced in the registration algorithm.

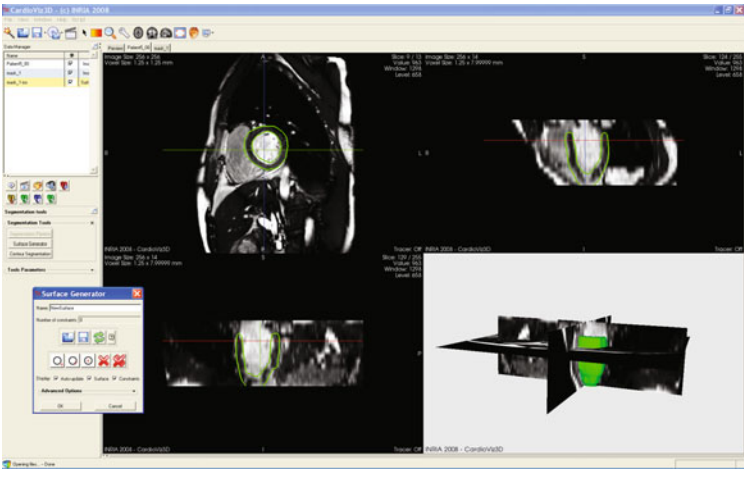

Fig. 2. A screenshot of the interactive segmentation tool in CardioViz3D which can be downloaded from *http://www-sop.inria.fr/asclepios/software/CardioViz3D/*. The tool requires the user to place control points, from which a surface is build using implicit variational surfaces approach.

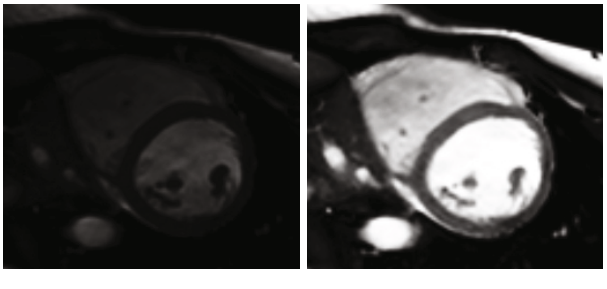

Fig. 3. Original image (left) and processed image (right) after histogram clamping and normalization to improve image contrast

4 Application to Challenge Data

The algorithm was applied to a data-set of 15 volunteers and one phantom, each with cine-MR, tagged-MR and echocardiography images. The resulting deformation fields for each modality are included in the motion tracking challenge. To demonstrate the performance of this method we show the results for each modality for one patient from the data-set of 15 volunteers as well as the results for the phantom data. Similar results were obtained for the remaining volunteers.

4.1 Results for Echocardiography Sequences

The method was first applied to echocardiography image sequences. In this case, the images show well the endocardium (inside the heart) but the epicardium is difficult to see, particularly in the free wall. However, the motion is more apparent in the echocardiography sequences than in cine-MR due to the speckle that is "stitched" to the muscle and thus follows it as the heart deforms, though this speckle is consistent only between few time frames. Figure 4 (first two rows) shows one patient image at full contraction (systole) with the mask propagated using the deformation field computed in the registration overlaid on the image and similarly for the phantom. The masked deformation field is shown on the patient and phantom at full contraction to illustrate the direction and magnitude of motion. In each case the registration captures the expected longitudinal contraction, and circumferential twisting of the ventricle. We can also observe that, although it is difficult to distinguish clearly the epicardium for this modality, the algorithm is able to produce reasonable strain curves, as shown in Fig 5.

4.2 Results for Cine-MR Image Sequences

The algorithm was applied to the short-axis cine-MR images. These images show clearly the myocardium, though there is little information in the apex due to too few slices in the through plane. The algorithm is able to capture a realistic motion of the myocardium, as shown in the middle two rows of Fig 4. The strain curves for cine-MR are under-estimated mainly due to lack of texture information in the images but show the expected trends (increase in strain towards peak systole, followed by decrease at rest (see Fig 5).

4.3 Results for Tagged-MR Image Sequences

As expected, the tagged-MR registration captures the twisting motion of the myocardium very well, this is particularly evident in the phantom (see Fig 4 bottom row second to the right), as well as the longitudinal contraction. The strain curves for the tagged-MR data shown in Fig 5 show a reasonable trend, however the standard deviation over the given regions is high in this case.

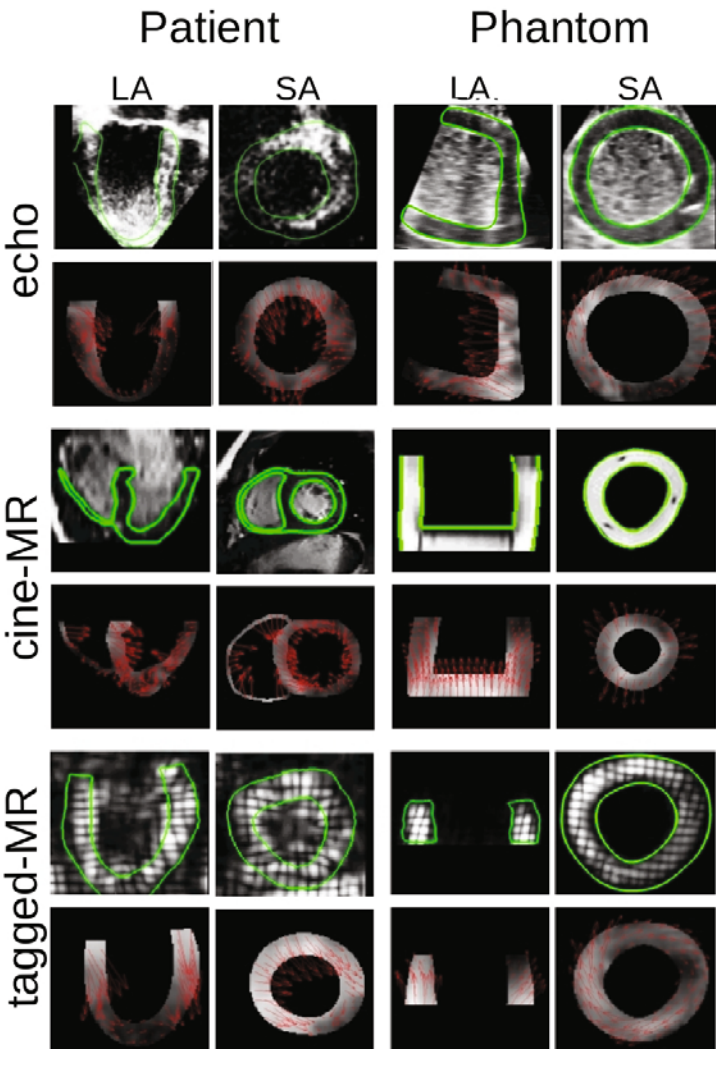

Fig. 4. Top row: Long axis and short axis views of echocardiography images for one patient (left two columns) and the phantom (right two columns) shown at full contraction overlaid with the mask deformed by the deformation computed using iLogDemons. Second row: Two views of the computed deformation field (normal of intensities and vectors) shown only in the mask region for one patient image (left columns) and the phantom (right columns). Similarly for cine-MR (third and fourth rows) and tagged-MR (fifth and sixth rows). For each modality a realistic motion is obtained (rows one, three and five), as well as the desired direction and magnitude of motion (rows two, four and six), particularly for the phantom. In particular, the longitudinal motion captured by the algorithm can be seen by the vectors pointing downwards towards the apex in the long axis views of rows two, four and six, and the circumferential motion can be seen in the short axis views where the vectors appear to be wrapping around the muscle to an extent.

5 Strain Estimation

The strain curves in each of the 17 AHA regions in each of the radial, circumferential and longitudinal directions were computed for each of the modalities. The strain was computed using the 3D Lagrangian finite strain tensor

$$E(x) = \frac{1}{2}[\nabla \mathbf{u}(x) + \nabla \mathbf{u}^T(x) + \nabla \mathbf{u}^T(x)\nabla \mathbf{u}(x)] \tag{4}$$

for the estimated displacement $\mathbf{u}(x)$ from the iLogDemons registration at the spatial positions x. The computed strain tensors were then projected onto a local prolate coordinate system as described in [1].

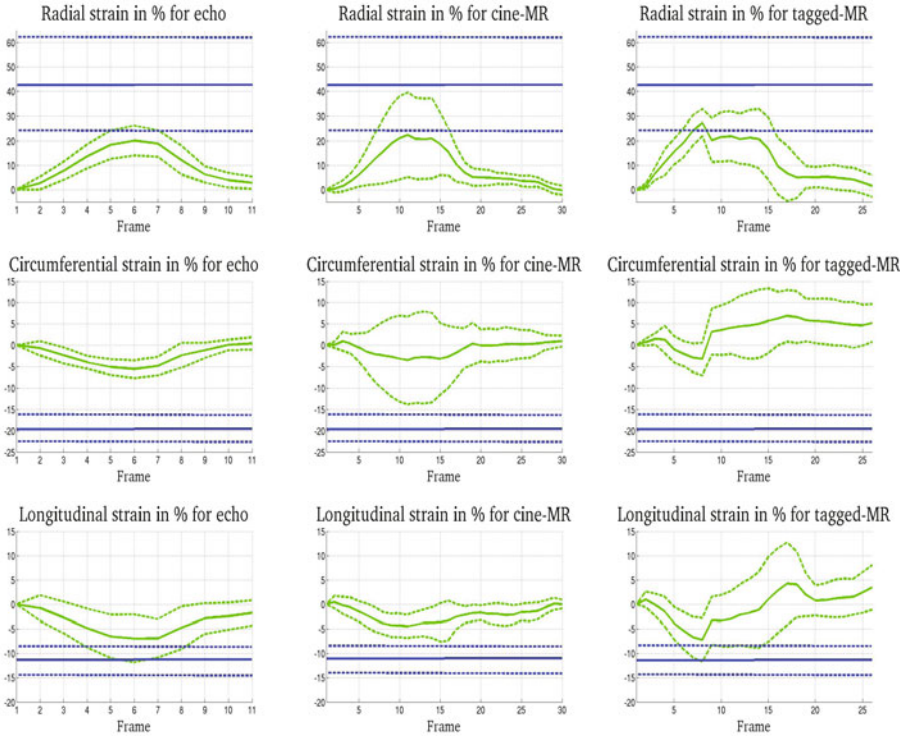

Fig. 5. Strain curves in the radial (left), circumferential (middle) and longitudinal (right) directions for echocardiography sequence (top row), cine-MR sequence (middle row) and tagged-MR sequence (bottom row) for one subject. Mean (solid line) and standard deviation (dashed line) are shown for one patient in green, and the mean and standard deviations for systolic strain reported in [8] are shown in blue. Note that the curves have not been temporally synchronized. We can see that the magnitudes are under-estimated, though the curve trends are consistent with what is expected with a peak strain at peak contraction in the radial direction, minimum strain at peak contraction for circumferential and longitudinal strain.

The strain curves for each modality in each direction are shown in Fig 5. The curves show a good consistency between the modalities in respect to curve trends, with the strain rising to a peak in the middle of the cycle at peak systole, and decreasing back towards zero (note that the curves are not temporally synchronized). The curves for the echocardiography sequence show a good agreement to those previously found for cine-MR and tagged-MR presented in [1]. However, the curves for the cine-MR sequence show less consistency with previously published results in [8], as they are under-estimated in all directions. Possible reasons for this could be too much smoothing, a lack of texture information, poor image resolution or errors in the tracking. The curves of the standard deviation among the zones shown are similar to the mean curves shown in green, which displays the consistency among the AHA regions which is expected in healthy subjects with synchronized movement among the regions. Note that here we exclude the apical regions since the apex is not clearly visible in all images.

6 Discussion

In general, this method provides reasonable results for tracking the myocardium in the three modalities. In particular, the method gives good results for the echocardiography sequences for both the tracking and estimation of strain even given data with poor visibility and little structural information. The method is particularly useful for cardiac motion tracking due to the fact that it can be applied to the imaging modalities that are most commonly used in cardiology.

6.1 Incompressibility Constraint

We discuss here the advantages and disadvantages of enforcing the incompressibility constraint in the myocardium. The constraint was integrated into the LogDemons method initially to be used on cine-MR sequences, which are known to exhibit only apparent motion in the image. For this reason, it seemed natural to constrain the myocardium to be incompressible to reduce the number of unknowns to force a circumferential and longitudinal deformation when there is a radial contraction/expansion. In the case of echocardiography sequences and tagged-MR sequences, there is more texture information in the image that aids in capturing this motion (speckles in echocardiography images, tag grids in tagged-MR). Nonetheless, for the purposes of the challenge we applied the method to all modalities to analyse the results.

Myocardium Segmentation. Since the method requires a mask of the myocardium, we segmented these prior to running the algorithm using the tool described in Section 3. The incompressibility constraint relies heavily on the accuracy of the segmentation, therefore errors in the tracking can arise due to mis-segmentation

of the tissue. This is a problem in particular for the echocardiography and tagged-MR images, which are known to be hard to segment given the poor image quality, poor visibility of the myocardium and noise from the top of the cone in echo images. However, this is the case for any method using localized incompressibility constraint to track the myocardium. In this work, we used a binary mask for the myocardium. To avoid possible problems related to the boundary conditions, we dilated the mask by 2 voxels.

Constrained Incompressibility vs. Compressibility. A common point of discussion for constraining the myocardium to be incompressible is that the myocardium is not in fact fully incompressible. In the literature, the myocardium is observed to have a volume change of around 5% [9]. In the case of the LogDemons algorithm, there is no constraint on the compressibility of the myocardium, which results in up to 30% volume change, compared to less than 7% of numerical volume change for the iLogDemons algorithm (see Fig 6). Therefore, while the iLogDemons algorithm may under-estimate the volume change in general, with the unconstrained LogDemons algorithm it can be greatly-overestimated. Furthermore, improved strain curves were obtained in [1] compared to those computed from the LogDemons algorithm. Hence, the incompressibility constraint is a useful prior for cardiac motion tracking, though penalising rather than constraining the compressibility may be more physiologically realistic.

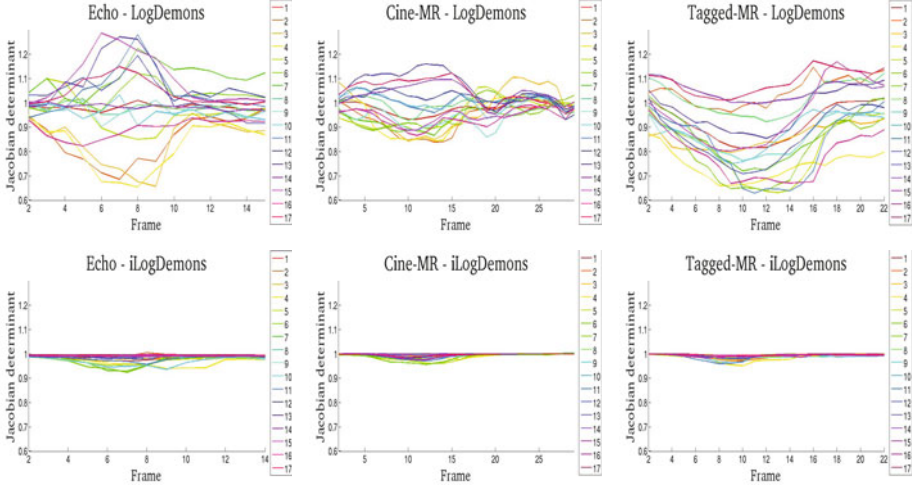

Fig. 6. Average jacobian determinant in each of the 17 AHA regions for the LogDemons algorithm (top row) and iLogDemons (bottom row) for each of the modalities (echo-left column, cine-MR - centre column, tagged-MR - right column). The iLogDemons algorithm constrains the compressibility to be less than 7% for each modality compared to up to 30% compressibility for LogDemons.

6.2 Field of View

In some of the sequences in the challenge data-set, the myocardium was on or very close to the border of the image, particularly in the tagged-MR sequences which have a very narrow field of view. How the image and the deformation are treated at the boundary of the image (extrapolated to invisible data) is a key problem in most registration algorithms. Currently the iLogDemons algorithm works in such a way that the intensities on the border of the image are extrapolated outside the image in a given region.

7 Conclusion

The iLogDemons algorithm was applied to a data-set of 15 subjects and one phantom each with an echocardiography, cine-MR and tagged-MR image sequence. This method was developed for the heart to model elasticity of the tissue and incompressibility in the myocardium. The results show that given few changes in the input parameters, the method is able to retrieve realistic motion of the heart as well as reasonable strain curves for each of the three modalities and is thus a versatile registration algorithm for cardiac motion tracking. However, future work is needed to further analyse the incompressibility prior, possibly including a change in the way the prior is incorporated into the model by means of a penalisation of the compressibility rather than the current method of constraining the velocity fields to be divergence-free.

Acknowledgements. This project was partially funded by the Care4Me ITEA2 project.

References

1. Mansi, T., Pennec, X., Sermesant, M., Delingette, H., Ayache, N.: Ilogdemons: A demons-based registration algorithm for tracking incompressible elastic biological tissues. Int. J. of Computer Vision (2011)
2. Vercauteren, T., Pennec, X., Perchant, A., Ayache, N.: Symmetric Log-Domain Diffeomorphic Registration: A Demons-Based Approach. In: Metaxas, D., Axel, L., Fichtinger, G., Székely, G. (eds.) MICCAI 2008, Part I. LNCS, vol. 5241, pp. 754–761. Springer, Heidelberg (2008)
3. Arsigny, V., Commowick, O., Pennec, X., Ayache, N.: A Log-Euclidean Framework for Statistics on Diffeomorphisms. In: Larsen, R., Nielsen, M., Sporring, J. (eds.) MICCAI 2006, Part I. LNCS, vol. 4190, pp. 924–931. Springer, Heidelberg (2006)
4. Dru, F., Vercauteren, T.: An ITK implementation of the symmetric log-domain diffeomorphic demons algorithm. Insight Journal (January-June 2009)
5. Simard, P.Y., Mailloux, G.E.: A projection operator for the restoration of divergence-free vector fields. IEEE Transaction on Pattern Analysis and Machine Intelligence 10, 248–256 (1988)

6. Saad, Y.: Iterative methods for sparse linear systems. Society for Industrial Mathematics, vol. 73. PWS (2003)
7. Mansi, T.: Image-Based Physiological and Statistical Models of the Heart, Application to Tetralogy of Fallot. Thèse de sciences (phd thesis), Ecole Nationale Supérieure des Mines de Paris (September 2010)
8. Moore, C., Lugo-Olivieri, C., McVeigh, E., Zerhouni, E.: Three-dimensional systolic strain patterns in the normal human left ventricle: Characterization with tagged MR imaging. Radiology 214, 453–466 (2000)
9. Glass, L., Hunter, P., McCulloch, A.: Theory of Heart: Biomechanics, Biophysics, and Nonlinear Dynamics of Cardiac Function. Springer, Heidelberg (1991)

Temporal Diffeomorphic Free Form Deformation (TDFFD) Applied to Motion and Deformation Quantification of Tagged MRI Sequences

Mathieu De Craene[1,2], Catalina Tobon-Gomez[1,2], Constantine Butakoff[1,2], Nicolas Duchateau[1,2], Gemma Piella[1,2], Kawal S. Rhode[3], and Alejandro F. Frangi[1,2]

CISTIB
[1] DTIC, Universitat Pompeu Fabra
[2] CIBER-BBN, Barcelona, Spain
[3] Division of Imaging Sciences and Biomedical Engineering, KCL, UK

Abstract. This paper presents strain quantification results obtained from the Tagged Magnetic Resonance Imaging (TMRI) sequences acquired for the 1^{st} *cardiac Motion Analysis Challenge (cMAC).* We applied the Temporal Diffeomorphic Free Form Deformation (TDFFD) algorithm to the phantom and the 15 healthy volunteers of the cMAC database. The TDFFD was modified in two ways. First, we modified the similarity metric to incorporate frame to frame intensity differences. Second, on volunteer sequences, we performed the tracking backward in time since the first frames did not show the contrast between blood and myocardium, making these frames poor choices of reference.

On the phantom, we propagated a grid adjusted to tag lines to all frames for visually assessing the influence of the different algorithmic parameters. The weight between the two metric terms appeared to be a critical parameter for making a compromise between good tag tracking while preventing drifts and avoiding tag jumps. For each volunteer, a volumetric mesh was defined in the Steady-State Free Precession (SSFP) image, at the closest cardiac time from the last frame of the tagging sequence. Uniform strain patterns were observed over all myocardial segments, as physiologically expected.

1 Introduction

TMRI provides non invasively image markers for tracking tissue motion and deformation along the cardiac cycle. The introduction of CSPAMM [1] efficiently solved tag fading issues that were traditionally hampering the analysis of TMRI data in diastole. Breathing artifacts producing unaligned slices have been corrected by the introduction of navigator-driven protocols and the move to fully 3D acquisitions. In [3], a CSPAMM-based protocol was proposed by performing three acquisitions sequentially with line tag preparation in each orthogonal direction. Each of these three acquisitions is performed in a single breath-hold of 18 heartbeats duration and retrospectively corrected for misalignment using a respiratory navigator.

O. Camara et al. (Eds.): STACOM 2011, LNCS 7085, pp. 68–77, 2012.

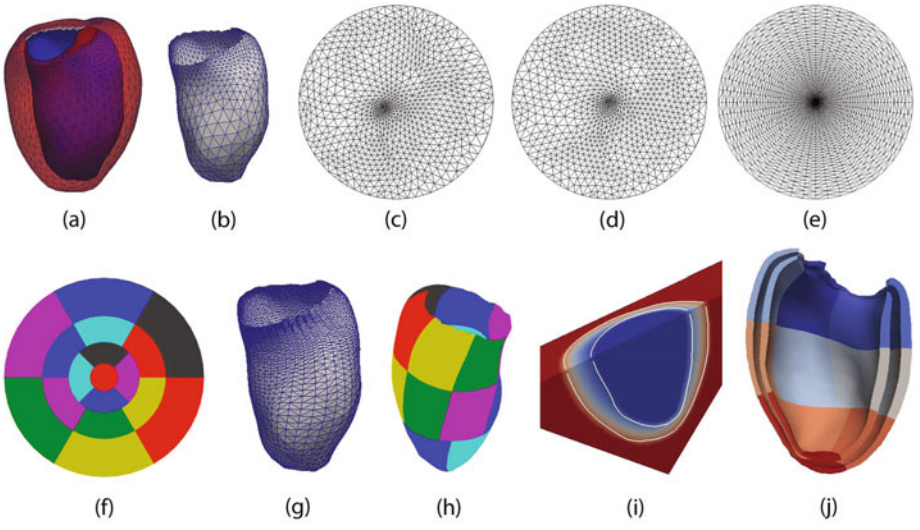

Fig. 1. Remeshing process: From (a) the LV mesh, extract (b) endocardial surface, and (c) map it to a disk, (d) correct the mapping by moving the apical point to the center, (e) create a new parametrization that maps the new vertices onto the surface and (f,g,h) add AHA regions, (i) solve Laplace equation in 3D, (j) produce volumetric mesh with 3 layers of wedge elements (the middle layer was hidden for clarity)

In this paper, we extend the TDFFD algorithm [4], initially designed for 3D US images quantification and applied it to the 1^{st} cMAC TMRI database. We present and discuss strain quantification results on the set of healthy volunteers and the phantom acquisitions.

2 Methods

2.1 Preprocessing

The cMAC database was acquired according to the imaging protocols defined in [5]. In this paper, we worked on the resampled grid TMRI images. For obtaining these fused images, the three images resulting from each acquisition direction were first resampled to a common reference space (usually taken as the short axis space) with isotropic voxel resolution. The geometric mean of intensities of the three resampled volumes were then computed at each voxel to produce the reconstructed TMRI images with a tagging grid pattern, as shown in Fig. 2(c,d).

2.2 Segmentation

Myocardial borders were defined on the reference image (here taken as the last frame of the sequence) by segmenting the SSFP images. The corresponding frame

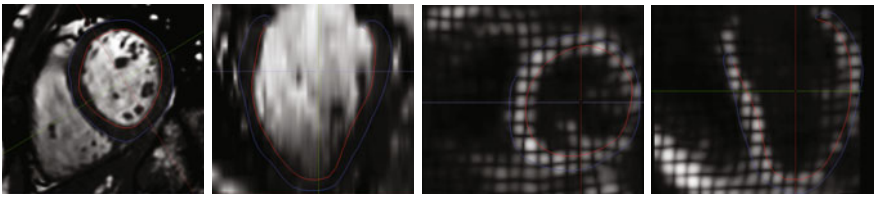

(a) (b) (c) (d)

Fig. 2. Segmentation obtained from the SSFP short axis image (a,b) mapped using the DICOM transformation to the TMRI image (c,d)

in the SSFP sequence was selected by looking for the closest trigger time. The left ventricular (LV) cavity was then segmented from the selected short axis dataset by a human observer experienced in cardiac magnetic resonance postprocessing. 3D meshes of the LV were obtained by manually deforming a LV model [6]. Both the visualization and the segmentation was performed with GIMIAS v1.3.0[1]. The manually segmented mesh was then registered to the coordinates of the TMRI sequence using DICOM header information. The result of mapping the SSFP segmentation on the TMRI image is shown in Fig. 2 for the first volunteer.

2.3 Mesh Postprocessing

The goal of this postprocessing is to produce a mesh meeting the following requirements: 1) to provide a regular definition of the 17 American Heart Association (AHA) segments, 2) to provide a definition of the local radial direction that is consistent at endo- and epicardium and 3) to be a volumetric mesh for quantifying strain in the whole endocardium. We introduce here a two-step pipeline meeting these requirements.

Imposing a regular mesh structure for improved definition of AHA segments. Any surface, homeomorphic to a disk, can be mapped to a disk by requiring that every coordinate has a vanishing Laplacian. We want to compute a bijective mapping $\varphi : \mathcal{M} \rightarrow \mathcal{D} \subset \mathbb{R}^2$, where $\mathcal{M}$ is a surface and $\mathcal{D}$ is a disk. First we need to define the boundary $\partial\mathcal{D}$ of $\mathcal{D}$ by uniformly sampling a circle (a unit circle for simplicity), onto which we want to map the boundary $\partial\mathcal{M}$. Therefore, for every point of $\partial\mathcal{M}$ there is a corresponding point on the disk boundary $\partial\mathcal{D}$. The computed mapping will give us the coordinates of the remaining points inside the disk. Let us assume that the disk is in the XY coordinate plane, and the boundary coordinates are given by vector-columns $\mathbf{x}_0$ and $\mathbf{y}_0$ (concatenation of x and y coordinates of all boundary points). Let $\mathbf{L}_{\mathcal{M}\setminus\partial\mathcal{M}}$ be the Laplacian matrix of the mesh that represents the surface $\mathcal{M}$ with the rows corresponding to its boundary $\partial\mathcal{M}$ removed. Let $\mathbf{x}_{\partial\mathcal{D}}$, $\mathbf{y}_{\partial\mathcal{D}}$, $\mathbf{x}_{\mathcal{D}\setminus\partial\mathcal{D}}$ and $\mathbf{y}_{\mathcal{D}\setminus\partial\mathcal{D}}$ be the x,y coordinates of the points on the disk (the ones which we are calculating and that define our

[1] http://www.gimias.org

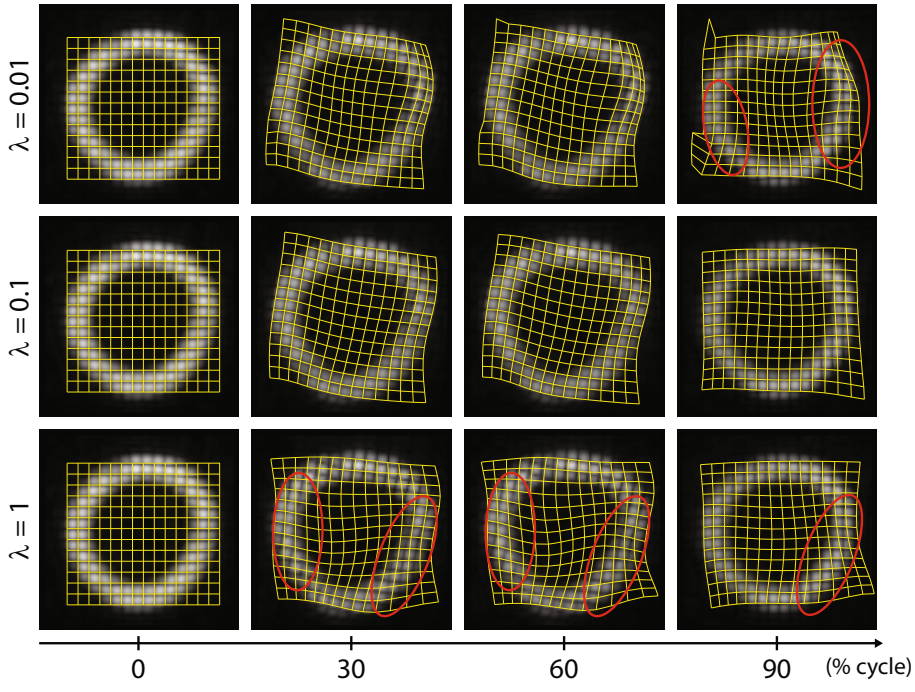

Fig. 3. Propagation of a synthetic grid using the TDFFD tracking results for 3 different λ values in Eq. 2. Drift errors (top row) and tag jumps (bottom row) are highlighted using red ellipses.

mapping) corresponding to the boundary and the interior, respectively. Then, the following two systems of linear equations give the desired mapping (vectors $\mathbf{x}$ and $\mathbf{y}$), while the connectivity information is retained from the mesh representation of $\mathcal{M}$ [7]:

$$\begin{cases} \mathbf{L}_{\mathcal{M}\setminus\partial\mathcal{M}} \cdot \mathbf{x}_{\mathcal{D}\setminus\partial\mathcal{D}} = 0 \\ \mathbf{x}_{\partial\mathcal{D}} = \mathbf{x}_0 \end{cases} ; \quad \begin{cases} \mathbf{L}_{\mathcal{M}\setminus\partial\mathcal{M}} \cdot \mathbf{y}_{\mathcal{D}\setminus\partial\mathcal{D}} = 0 \\ \mathbf{y}_{\partial\mathcal{D}} = \mathbf{y}_0 \end{cases} \tag{1}$$

The above methodology provides a simple method for mapping endocardium to a disk, where the edge of the endocardium (Fig. 1b) is mapped to an uniformly sampled circumference of the disk (Fig. 1c). However, it is in our interest to map the cardiac apex to the center of the disk. We employ the mass spring model to displace the apical point to the center while uniformly spreading the cell deformation to all the cells (Fig. 1d). Given this mapping, we can impose a regular mesh structure by generating vertices as points of intersection of concentric circles and rays emanating from the center (Fig. 1e). It is easy now to compute a transformation between Fig. 1d and Fig. 1e through barycentric coordinates. This transformation allows us to generate a new mesh (Fig. 1g) whereupon it is easy to define the 17 AHA segments (Fig. 1f), therefore satisfying the first requirement.

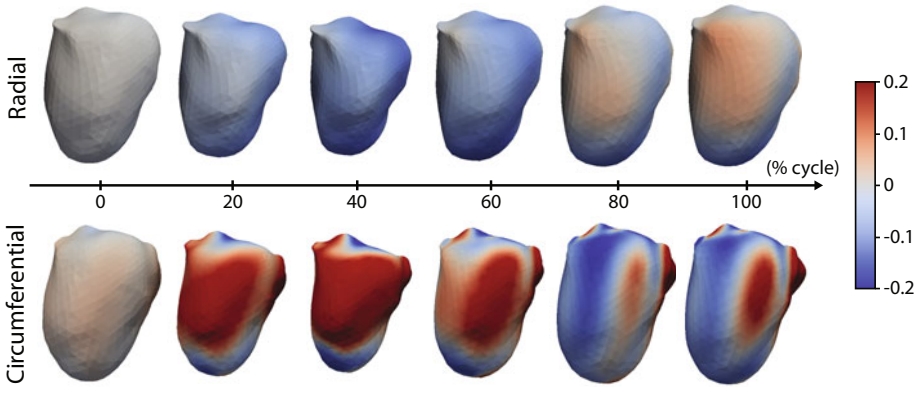

Fig. 4. Evolution of radial and circumferential strains for the first volunteer over the cardiac cycle, plotted using a colormap. An animated version of this figure is available at http://mathieu.decraene.info/stacom11/strain.gif.

Volumetric mesh generation by Laplace streamlines sampling. The generation of the volumetric mesh (third requirement) follows 4 steps:

- generate an image, between epi- and endocardium, that is a solution to Laplace equation $\Delta\Psi = 0$, by successive over relaxation (see Fig. 1i, Δ is the Laplace operator)
- compute streamlines of the normalized gradient of Ψ starting from each endocardial vertex towards the epicardial surface
- generate layers of vertices equidistantly along the line connecting the endpoints of the streamlines
- use the connectivity information of the endocardial surface mesh to generate 6-node wedge elements connecting all the layers (Fig. 1j)

At each node, the direction of the outgoing streamline is taken as radial direction. This ensures a consistent definition of the normal direction across the different 'layers' of the volumetric mesh (second requirement).

2.4 Motion and Deformation Quantification

The TDFFD algorithm described in [4] optimizes a 4D velocity field parametrized by B-Spline spatiotemporal kernels. The advantage of representing the velocity rather than the displacement is to introduce temporal consistency in the recovered transformation, *i.e.*, that motion at a given time point depends on all previous times. In this paper, the TDFFD algorithm was modified in two aspects. First, the tracking was performed backward in time starting from the last image. This option was taken because in the first images of a TMRI sequence, the blood is magnetized in the same way as the tissue. The distinction between blood and myocardial borders is therefore invisible, making the first frames a poor choice of reference.

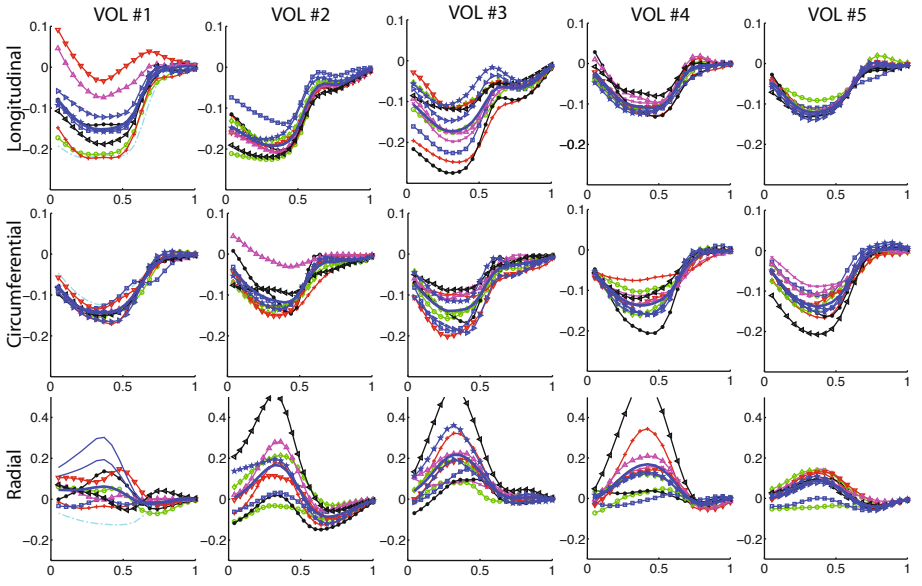

Fig. 5. Longitudinal, circumferential and radial strains for Volunteers #1 to #5 of the cMAC database plotted as a function of time (normalized by one heart period)

The second change affects the similarity metric. The original TDFFD similarity metric [4] sums the squared intensity differences between each image with respect to the first image in the sequence. This choice was shown to be efficient for limiting the accumulation of motion errors generating drift effects. However, quantifying similarity from frame to frame is expected to be more sensitive to small incremental displacements. It is also more robust to possible intensity changes due to smooth alterations of tissue magnetization in time. For this reason, we extended the original metric by summing similarities quantified both from frame to frame and to the reference image. For this, we consider two sets of samples. The first set of samples is defined as $X = \{\mathbf{x}_i, i \in [1, N_X]\}$ where all $\mathbf{x}_i$ belongs to the space of coordinates of the reference image. The second set of samples is taken through the full 3D+t space: $Y = \{(\mathbf{y}_k, f_k), k \in [1, N_Y]\}$ where each $\mathbf{y}_k$ belongs to the space of coordinates of a frame $f_k \in [2, F]$ that is part of the Y samples set generation and F is the number of frames in the sequence.

The full metric is then defined as

$$M = \sum_{i=1}^{N_X} \sum_{j=1}^{F-1} \left(I_j(\boldsymbol{\varphi}_F^j(\mathbf{x}_i; \mathbf{p})) - I_F(\mathbf{x}_i) \right)^2 + \lambda \sum_{k=1}^{N_Y} \left(I_{f_k-1}(\boldsymbol{\varphi}_{f_k}^{f_k-1}(\mathbf{y}_k; \mathbf{p})) - I_{f_k}(\mathbf{y}_k) \right)^2, \quad (2)$$

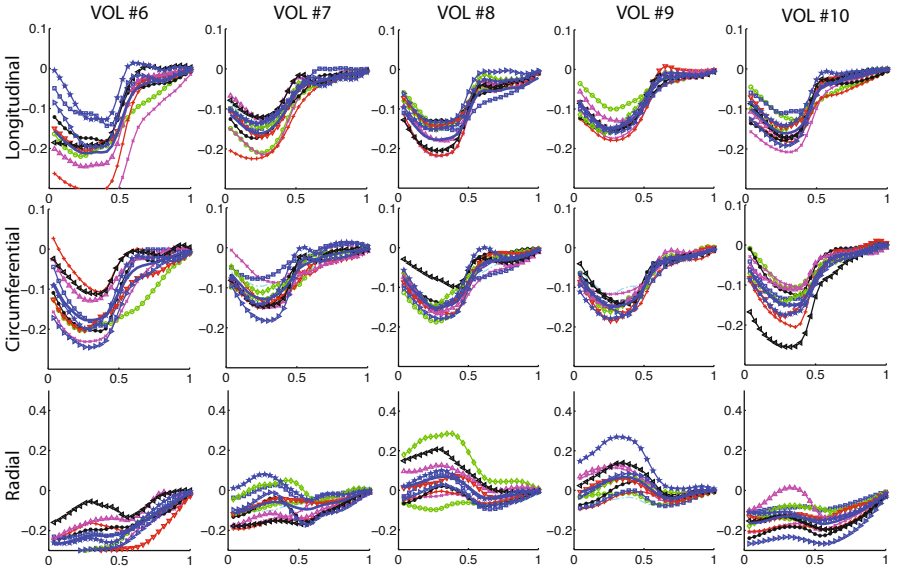

Fig. 6. Longitudinal, circumferential and radial strains for Volunteers #6 to #10 of the cMAC database plotted as a function of time (normalized by one heart period)

where $\boldsymbol{\varphi}_m^n(\mathbf{x})$ stands for the transport of a coordinate $\mathbf{x}$ at time m to the time n and λ is a factor balancing the metric terms. This transport is made by following the flow of a continuous 3D+t velocity field $\mathbf{v}(\mathbf{x}, t; \mathbf{p})$, parametrized by B-Spline kernels, and controlled by the set of parameters $\mathbf{p}$:

$$\boldsymbol{\varphi}_m^n(\mathbf{x}; \mathbf{p}) = \mathbf{x} + \int_m^n \mathbf{v}(\boldsymbol{\varphi}_m^t(\mathbf{x}; \mathbf{p}), t; \mathbf{p}) \mathrm{d}t \,. \tag{3}$$

It was shown in [4] that for a time step $\Delta t << 1$, the derivative of $\boldsymbol{\varphi}_s^{t+\Delta t}(\mathbf{x}; \mathbf{p})$ w.r.t $\mathbf{p}$ can be computed from $\mathrm{d}\boldsymbol{\varphi}_s^t(\mathbf{x}; \mathbf{p})/\mathrm{d}\mathbf{p}$

$$\frac{\mathrm{d}\boldsymbol{\varphi}_s^{t+\Delta t}(\mathbf{x}; \mathbf{p})}{\mathrm{d}\mathbf{p}} = \Big(\mathbf{I} + \mathbf{D}\mathbf{v}(\mathbf{x}, t; \mathbf{p})\Delta t\Big) \frac{\mathrm{d}\boldsymbol{\varphi}_s^t(\mathbf{x}; \mathbf{p})}{\mathrm{d}\mathbf{p}} + \frac{\partial \mathbf{v}(\mathbf{x}, t; \mathbf{p})}{\partial \mathbf{p}} \Delta t \,. \tag{4}$$

By iterating Eq. 4 from $(s, t) = (m, m)$ to $(s, t) = (n - \Delta t, n)$, one can obtain the derivative of $\boldsymbol{\varphi}_m^n(\mathbf{x}; \mathbf{p})$ and compute the total derivative of the metric given in Eq. 2 by application of the chain rule.

2.5 Strain Quantification

Strain is computed in the space of coordinates of the last frame, being a good approximation of Lagrangian strain at end-diastole. The computation of the strain tensor involves the backward multiplication of spatial derivatives of the velocity

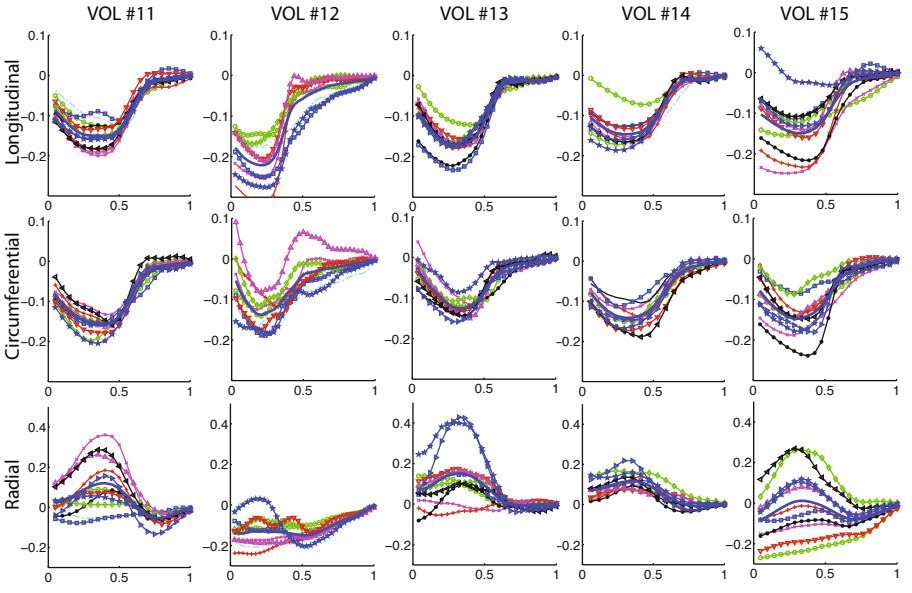

Fig. 7. Longitudinal, circumferential and radial strains for Volunteers #11 to #15 of the cMAC database plotted as a function of time (normalized by one heart period)

fields, corresponding to the factor between brackets in the first term of Eq. 4. The strain tensor is then projected on a set of local directions: radial, circumferential and longitudinal [4]. The radial direction is computed as described in Section 2.3. The longitudinal direction is taken as constant over the whole LV and is defined as the difference between the endocardial apex and the center of the mitral valve. The circumferential direction is computed as the cross product of the two other directions.

3 Experiments

In-vitro phantom. Fig. 3 shows the propagation of a regular grid from the first frame to each image of the sequence for one slice of the phantom sequence. The B-Spline velocity grid had a resolution of 4 control points in each dimension. The number of samples N_X and N_Y were chosen to represent about 15% of the total number of voxels. The λ weight in Eq. 2 was adjusted by visual inspection of the tracking results. Fig. 3 shows that for low values of λ, i.e. when the frame to frame term of the metric predominates, TDFFD efficiently tracks tags crossing at mid-cycle but suffers from drift in the last frame (see red ellipses in first row, last column). Alternatively, when giving too much importance to the non-sequential term, the tracking suffers from tag jumps (e.g red ellipses in the last row). In this experiment, we found a value of $\lambda = 0.1$ qualitatively optimal for weighting the two terms in Eq. 2.

Healthy volunteers. Motion and strain were quantified using the modified TDFFD algorithm (Section 2.4 and 2.5) and the set of local directions computed at each node of the volumetric mesh (Section 2.3). Each of the three components of strain was averaged across 12 AHA regions (corresponding to basal and mid-regions) and plotted for all patients of the cMAC database in Fig. 5, 6 and 7. The recovered strain curves showed a similar pattern in all volunteers, in good agreement with clinical literature [2]. It is expected in healthy volunteers that all regions contract synchronously with a similar strain amplitude. Fig. 5, 6 and 7 show that strain curves were in general uniform over all segments for each patient, except for radial strain. Although radial strain was reported to show the highest variability [2], the dispersion of radial strain in Fig. 5 is more likely due to the smaller number of tags in the radial direction (between 2 and 3 tags). An alternative way of plotting strain is to show on a surface mesh and for a given cardiac time the value of one strain component using a color map. This representation mode is used in Fig. 4 for the first volunteer. Drift errors in the radial strain values are visible at the end of the cycle.

4 Conclusions

In this paper, the TDFFD algorithm was extended to TMRI sequences. Preliminar motion and deformation results were reported for the set of 15 healthy volunteers and the phantom of the 1^{st} cMAC database. On the phantom the weighting between non-sequential (prone to correct drift) and sequential (sensitive to accurate frame to frame tracking) was critical for the obtention of correct tracking results. We observed for healthy volunteers the uniformity of the strain pattern among different segments of the LV, in accordance with clinical literature. The current quantification results exclude the first frames. These could potentially be taken into account by segmenting the SSFP images for generating regions of interest when doing the tracking.

Acknowledgments. This research has been partially funded by the Spanish Industrial and Technological Development Center (CDTI) under the CENIT Programme (cvREMOD Project), the Spanish Ministry of Science and Innovation (MICINN) and the European Regional Development Fund (ERDF) through the research project STIMATH (TIN2009-14536-C02-01), and the European Community's Seventh Framework Program (FP7/2007-2013) under the euHeart project (FP7-ICT-2007-2-224495).

References

1. Fischer, S.E., McKinnon, G.C., Maier, S.E., Boesiger, P.: Improved myocardial tagging contrast. Magnetic Resonance in Medicine 30(2), 191–200 (1993)
2. Moore, C.C., Lugo-Olivieri, C.H., McVeigh, E.R., Zerhouni, E.A.: Three-dimensional systolic strain patterns in the normal human left ventricle: Characterization with tagged MR imaging. Radiology 214(2), 453–466 (2000)

3. Rutz, A.K., Ryf, S., Plein, S., Boesiger, P., Kozerke, S.: Accelerated whole-heart 3D CSPAMM for myocardial motion quantification. Magnetic Resonance in Medicine 59(4), 755–763 (2008)
4. De Craene, M., Piella, G., Camara, O., Duchateau, N., Silva, E., Doltra, A., D'hooge, J., Brugada, J., Sitges, M., Frangi, A.F.: Temporal Diffeomorphic Free-Form Deformation: Application to Motion and Strain Estimation from 3D Echocardiography. Medical Image Analysis (accepted, to appear)
5. Tobon-Gomez, C., De Craene, M., Dahl, A., Kapetanakis, S., Carr-White, G., Lutz, A., Rasche, V., Etyngier, P., Schaeffter, T., Riccobene, C., Martelli, Y., Camara, O., Frangi, A.F., Rhode, K.S.: A multimodal database for the 1st cardiac motion analysis challenge. In: Camara, O., Konukoglu, E., Pop, M., Rhode, K., Sermesant, M., Young, A. (eds.) STACOM 2011. LNCS, vol. 7085, pp. 33–44. Springer, Heidelberg (2012)
6. Ordas, S., Oubel, E., Leta, R., Carreras, F., Frangi, A.F.: A statistical shape model of the whole heart and its application to model-based segmentation. In: SPIE Medical Imaging: Physiology, Function, and Structure from Medical Images, vol. 6511, p. 65111K (2007)
7. Tutte, W.T.: How to draw a graph. Proc. London Math. Soc. 13(3), 743–768 (1963)

Motion Analysis with Quadrature Filter Based Registration of Tagged MRI Sequences

Lennart Tautz, Anja Hennemuth, and Heinz-Otto Peitgen

Fraunhofer MEVIS, Bremen, Germany

Abstract. Analysis of tagged MRI is a valuable tool for assessing regional myocardial function. One major obstacle for existing methods based on feature extraction and registration is the desaturation of the tagging grid over time. We propose a method based on quadrature filters that is invariant to changes in intensity, robust with respect to the grid geometry and provides a dense motion field that allows for the analysis of both global and local movements. A multi-scale and multi-resolution scheme is used to cover different scales of motion and to speed up registration. The described method has been integrated into a prototypical application and applied to a phantom data set and 15 volunteer data sets provided by the STACOM'11. The automatic detection of the 4D motion field took about 130 minutes per MRI data set and about 90 minutes per US data set and resulted in plausible motion fields, which will be quantitatively assessed within the motion tracking challenge at MICCAI 2011.

Keywords: Tagged MRI, Morphon, Registration, Quadrature filter.

1 Introduction

MRI tagging is a non-invasive imaging method for the assessment of regional myocardial motion, thus having the potential of being an important tool for the clinical evaluation of cardiac dysfunction [7]. The method is based on the labeling of image regions with saturation planes, whose deformation can then be tracked. Different approaches have been proposed to determine a motion field from the tagged MRI sequences, including segmentation-based methods [16], analysis of the harmonic phase (HARP) [14,1,12,9], optical flow or related signal processing concepts (e.g., Gabor filters) [15,3,5], and conventional registration approaches [4,13]. Because the tagging grid desaturates over time in common tagging MRI sequences, the contrast to the surrounding structures decreases, and the grid can fade completely. This presents a major obstacle for existing methods. Modern CSPAMM sequences do not suffer from tag fading, but exhibit a lower spatial resolution and can still show intensity inhomogeneities. We propose an intensity-invariant registration method driven with local phase information obtained by quadrature filters that produces a dense deformation field.

O. Camara et al. (Eds.): STACOM 2011, LNCS 7085, pp. 78–87, 2012.

2 Materials and Methods

2.1 Image Data

The STACOM'11 organizers provided a total of 16 tagged 4D MRI and 4D US data sets, acquired from 15 healthy subjects and one dynamic physical phantom. This phantom allows compression and rotation with a speed that enables the simulation of a heart cycle through compression and relaxation within 1s [8].

MRI Data. The MRI data sets were acquired with a 3D CSPAMM sequence that enables the generation of 4D volumes with tag planes in three orthogonal orientations [10]. Data was acquired in short-axis orientation (see Fig. 1). The volunteer data sets were obtained with a voxel size of 0.96 x 0.96 x 0.96 mm^3 and 20 to 38 time points. The phantom was scanned with a spatial resolution of 1.01 x 1.01 x 1.01 mm^3 over 23 time points.

US Data. The US data sets were acquired with a full-volume apical view (see Fig 5). The volunteer datasets have voxel sizes between 0.66 x 0.66 x 0.58 mm^3 and 0.96 x 0.96 x 0.72 mm^3 and consist of 11 to 24 time frames whereas the phantom dataset was acquired with a voxel size of 1.35 x 1.16 x 0.96 mm^3 over 19 time points.

The temporal resolution of the data sets was not included in the provided image information.

2.2 Method

The described method is based on the Morphon algorithm introduced by Knutsson et al. [6]. In previous work, this method has been successfully applied to MRI perfusion data, where the problem of contrast variation appears due to the wash-in and wash-out of contrast agent [11].

Background. Phase-based image registration is based on the Fourier Shift Theorem, which states that the Fourier transforms of a signal $f(x)$ and a shifted signal $f(x-d)$ are related via a phase factor $\mathcal{F}\{f(x-d)\} = e^{-jd\omega}\mathcal{F}\{f(x)\}$. For two signals $f_1(x) = f(x)$ and $f_2(x) = f(x-d)$, we have a d proportional to $\arg\left(\mathcal{F}\{f_1(x)\}\overline{\mathcal{F}\{f_2(x)\}}\right)$, with $\overline{\ }$ denoting the complex conjugate. By using the *local* phase $\phi(x)$, derived from the complex analytical signal $f_a(x) = A(x)e^{j\phi(x)}$ of $f(x)$, the above approach can be used to estimate non-stationary shifts in 1D. The analytic signal is in practice estimated by applying a quadrature filter, $q(x)$, $\hat{f}_a(x) = (f * q)(x)$, which has a band-pass character that determines the scale of the structures or shifts of interest.

To generalize the analytic signal, which inherently is a 1D construct, to images of higher dimensions, a set of quadrature filters $q^{(i)}(\mathbf{x})$ with different orientations $\hat{\mathbf{n}}_i$ is applied. The generalized analytic signal in direction $\hat{\mathbf{n}}_i$ for an image $I(\mathbf{x})$ is then obtained as $I_a^{(i)}(\mathbf{x}) = (I * q^{(i)})(\mathbf{x})$. Assume now that we have a deformed

image $J(\mathbf{x}) = I(\mathbf{x} + \mathbf{d}(\mathbf{x}))$, where $\mathbf{d}(\mathbf{x})$ is an unknown deformation field that we wish to estimate. The displacement $\hat{d}_i(\mathbf{x})$ along the orientation $\hat{\mathbf{n}}_i$ can then be estimated by the local phase difference of the complex product

$$p_{IJ}^{(i)}(\mathbf{x}) = I_a^{(i)}(\mathbf{x})\,\overline{J_a^{(i)}(\mathbf{x})}. \tag{1}$$

Following the Shift Theorem, $\hat{d}_i(\mathbf{x})$ is proportional to $\arg\left(p_{IJ}^{(i)}(\mathbf{x})\right)$. For each oriented quadrature filter $q^{(i)}(\mathbf{x})$, a displacement estimate is obtained. A confidence measure $c_i(\mathbf{x})$ can be associated with the estimate in each filter direction,

$$c_i(\mathbf{x}) = \sqrt{\left|p_{IJ}^{(i)}(\mathbf{x})\right|}\left[1 + \cos\left(\arg\left(p_{IJ}^{(i)}(\mathbf{x})\right)\right)\right] \tag{2}$$

and the individual measures contribute to a combined confidence measure $c(\mathbf{x})$ formulated as

$$c(\mathbf{x}) = \sum_i c_i(\mathbf{x}). \tag{3}$$

The rationale behind this confidence measure is that the magnitude of $p_{IJ}^{(i)}(\mathbf{x})$ is large if there is a strong response of the filter $q^{(i)}(\mathbf{x})$ in both images, indicating similar structures. If the phase of $p_{IJ}^{(i)}(\mathbf{x})$, that is, the phase difference between $I_a^{(i)}(\mathbf{x})$ and $J_a^{(i)}(\mathbf{x})$, is large, the quadrature filter has likely picked up different structures, which makes the estimate less certain. A first estimate of the complete deformation field can be formulated by weighting the displacement estimates with the associated confidence measures

$$\mathbf{d}(\mathbf{x}) = \frac{\sum_i c_i(\mathbf{x}) d_i(\mathbf{x}) \hat{\mathbf{n}}_i}{\sum_i c_i(\mathbf{x})}. \tag{4}$$

Biological tissue generally deforms smoothly, and a spatial regularization should be applied to reflect this prior knowledge in the deformation field $\mathbf{d}(\mathbf{x})$. By applying so-called normalized averaging, the confidence measure contributes to the regularized deformation field,

$$\mathbf{d}_{reg}(\mathbf{x}) = \frac{[\mathbf{d}(\mathbf{x})c(\mathbf{x})] * g(\mathbf{x}; \sigma^2)}{c(\mathbf{x}) * g(\mathbf{x}; \sigma^2)}, \tag{5}$$

where the division is taken voxel-wise, and g is a Gaussian kernel. In the resulting field uncertain displacements have been penalized, allowing the convergence to a smooth field.

To estimate large deformations, the displacement estimation outlined above must be implemented in a scale space, and it is also necessary to iterate the estimation several times on each scale to refine the estimation. The deformation estimates are accumulated in $\mathbf{d}_{tot}(\mathbf{x})$ as

$$\mathbf{d}_{tot}(\mathbf{x}) \leftarrow \mathbf{d}_{tot}(\mathbf{x}) + \frac{c(\mathbf{x})}{c_{tot}(\mathbf{x}) + c(\mathbf{x})}\,\mathbf{d}_{reg}(\mathbf{x}), \tag{6}$$

where $c_{tot}(\mathbf{x})$ is an accumulated confidence measure that is updated for each iteration as

$$c_{tot}(\mathbf{x}) \leftarrow \frac{c_{tot}^2(\mathbf{x}) + c^2(\mathbf{x})}{c_{tot}(\mathbf{x}) + c(\mathbf{x})}. \tag{7}$$

After convergence, $\mathbf{d}_{tot}(\mathbf{x})$ is the final estimate of the true deformation field $\mathbf{d}(\mathbf{x})$.

Implementation. To derive the motion fields from the tagged MRI data, the image data is analyzed slice-wise with a set of four 2D filters in orthogonal directions. We do not employ a true 3D registration for two reasons: the tagging grid is composed of tag lines in three orthogonal directions, and the computational costs for a 3D registration are significantly higher when compared to a 2D registration, making a distributed computation scheme highly desirable. Thus, the total motion field is obtained by combining three 2D motion vector fields from orthogonal directions (Fig. 1), which can be computed independently. Because each 3D vector component is present in two fields, out-of-plane motion and other artifacts can be compensated for by combining the corresponding components.

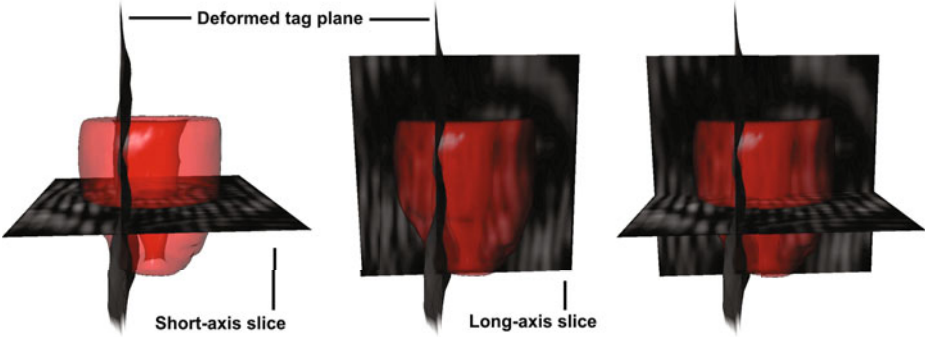

Fig. 1. The image shows a deformed tag plane and two exemplary slices of the orientations used for the motion analysis. The deformation of a tag plane is analyzed in two orthogonal orientations and the obtained 2D vector fields (left and middle) are combined to describe the 3D motion of the tag planes.

We apply log-normal quadrature filters that can be expressed in the Fourier domain as polar separable functions:

$$Q_i(\mathbf{u}) = R(\|\mathbf{u}\|) D_i(\hat{\mathbf{u}}) \tag{8}$$

with

$$R(\|\mathbf{u}\|) = e^{C \ln^2(\|\mathbf{u}\|/u_0)},\ C = -\frac{4}{B^2 \ln(2)}. \tag{9}$$

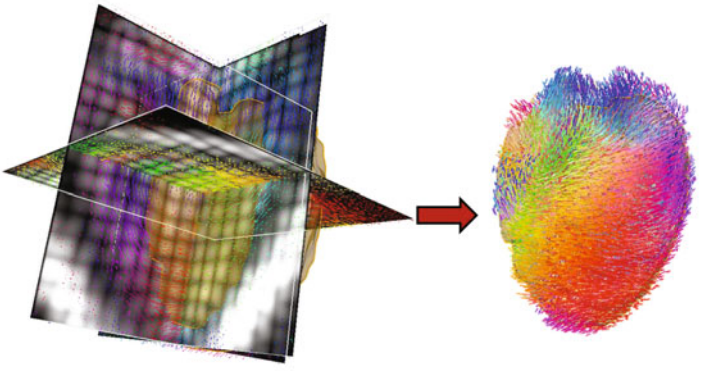

Fig. 2. Orthogonal planes for vector field calculation. The image shows three slice orientations used for the vector field calculation. Vectors are colored according to their direction ($(x, y, z) \rightarrow (R, G, B)$). The orthogonal 2-dimensional vector fields are combined to one 3-dimensional field.

$R(\|\mathbf{u}\|)$ is a Gaussian function on a logarithmic scale, giving the filters a band-pass character. u_0 is the center frequency and B is the width of the passband in octaves. We use two different u_0 to capture displacements on different scales and the bandwidth is fixed to $B = 2$ octaves. $D_i(\hat{\mathbf{u}})$ in (8) gives the filters a direction $\hat{\mathbf{n}}_i$, and the quadrature property by setting one half of the Fourier domain to zero as follows:

$$D_i(\hat{\mathbf{u}}) = \begin{cases} \left(\hat{\mathbf{u}}^T \hat{\mathbf{n}}_i\right)^2 & \text{if } \hat{\mathbf{u}}^T \hat{\mathbf{n}}_i > 0, \\ 0 & \text{otherwise,} \end{cases} \tag{10}$$

where $\hat{\mathbf{n}}_i$ is the filter direction. A filter optimization procedure was applied to obtain finite filter kernels with good spatial localization and a frequency response that closely match the ideal shape given by (8). This approach does not rely on the tagging directly, but on intensity differences, which makes it suitable for both the tagging MRI and the US data.

A coarse to fine scale-space approach with three resolution levels is adopted to capture both global and local deformations and to increase efficiency. The resample factor between the scales was chosen as 0.63, which is a reasonable compromise between the number of scales and the size of perceivable deformations, and avoids artifacts due to dyadic resampling. In addition, two different quadrature filter sets with center frequencies u_0 of $\frac{\pi}{4}$ and $\frac{\pi}{2\sqrt{2}}$ are used, so that deformations on six different scales are considered in total. It should be noted that the frequencies are not related to the spatial frequency of the tagging grid, but were selected to give the scale-space scheme good coverage of motions with different magnitudes. On scales with resampled resolution four iterations are performed, while only three are carried out on scales with the original resolution to reduce computation time. The regularization of the deformation field is

performed using a Gaussian kernel, whose parameters were empirically optimized to produce smooth deformation fields. Because the US data sets show more noise than the MRI data sets, their deformation fields are more strongly regularized.

For each of the three orthogonal slice orientations, a stack of a slice-wise 2-component vector field is calculated. Each slice in this vector field stack represents the motion between two adjacent time points. These partial motion fields are reformatted to the transversal orientation. Every orientation contributes to two components of the final 3D vector (Fig. 2) that is determined by averaging the respective components. The US data sets are downsampled by a factor of 2 for processing to compensate for their size and the increased noise level in comparison to the MRI data sets, and upsampled with linear interpolation afterwards.

3 Results

The described registration approach has been implemented within the MeVisLab platform [2] and applied to the tagged MRI and US data sets of one phantom and 15 healthy subjects provided by the organization team of the STACOM'11 motion challenge. Figure 3 shows the streamline visualization over one heart cycle. Computation time depends heavily on the number of time points in the data set.

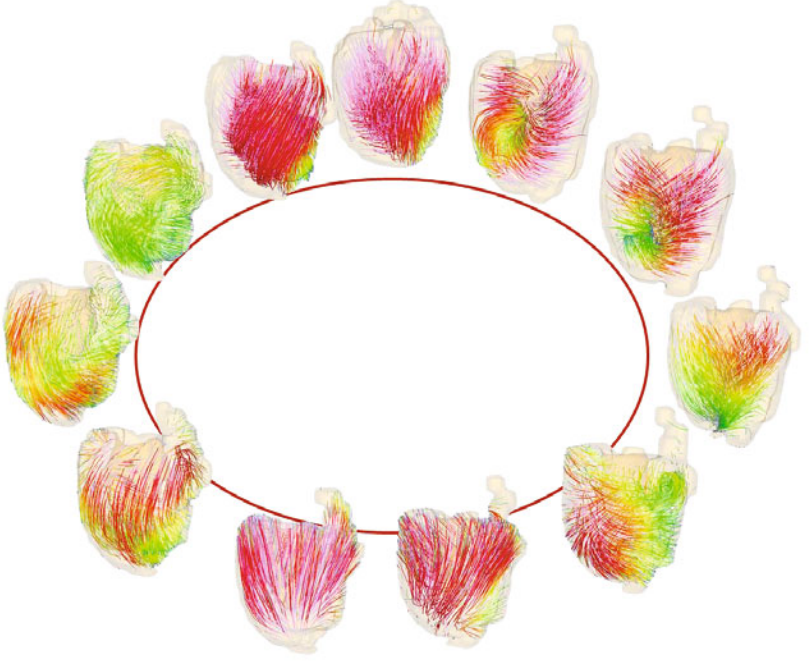

Fig. 3. Streamline visualization of the vector field calculated for the MRI data of volunteer 15. The images represent the motion between every second subsequent time points starting with time point one in the upper left part of this image.

For one MRI data set, the computation time ranges from 120 minutes (23 time points) to 500 minutes (38 time points). For one US data set, the duration ranges from 60 minutes (11 time points) to 150 minutes (24 time points). Figure 4 shows the vector fields calculated for the phantom data sets. The motion field derived from the tagged MRI data shows two continuous movements interrupted by a period with little motion. The US motion field on the other hand shows alternating phases of strong and little motion.

4 Discussion

The deformation fields calculated for the MRI tagging data appear plausible when visually assessed with regard to the underlying image data sets. Global and regional deformations that can be perceived in the tagging grid motion are present in the results. Motion on the scale of single voxels, on the other hand, is hard to evaluate. The data sets did not contain proper timing information, preventing assessment based on, e.g., the speed of changes.

The introduced method depends on contrast at the borders of the moving structures to analyze. Thus, it was expected that the results for the MRI images with the tagging grid would be better than those calculated for the US data. Due to increased noise and motion-related artifacts, more regions in the US results showed inaccurate or even unreasonable motion.

The deformation behavior over time appears plausible for the MRI motion fields (upper row in Fig. 4), assuming that one simulated heart cycle is covered by the image sequence. The temporal coverage of the US image sequence however does not seem to correspond with the MRI sequence. The motion field shows alternating phases of little and strong motion, indicating a considerably smaller or larger timestep between subsequent images (lower row). As shown in Fig. 5, in the apical region, where the myocardium is not recognizable due to the proximity to the sonographic unit, no reasonable motion field is calculated. While the general contraction behavior is still visible, we do not expect the method to

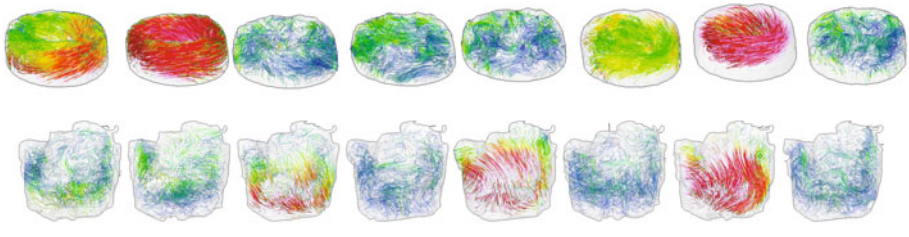

Fig. 4. Streamline visualization of vector fields derived from the MRI phantom sequence (upper row) and the US phantom sequence (lower row). The color indicates the velocity of the movement. Blue means slow motion, whereas red is used for high velocities.

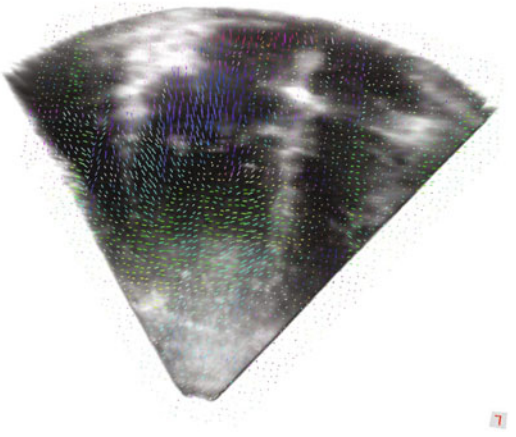

Fig. 5. Motion field derived from the US sequence of volunteer 2. The motion field close to the sonographic unit is perturbed by misleading image intensities.

work with this kind of data without major modifications, such as more robust filters, an adapted regularization, and the incorporation of model assumptions.

The performance of the method is inherently limited in regions with very homogeneous gray values, or when out-of-plane motion or rapid contrast changes are encountered. For data sets with these properties, a mask restricting the quadrature filter application, 3D filters or a temporal regularization of the field could improve the deformation field.

To improve the algorithm with regard to artifacts and accuracy, a robust and objective evaluation scheme is required. This scheme must include model or expert knowledge, as the analysis of the vector field alone and the application of standard error measures are insufficient for non-rigid deformations in data with varying contrast and substantial noise and motion artifacts.

The measured computation times appear too long for clinical use, but as the algorithm runs fully automatic it can be applied in a pre-processing step. The approach is ideally suited to be implemented with an extended scale-space and a data partition scheme for parallel or distributed computing, which could result in a considerable speedup.

5 Conclusions

We introduced an algorithmic approach for the analysis of myocardial motion based on tagged MRI data. The method is a phase-based approach, which applies quadrature filters to derive dense motion fields between subsequent image time frames. The algorithm was successfully applied to all data sets provided by the STACOM'11 challenge. We obtained motion fields with visually reasonable deformations for tagged MRI data, and fields with less accurate deformations

for US data. A thorough evaluation is required, though, firstly to show that the computed motion fields are biologically reasonable, and secondly to fine-tune the algorithms. Future work will also focus on the reduction of computation times to enable the usage in a clinical environment.

References

1. Abd-Elmoniem, K.Z., Stuber, M., Prince, J.L.: Direct three-dimensional myocardial strain tensor quantification and tracking using zHARP. Medical Image Analysis 12(6), 778–786 (2008)
2. Bitter, I., Van Uitert, R., Wolf, I., Ibanez, L., Kuhnigk, J.M.: Comparison of four freely available frameworks for image processing and visualization that use ITK. IEEE Transactions on Visualization and Computer Graphics 13(3), 483–493 (2007)
3. Carranza-Herrezuelo, N., Bajo, A., Sroubek, F., Santamarta, C., Cristobal, G., Santos, A., Ledesma-Carbayo, M.: Motion estimation of tagged cardiac magnetic resonance images using variational techniques. Computerized Medical Imaging and Graphics 34(6), 514–522 (2010)
4. Chandrashekara, R., Mohiaddin, R., Rueckert, D.: Analysis of 3-D myocardial motion in tagged MR images using nonrigid image registration. IEEE Transactions on Medical Imaging 23(10), 1245–1250 (2004)
5. Chen, T., Chung, S., Axel, L.: Automated Tag Tracking Using Gabor Filter Bank, Robust Point Matching, and Deformable Models. In: Sachse, F., Seemann, G. (eds.) FIHM 2007. LNCS, vol. 4466, pp. 22–31. Springer, Heidelberg (2007)
6. Knutsson, H., Andersson, M.: Morphons: Segmentation using elastic canvas and paint on priors. In: Symposium on Image Analysis, SSBA 2005, pp. 73–76 (2005)
7. Kramer, U., Hennemuth, A., Fenchel, M.: Myocardial MR tagging: analysis of regional and global myocardial function. Radiologe 50(6), 532–540 (2010)
8. Manzke, R., Lutz, A., Schenderlein, M., Bornstedt, A., Chan, R., Dietmeyer, K., Rasche, V.: A new PVA-based dynamic cardiac phantom for evaluation of functional MR imaging methods at 3T. In: Proc. ISMRM (2010)
9. Pan, L., Prince, J., Lima, J., Osman, N.: Fast tracking of cardiac motion using 3D-HARP. IEEE Transactions on Biomedical Engineering 52(8), 1425–1435 (2005)
10. Rutz, A.K., Ryf, S., Plein, S., Boesiger, P., Kozerke, S.: Accelerated whole-heart 3D CSPAMM for myocardial motion quantification. Magnetic Resonance in Medicine 59(4), 755–763 (2008)
11. Tautz, L., Hennemuth, A., Andersson, M., Seeger, A., Knutsson, H., Friman, O.: Phase-based non-rigid registration of myocardial perfusion MRI image sequences. In: 2010 IEEE International Symposium on Biomedical Imaging: From Nano to Macro, pp. 516–519 (April 2010)
12. Tecelão, S.R., Zwanenburg, J.J., Kuijer, J.P., Marcus, J.T.: Extended harmonic phase tracking of myocardial motion: Improved coverage of myocardium and its effect on strain results. Journal of Magnetic Resonance Imaging 23(5), 682–690 (2006)
13. Tustison, N., Davila-Roman, V., Amini, A.: Myocardial kinematics from tagged MRI based on a 4-D B-spline model. IEEE Transactions on Biomedical Engineering 50(8), 1038–1040 (2003)

14. Wang, H., Amini, A.A.: Cardiac motion tracking with multilevel B-splines and SinMod from tagged MRI. In: Proc. SPIE, vol. 7965 (2011)
15. Xu, C., Pilla, J., Isaac, G., Gorman, J., Blom, A., Gorman, R., Ling, Z., Dougherty, L.: Deformation analysis of 3D tagged cardiac images using an optical flow method. Journal of Cardiovascular Magnetic Resonance 12(1), 19+ (2010)
16. Yuan, X., Zhang, J., Buckles, B.: A multiresolution method for tagline detection and indexing. IEEE Transactions on Information Technology in Biomedicine 14(2), 507–513 (2010)

Left Ventricular Segmentation Challenge from Cardiac MRI: A Collation Study

Avan Suinesiaputra[1], Brett R. Cowan[1], J. Paul Finn[2], Carissa G. Fonseca[2], Alan H. Kadish[3], Daniel C. Lee[3], Pau Medrano-Gracia[1], Simon K. Warfield[4], Wenchao Tao[2], and Alistair A. Young[1]

[1] Auckland Bioengineering Institute, University of Auckland, New Zealand
[2] Department of Radiological Sciences, University of California Los Angeles, USA
[3] Division of Cardiology, Northwestern University, USA
[4] Computational Radiology Laboratory, Harvard Medical School, USA

Abstract. This paper presents collated results from the left ventricular (LV) cardiac MRI segmentation challenge as part of STACOM'11. Clinical cases from patients with myocardial infarction (100 test and 100 validation cases) were randomly selected from the Cardiac Atlas Project (CAP) database. Two independent sets of expert (manual) segmentation from different sources that are available from the CAP database were included in this study. Automated segmentations from five groups were contributed in the challenge. The total number of cases with segmentations from all seven raters was 18. For these cases, a ground truth "consensus" segmentation was estimated based on all raters using an Expectation-Maximization (EM) method (the STAPLE algorithm).

1 Introduction

In cardiac MRI, the LV segmentation is typically performed to derive important clinical indices such as LV mass and volume. The current clinical standard is manual contouring of the myocardial boundaries, a time consuming and error-prone process, requiring substantial training. The development of automated segmentation algorithms has been problematic due to the lack of "ground truth" in real clinical cases. Even expert manually drawn segmentations still suffer from inter- and intraobserver variability. This problem particularly applies in cardiac imaging, where the presence of papillary muscles, the heart dynamics, and soft tissue contrast variations are just some of the problematic areas in cardiac MRI.

In this segmentation challenge, we created a framework to solve this problem by providing the same data set to researchers to test their segmentation algorithms and also to estimate better set of ground truth segmentations at the same time. We applied the EM-based STAPLE method [6] to estimate the consensus ground truth segmentations. Therefore, the challenge was performed as a collaborative work rather than a competition. A large data set of clinical cardiac MRI cases was made available through the Cardiac Atlas Project[1] [2]. By using the

[1] http://www.cardiacatlas.org

O. Camara et al. (Eds.): STACOM 2011, LNCS 7085, pp. 88–97, 2012.

Table 1. Baseline characteristics of the data used in this challenge

	test set (N=100)	validation set (N=100)
EDV (ml)	193.86 (46.45)	199.44 (54.97)
ESV (ml)	113.41 (43.44)	123.80 (53.81)
LV mass (gr)	172.24 (42.57)	165.38 (40.30)
EF (%)	42.95 (10.88)	39.87 (11.25)
SV (ml)	80.41 (18.65)	75.59 (18.62)

EDV = endocardial volume at ED, ESV = endocadial volume at ES, EF = ejection fraction, and SV = stroke volume.

same data set, confounding difficulties to compare segmentation results between peers can therefore be eliminated.

2 Methods

2.1 Cardiac MRI Data

Cardiac MR images were randomly selected from the DETERMINE (Defibrillators To Reduce Risk by Magnetic Resonance Imaging Evaluation) cohort [4]. This study consists of patients with coronary artery disease and prior myocardial infarction. Two separate groups were defined as test (N=100) and validation (N=100) groups, by random selections (see Table 1). Cine MR images in short-axis and long-axis views were selected for this challenge. These MR images were acquired by using a Steady-State Free Precession (SSFP) pulse sequence. MRI parameters varied between cases, giving a heterogenous mix of scanner types and imaging parameters consistent with typical clinical cases.

2.2 Raters

Five automated raters (SCR, INR, DS, AO and EM) and two expert raters (AU and NU) participated in this study. Rater descriptions are given in Table 2. Two raters (SCR and INR) were fully automatic, although SCR required repositioning the center of LV segmentation in four cases. Three raters required some manual interactions, either by drawing initial contours (DS, EM and AO) or by having some parameter initialization (EM). One rater (INR) used the test dataset to train the algorithm, the others did not.

The expert NU rater was a manually drawn myocardial contour, traced by the DETERMINE MRI core laboratory using QMass software (Medis, Leiden, the Netherlands), while the AU rater was an expert-guided interactive customization of a finite element heart model using Cardiac Image Modeller (CIM) software (AMRG, Auckland, New Zealand). To generate the intersection between cardiac MRI with the 3D AU models and the image planes, the CAPClient software was used[2].

[2] The CAPClient is an open source software, available for download at http://www.cardiacatlas.org/web/guest/tools

Table 2. Rater characteristics

Rater	Method description	Dimensionality	Ref.
SCR	A combined deformable registration method with gray level based shortest path segmentation algorithm.	2D pixels	[3]
INR	A supervised voxelwise classification technique using layered spatio-temporal forests.	3D models	[5]
AO	A greedy optical flow algorithm with additional smoothing constraint.	2D lines/pixels	[1]
DS	A successive contour tracking algorithm based on matching correlation coefficients.	2D lines/pixels	†
EM	An active contour model framework with an optical flow energy force.	2D pixels	†
AU	An expert-guided 3D finite element heart model fitting based on guide point modeling.	3D models	-
NU	A manually expert-drawn myocardial contours.	2D contours	-

† Rater submitted the segmentation results but did not publish the corresponding methodology.

2.3 Evaluation Method

Individual rater performance was measured in two aspects: (1) the accuracy of the segmentation results against the ground truth and (2) the clinical assessment of global LV mass and volume. For the rater accuracy assessment, sensitivity (p), specificity (q), positive predictive value (PPV) and negative predictive value (NPV) were the main quantitative values. These were calculated by using the following equations:

$$p = \frac{T_1}{N_1}, \quad q = \frac{T_0}{N_0}, \quad PPV = \frac{T_1}{T_1 + F_1}, \quad NPV = \frac{T_0}{T_0 + F_0} \tag{1}$$

where T_1 and T_0 are the number of detected pixels characterized correctly as myocardium and non-myocardium, while F_1 and F_0 are the number of misclassified pixels detected as myocardium and non-myocardium, respectively. The total number of myocardial and non-myocardial pixels are N_1 and N_0, respectively.

Other commonly used evaluation metrics include similarity indices in terms of the Dice index:

$$\mathcal{D}(D_1, T_1) = \frac{2|D_1 \cap T_1|}{|D_1| + |T_1|} \tag{2}$$

and the Jaccard index:

$$\mathcal{J}(D_1, T_1) = \frac{|D_1 \cap T_1|}{|D_1 \cup T_1|} \tag{3}$$

where D_1 and T_1 are raters and ground truth sets of myocardial pixels, and $|X|$ denotes the number of elements in the set X. In both cases, values closer to 1 represent better performance.

2.4 Region of Interest Definition

It is well known that if $N_0 \gg N_1$, then the specificity (q) and NPV results are not particularly informative. To avoid this, we defined a region of interest around myocardium such that N_0 is comparable with N_1. For each image slice, a region of interest (ROI) around myocardium was defined to reduce N_0. Two

expert segmentation results (AU and NU) were added and subsequently dilated 1.5 times the width of myocardium to generate the ROI image (see Fig. 1). This produced sufficient area for each rater decision without introducing an excessive amount of background pixels. The ROI images were applied as image masks during the STAPLE iteration, as well as for the rater performance evaluation.

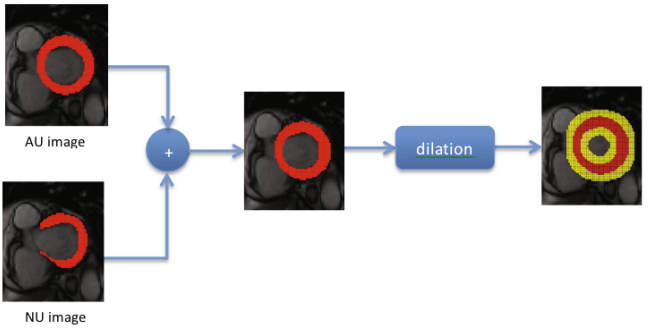

Fig. 1. A diagram to define a region of interest around the myocardium

2.5 Binary STAPLE Algorithm

In this collation study, we estimated the ground truth from all raters. Warfield et. al. [6] developed a method to estimate ground truth images from a set of segmentation results produced by raters (human and/or algorithmic) based on the EM method. The method, known as Simultaneous Truth And Performance Level Estimation or STAPLE, collects rater results and then simultaneously computes both probabilistic estimates of the true segmentation and the rater performances.

Let $\{\boldsymbol{D}\}_R$ be a set of R rater segmentations, each of which is an N-length of binary vector consisting of 0 (non-object) and 1 (object) values. Let $\boldsymbol{T}$ be the hidden true binary vector that is going to be estimated. The objective of STAPLE algorithm is to estimate rater performance parameter $\boldsymbol{\theta}$ by maximizing the complete data log-likelihood,

$$\hat{\boldsymbol{\theta}} = \arg\max_{\boldsymbol{\theta}} \ln f\left(\boldsymbol{D}, \boldsymbol{T}|\boldsymbol{\theta}\right). \tag{4}$$

The performance parameters are $\boldsymbol{\theta}_j = (p_j, q_j)^T$ or the sensitivity and the specificity of rater j, which can be estimated as follows

$$p_j = Pr\left(D_{ij} = 1|T_i = 1\right) \tag{5}$$
$$q_j = Pr\left(D_{ij} = 0|T_i = 0\right) \tag{6}$$

where $i = 1, \ldots, N$ and $j = 1, \ldots, R$. The parameters $p_j, q_j \in [0, 1]$ define rater performance characteristics, which are generally not equal between raters.

Applying (4) into the EM algorithm, we can define the *maximization step* as follows

$$\begin{aligned}\hat{\boldsymbol{\theta}}^{(k)} &= \arg\max_{\boldsymbol{\theta}} E\left[\ln f\left(\boldsymbol{D},\boldsymbol{T}|\boldsymbol{\theta}\right)|\boldsymbol{D},\boldsymbol{\theta}^{(k-1)}\right] \\ &= \arg\max_{\boldsymbol{\theta}} E\left[\ln f\left(\boldsymbol{D}|\boldsymbol{T},\boldsymbol{\theta}\right) f\left(\boldsymbol{T}\right)|\boldsymbol{D},\boldsymbol{\theta}^{(k-1)}\right]\end{aligned} \tag{7}$$

where k denotes an iteration number and $f\left(\boldsymbol{T}\right)$ is the stationary prior. The *expectation step* is defined by estimating the posterior probability given the current estimate of parameters at each kth iteration, i.e.,

$$f\left(\boldsymbol{T}|\boldsymbol{D},\boldsymbol{\theta}^{(k)}\right) = \frac{f\left(\boldsymbol{D}|\boldsymbol{T},\boldsymbol{\theta}^{(k)}\right) f\left(\boldsymbol{T}\right)}{\sum_{\boldsymbol{T}} f\left(\boldsymbol{D}|\boldsymbol{T},\boldsymbol{\theta}^{(k)}\right) f\left(\boldsymbol{T}\right)}. \tag{8}$$

Note that the following holds for binary segmentation, i.e.,

$$f\left(T_i = 0|\boldsymbol{D},\boldsymbol{\theta}^{(k)}\right) = 1 - f\left(T_i = 1|\boldsymbol{D},\boldsymbol{\theta}^{(k)}\right) \tag{9}$$

In this study, we used global stationary prior, which means that the prior of label v for all pixels are equal. In [6], the global stationary prior $f(\boldsymbol{T})$ was estimated from all raters. In this study, we calculated the global stationary prior from expert raters only, i.e. AU and NU raters. Hence,

$$Pr\left(T = v\right) = \frac{1}{2N}\sum_{i=1}^{N}\sum_{j\in R':D_{ij}=v} 1 \tag{10}$$

where N is the number of pixels and $R' = \{\mathrm{AU}, \mathrm{NU}\}$.

3 Results

After the challenge submission, 18 cases had segmentations from all seven raters. Only short-axis image series at end-diastole (ED) and end-systole (ES) frames were included in the collation study, because the NU segmentations were only available at these frames. STAPLE images were estimated on each 2D image slice, independently. The total number of image slices was 330.

Clinical assessment on ED volume (EDV), ES volume (ESV) and mass were validated against the AU rater (since mass and volume were not available for the NU rater). Each automated rater provided their volume and mass estimations, while the AU volume and mass were calculated from 3D finite element models of the heart [7]. Table 3 shows the clinical assessment results in terms of mean (μ_d) and standard deviation (σ_d) of the differences.

Due to individual algorithm features, raters might not segment myocardium on a particular slice, particularly at the apical tip or basal planes. The binary STAPLE algorithm was implemented in Matlab, based on [6]. The STAPLE

Table 3. Clinical validations on global LV functions with the AU models as the reference

Rater	EDV diffs (ml)		ESV diffs (ml)		Mass diffs (gr)	
	μ_d	σ_d	μ_d	σ_d	μ_d	σ_d
SCR	13.03	18.13	18.98	16.20	-9.56	22.58
INR	-79.88	39.62	-61.96	38.83	74.75	53.74
AO	8.69	99.39	13.36	64.16	51.49	95.65
DS	3.94	23.14	25.65	17.71	1.08	28.40
EM	-77.75	50.60	-45.46	36.44	-51.92	39.92

Table 4. Segmentation accuracy validations with STAPLE segmentation as the reference. All numbers are in 'average (standard deviation)' format.

Rater	Sensitivity	PPV	Specificity	NPV	Dice	Jaccard
SCR	0.78 (0.15)	0.92 (0.07)	0.96 (0.04)	0.87 (0.08)	0.83 (0.11)	0.73 (0.14)
INR	0.75 (0.24)	0.66 (0.14)	0.73 (0.16)	0.85 (0.12)	0.68 (0.17)	0.53 (0.17)
AO	0.90 (0.12)	0.83 (0.09)	0.87 (0.09)	0.94 (0.06)	0.86 (0.09)	0.76 (0.12)
DS	0.79 (0.16)	0.82 (0.13)	0.88 (0.08)	0.87 (0.09)	0.80 (0.14)	0.68 (0.16)
EM	0.89 (0.10)	0.89 (0.09)	0.91 (0.08)	0.93 (0.06)	0.88 (0.07)	0.80 (0.10)
AU	0.85 (0.11)	0.93 (0.09)	0.96 (0.04)	0.90 (0.08)	0.88 (0.09)	0.80 (0.13)
NU	0.63 (0.12)	0.96 (0.06)	0.99 (0.02)	0.81 (0.06)	0.75 (0.10)	0.61 (0.12)

algorithm was performed with the following settings: maximum of 500 iterations, a relative convergence rate of 1e-16, and the average of all raters was used as the initial weight image to define $\boldsymbol{\theta}^{(0)}$. ROI images were applied.

Two examples of STAPLE images from basal and mid-ventricular slices are shown in Fig. 2. The performance of each rater is shown in Table 4. The distribution of sensitivity and specificity values are given in Fig. 3. In Fig. 4, PPV and NPV values of each rater were compared against different references: AU, NU and STAPLE. Finally, receiver operating characteristic (ROC) curves are shown in Fig. 5. Area under ROC curves (AUC) are also shown in Fig. 5.

4 Discussion

A collation study from the LV segmentation challenge has been presented in this paper. A consensus segmentation was generated by using the STAPLE algorithm, which has been modified to include expert raters when estimating the global priors and to limit the segmentation area with ROI images. In general, the STAPLE algorithm produced satisfactory segmentation results, which can be regarded as the 'ground truth'. The STAPLE method was able to resolve disagreements in the septal region of the basal plane as seen in Fig. 2(a). It also excluded papillary muscles in the mid-ventricular slices, because the majority of the raters excluded these areas from myocardium (see Fig. 2(b)).

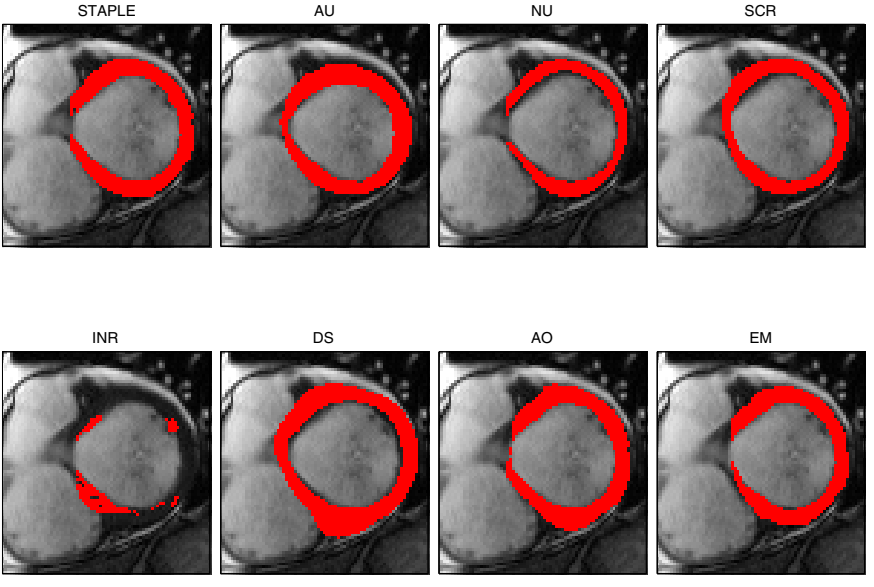

(a) Basal slice

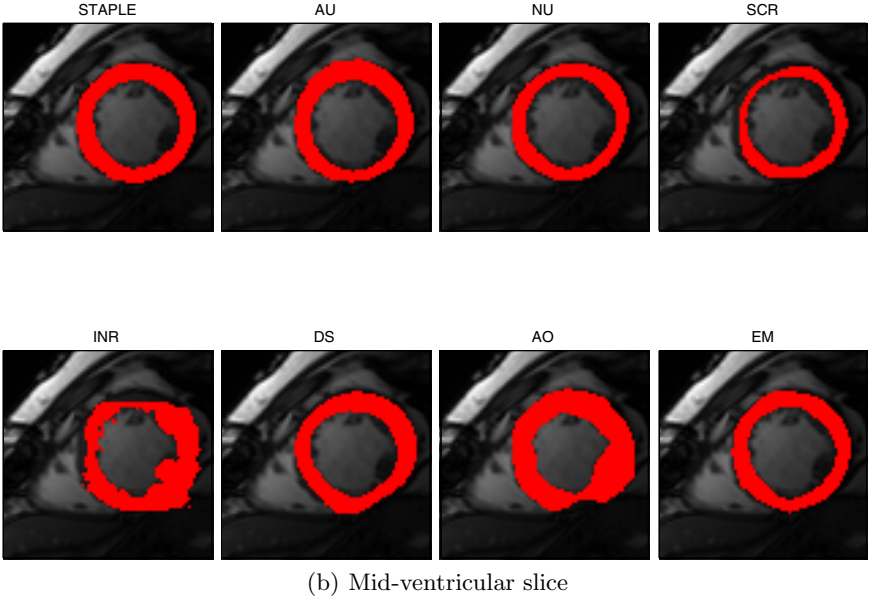

(b) Mid-ventricular slice

Fig. 2. Examples of STAPLE images compared with other raters

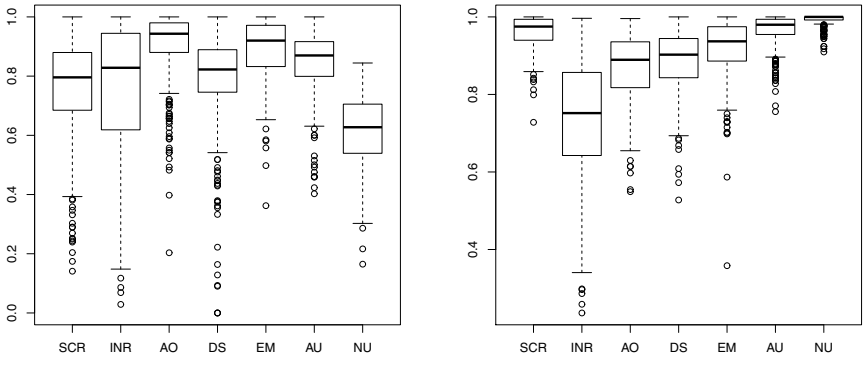

(a) Sensitivity (b) Specificity

Fig. 3. Distributions of sensitivities and specificities against STAPLE images. Whiskers denote ± interquartile-range, circles are outliers, and boxes are defined from lower to upper quartiles with median values as thick lines inside the boxes.

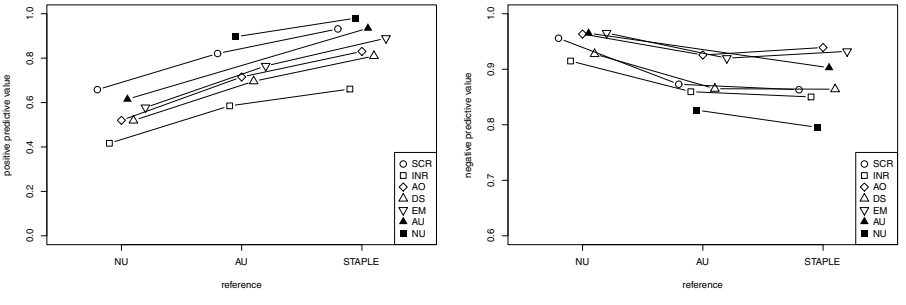

(a) PPV (b) NPV

Fig. 4. Comparisons of the average PPV and NPV values by using AU, NU and STAPLE as the references

From the clinical validation (Table 3), SCR was the closest to the expert rater AU. In terms of segmentation accuracy (Table 4), AO rater produced the highest sensitivity, while NU showed the highest predictive value. The highest similarity indices were AU and EM, both in Dice and Jaccard indices. The box plot distributions of the sensitivity and specificity values in Fig. 3 show how each rater performed. Generally, INR produced wide spread of sensitivity and specificity values, while NU maintained the highest specificity distribution values.

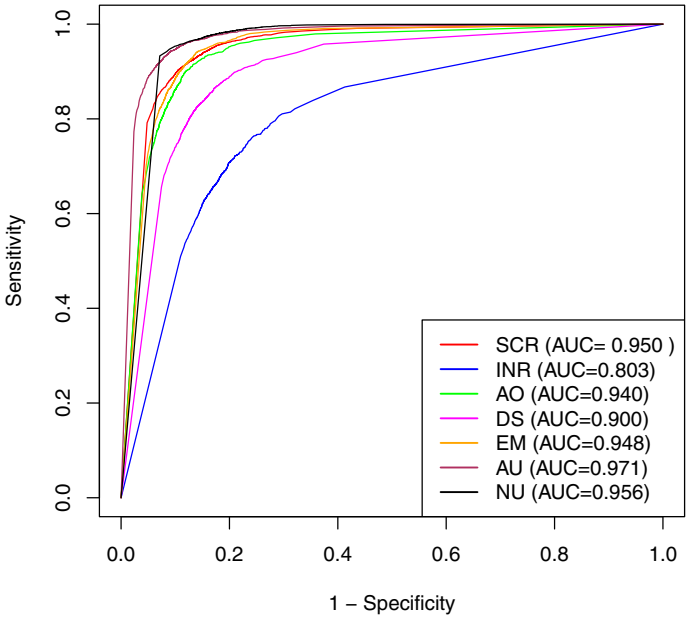

Fig. 5. Receiver operating characteristic curves from all raters. Area under the ROC curves (AUC) are captioned in the legend

Figure 4 shows how PPV and NPV values varied when different expert raters were used as the reference. Applying STAPLE generally increased PPV values, but not the NPV values. The overall performances of the expert raters, as seen by the ROC curves in Fig. 5, were the highest among other raters. However, the expert raters did not always outperform the automated raters when compared to the STAPLE results. It is interesting to note that the expert NU rater has the lowest sensitivity among all others. The NU rater PPV values, however, were the highest. Both the lower sensitivity and higher PPV values are attributable to the smaller NU myocardium compared to other raters. This was in part due to manual exclusion of non-myocardial pixels by the NU rater, e.g., aortic root on basal slice (Fig. 2(a)) and adjacent pericardial fat on mid slice (Fig. 2(b)). The NU rater also integrated information from the entire cardiac MR study to determine the location of myocardial borders, including long-axes cine MRI and late gadolinium enhanced images. This result highlights the need for a greater consensus within the cardiac imaging community as to the acceptable criteria for accurate and reproducible segmentations.

In conclusion, STAPLE provides a mathematically objective ground truth based on the evidence from the contributing raters. This will be useful in the future to not only evaluate automated segmentation methods, but also to inform the expert decisions on what constitutes an expert consensus.

References

[1] Fahmy, A.S., Othman, A., Khalifa, A.: Myocardial segmentation using contour-constrained optical flow tracking. In: Camara, O., Konukoglu, E., Pop, M., Rhode, K., Sermesant, M., Young, A. (eds.) STACOM 2011. LNCS, vol. 7085, pp. 117–125. Springer, Heidelberg (2012)

[2] Fonseca, C.G., Backhaus, M., Bluemke, D.A., Britten, R.D., Chung, J.D., Cowan, B.R., Dinov, I.D., Finn, J.P., Hunter, P.J., Kadish, A.H., Lee, D.C., Lima, J.A.C., Medrano-Gracia, P., Shivkumar, K., Suinesiaputra, A., Tao, W., Young, A.A.: The Cardiac Atlas Project – An imaging database for computational modeling and statistical atlases of the heart. Bioinformatics 27(16), 2288–2295 (2011)

[3] Jolly, M.P., Guetter, C., Lu, X., Xue, H., Guehring, J.: Automatic segmentation of the myocardium in cine MR images using deformable registration. In: Camara, O., Konukoglu, E., Pop, M., Rhode, K., Sermesant, M., Young, A. (eds.) STACOM 2011. LNCS, vol. 7085, pp. 96–105. Springer, Heidelberg (2012)

[4] Kadish, A.H., Bello, D., Finn, J.P., Bonow, R.O., Schaechter, A., Subacius, H., Albert, C., Daubert, J.P., Fonseca, C.G., Goldberger, J.J.: Rationale and design for the Defibrillators to Reduce Risk by Magnetic Resonance Imaging Evaluation (DETERMINE) trial. J. Cardiovasc. Electrophysiol. 20(9), 982–987 (2009)

[5] Margeta, J., Geremia, E., Criminisi, A., Ayache, N.: Layered spatio-temporal forests for left ventricle segmentation from 4D cardiac MRI data. In: Camara, O., Konukoglu, E., Pop, M., Rhode, K., Sermesant, M., Young, A. (eds.) STACOM 2011. LNCS, vol. 7085, pp. 106–116. Springer, Heidelberg (2012)

[6] Warfield, S.K., Zou, K.H., Wells, W.M.: Simultaneous truth and performance level estimation (STAPLE): an algorithm for the validation of image segmentation. IEEE Trans. Med. Imaging 23(7), 903–921 (2004)

[7] Young, A.A., Cowan, B.R., Thrupp, S.F., Hedley, W.J., Dell'Italia, L.J.: Left ventricular mass and volume: fast calculation with guide-point modeling on MR images. Radiology 216(2), 597–602 (2000)

Automatic Segmentation of the Myocardium in Cine MR Images Using Deformable Registration

Marie-Pierre Jolly[1], Christoph Guetter[1], Xiaoguang Lu[1], Hui Xue[1], and Jens Guehring[2]

[1] Siemens Corporate Research, Image Analytics and Informatics, Princeton, NJ, USA
[2] Siemens AG, Healthcare Sector, Erlangen, Germany
marie-pierre.jolly@siemens.com

Abstract. This paper proposes a system to automatically segment the left ventricle in cardiac MR cine images. Individual frames are segmented using a shortest path algorithm and temporal consistency is enforced through the backward and forward deformation fields of an inverse consistent deformable registration. In addition, a segmentation of the mitral valve plane is obtained from long axis images. This algorithm was applied to 95 datasets as part of the STACOM'11 4D LV Segmentation Challenge. We analyze the results and evaluate the strengths and weaknesses of our system.

1 Introduction

Cardiovascular disease is the leading cause of death in the western world and there is a need to efficiently diagnose the health of the heart and the myocardium. Magnetic resonance imaging (MRI) is a possible means to observe the behavior of the heart. Physicians are most interested in the left ventricle (LV) because it pumps oxygenated blood to the rest of the body. MRI cine data consists of slices of the heart over time. In order to quantify measures such as ejection fraction, LV volume over time, myocardial mass, and myocardial thickening, they need a precise outline of the myocardium in all slices and all temporal phases. This can be extremely time consuming and physicians would like to rely on automatic software for this task. This paper proposes a system to automatically segment the LV endocardium and epicardium in all images of a cardiac MRI cine study.

The main difficulties in segmenting the myocardium are: a) the presence of papillary muscles and trabeculation in the blood pool (both in the LV and in the right ventricle) that contribute to partial voluming effect between the blood and muscle; b) there are often no clear edges between the myocardium and the liver; c) if there is fat around the heart, the fat/lung edges are stronger than the myocardium/fat edges; d) the myocardium becomes blurry in the apex slices; e) the cut between the LV and the left atrium in the base slice is very subtle (the muscle becomes thinner in the left atrium). Given all these difficulties, there has been a large number of publications on LV segmentation in cine MRI images [11],[12].

O. Camara et al. (Eds.): STACOM 2011, LNCS 7085, pp. 98–108, 2012.

Having studied all this work and having implemented some of the techniques, we believe that a pure 4D segmentation approach is currently not ideal since it is very difficult to build a model that is general enough to cover all possible shapes and dynamics of the LV. The segmentation usually results in surfaces that are too smooth and do not follow the true contours accurately enough. In addition, MR slices are very far apart (8-10mm) compared to the in-slice resolution (1-2 mm) such that the 3D segmentation becomes very anisotropic. Finally the slices might be mis-registered due to different breath-hold positions, which creates additional problems in fitting the model. Of course, the opposite approach of segmenting each image individually results in little cohesion between images, and contours that are not smooth over time.

We have chosen to segment all frames in one slice using deformable registration, taking advantage of the strong temporal correlation between frames. The main idea in our algorithm is to use an inverse consistent deformable registration to register all frames to the first frame in one slice. Then, the segmentation can be applied to any frame and propagated to any other frame in the sequence through the forward and backward deformation fields. We model the gray levels of the different regions in the heart area, including the partial voluming region, to help with difficulty a) and c). In addition, to try to overcome difficulty e), we use the long axis slices to recover a mitral valve base plane which is used to cut the short axis slices and compute a more accurate volume of the LV. The following sections describe individual steps of the algorithm in more detail.

2 Left Ventricle Segmentation

The segmentation of the left ventricle is divided into 4 steps: 1) detection of the left ventricle in the images; 2) mitral valve base plane segmentation; 3) slice segmentation through inverse consistent deformable registration and shortest path recovery; and 4) propagation between slices to segment the whole LV. Each of these steps will be described in the following sections.

2.1 LV Blood Pool Detection

The method for automatic detection of the LV blood pool is described in [6]. We threshold the first harmonic of the Fourier transform in each slice to detect the beating heart. Bright connected components are then extracted in each slice and characterized by their shape, motion, connectivity over time, etc. A graph is built by creating a node for each connected component. Pairs of nodes corresponding to connected components on neighboring slices are linked based on their similarity in shape, temporal behavior, distance, etc. The graph is then partitioned using isoperimetric clustering [3] and the corresponding connected components form 3D objects. The cluster that is roundest and "shrinks nicely" over time corresponds to the connected components inside the blood pool. Even though this process does not generate a blood pool region on all slices, it is a good starting point for the rest of the algorithm.

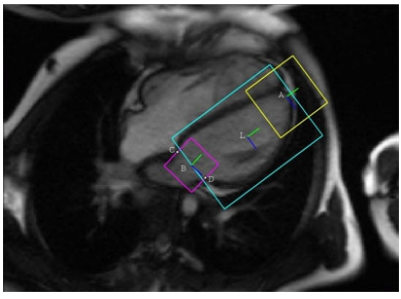

Fig. 1. Boxes to define the mitral valve area, the apex area, and the combined area

2.2 Mitral Valve Base Plane Segmentation

If long axis slices were acquired, they can be used to generate a plane approximation for the mitral valve in the following manner. We use the algorithm proposed in [9] to detect the mitral valve leaflet anchor points and the apex point in the end-diastolic (ED) and end-systolic (ES) frames (roughly estimated from the approximate blood pool). The mitral valve area, the apex area, and the combined area are each represented by 2D bounding boxes (as illustrated in Fig. 1 with 5 degrees of freedom (2 translations, 2 scale factors, and 1 rotation angle) to be estimated in the current image. We use a marginal space search strategy [14] where each position, orientation, and scale detector is a probabilistic boosting tree based on Haar wavelet-like and steerable features. The combined area is used to provide additional constraints to the search. Mitral valve points and apex points are then generated on frames other than ED and ES through linear interpolation and the mitral valve plane is fitted using a least squares approach by combining all mitral valve points on multiple long axis slices.

2.3 Slice Segmentation

The segmentation of the left ventricle is described in more details in [7]. The main idea behind the algorithm is the use of an inverse consistent deformable registration [4]. The registration computes a dense deformation field between any two frames in a slice without having to explicitly register every possible pair of frames. This is achieved by making the registration inverse consistent so that forward and backward deformation fields are recovered during the registration process, by alternately updating each deformation field at each step of the gradient descent minimization. So all frames are registered to an arbitrary keyframe (say the 1^{st} frame) using the consecutive strategy illustrated in Fig. 2. Then, the deformation field between frames i and j is obtained by compounding the deformation field between frames 1 and j and the inverse deformation field between frames 1 and i.

The core of the algorithm is illustrated in Fig. 3 for a given slice. Each frame is examined one at a time (this corresponds to the different rows in Fig. 3).

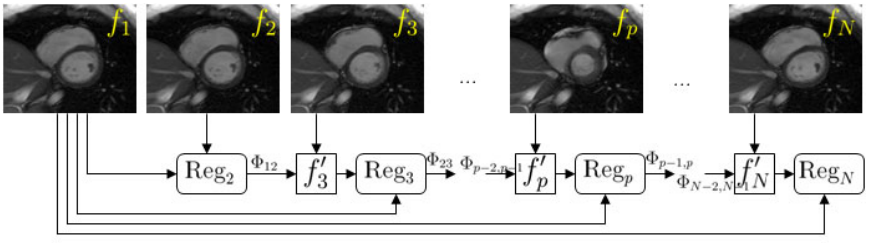

Fig. 2. Consecutive registration process

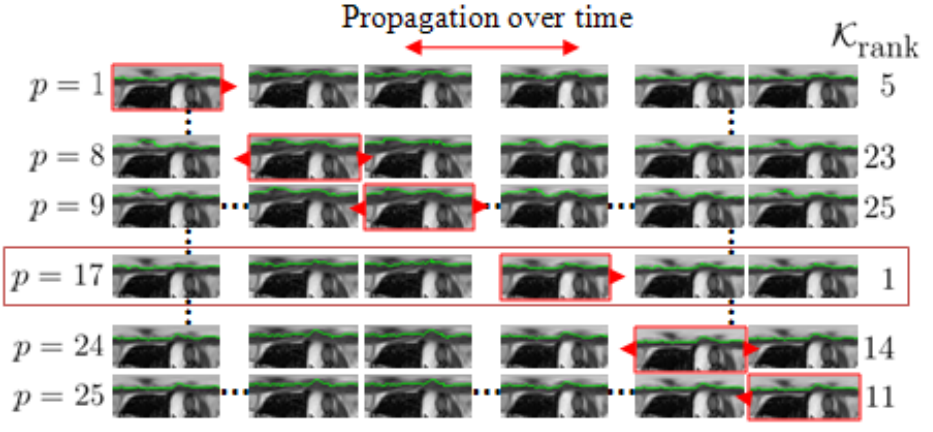

Fig. 3. Slice segmentation algorithm: for each frame $p = 1, ..., P$, recover a contour using Dijkstra's algorithm in polar space, propagate the contour to all other frames, and repeat. Choose the combination of contours (in this case recovered from frame 17) with the lowest cost.

For a frame p, the contour C_p is recovered in polar space using a minimum path algorithm as described later. The contours C_q in the other frames $q = 1, ..., P, q \neq p$ are generated using the deformation fields converted to polar space by $C_q(C_p) = \Phi_{1q}(\Phi_{1p}^{-1}(C_p))$ where Φ_{ij} is the deformation field between frames i and j (this corresponds to the different columns in Fig. 3). Then, the energy of this series of contours is given by $\mathcal{K}(p) = \sum_q E(C_q(C_p))$ where $E(C)$ is the edge cost associated with contour C. This same process is applied to all phases $p = 1, ..., P$ and the final segmentation is the one whose energy is lowest: $\mathcal{K} = \min_p \mathcal{K}(p)$. Once the best sequence has been recovered, the best polar contour in the best frame is converted to Cartesian space and propagated to the other frames using the forward and backward deformation fields in Cartesian space. In addition, the convex hull of the endocardium contour is generated to further enforce that it goes behind the papillary muscles.

The recovery of a contour in one frame is based on gray level properties of the image as described in [7]. The histogram of the LV region is analyzed to

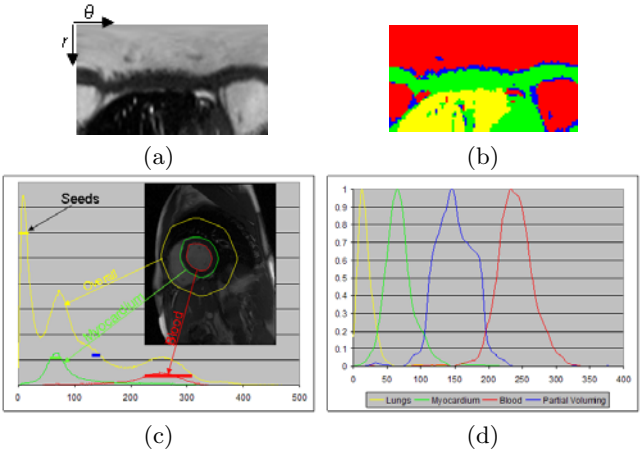

Fig. 4. Gray level analysis: (a) Polar image; (b) Multiseeded fuzzy connectedness region labeling; (c) Original histograms; (d) Final histograms (view in color)

find seeds for a multi-seeded fuzzy connectedness algorithm [5] and generate gray level properties of the different regions (blood, muscle, air, and partial voluming) as illustrated in Fig. 4. Then, the edge costs for the endocardium and the epicardium are computed using the Deriche filter edge detector on the original images and on the region probability images. The contour with smallest edge cost is recovered in polar space using Dijkstra's algorithm.

2.4 Segmentation of the Entire LV

The first slice to be segmented is the slice where the detected blood pool is the roundest. These contours are then propagated to the previous slice by applying the deformable registration and the deformed contours are used as priors to segment the previous slice. This process is repeated all the way to the base slice, where the base slice is identified as the slice closest to the mitral valve anchor points detected in the long axis slices. In the base slice, there is an additional process to identify when the myocardium cuts through the aortic valve and replace those segments of the endocardium and epicardium contours by straight lines (see Fig. 5(e)).

The initial slice contours are also propagated to the next slice toward the apex in the same way. An apex point is extracted in the long axis slices using the algorithm in [9] in conjunction with the extraction of the mitral valve leaflet anchor points. When reaching slices close to this apex point, tests are performed to determine if the apex has been reached and the downward propagation should stop. These tests include large shrinking of the contours compared to the previous slice, inconsistency in the modeling of the regions gray level properties (in which case the last segmentation is removed before the propagation is stopped), etc.

The last step of the workflow consists of intersecting the mitral valve base plane with the short axis slices and removing the parts of the contours that are above the plane (see Fig. 5(e)).

3 Experiments

We have tested our algorithm on the 100 validation datasets from the STACOM'11 4D LV Segmentation Challenge run by the Cardiac Atlas Project (CAP) [2]. All the data came from the DETERMINE [8] cohort which consists of patients with coronary artery disease and prior myocardium infarction. The data were acquired using steady-state free precession (SSFP) MR imaging protocols with thickness ≤ 10 mm, gap ≤ 2 mm, TR 30-50 ms, TE 1.6 ms, flip angle 60°, FOV 360 mm, and 256×256 image matrix. The data were acquired at multiple sites using scanners from different vendors.

The ground truth images provided in this challenge were defined by an expert using an interactive guide point modeling segmentation algorithm [13]. A finite element model of a heart was fitted with this algorithm to the cardiac MR images and the expert refined the fitted model following the wall motion throughout the cardiac cycle by using guide points, interactively. To get binary images of the myocardium, software from the CAP group was applied to calculate the intersection between the fitted heart model and the original MRI slices.

We were able to process 95 of the 100 datasets. Five of the datasets (DET0006901, DET0044401, DET0008401, DET0012301, and DET0014301) violated our assumptions, namely that all short axis slices should have the same number of phases, and all images within one slice and all images in the short axis matrix should have the same geometry (number of rows, number of columns, and pixel size). We generated contours for all 95 datasets and obtained the binary images of the myocardium by automatically painting all pixels inside the epicardium and outside the endocardium. Since we did not segment the long axis images (we only used them to compute the mitral valve plane), we reported the binary images for the short axis images only. In 4 of the 95 cases, the automatic detection of the LV did not work (DET0007901, DET0011501, DET0012001, and DET0013801). For these cases, the system allows the user to move the center of the segmentation to the blood pool and rerun the segmentation.

The validation performed by the CAP team produced the following measures from the binary images of the ground truth and segmented myocardium: sensitivity, specificity, accuracy, positive predictive value (PPV), negative predictive value (NPV), dice, and jaccard (see `http://en.wikipedia.org/wiki/Sensitivity_and_specificity` for a very good description of these statistical measures). In addition, we calculated ED volume, ES volume, and mass, and the CAP team provided us with the difference between our values and the ground truth. Fig. 5 shows some segmentation examples. The speed of the system was measured on a dual core laptop (2.93GHz with 4GB of RAM) for an average size dataset with 18 slices (14 short axis and 4 long axis) and 20 phases. The segmentation takes less than 3 minutes: 2 minutes to compute the deformation fields for the entire dataset, 5 seconds

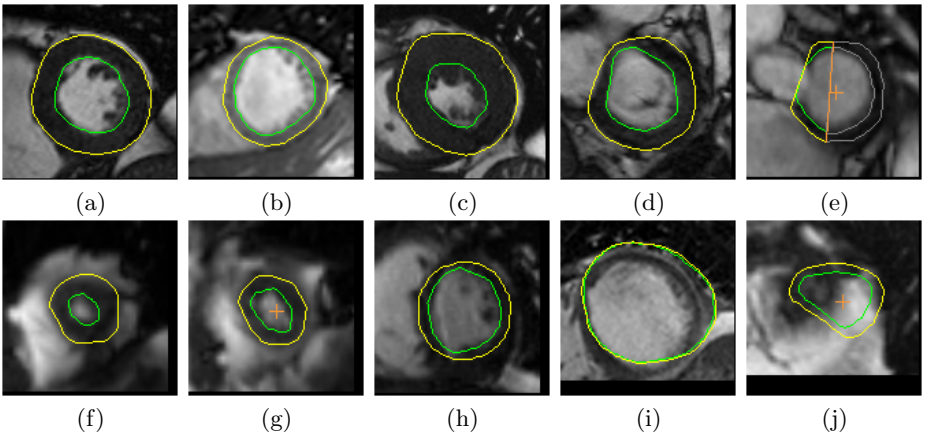

Fig. 5. Examples of segmentation results: (a) mid ventricular slice; (b) mid ventricular slice at ED; (c) mid ventricular slice at ES; (d) slice close to the valve; (e) base slice with mitral valve base plane cut and aortic valve straight line; (f) apex slice; (g) apex slice; (h) inaccurate segmentation; (i) poor segmentation; (j) poor apex segmentation

to detect the heart and the blood pool, 3 seconds to segment the base plane, 1 second for the segmentation of each slice, and 1 second to register neighboring slices and define the contour priors for the next slice. It can be seen that the registration is the bottleneck but since our implementation is parallelized, the timings on a system with more than 2 processors are actually faster.

We first present the overall results, focusing on the 95 datasets that were processed. There were a total of 28213 short axis images, 25481 of which contained ground truth. For 934 images with ground truth, our algorithm did not produce any segmentation result. This happens in the base and apex slices when the algorithm did not propagate up or down enough. Reciprocally, our algorithm segmented 861 images which should not have been segmented, because the algorithm propagated too far up or down. Considering that wrong images being segmented would require the user to delete contours or manually add contours, our system achieves very good results, with a sensitivity of 0.96, specificity of 0.68, accuracy of 0.94, PPV of 0.97, and NPV of 0.67 for predicting a segmentation on a particular image.

We now focus on the results for the images where both ground truth and segmented myocardium were available. The statistics over all segmentations are given in Table 1. Given that the images are so much larger than the myocardium, the size of the true negative (TN) set is so large, and the specificity, accuracy, and NPV are all very close to 1 and not very interesting to study. We will therefore concentrate on the other measures which are much more meaningful. The median values for the sensitivity (0.71), PPV (0.83), dice (0.77), and jaccard (0.62) indicate that the algorithm performs well. It is important to note that these numbers are sensitive to the pixels on the boundary of the region. We are not comparing the endocardium and epicardium regions. Instead, we are comparing

Table 1. Overall results for all 95 datasets

measure	avg	std	min	1st	med	3rd	max
sensitivity	0.621	0.272	0.000	0.443	0.714	0.837	1.000
specificity	0.998	0.002	0.980	0.997	0.998	0.999	1.000
accuracy	0.993	0.005	0.965	0.991	0.994	0.996	1.000
PPV	0.748	0.226	0.000	0.696	0.826	0.895	1.000
NPV	0.995	0.004	0.976	0.994	0.996	0.998	1.000
dice	0.656	0.253	0.000	0.545	0.766	0.840	0.953
jaccard	0.533	0.242	0.000	0.375	0.620	0.724	0.911

the myocardium region which is relatively thin. Therefore, a few pixels included or excluded at the boundary of the segmentation on the endocardium side or on the epicardium side do not change the overall appearance of the segmentation much, but change these statistical measures.

Fig. 6 shows box plots of the dice coefficient distribution for each dataset. The box plots for sensitivity, PPV, and jaccard look very similar to this one. It can be seen that, aside from 5 datasets where the algorithm performed very poorly (DET0007901, DET0023801, DET0011501, DET0011601, and DET0013801), and 2 datasets where the results were not very good (DET0030301 and DET0014901), in general, the segmentation is in good agreement with the ground truth. In all cases of bad segmentation, the algorithm had trouble with the modeling of the gray levels for the different regions. In some cases, it resulted in a very thin myocardium as in Fig. 5(i), and in other cases, parts of the myocardium were missed as in Fig. 5(h). Dataset DET0007901 is particularly difficult because alternating slices have very different brightness levels. Since our algorithm uses the gray level distributions of the previous slice to initialize the modeling in the current slice, the algorithm breaks.

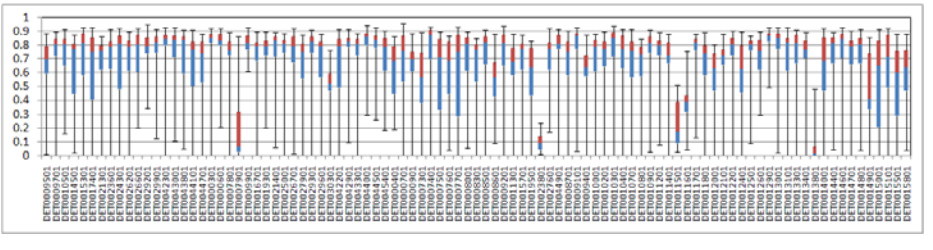

Fig. 6. Box plots of the dice coefficient distribution for each dataset

Fig. 7 shows box plots of the dice coefficient distribution for different slice positions in the dataset. Again, box plots for sensitivity, PPV, and jaccard look very similar. For each image, the relative slice position (between 0 and 1) was calculated with respect to the slices containing ground truth. It can clearly be seen that the segmentation results get worse toward the base and toward the

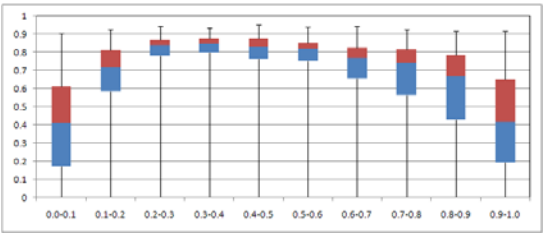

Fig. 7. Box plots of the dice coefficient distribution over various relative slice positions

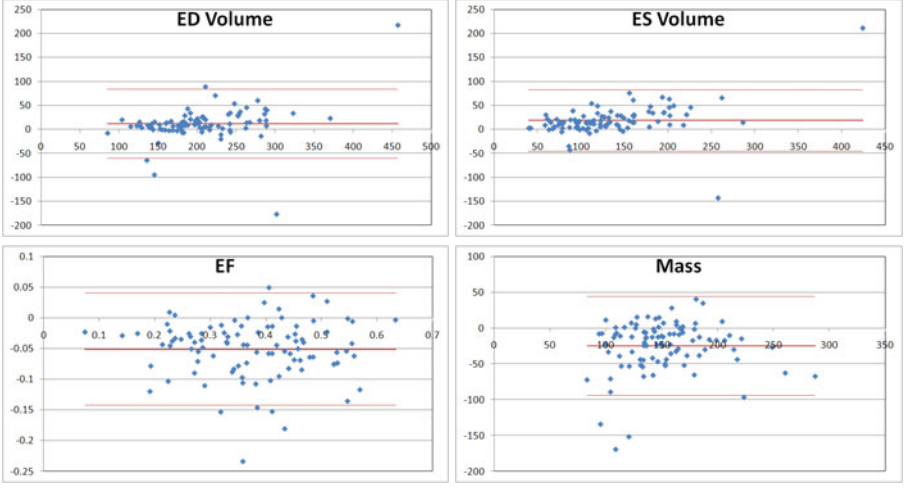

Fig. 8. Bland-Altman plots for the ED volume, ES volume, ejection fraction, and mass

apex. Going toward the apex, the algorithm sometimes has difficulties shrinking the shape of the left ventricle enough as seen in Fig. 5(j). In the base, the discrepancies are due to two factors, namely the thickness of the myocardium, and the exact positions of the mitral valve and aortic valve. Indeed, since the contours are cut by the mitral valve plane and parts are erased (see Fig. 5(e)), if the plane is estimated wrong, the cuts might be completely off and the overlap between the ground truth and segmented myocardium might be very small.

Finally, we compared the clinical measurements. Fig. 8 shows Bland-Altman plots for the ED volume, ES volume, ejection fraction, and mass computed from the ground truth and the segmentation results. Our volumes are calculated by multiplying the area of the contours by half the distance to the previous slice plus half the distance to the next slice. When the contour intersects with the base plane, each individual pixel area multiplied by its distance to the base plane is added to the entire volume. It can be seen that the volumes are slightly over-estimated, by 11.67ml for ED and 18.48ml for ES. The two outliers correspond to datasets DET0011601 and DET0023801 which we have already mentioned

for having poor segmentation results. Even though the volumes are over estimated, the ejection fraction turns out to be very accurate, underestimated by only 0.05%. The mass is underestimated by 25g. We believe that these numbers are clinically acceptable. The bias in volume and mass are likely due to differences in methods used to calculate the measurements from the segmented slices.

4 Conclusions

We have presented a system to automatically segment the left ventricle in cardiac cine MR images. The system segments short axis images, and uses long axis images, when available, to extract the mitral valve leaflet anchor points and generate a mitral valve base plane. The segmentation of the short axis images is performed one slice at a time using an inverse consistent deformable registration algorithm to enforce an implicit smoothness constraint over time. The contours themselves are recovered using a minimum cost path algorithm.

We have tested our system on 95 datasets from the STACOM'11 4D LV Segmentation Challenge validation set and have analyzed the results. This exercise was very useful to understand the strengths and weaknesses of our system. We were aware that the base and apex areas are more challenging and have some ideas on how to improve this by combining the slice based segmentation with a model-based approach [10]. Also, we know that the weakest link in the slice segmentation is the gray level modeling. We might be able to model the different regions distributions better using linear combinations of discrete Gaussians [1].

References

1. El-Baz, A., Gimel'farb, G.: EM based approximation of empirical distributions with linear combinations of discrete Gaussians. In: ICIP, pp. 373–376 (2007)
2. Fonseca, C.G., Backhaus, M., Bluemke, D.A., Britten, R.D., Chung, J.D., Cowan, B.R., Dinov, I.D., Finn, J.P., Hunter, P.J., Kadish, A.H., Lee, D.C., Lima, J.A.C., Medrano-Gracia, P., Shivkumar, K., Suinesiaputra, A., Tao, W., Young, A.A.: The Cardiac Atlas Project – an imaging database for computational modeling and statistical atlases of the heart. Bioinformatics (2011)
3. Grady, L., Schwartz, E.L.: Isoperimetric partitioning: A new algorithm for graph partitioning. SIAM Journal on Scientific Computing 27(6), 1844–1866 (2006)
4. Guetter, C., Xue, H., Chefd'hotel, C., Guehring, J.: Efficient symmetric and inverse-consistent deformable registration through interleaved optimization. In: ISBI, pp. 590–593 (2011)
5. Herman, G.T., Carvalho, B.M.: Multiseeded segmentation using fuzzy connectedness. IEEE Trans. Pattern Analysis and Machine Intelligence 23(5), 460–474 (2001)
6. Jolly, M.-P.: Automatic Recovery of the Left Ventricular Blood Pool in Cardiac Cine MR Images. In: Metaxas, D., Axel, L., Fichtinger, G., Székely, G. (eds.) MICCAI 2008, Part I. LNCS, vol. 5241, pp. 110–118. Springer, Heidelberg (2008)
7. Jolly, M.P., Guetter, C., Guehring, J.: Cardiac segmentation in MR cine data using inverse consistent deformable registration. In: ISBI (2010)

8. Kadish, A.H., Bello, D., Finn, J.P., Bonow, R.O., Schaechter, A., Subacius, H., Albert, C., Daubert, J.P., Fonseca, C.G., Goldberger, J.J.: Rationale and design for the Defribrillators to Reduce Risk by Magnetic Resonance Imaging Evaluation (DETERMINE) trial. J. Cardiovascular Electrophysiology 20(9), 982–987 (2009)
9. Lu, X., Georgescu, B., Jolly, M.-P., Guehring, J., Young, A., Cowan, B., Littmann, A., Comaniciu, D.: Cardiac Anchoring in MRI Through Context Modeling. In: Jiang, T., Navab, N., Pluim, J.P.W., Viergever, M.A. (eds.) MICCAI 2010, Part I. LNCS, vol. 6361, pp. 383–390. Springer, Heidelberg (2010)
10. Lu, X., Wang, Y., Georgescu, B., Littman, A., Comaniciu, D.: Automatic Delineation of Left and Right Ventricles in Cardiac MRI Sequences using a Joint Ventricular Model. In: Metaxas, D.N., Axel, L. (eds.) FIMH 2011. LNCS, vol. 6666, pp. 250–258. Springer, Heidelberg (2011)
11. Petitjean, C., Dacher, J.N.: A review of segmentation methods in short axis cardiac MR images. Medical Image Analysis 15, 169–184 (2011)
12. Radau, P., Lu, Y., Connelly, K., Paul, G., Dick, A.J., Wright, G.A.: Evaluation framework for algorithms segmenting short axis cardiac MRI. MIDAS Journal - Cardiac MR Left Ventricle Segmentation Challenge (2009)
13. Young, A.A., Cowan, B.R., Thrupp, S.F., Hedley, W.J., Dell'Italia, L.J.: Left ventricular mass and volume: Fast calculation with guide-point modeling on MR images. Radiology 202(2), 597–602 (2000)
14. Zheng, Y., Barbu, A., Georgescu, B., Scheuering, M., Comaniciu, D.: Fast automatic heart chamber segmentation from 3D CT data using marginal space learning and steerable features. In: ICCV (2007)

Layered Spatio-temporal Forests for Left Ventricle Segmentation from 4D Cardiac MRI Data

Ján Margeta[1], Ezequiel Geremia[1], Antonio Criminisi[2], and Nicholas Ayache[1]

[1] Asclepios Research Project, INRIA Sophia-Antipolis, France
[2] Machine Learning and Perception Group, Microsoft Research Cambridge, UK

Abstract. In this paper we present a new method for fully automatic left ventricle segmentation from 4D cardiac MR datasets. To deal with the diverse dataset, we propose a machine learning approach using two layers of spatio-temporal decision forests with almost no assumptions on the data nor explicitly specifying the segmentation rules. We introduce 4D spatio-temporal features to classification with decision forests and propose a method for context aware MR intensity standardization and image alignment. The second layer is then used for the final image segmentation. We present our first results on the STACOM LV Segmentation Challenge 2011 validation datasets.

1 Introduction

The left ventricle plays a fundamental role in circulation of oxygenated blood to the body. To assess its function, several indicators are often calculated in clinical practice. Many of these are based on ventricular volume and mass measurements at reference cardiac phases. To calculate these an accurate delineation of the myocardium and the cavity is necessary. To remove the bias and variance of manual segmentation, and obtain reproducible measurements, an automatic segmentation technique is desirable.

Compared to computed tomography (CT), cardiac magnetic resonance imaging (cMRI) offers superior temporal resolution, soft tissue contrast, no ionizing radiation, and a vast flexibility in image acquisition characteristics. As a disadvantage, cMRI scans often yield significantly lower resolution in the plane orthogonal to the plane of acquisition, the images can suffer from magnetic field inhomogeneities and respiration artifacts can manifest as slice shifts. Moreover, the lack of standard units (compared to the Hounsfield scale in CT) makes it difficult to directly apply most of the intensity based segmentation techniques.

Motivated by the success of Lempitsky et al. [1] in myocardium segmentation from 3D ultrasound sequences in near real time and Geremia et al. [2] for multiple sclerosis lesion segmentation, we propose a fully automated voxel-wise segmentation method based on decision forests (DF) with no assumptions on shape, appearance, motion (except for periodicity and temporal ordering) or knowledge about the cardiac phase of the images in the sequence. The left ventricle

O. Camara et al. (Eds.): STACOM 2011, LNCS 7085, pp. 109–119, 2012.

segmentation problem is defined as the classification of voxels into myocardium and background.

Instead of robustly registering to an atlas [3], building a model [4] or running a highly specialized segmentation algorithm we leave the learning algorithm to automatically decide the relevant features for solving the segmentation problem using the provided ground-truth only. In principle, any pathology can be learnt once a similar example is represented within the training dataset. The previously used decision forests [1,2] rely on features that work best when image intensities and orientations are very similar. To tackle the highly variable dataset, we propose a layered learning approach, where the output of each layer serves a different purpose. The first layer is used to prepare the data for a more semantically meaningful and accurate segmentation task in the second layer.

The main contributions of this paper are: a method to use decision forests to solve the MR intensity standardization problem (Section 3.1) and, similarly, perform a context sensitive rigid registration (Section 3.2) to align all images to a reference pose. We also suggest a way to introduce temporal dimension into the currently used 3D random features (Section 2.2). Using the intensity standardized and pose normalized images, which we add spatial information to, we then train a second forest layer (Section 4). This helps the trees to automatically build their own latent shape representation.

Dataset. STACOM 2011 LV segmentation challenge data [5] were divided into two sets. Training set (100 3D+t short axis (SA) volumes with manually delineated myocardia at each cardiac phase) and validations sets (5×20 3D+t SA volumes with no delineation provided).

This dataset clearly shows the anatomical variability of heart shape and appearance and some of the main issues of cMRI mentioned above.

2 Layered Spatio-temporal Decision Forests

Decision forests are an ensemble supervised learning method consisting of a set of binary decision trees. The training set contains a set of feature measurements and associated labels (myocardium/background) for each of the voxels in the set.

The trees are built in a top-down fashion, from the root, down to the leaves. At each node, local features and a randomly sampled subset of context-rich features are considered for feature selection. Random sampling of the features leads to increased inter-node and inter-tree variability and improved generalization. Each feature θ can be regarded as a binary decision (in our case $\tau_l < \theta < \tau_h$) that splits the original set into two disjoint subsets. The trees then select the most discriminative features for each split such that the information gain is maximized. The data division then recursively continues until a significant part of the voxels at the node belongs to a single class or no significant information gain can be obtained by further splitting. The node then becomes a leaf. The averaged class distributions of all the leaves in the forest reached by the voxel then represent the posterior probabilities of it belonging to either the myocardium or the background. See Geremia et al. [2] for more details.

2.1 Strategy to Learn from Spatio-temporal Data

In our approach, we serially train two layers of decision forests, each with the aim to learn to segment, but using slightly modified training data and features. Training with all the 3D+t data was not feasible within the time limits of the challenge, therefore a reduced strategy was designed. This strategy is repeated for each tree:

1. Select a random subset of k 4D volumes from the whole training set
2. Randomly choose a reference 3D frame I^c for each selected 4D volume
3. Select two frames I^{c-o}, I^{c+o} with a fixed offset o on both sides from the reference cardiac image I^c (with periodic wrapping at sequence boundaries)
4. Train the tree using a set of k triplets (I^c, I^{c-o}, I^{c+o})

To reduce the computational time, the size of the subset for each tree was set to $k = 15$, and only one fixed offset $o = 4$ is currently used. The choice of o was made such that the motion between the selected frames is significant even when more stable cardiac phases (end systole or end diastole) are selected as the reference frame and that almost a half of the cardiac cycle could be covered.

2.2 Features

We use several features families to generate the random feature pool operating on the triplets of frames. Their overview can be seen on Figure 2.2).

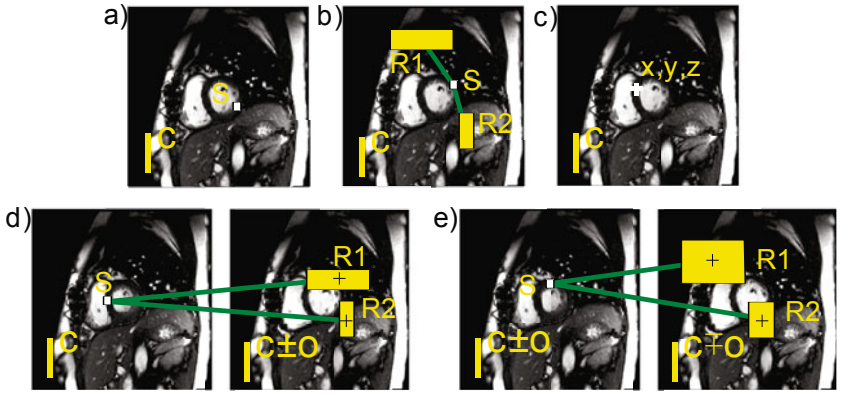

Fig. 1. Illustration of image based features extracted from the images. a) Local features ($3\times3\times3$ box average S around the source voxel in the current frame I^c) [2]. b) Context rich features [2] measuring the difference between source box average S and the sum of remote region averages $R1$ and $R2$. c) Components x,y,z of voxel coordinates as features[1]. d) Spatio-temporal context rich features with the current frame as the source image and offset frame $I^{c\pm o}$ as the remote. e) Spatio-temporal context rich features with one of the offset frames as the source image and the other as remote.

Local Features. Proposed in [2] as an average of intensities in the vicinity of the tested voxel to deal with noise in magnetic resonance imaging:

$$\theta^{loc}_{I^c}(x) = \theta^{loc}_{I^c}([x,y,z]) = \sum_{x'=x-1}^{x'\leq x+1} \sum_{y'=y-1}^{y'\leq y+1} \sum_{z'=z-1}^{z'\leq z+1} I^c([x',y',z']) \tag{1}$$

Although these features are not intensity invariant, they can still quite well reject some highly improbable intensities.

Context Rich Features. Defined also in [2], for multichannel MR acquisitions as a difference between the local source image intensity I^S and box averages of remote regions in image I^R:

$$\theta^{CR}_{I^S,I^R}(x) = I^S(x) - \frac{1}{Vol(R_1)} \sum_{x' \in R_1} I^R(x') - \frac{1}{Vol(R_2)} \sum_{x' \in R_2} I^R(x') \tag{2}$$

The 3D regions R_1 and R_2 are randomly sampled in a large neighborhood around the origin voxel. These capture strong contrast changes and long-range intensity relationships. In our case we define context-rich features as $\theta^{CR}_{I^c,I^c}(x)$.

Spatio-Temporal Context Rich Features. The domain of the moving heart can be coarsely extracted by just thresholding the temporal difference magnitude of the image. We propose to exploit this wealth of information and extend the previous context-rich features into the temporal domain by comparing the "current" 3D frame I^c and another frame offset from c by $\pm o$. The temporal context-rich features can be defined as $\theta^{TCR1}_{I^c} = \theta^{CR}_{I^c,I^{c+o}}(x)$ and $\theta^{TCR1}_{I^c} = \theta^{CR}_{I^c,I^{c-o}}(x)$.

Similarly, we measure the differences between the symmetrically offset frames contained in the triplet as $\theta^{TCR2}_{I^c}(x) = \theta^{CR}_{I^{c+o},I^{c-o}}(x)$ and $\theta^{TCR2}_{I^c}(x) = \theta^{CR}_{I^{c-o},I^{c+o}}(x)$. These spatio-temporal features can be seen as an approximation of a temporal differentiation around the center frame. Note that we use both $+o$ and $-o$ to keep some symmetry of the remote region distribution.

Voxel Coordinates. Finally, as in [1], we can insert absolute voxel coordinates: $\theta^X_C(x) = x_x$, $\theta^Y_C(x) = x_y$, $\theta^Z_C(x) = x_z$ into the feature pool. However, not until these coordinates have a strong anatomical meaning. This happens later, in the second forest layer when the images are reoriented into the standard pose.

2.3 Data Preprocessing

To use fast evaluation of previously defined features based on integral images [6], it is necessary to have consistent spacing. Therefore, all the volumes were resampled to one of the most common spatial spacings in the dataset $(1.56, 1.56, 7.42mm)$ and temporal sequence length (20 frames).

Intensity ranges of the images were all linearly rescaled to a fixed range. Similarly to Nyúl et al. [7], we clamp intensities beyond the 99.8 percentile as they usually do not convey much useful information.

3 First Layer: Decision Forests for Image Intensity Standardization and Position Normalization

Following the above mentioned training subset selection strategy we can train the first layer of the forests. This is done directly on the images after intensity rescaling i.e. images are brought into the same intensity range but have their original poses. Although short axis scans are often acquired close to a position where the ventricular ring is centered, slice orientation is chosen manually during the acquisition, and precise alignment cannot be guaranteed. Therefore we skip the usage of absolute voxel coordinate features at this step.

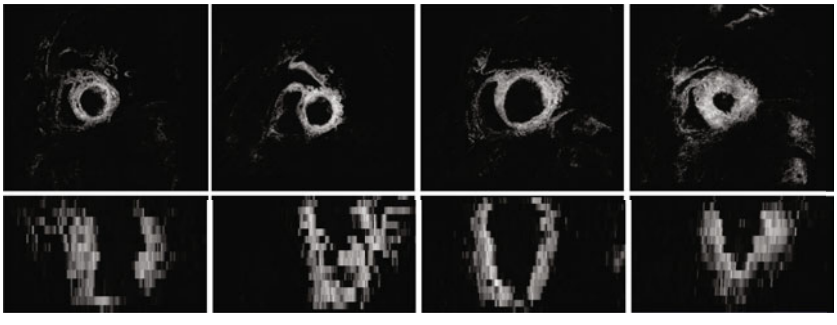

Fig. 2. Short (top) and long (bottom) axis views of the posterior probabilities after the first layer. Brighter value means higher probability.

Several authors (e.g. [3]) have proposed to use Haar like features to detect the heart and crop the heart region. Images can be then registered using the cropped volumes. This removes the influence of background structures and improves the success rate for the registration. However, an extraction of the cropped region will not be necessary to perform a robust registration in our case. We train the first layer of the forests on a rather general scenario, to end up with at least a very rough classification performance (see Figure 2). As we show in the next two sections, using the rough posterior probability map of a tissue belonging to a ventricle this performance can be already good enough for ventricle detection, intensity standardization and alignment onto a reference orientation without any prior knowledge of the data apart from the ground-truth.

3.1 Intensity Standardization

MR intensity value differences of the same tissue are significant not only between scanners and acquisition protocols [8] but also for the same follow-up patients [7]. Therefore good intensity standardization is crucial for any intensity based segmentation algorithm. The variance in median intensities of the myocardia between different cases in the STACOM training set is quite large. There is

no unique mode and the distribution is fairly spread in the whole intensity range $(0, 65535)$. Median myocardial intensities span range $(1954, 36430)$, with standard deviation of 5956 and inter-quantile range 7663). This is a serious problem for any intensity based segmentation method.

Many of the intensity standardization algorithms [9] used today are based on the methods of Nyúl et al. [7][10] and the alignment of histogram based landmarks (e.g. modes, percentiles or statistics of homogeneous connected regions) by rescaling image intensities with a piecewise linear mapping. Many of these methods do work reasonably well for brain images where the white matter is clearly the most dominant tissue. In cMRI, the largest homogeneous regions would most of the time belong to the lungs, liver or cavities, rather than the myocardium.

However, from the rough image first layer classification we already obtain some information about the strength of the belief in the foreground and background object. We propose to remap the source image intensities by a piecewise linear function such that the weighted median (as median is more robust to outliers than the mean) M^c_{source} of the images is transformed to a reference value M_{ref}. The weighted median is defined as follows:

$$M^c_{source} = \arg\min_{\mu} \sum_{x \in I^c} w(x).|I^c(x) - \mu| \tag{3}$$

Where x is the voxel iterator and $w(x)$ are the weights (first layer posterior probabilities). We avoid sorting all volume intensities by approximating the weighted median with the weighted version of the P^2 algorithm [11][12]. This algorithm dynamically approximates the cumulative probability density function with a piece-wise quadratic polynomial by adjusting positions of just five markers as the weighted samples are streamed in. Each of these markers are associated with their position, percentile and an intensity value corresponding to that percentile. The positions are updated such that they correspond to the sum of weights of samples whose intensity value is smaller than the value the markers hold.

3.2 Orientation Normalization

In the approach of Lempitsky et al. [1] voxel absolute coordinates are used as features directly. This choice cannot be justified without aligning the images onto a reference pose. Moreover, features we use for classification are not rotation invariant. Therefore if all the volumes could be registered to have the same orientation, the classification would certainly benefit from it. The interpatient cardiac registration is generally a difficult problem due to the high variability in the thoracic cage. Shi et al. [3] do first learning based heart detection and then apply a locally affine registration method which they claim to be robust for large differences.

A robust learning based linear inter-patient organ registration was proposed by Konukoglu et al.[13]. Here, each organ is represented with a smooth probability map fit to the bounding boxes obtained as a result of a regression forest. Then, registration of these probability maps is performed.

This sigmoid representation is however rather limiting since it disregards the orientation that we would like to correct for. Without any assumptions on the shape of the distribution, we propose to rigidly align the myocardium enhanced first layer posterior probability maps instead. For this step we propose to use a fast and robust rigid block matching registration technique [14]. The reference we used was chosen randomly among the images where the apex was at least partially closed. A better choice of the reference, is currently out of scope of this paper. However, an algorithm similar to Hoogendoorn et al.[15] or a generative technique similar to [16] could be used.

To reduce the computational time, only probability maps of frames from the middle of the sequence are used to estimate the intensity and pose transformations. The same transformations are then applied for all the frames and ground truths in the sequence which will be needed to train the second layer.

4 Second Layer: Learning to Segment with the Shape

4.1 Using Voxel Coordinates

Once the images are registered to a reference volume, the voxel coordinates start to encode spatial relationships with respect to the reference coordinate frame and the coordinate features can be now included in training of the second decision forest layer. Moreover, if the intensity standardization step succeeds, the intensities have more tissue specific meaning (at least for the myocardium).

Thanks to the incorporation of coordinate based features, the tree can completely automatically learn its own latent representation of the possible set of shapes, regularize the classification, and help to remove objects far away from the ventricle. However, this step strongly relies on the success of the previous registration step. Currently, only one reference image is used. Registration to multiple targets should therefore improve robustness and alleviate this problem.

4.2 Transforming the Volumes Back

After the classification is done in the reference space, the posterior probability maps can be transformed back to the original reference frame and resampled accordingly. This shows the advantage of a soft classification technique where the final binary mask is obtained by thresholding the transformed non-integer posterior map, thus avoiding some of the interpolation artifacts.

5 Results

Here we show the preliminary results of our method. The forest parameters for the first layer were fixed as follows: 20 trees with depth 20 each. To train each tree, 15 triplets of frames were randomly selected from different volumes of the training set (91 volumes in total). For the second layer: 27 trees each with depth 20. For each tree 12 triplets were randomly selected from different volumes of

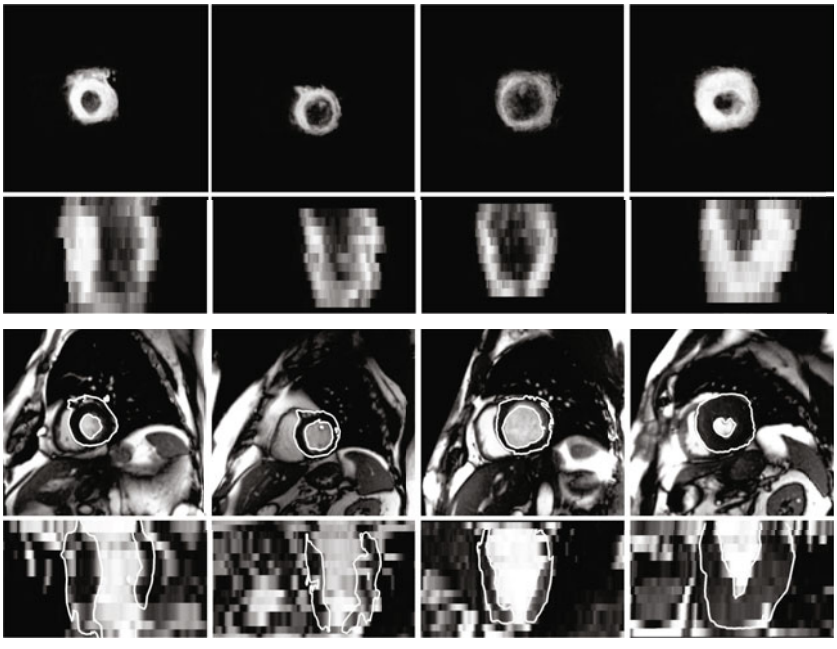

Fig. 3. Short (top) and long (bottom) axis views on the posterior probabilities after the second layer and segmentation results (isocontour of the probability map at 0.5)

the training set (91 volumes in total). This leads to usage of only 8% triplets from the whole training set. Hence, there is a vast reserve in utilisation of the training data and setting optimal forest sizes. These parameters were chosen rather empirically to fit into the time limits of the challenge.

The following results were obtained after blind evaluation of our classifications on 90 previously unseen test volumes i.e. 25415 slices from the validation dataset by the STACOM LV segmentation workshop organisers (See Table 1).

In most of the cases, the algorithm was able to correctly identify the left ventricle myocardium (with median specificity of 0.81). This was possible without the need to explicitly define the segmentation rules and problem specific assumptions (e.g. circularity of the myocardium or cavity contrast). It was also not neccessary to include additional information into the training set (e.g. mitral valve plane position or manual segmentation of a frame in the sequence) nor to rely on a robust non-rigid registration technique.

All the measures were calculated per-slice. This way of calculating the measures caused some of them (specificity, accuracy and NPV) to reach high values but also to have less explicative power since the number of the background voxels (TN) dominates the expression. Some of these measures (sensitivity and PPV) strongly penalize any voxel misclassifications in the apical and basal areas where the slices contain only very few true myocardial voxels. Performance of our algorithm is currently rather mediocre at basal and apical slices

(with median specificity as low as 0.23 at the apex). This is partly due to limited feature evaluation at image borders and the pose standardization step, where voxels at boundaries can get transformed out of the classified volume. The poor performance at these regions results in increased variance of the measures and helps to explain the significant differences between mean and the median values of the measures.

Table 1. Statistics on the per-slice measures of our segmentation results on 90 volumes from the validation dataset calculated from the entire slices with no region of interest specified. The basal and apical slices contribute to the large differences between the mean and median values and also contribute to the higher variance.

	sensitivity $\frac{TP}{TP+FN}$	specificity $\frac{TN}{FP+TN}$	accuracy $\frac{TP+TN}{P+N}$	PPV $\frac{TP}{TP+FP}$	NPV $\frac{TN}{TN+FN}$	dice $\frac{2\lvert A\cap B\rvert}{\lvert A\rvert+\lvert B\rvert}$	jaccard $\frac{\lvert A\cap B\rvert}{\lvert A\cup B\rvert}$
mean	0.6857	0.9897	0.9861	0.4791	0.9962	0.5045	0.3730
median	0.8099	0.9907	0.9875	0.5234	0.9978	0.5995	0.4281
σ	0.3137	0.0077	0.0077	0.2069	0.0046	0.2571	0.2098

Compared to the state of the art algorithms for left ventricle segmentation, slightly lower segmentation performance was achieved. It should be noted that the classification is run independently for each voxel. No smoothness, connectivity nor temporal consistency constraints are enforced to demonstrate the performance of the pure machine learning approach. Therefore, isolated segmentation islets or holes in the resulting binary segmentation can occur as a result of misclassification. However, thanks to the coordinate features, most of the voxels far from the myocardium are usually well discarded and also the solution becomes more regular as a result of the latent cardiac shape model built by the forests. In the soft classification, the holes are represented as a drop in the segmentation confidence but rarely fall to zero. This information could be easily considered in a subsequent postprocessing step to further improve the segmentation. However, adding these was not the goal of this paper.

6 Conclusions

We aimed to present a fully automatic machine learning based algorithm for left ventricle segmentation with no explicit definition of task specific segmentation rules, model creation, user interaction nor post-processing. The algorithm learnt to automatically select the most discriminative features for the task using the ground-truth only. The only assumptions we make is that the motion of the object to be segmented is periodic for the construction of frame triplets and that the tissue intensity mapping between two different cases can be roughly approximated by a piecewise linear function. We also introduced a machine learning based intensity standardization method that allows to do tissue specific remapping of intensities and obtain a more CT like behaviour.

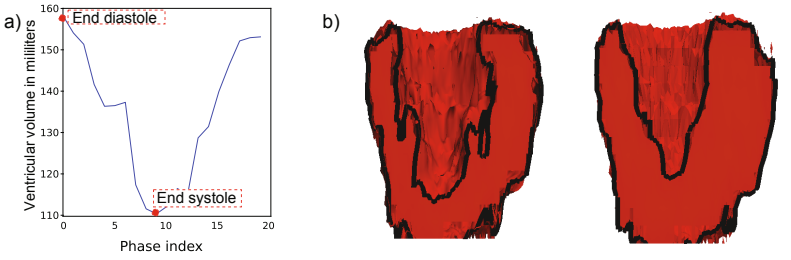

Fig. 4. a) Automatically calculated volume curve from patient DET0026701 during a single cardiac cycle with detected end systole (ES) and end diastole (ED) frames at the volume maximum and minimum respectively. b) Long axis crosssection through the binarized segmentations at ED and ES.

Finally, using a curvature-based iterative hole filling algorithm [17] on the binarized segmentation, we could automatically calculate volumetric measurements and detect the main cardiac phases as the volume curve extremas (see Figure 4).

Acknowledgements. This work was partly supported by Microsoft Research through its PhD Scholarship Programme. We used data and infrastructure made available through the Cardiac Atlas Project (www.cardiacatlas.org) [5].

References

1. Lempitsky, V., Verhoek, M., Noble, J., Blake, A.: Random Forest Classification for Automatic Delineation of Myocardium in Real-Time 3D Echocardiography. In: Ayache, N., Delingette, H., Sermesant, M. (eds.) FIMH 2009. LNCS, vol. 5528, pp. 447–456. Springer, Heidelberg (2009)
2. Geremia, E., Clatz, O., Menze, B.H., Konukoglu, E., Criminisi, A., Ayache, N.: Spatial decision forests for MS lesion segmentation in multi-channel magnetic resonance images. NeuroImage 57(2), 378–390 (2011)
3. Shi, W., Zhuang, X., Wang, H., Duckett, S., Oregan, D., Edwards, P., Ourselin, S., Rueckert, D.: Automatic Segmentation of Different Pathologies from Cardiac Cine MRI Using Registration and Multiple Component EM Estimation. In: Metaxas, D., Axel, L. (eds.) FIMH 2011. LNCS, vol. 6666, pp. 163–170. Springer, Heidelberg (2011)
4. Lu, X., Wang, Y., Georgescu, B., Littman, A., Comaniciu, D.: Automatic Delineation of Left and Right Ventricles in Cardiac MRI Sequences Using a Joint Ventricular Model. In: Metaxas, D., Axel, L. (eds.) FIMH 2011. LNCS, vol. 6666, pp. 250–258. Springer, Heidelberg (2011)
5. Fonseca, C., Backhaus, M., Bluemke, D., Britten, R., Chung, J., Cowan, B., Dinov, I., Finn, J., Hunter, P., Kadish, A., Lee, D., Lima, J., Medrano-Gracia, P., Shivkumar, K., Suinesiaputra, A., Tao, W., Young, A.: The Cardiac Atlas Project-an Imaging Database for Computational Modeling and Statistical Atlases of the Heart. Bioinformatics 27(16), 2288–2295 (2011)

6. Viola, P., Jones, M.: Rapid object detection using a boosted cascade of simple features. In: Proceedings of the 2001 IEEE Computer Society Conference on Computer Vision and Pattern Recognition, CVPR 2001, pp. I-511–I-518. IEEE Computer Society (2001)
7. Nyúl, L.G., Udupa, J.K.: On standardizing the MR image intensity scale. Magnetic Resonance in Medicine 42(6), 1072–1081 (1999)
8. Shah, M., Xiao, Y., Subbanna, N., Francis, S., Arnold, D.L., Collins, D.L., Arbel, T.: Evaluating intensity normalization on MRIs of human brain with multiple sclerosis. Medical Image Analysis 15(2), 267–282 (2010)
9. Bergeest, J., Florian Jäger, F.: A Comparison of Five Methods for Signal Intensity Standardization in MRI. In: Tolxdorff, T., Braun, J., Deserno, T.M., Horsch, A., Handels, H., Meinzer, H.P., Brauer, W. (eds.) Bildverarbeitung für die Medizin 2008, pp. 36–40. Springer, Heidelberg (2008)
10. Nyúl, L.G., Udupa, J.K., Zhang, X.: New Variants of a Method of MRI Scale Standardization. IEEE Transactions on Medical Imaging 19(2), 143–150 (2000)
11. Jain, R., Chlamtac, I.: The P2 algorithm for dynamic calculation of quantiles and histograms without storing observations. Communications of the ACM 28(10), 1076–1085 (1985)
12. Egloff, D.: Weighted P2 quantile, Boost Accumulators 1.46 (2005), www.boost.org
13. Konukoglu, E., Criminisi, A., Pathak, S., Robertson, D., White, S., Haynor, D., Siddiqui, K.: Robust linear registration of CT images using random regression forests. In: SPIE Medical Imaging, vol. 7962, pp. 79621X–79621X-8 (2011)
14. Ourselin, S., Roche, A., Prima, S., Ayache, N.: Block Matching: A General Framework to Improve Robustness of Rigid Registration of Medical Images. In: Delp, S., DiGoia, A., Jaramaz, B. (eds.) MICCAI 2000. LNCS, vol. 1935, pp. 557–566. Springer, Heidelberg (2000)
15. Hoogendoorn, C., Whitmarsh, T., Duchateau, N., Sukno, F.M., De Craene, M., Frangi, A.F.: A groupwise mutual information metric for cost efficient selection of a suitable reference in cardiac computational atlas construction. In: SPIE Medical Imaging, vol. 7962, pp. 76231R–76231R-9 (2010)
16. Iglesias, J., Konukoglu, E., Montillo, A., Tu, Z., Criminisi, A.: Combining Generative and Discriminative Models for Semantic Segmentation of CT Scans via Active Learning. In: Székely, G., Hahn, H.K. (eds.) IPMI 2011. LNCS, vol. 6801, pp. 25–36. Springer, Heidelberg (2011)
17. Krishnan, K., Ibanez, L., Turner, W., Avila, R.: Algorithms, architecture, validation of an open source toolkit for segmenting CT lung lesions. In: Brown, M., de Bruijne, M., van Ginneken, B., Kiraly, A., Kuhnigk, J.M., Lorenz, C., McClelland, J.R., Mori, K., Reeves, A., Reinhardt, J.M. (eds.) MICCAI Workshop on Pulmonary Image Analysis, CreateSpace, pp. 365–375 (2009)

Myocardial Segmentation Using Contour-Constrained Optical Flow Tracking

Ahmed S. Fahmy[1,*], Ahmed O. Al-Agamy[1], and Ayman Khalifa[2]

[1] Center for Informatics Science, Nile University, Cairo, Egypt
[2] Biomedical Engineering Department, Helwan University, Cairo, Egypt
asfahmy@nileuniversity.edu.eg

Abstract. Despite the important role of object tracking using the Optical Flow (OF) in computer graphics applications, it has a limited role in segmenting speckle-free medical images such as magnetic resonance images of the heart. In this work, we propose a novel solution of the OF equation that allows incorporating additional constraints of the shape of the segmented object. We formulate a cost function that include the OF constraint in addition to myocardial contour properties such as smoothness and elasticity. The method is totally different from the common naïve combination of OF estimation within the active contour model framework. The technique is applied to dataset of 20 patients and comparison with manual segmentation shows sensitivity and specificity levels of 93% and 99% respectively is obtained through the challenge validation system.

Keywords: Myocardial segmentation, Short Axis, Optical Flow, Active Contour Models.

1 Introduction

Quantitative assessment of the cardiac function from cine MRI images requires delineation of the inner and outer surfaces of the left ventricle throughout the phases of the cardiac cycle. Usually, this is done by delineating the endo- and epi- cardium contours in multiple 2D sequences of short-axis (SA) cross-sections of the heart. Although manual segmentation is considered the golden reference for myocardial segmentation, it is a tedious and time-consuming process. Several automatic (and semi-automatic) techniques for segmenting the myocardium have been proposed in literature. A large class of automatic segmentation techniques depends mainly on the spatial information of each image. Examples include using 2D active contour models [1], region growing [2], or morphological operators [3]. Nevertheless, these techniques ignore the temporal relationship between the consecutive time frame s which can be useful for consistent segmentation of the myocardium. A number of techniques have been proposed in literature employing temporal information. Examples include active shape/appearance model segmentation techniques that use learning datasets to model the shape, appearance, and motion parameters of the myocardial borders [4-6]. Although these methods

* Corresponding author.

O. Camara et al. (Eds.): STACOM 2011, LNCS 7085, pp. 120–128, 2012.

can successfully delineate the myocardium, they require manual segmentation of huge number of images spanning a wide range of normal and abnormal case which is, to date, prohibitively expensive.

To avoid the need for a huge training dataset, one possible way is to track the myocardial contours from time frame to another using standard computer vision technique such as optical flow (OF) [7]. The technique can provide a rough estimate of the (initial) contour location at each time frame. This contour can then be refined using an appropriate technique such as active contour model (ACM). For example, Mikic et al [9] used the tracked points as an initial contour for the ACM algorithm. Nevertheless, after few iterations of the algorithm, the contour evolves away from its initial location and thus the effect of the temporal information vaporizes. To avoid this loss of temporal information, Hamarneh et al [8] proposed modifying the ACM algorithm to include an external force representing the contour location estimated by the OF method. Although this method successfully attracts the iterated solution to the locations predicted by the OF, it has a major disadvantage of having the OF algorithm runs independent of the ACM algorithm. That is, inaccurate results of the OF algorithm propagates into the ACM algorithm and bias its output. It is worth noting that the above two attempts were applied to ultrasound images which are rich in image textures (i.e. speckles). This resulted in accurate OF tracking of the myocardium contours and thus reasonably accepted segmentation results. Unfortunately, in speckle-free MRI images, such techniques are vulnerable to inaccurate OF tracking.

In this work, we propose a novel solution of the OF equation that allows incorporating additional constraints of the shape of the segmented object. We formulate a new cost function that include the OF constraint in addition to myocardial contour properties such as smoothness and elasticity. That is, the solution minimizing this cost function, simultaneously (and optimally) satisfies both the OF constraint and the contour smoothness constraint. The results of the new formulation outperform classical methods of combining OF and ACM methods because it involves simultaneous optimization of both the OF and the ACM algorithm.

2 Method

2.1 Energy Function of the Optical Flow Constraint

Given an image sequence I(x, y; t) with t=1, 2, .., n, it is required to estimate the displacement (or equivalently, the velocity) of each image point (x,y), from one time frame to the other. Let u_i^t and v_i^t be the required displacement in the x- and y-direction, respectively, at a given time frame, t, and point $P_i \coloneqq (x_i, y_i)$. In the optical flow framework, the displacements $u_i^t$and v_i^t can be estimated by solving the optical flow constraint equation given by [7],

$$I_x u_i^t + I_y v_i^t = -I_t \tag{1}$$

where I_x, I_y are the first-order derivative of the image in the x- and y- direction respectively calculated at$P_i$and I_t is the time derivative of the image $I(x_i, y_i; t)$. The latter can be approximated by taking the difference between two successive images $I(x_i, y_i; t-1)$and $I(x_i, y_i; t)$.

In our formulation, we use a different form of Eq (1) by noticing that Eq (1) can be obtained by minimizing a quadratic term, i.e. an energy function, E_{OF}, given by the following equation [9],

$$E_{OF}(u_i^t, v_i^t) = [u_i^t, v_i^t \ 1] \, . \, J(\nabla I) \, . \begin{bmatrix} u_i^t \\ v_i^t \\ 1 \end{bmatrix} \tag{2}$$

Where $\nabla I := [I_x I_y I_t]^T$ and $J(\nabla I) := (\nabla I) \bullet (\nabla I)^T$.

If we have a set of *N* points forming a contour, then the energy term for the contour at a time frame, *t*, is given by:

$$E_{OF}^t = \sum_{i=1}^{N} \mathrm{E_{OF}}(u_i^t, v_i^t) \tag{3}$$

It is worth noting that the above equation is equivalent to Eq. (2); and thus, there is still no unique solution that minimizes Eq (2). Therefore, more constraints are still required in order to obtain a solution to Eq. (3).

2.2 Contour Constraints

In this work, we use the property that myocardial contours are smooth and elastic as the additional constraints. These additional assumptions can be formulated in a way similar to that of the active contour model (ACM) energy function. That is, at a given time frame, *t*, the following energy term is calculated at each contour point, P_s^t, (see [11] for more details of the ACM energy function),

$$\mathrm{E_{ACM}} = \mathrm{E_{\ Elasticity}} + \mathrm{E_{\ Curvature}} \tag{4.1}$$

$$\mathrm{E}_{ACM}^t = \alpha \left| \frac{dP_i^t}{ds} \right|^2 + \beta \left| \frac{d^2 P_i^t}{ds^2} \right|^2 \tag{4.2}$$

where the first- and second- order derivatives in the above equation measure the amount of contour stretching (elasticity energy) and contour bending (curvature energy) respectively. The weighting parameters, α and β, represent the contour internal properties of elasticity and curvaturerespectively.

2.3 Contour-Constrained Optical Flow Energy Function

Combing equation (3) and (4) yields an energy function that contains the temporal information from the image sequence in addition to the contour properties. That is, the desired contour that delineates the myocardial border is the one that minimizes the following cost function:

$$E = \mathrm{E_{OF}} + \mathrm{E_{ACM}} \tag{5.1}$$

$$E^t = \sum_{i=1}^{N} \left(\alpha \left| \frac{dP_i^t}{ds} \right|^2 + \beta \left| \frac{d^2 P_i^t}{ds^2} \right|^2 + \gamma \, \mathrm{E_{OF}}(u_i^t, v_i^t) \right) \tag{5.2}$$

A greedy algorithm is used to solve the above minimization problem, where the weighting factors (α, β and γ) are preset experimentally and kept fixed for the

different runs of the algorithm (i.e. are not changed from dataset to another).To determine the values of these parameters, first, the algorithm was applied several times values to segment four training datasets. In each run, the parameter values were selected randomly and kept fixed for all four datasets and the segmentation results were recorded. Then, the parameter values that yielded the best segmentation results were determined and stored. To study the effect of changing these parameters on the performance of the algorithm, their values were changed by 20% and the changes in the segmentation results were observed. It was found that the overall performance is not sensitive to such changes in the parameters and thus they were kept fixed in all other runs of the algorithm (currently, we use α=0.5, β=1.5 and γ=0.5).

Figure 1 shows a block diagram of the proposed algorithm and Figure 2 shows how the E_{OF} energy term is calculated for the two consecutive time frames *t-1*, *t*. At time frame t the mask points N_i of the center point $P`_1$ are compared to the reference point P_1 at time frame *t-1*. (U, V) are determined based on Nx_i and Ny_i coordinate values and the E_{OF} energy term is calculated as described in Eq (2).

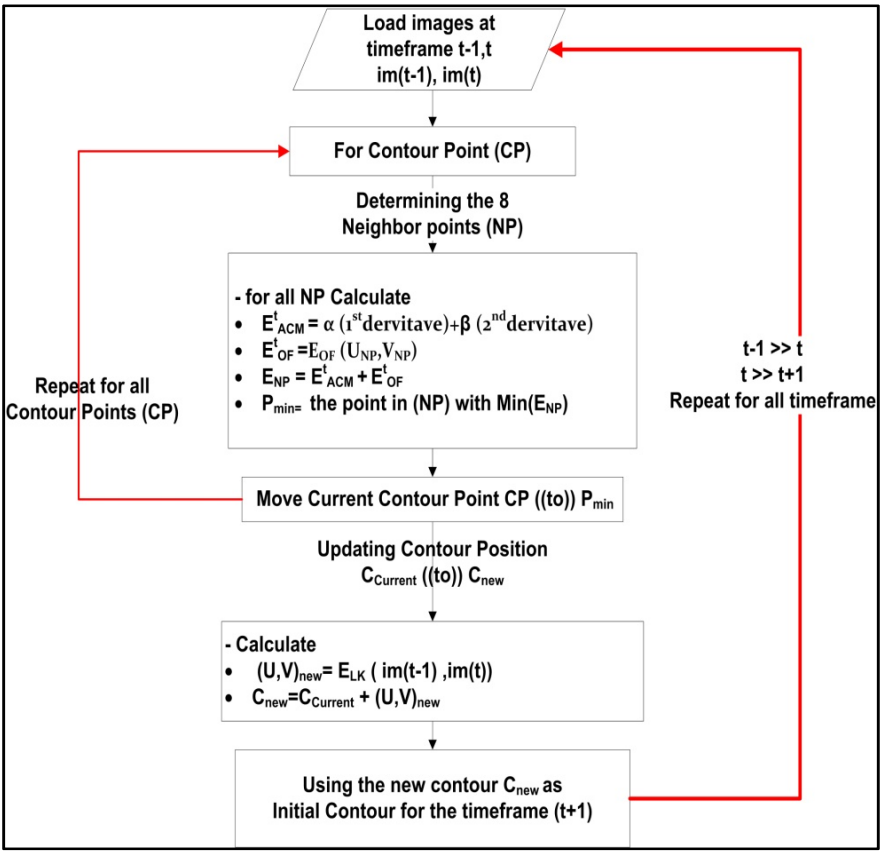

Fig. 1. The workflow of the proposed algorithm

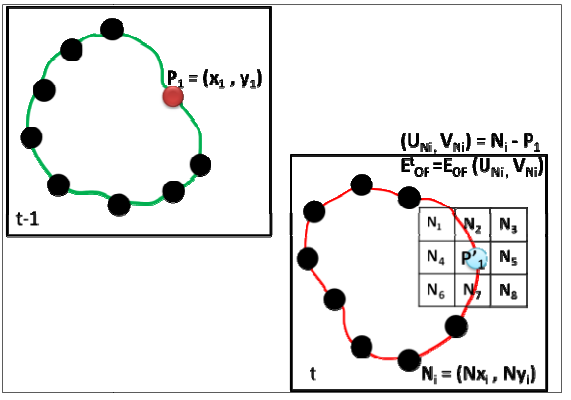

Fig. 2. Calculation of E_{OF} from two consecutive time frames *t-1*, *t*

2.4 Evaluation of the Segmentation Method

For the purpose of performance evaluation, the proposed segmentation method was applied to a dataset of 20 patients provided by the *Cardiac Atlas Project* [12]. The provided details of the dataset are as follow. Each patient has ~15 short-axis slices with ~25 frame/slice. These frames were acquired with Steady-State Free Precision (SSFP) MR imaging protocol with typical thickness ≤ 10mm, gap ≤ 2mm, TR 30-50ms, TE 1.6ms, flip angle 60 deg., FOV 360mm and 256x256 image matrix. The dataset's studies were acquired at multiple sites using a range of different scanner types and manufacturers.

The evaluation of the proposed method is assessed by using two different metric types. The first one is the technical performance analysis (standard sensitivity, specificity and accuracy) and similarity measurement between the automated segmentation results with the manual result (Dice and Jaccard similarity indices). The second one is the clinical performance analysis in terms of global LV function (volume and mass).

In addition to the evaluation metrics stated above, the results of the proposed method was compared to two other techniques. The first is standard ACM initialized, at a given time frame, with a contour estimated by the Lucas-Kanade optical flow. The second technique is also an active contour model whose energy function includes a term representing the distance of the current contour from that predicted by the Lucas-Kanade optical flow method.

2.4.1 Manual Segmentation

The ground truth of the dataset for the 20 patients were obtained from "The Statistical Atlases and Computational Models in the Heart (STACOM'11) - Cardiac Left Ventricular Segmentation Challenge" where each image has a corresponding binary image representing the regions of the myocardium as determined manually by an expert grader. Different evaluation parameters – e.g. sensitivity, specificity, accuracy, Dice, and Jaccared similarity indexes - have been calculated for the segmentation results using the manual segmentation as ground truth.

2.4.2 Standard ACM with Optical Flow Initialization

A total of 3 datasets (15 slices, 25 time frame/slice) have been used to compare the proposed method to standard ACM technique. The ACM algorithm was initialized at each time frame by the OF tracking results of the final contour obtained in the previous time frame. Details of this method can be found in [9].

2.4.3 ACM with Naïve Optical Flow Energy Function

A total of 3 datasets (15 slices, 25 time frame/slice) have been used to compare the proposed method to standard ACM technique with a modified energy function. The ACM algorithm was initialized at each time frame by the final contour obtained in the previous time frame. The modified energy function at a given contour point, *s*, is formulated as,

$$\grave{E} = E_{ACM} + E_{OF} \tag{6.1}$$

$$E_{OF} = \|P_c(s) - P_{OF}(s)\| \tag{6.2}$$

Where $P_c(s)$ is the location of the s^{th} contour point in the current iteration (at any step during the evolution of the ACM solution); P_{OF}(s) is the location of the s^{th} contour point predicted by the OF algorithm; and ‖.‖ is the vector Euclidian norm.

3 Results and Discussion

Table 1 shows a summary of the quantitative evaluation of the proposed method when applied to the 20 patient datasets. High sensitivity and specificity values are evident from the table. In addition, the dice index shows a relatively high similarity between the segmentation results of the proposed method and the ground truth obtained by the manual grading of the images. It is evident also from the table that all the quantitative measures of the proposed method are better than the other two techniques. This performance is due to the global nature of the energy function associated with the proposed technique. That is, the proposed method tries to find the optimal solution that simultaneously minimizes the constraints implied by the contour elasticity and smoothness properties as well as the OF constraints. On the other hand, the other two techniques sequentially perform two optimization problems; one to solve the OF constraint and the other to solve the ACM problem.

Figure 3 shows 5 time frames of a basal short axis slice. The first row displays the results of the proposed technique. The second and third rows show the results of the two other methods: ACM initialized by OF estimated contour; and ACM algorithm with a naïve energy term representing the OF solution. It can be seen from the figure that the results of the proposed method are better than those of the other method. Two reasons can be stated for the failure of this particular case. First, the displacement field obtained by the OF at some points was overestimated and the contour was pushed away from the true myocardium border. In addition, the elasticity energy term of the ACM model tried to overcome this sudden motion of the contour at these points

so it pushed more points towards the direction of the motion. These two factors caused the contour to significantly shrink and get attached to the inner edges of the papillary muscles (red arrows). The yellow arrows on the figure show some segmentation errors at the epicardium. Nevertheless, the error is not large because of the small displacement of epicardium which results in reliable OF estimation.

Finally, it is worth noting that the proposed method does not impose the classical OF constraints proposed by Lucas and Kanade (spatial constancy of the motion field) or Horn and Schunk (smooth motion field). Instead, the new method uses a different type of constraints related to the shape of the object being segmented, i.e. the myocardium contours. Further investigation might be done to study the effect of adding other constraints to the energy function orusinga term representing recent non-rigid registration techniques instead of the classical Lucas Kanadeoptical flow formulation.

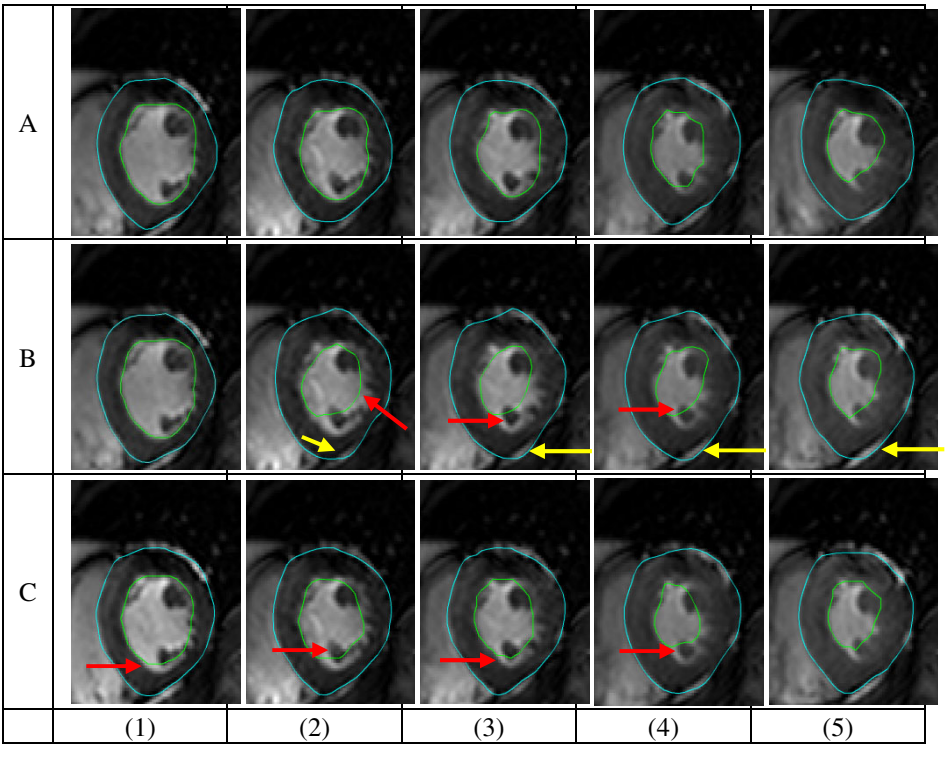

Fig. 3. Segmentation results using: (A) The Proposed Algorithm; (B) ACM + OF Initialization; and (C) ACM + naïve OF Energy Function

Table 1. Quantitative comparison between different techniques and the ground truth

	Proposed Algorithm	ACM +OF Initialization	ACM + naïve OF Energy Function	Challenge Validation
	Mean ± STD			
Sensitivity %	96.017 ± 2.742	90.786 ± 2.862	90.266 ± 7.264	93.947± 5.709
Specificity %	99.407 ± 0.188	99.374 ± 0.178	99.42 ± 0.154	99.262± 0.11
Accuracy %	99.417 ± 0.157	99.404 ± 0.169	99.455 ± 0.127	99.094± 0.084
PPV %	83.499± 5.058	72.168± 6.585	73.172± 7.012	67.466± 7.913
NPV %	99.914± 0.038	99.935± 0.031	99.94± 0.047	99.815± 0.058
Dice index	0.858 ± 0.033	0.807 ± 0.049	0.75 ± 0.072	0.757 ± 0.062
Jaccard index	0.752 ± 0.045	0.681 ± 0.065	0.702 ± 0.083	0.624± 0.08

4 Conclusion

In this work, a method for segmenting the myocardium in MRI images was proposed. The method is based on a novel formulation of the OF constraint equation. First, an energy function including the OF constraints as well as shape constraints of the myocardium contour was formulated. Then, the energy function was iteratively minimized to obtain the optimum contour satisfying both constraints. The technique is applied to dataset of 20 patients provided by Cardiac Atlas Project and the comparison with manual segmentation shows high sensitivity and specificity levels.

Acknowledgments. This work was supported in part by a research grant from the Science and Technology Development Fund, Ministry of Scientific Research, Egypt. This work used data and infrastructure made available through the Cardiac Atlas Project (www.cardiacatlas.org) [12].

References

1. Moura, C., Fellow, J.M., Wu, Y.J., Ho, C.: STACS: new active contour scheme for cardiac MR image segmentation. IEEE Trans. Med. Imag. 24, 593–603 (2005)
2. Alattar, M., Osman, N.F., Fahmy, A.S.: Myocardial Segmentation Using Constrained Multi-Seeded Region Growing. In: Campilho, A., Kamel, M. (eds.) ICIAR 2010. LNCS, vol. 6112, pp. 89–98. Springer, Heidelberg (2010)
3. Lu, Y., Connelly, K.A., Dick, A.J., Wright, G.A., Radau, P.E.: Watershed segmentation of basal left ventricle for quantitation of cine cardiac MRI function. J. Cardiovasc. Magn. Reson. 13, 4 (2011)
4. Park, J., Metaxas, D.: Deformable models with parameter functions for left ventricle 3-D Wall motion analysis and visualization. In: Computers in Cardiology, pp. 241–244. IEEE Computer Society Press, New York (1995)
5. Stalidis, G., Maglaveras, N., Efstratiadis, S.N., Dimitriadis, A.S., Pappas, C.: Model-Based Processing Scheme for Quantitative 4-D Cardiac MRI Analysis. IEEE Trans. on Inform. Tech. in Biomed. 6(1), 59–72 (2002)

6. Pednekar, A., Kurkure, U., Muthupillai, R., Flamm, S., Kakadiaris, I.A.: Automated left ventricular segmentation in cardiac MRI. IEEE Trans. on Biomed. Eng. 53(7), 1425–1428 (2006)
7. Baker, S., Matthews, I.: Lucas-Kanade 20 Years On: A Unifying Framework-Part 1. Int. J. of Computer Vision 56(3), 221–255
8. Hamarneh, G., Althoff, K., Gustavsson, T.: Snake Deformations Based on Optical Flow Forces for Contrast Agent Tracking in Echocardiography. In: Proc. of the Swedish Symp. on Image Analysis, SSAB (2000)
9. Mikic, I., Krucinski, S., Thomas, J.D.: Segmentation and Tracking in Echocardiographic Sequences: Active Contours Guided by Optical Flow Estimates. IEEE Trans. on Med. Imag. 17(2) (1998)
10. Bruhn, A., Weickert, J., Schnorr, C.: Lucas/Kanade meets Horn/Schunck: Combining local and global optical flow methods. Int. J. of Computer Vision 61(3), 211–231 (2005)
11. Kass, M., Witkin, A., Terzopoulos, D.: Snakes: Active contour models. Int. J. Computer Vision 1(4), 321–331 (1987)
12. Fonseca, C.G., Backhaus, M., Bluemke, D.A., Britten, R.D., Chung, J.D., Cowan, B.R., Dinov, I.D., Finn, J.P., Hunter, P.J., Kadish, A.H., Lee, D.C., Lima, J.A.C., Medrano-Gracia, P., Shivkumar, K., Suinesiaputra, A., Tao, W., Young, A.A.: The Cardiac Atlas Project- an Imaging Database for Computational Modeling and Statistical Atlases of the Heart. Bioinformatics (in press, 2011)

Optimization for Multi-Region Segmentation of Cardiac MRI

Johannes Ulén, Petter Strandmark, and Fredrik Kahl

Centre for Mathematical Sciences
Lund University, Sweden
{ulen,petter,fredrik}@maths.lth.se

Abstract. We introduce a new multi-region model for simultaneous segmentation of the left and right ventricles, myocardium and the left ventricular papillary muscles in MRI. The model enforces geometric constraints such as inclusion and exclusion between the regions, which makes it possible to correctly segment different regions even though the intensity distributions are identical. We efficiently optimize the model using Lagrangian duality which is faster and more memory efficient than current state of the art. As the optimization is based on global techniques, the resulting segmentations are independent of initialization. We evaluate our approach on two benchmarks with competitive results.

1 Introduction

Automatic segmentation of cardiac MR images is an acknowledged difficult task. Many successful approaches concentrate on segmenting the left ventricle (LV) as this part is the most interesting for diagnostic purposes. Still, quantifiable information about the cardiac function is gained from segmenting the right ventricle (RV) as well. In this paper, we use a joint model of the whole heart where the final result is improved compared to segmenting the parts independently.

This paper introduces a new mathematical model for cardiac MR segmentation. It is based on the following list of desiderata. Firstly, the human heart is composed of several interacting geometric parts — this fact should be reflected in the model. Secondly, the model should be complete in the sense that every voxel of the image should be modeled, both in terms of geometry/shape and appearance using statistical principles. This avoids many ad hoc procedures. Finally, it should be possible to estimate a global solution to the resulting optimization problem which is not dependent on a good initialization. There is always a compromise between the complexity of the model and the tractability of the optimization problem. For example, image-driven methods do not have a strong model and are typically designed to be efficient; however, they rely on good heuristics. The main contribution of this paper is that we advance the state of the art by showing that despite a rather sophisticated model, we can in an efficient manner compute solutions very close to the global optimum for the segmentation problem.

O. Camara et al. (Eds.): STACOM 2011, LNCS 7085, pp. 129–138, 2012.

Most segmentation approaches in medical imaging rely on local descent techniques, e.g. [11,12,14], and may get stuck in local optima. It has been shown that it is possible to apply global optimization techniques to make the segmentation more robust to poor initialization, e.g. [2,10]. We follow this trend. Our framework builds on the multi-region scheme presented in [5] where it is shown that geometric relationships, e.g. when one object is included in another, can be modeled and globally optimized via graph cuts. The key property that makes this possible is that the resulting energy minimization problem is submodular [9]. We also identify submodular relationships; however, we go beyond submodularity to enable other geometric relationships and priors to be incorporated into the model. The standard technique for solving non-submodular energies of this type is roof duality (RD) [15]. However, the method is quite memory intensive and may fail in giving a complete segmentation without time-consuming probing. Instead we develop a Lagrangian dual approach that uses half of the memory compared to RD and it always produces a segmentation. The method can easily be parallelized as described in [16]. Our algorithm is tested on two different data sets, one of which was used in the MICCAI 2009 Cardiac MR Left Ventricle Segmentation Challenge [1], on which we achieve results on par with the competing methods.

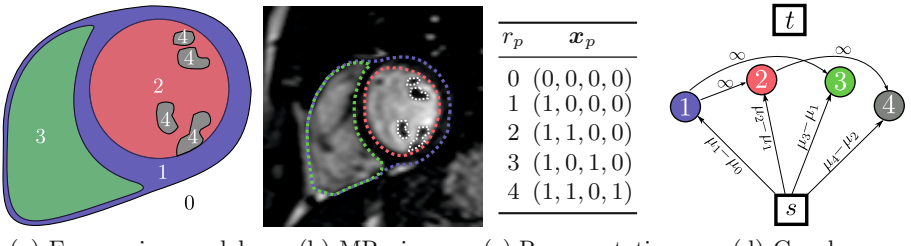

(a) Four-region model (b) MR view (c) Representation (d) Graph

Fig. 1. (a) A constructed short-axis view showing how the heart is modeled. Region 0 is the background, region 1 contains myocardium *and* the left and right ventricular cavities. Region 2 is the left ventricular cavity and region 3 the right ventricular cavity. Region 4 is the papillary muscles of the left ventricle. **(b)** An example of a slice from a short-axis image acquired with MRI where all four regions have been manually delineated. **(c)** The Boolean representation of the four regions reflect their geometric relationships as given in (a). **(d)** Graph construction for one voxel. The circled number corresponds to a vertex associated with the region number. The directed arrows are the directed edges in the graph.

2 Model

In our model, the heart below the atrioventricular plane consists of four different regions as shown in Fig. 1(a) and (b). The joint model describes both the geometry of the different regions and their appearances in the MR images.

An energy minimization approach is proposed in which a minimizer of the energy function gives the desired segmentation.

Let $\mathcal{L}$ be the set of region indices and let $\mathcal{P}$ be the set of voxel indices. Each voxel should be assigned a region index $r_p \in \mathcal{L}$. We introduce $\boldsymbol{x} \in \mathbb{B}^{|\mathcal{L}|\times|\mathcal{P}|}$, where $\mathbb{B} = \{0, 1\}$ and $\boldsymbol{x}$ is indexed as $\boldsymbol{x}_p^i$ with $i \in \mathcal{L}$ and $p \in \mathcal{P}$. Further, $\boldsymbol{x}^i$ represents all Boolean variables associated with region i and $\boldsymbol{x}_p$ represents all Boolean variables associated with voxel p. Each voxel in the image is represented by $|\mathcal{L}|$ Boolean variables, making it possible to directly encode geometric relationships between regions, like inclusion and exclusion. Fig. 1(c) shows the correspondence between r_p and $\boldsymbol{x}_p$.

The energy function to be minimized is $E(\boldsymbol{x}) = D(\boldsymbol{x}) + V(\boldsymbol{x}) + W(\boldsymbol{x})$, whose three components are, in order, the unary terms, the pairwise terms (regularization) and the geometric interaction terms. For every voxel p, the unary terms introduce a cost for each labeling of $\boldsymbol{x}_p$:

$$D(\boldsymbol{x}) = \sum_{p\in\mathcal{P}} \sum_{i\in\mathcal{L}} D_p^i\left(\boldsymbol{x}_p^i\right). \tag{1}$$

The pairwise terms use a connectivity $\mathcal{N}$ to favor smooth and correctly located boundaries:

$$V(\boldsymbol{x}) = \sum_{i\in\mathcal{L}} \sum_{p,q\in\mathcal{N}} V_{p,q}^i\left(\boldsymbol{x}_p^i, \boldsymbol{x}_q^i\right). \tag{2}$$

The geometric interaction terms associate a cost with labeling voxel p with different combinations of the two regions i and j and are used either to attract or repel different regions to each other:

$$W(\boldsymbol{x}) = \sum_{p\in\mathcal{P}} \sum_{\substack{i,j\in\mathcal{L}\\ i\neq j}} W_p^{i,j}\left(\boldsymbol{x}_p^i, \boldsymbol{x}_p^j\right). \tag{3}$$

Unary terms. The unary terms are constructed from the probability, P, of each voxel belonging to any of the four defined regions, cf. Fig. 1. We define $\mu_i(p) = -\log\left(\mathrm{P}\left(r_p = i\right)\right)$, for voxel p and region i. The probability P is estimated from training data under the assumption that the spatial location and the intensity of a voxel are independent. We split the possible locations into four categories: left ventricle, right ventricle, myocardium and background. Similarly the intensity is split into three categories: blood, muscle and background.

The spatial distribution is estimated by first resizing each heart in the training data to the same size by linear interpolation. Then a binary mask is constructed for each category and each heart. The masks are enlarged and smoothed and then they are all added together constructing the final probability mask.

The intensity distribution for each region is estimated by collecting all intensities from the examples in the training data. The histogram of intensities is then smoothed and a distribution is constructed. For both the location and intensity probability a lowest probability is set, in order to capture occurrences unseen in the training data. An example of the final μ_i's can be found in Fig. 2.

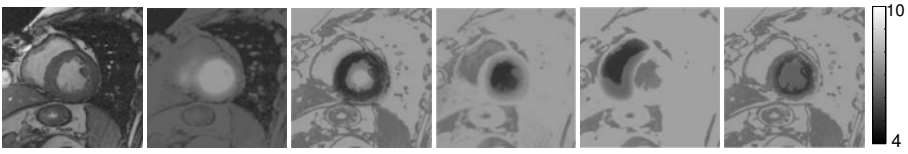

(a) Slice. (b) μ_0. (c) μ_1. (d) μ_2. (e) μ_3. (f) μ_4.

Fig. 2. Example of μ_i for the slice shown in (a). Recall that $\mu_i(p) = -\log(\mathrm{P}(r_p = i))$. A lower intensity corresponds to higher probability.

Having estimated μ_i, the unary terms $D_p^i(\boldsymbol{x}_p^i)$ need to be constructed to reflect Fig. 1(c):

$$\begin{aligned} D_p^1(1) &= \mu_1(p) - \mu_0(p), & D_p^2(1) &= \mu_2(p) - \mu_1(p), \\ D_p^3(1) &= \mu_3(p) - \mu_1(p), & D_p^4(1) &= \mu_4(p) - \mu_2(p), \end{aligned} \tag{4}$$

and $D_p^i(0) = 0$ for all i and p. For example, region 4 is according to Fig. 1(c) represented as $\boldsymbol{x}_p = (1, 1, 0, 1)$. The cost of this $\boldsymbol{x}_p$ is $(\mu_1(p) - \mu_0(p)) + (\mu_2(p) - \mu_1(p)) + (\mu_4(p) - \mu_2(p)) = \mu_4(p) - \mu_0(p)$.

Pairwise terms. The regularization weights are chosen differently for each region in a method related to the discussion in [6]. For each region i we choose the pairwise terms as:

$$V_{p,q}^i(p,q) = w_{p,q} \frac{1}{1 + \beta(\mathrm{P}(r_p = i) - \mathrm{P}(r_q = i))^2}, \tag{5}$$

where β can be used to tune the regularization. The neighborhood $\mathcal{N}$ for the regularization is chosen as 18-connectivity. The multipliers $w_{p,q}$ give different weights to different types of edges. One common choice is $w_{p,q} = 1/\operatorname{dist}(p,q)$; however, we instead use the arguably more correct way described in [3] based on solid angles. Since MRI have anisotropic resolution it is very important to take that into consideration both when calculating the distance between voxels and when using the method from [3].

Geometric interaction terms. In our model region 1 contains both region 2 and region 3. This is modeled by the use of geometric interaction terms as $W_p^{1,2}(0,1) = \infty$ and $W_p^{1,3}(0,1) = \infty$, $\forall p \in \mathcal{P}$. Furthermore, the left ventricular papillary muscle must be inside the left ventricle. This is modeled as $W_p^{2,4}(0,1) = \infty$, $\forall p \in \mathcal{P}$, see Fig. 1(d). By this construction any $\boldsymbol{x}_p$-labeling not listed in Fig. 1(c) will have ∞ cost except for $\boldsymbol{x}_p = \{1,1,1,1\}$ and $\boldsymbol{x}_p = \{1,1,1,0\}$, these two cases are handled in Section 3.

User interaction. The method needs the user to select which slices to be segmented and it also needs one click in the center of the right and left ventricle in one slice. The two center points are used to roughly align the hearts in order to get good spatial statistics. The algorithm can handle slices lacking any of the regions.

Pre-processing. Badly captured MRI are identified by looking at the distribution of the intensities. If there are multiple peaks in the histogram close to each other for the lower intensities, the image is assumed to be too bright and the intensity distribution is shifted to fit an average histogram.

Post-processing. In all ground truth data we come across, only the left ventricular epicardium is delineated. In our model we do not have this restriction — we segment the full myocardium. In order to compare our results with the ground truth we must remove all myocardium which is not part of the left ventricular epicardium. To do this, the thickness of the septum is approximated as the shortest distance between the left and right ventricles in the resulting segmentation. Then outlying myocardium is removed based on this thickness approximation, cf. Fig. 4(a).

We also assume that the left ventricle and the myocardium are convex. The resulting segmentation is taken as the convex hull in each slice.

The regularization can sometimes make the segmentation miss the most apical slice. In this case either the segmentation from the same slice at another time step or, if it is not available, the segmentation from a more basal slice is shrunk and fitted at the bottom.

3 Solving the Optimization Problem

The energy function is minimized using graph cuts by associating each binary variable with a vertex in an s-t graph. The global minimum is then found as the minimum cut of the graph. We use the maximum flow implementation [4] to compute minimum cuts.

It is well-known that an energy $E(\boldsymbol{x})$ can be minimized exactly by finding the minimum cut of a graph as long as all energy terms are submodular [9], but this is not the case for our energy. The unary and pairwise terms are of standard type and well-known to be submodular. All geometric interactions except the separation of region 2 and 3 can be represented with a submodular function. The corresponding graph construction for one voxel is shown in Fig. 1(d). As illustrated in the figure, we want region 1 to contain regions 2 and 3 and at the same time we want region 2 and 3 to be separated. Unfortunately, this last constraint leads to a frustrated cycle and cannot be modeled by a submodular energy function, see [5].

3.1 Using the Lagrangian Dual

Minimizing $E(\boldsymbol{x})$ is a difficult problem, since it contains the non-submodular separation of region 2 and 3. If we let $E'(\boldsymbol{x})$ be our energy without the separation constraint, E' will be easy to minimize. Our model has four different kinds of vertices, $(\boldsymbol{x}^1, \boldsymbol{x}^2, \boldsymbol{x}^3, \boldsymbol{x}^4) = \boldsymbol{x}$, where the superindex denotes the region label. The separation constraints dictate that $\boldsymbol{x}^2$ and $\boldsymbol{x}^3$ cannot be equal to 1 at the same time. Adding this constraint gives us the new problem

$$\begin{aligned} \min_{\boldsymbol{x}} \quad & E'(\boldsymbol{x}) \\ \text{subject to} \quad & \boldsymbol{x}^2 + \boldsymbol{x}^3 \leq 1. \end{aligned} \tag{6}$$

We note that this problem can be solved as an integer programming problem. However, this is not tractable due to the large number of variables. Instead, we look at the Lagrange dual problem:

$$\begin{aligned} \max_{\boldsymbol{\lambda}} \quad & d(\boldsymbol{\lambda}) \\ \text{subject to} \quad & \boldsymbol{\lambda} \geq 0, \end{aligned} \tag{7}$$

where $d(\boldsymbol{\lambda}) = \min_{\boldsymbol{x}} \left(E'(\boldsymbol{x}) + \boldsymbol{\lambda}^{\mathrm{T}} \left(\boldsymbol{x}^2 + \boldsymbol{x}^3 - 1\right)\right)$ is the Lagrange dual function. Let $d^\star$ denote the optimal value for (7) and $p^\star$ the optimal value for (6). By weak duality we then have that $d^\star \leq p^\star$.

The Lagrange dual function d is always concave. However, it is not differentiable in general, which precludes gradient ascent methods for its maximization. We can, however, use the projected supergradient method [13].

This looks very similar to a gradient ascent method but has some key differences. Specifically, the method is easy to implement, but in general has worse convergence properties than first-order gradient-based methods. We refer the reader to [13,16] for details.

Definition 1. *A* supergradient *to a function f at a point $\boldsymbol{x}_0$ is a vector $\boldsymbol{v}$ fulfilling $f(\boldsymbol{x}) - f(\boldsymbol{x}_0) \leq (\boldsymbol{x} - \boldsymbol{x}_0)^T \boldsymbol{v}$, for every point $\boldsymbol{x}$.*

Lemma 1 (from [16]). *Let $\boldsymbol{\lambda}$ be given and let $\boldsymbol{x}^\star$ be the optimal solution to $d(\boldsymbol{\lambda}) = \min_{\boldsymbol{x}} \left(f_1(\boldsymbol{x}) + \boldsymbol{\lambda}^T f_2(\boldsymbol{x})\right)$. Then $f_2(\boldsymbol{x}^\star)$ is a supergradient to f at $\boldsymbol{\lambda}$.*

Proof. For any $\boldsymbol{\lambda}$ it holds that

$$\begin{aligned} d(\boldsymbol{\lambda}) &\leq f_1(\boldsymbol{x}^\star) + \boldsymbol{\lambda}^T f_2(\boldsymbol{x}^\star) = f_1(\boldsymbol{x}^\star) + \boldsymbol{\lambda}_0^T f_2(\boldsymbol{x}^\star) + (\boldsymbol{\lambda} - \boldsymbol{\lambda}_0)^T f_2(\boldsymbol{x}^\star) \\ &= \min_{\boldsymbol{x}} \left(f_1(\boldsymbol{x}) + \boldsymbol{\lambda}_0^T (\boldsymbol{x}^\star)\right) + (\boldsymbol{\lambda} - \boldsymbol{\lambda}_0)^T f_2(\boldsymbol{x}^\star) = d(\boldsymbol{\lambda}_0) + (\boldsymbol{\lambda} - \boldsymbol{\lambda}_0)^T f_2(\boldsymbol{x}^\star). \end{aligned}$$

The projected supergradient method is very simple. Let $\boldsymbol{\lambda}_0$ be an initial guess of the optimal value of the concave function d. Then, in each step i a new possible solution $\boldsymbol{\lambda}_{i+1}$ is calculated as $\boldsymbol{\lambda}_{i+1} = [\boldsymbol{\lambda}_i + \tau_i \boldsymbol{v}_i]^+$, where $\boldsymbol{v}_i$ is any supergradient to d at $\boldsymbol{\lambda}_i$, τ_i is a step-length and $[\cdot]^+$ is a projection onto the feasible set $\{\boldsymbol{\lambda} \geq 0\}$.

From Lemma 1 we directly choose a supergradient for a given $\boldsymbol{\lambda}$ as $\boldsymbol{v} = \left(\boldsymbol{x}^2\right)^\star + \left(\boldsymbol{x}^3\right)^\star - \mathbf{1}$, where $\left(\boldsymbol{x}^i\right)^\star$ are the vertices belonging to label i for the optimal solution of $d(\boldsymbol{\lambda})$.

In each step, the optimal solution $\boldsymbol{x}^\star$ for a chosen $\boldsymbol{\lambda}_i$ can be calculated via a minimum graph cut. Furthermore, as the edges will be very similar in each step, the graph structure can be reused reducing the running time [8].

In the experiments the step size from [16] is used. Since supergradient methods do not guarantee improved value in each step the best solution thus far is always saved and once the *relative duality gap* $(p-d)/|p|$ is small enough the algorithm terminates. Here p and d are the currently best primal and dual energies.

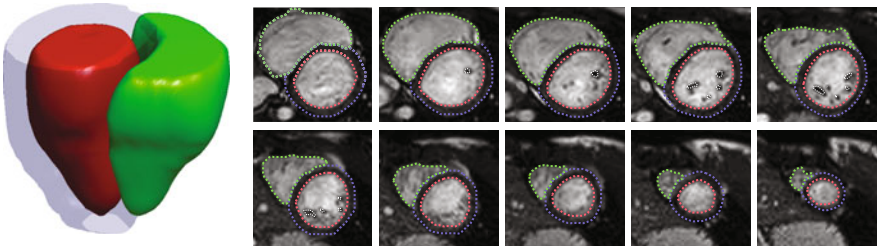

Fig. 3. Example segmentation from LUND

Table 1. Results in the Dice metric for LUND reported as mean ± one standard deviation. "ED" is end diastole and "ES" is end systole. Note that the multi-region model has a huge influence on the segmentation results.

	LV endo.	LV epi.	RV endo.
ED	$0.96_{\pm 0.02}$	$0.93_{\pm 0.03}$	$0.91_{\pm 0.07}$
ES	$0.87_{\pm 0.05}$	$0.88_{\pm 0.05}$	$0.80_{\pm 0.11}$

(a) Full multi-region model.

	LV endo.	LV epi.	RV endo.
ED	$0.62_{\pm 0.12}$	$0.90_{\pm 0.03}$	$0.57_{\pm 0.14}$
ES	$0.47_{\pm 0.25}$	$0.86_{\pm 0.04}$	$0.42_{\pm 0.14}$

(b) Each region segmented separately.

4 Experiments

The segmentation is only performed on the slices of the heart which are fully below the atrioventricular plane. The quality of the segmentation is measured by the *Dice metric*, which is given by $2\,|A \cap B| \,/\, (|A| + |B|)$, where A and B are the ground truth and the computed segmentation, respectively. The algorithm is evaluated on two data sets: LUND and SUNNYBROOK. Each data set is trained and evaluated separately.

LUND consists of cine short-axis steady state free precession MR images of 62 healthy normals captured on a Philips Interera CV 1.5T with five channel cardiac synergy coil. Each heart has the left and right ventricular endocardium and the left ventricular epicardium manually delineated by an expert. The data set is split into two equally sized parts, one used for training and one used for evaluation. Results are given in Table 1(a) and an example segmentation in Fig. 3. We also evaluate three clinical parameters. The left ventricular mass has an error of $15.6_{\pm 11.5}$ g. The left and right ventricular ejection fraction errors are $5.6_{\pm 2.9}\%$ and $7.1_{\pm 5.2}\%$, respectively.

We also compare our method to a simplified version where we run the segmentation for each region separately, see Table 1(b). Without the complete multi-region model, the localization of the ventricles becomes very difficult and the blood pools are often overestimated. Two examples where the multi-region model improves the segmentation are given in Fig. 4.

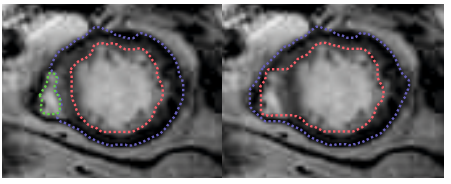

(a) (*left*) Complete model and (*right*) without modeling the right ventricle.

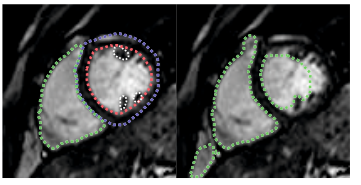

(b) (*left*) Complete model and (*right*) only the right ventricle.

Fig. 4. Examples of how modeling multiple regions improve the segmentation of the ventricular epi- and endocardium. The color scheme is the same as in Fig. **??**.

Our model was also optimized with roof duality (RD) [15]. Our method was constantly faster than RD and at the same time giving a very small relative duality gap. The small gap gives us certificates that the solutions are very close to (and in many cases exactly) the global minimum, see Table 2.

Sunnybrook consists of 30 patients with different heart diseases and is split up into two equally sized parts, one for training and one for evaluation. The data set was used in the 2009 MICCAI segmentation challenge [1]. Sunnybrook lacks ground truth for the right ventricles, so this was manually constructed by a non-expert. Therefore, this ground truth was only used for training and not for evaluation. The results given by the evaluation code used in the challenge is given in Table 3 along with results from competing methods. In the challenge, the Dice metric is calculated per slice and averaged over all slices.

Note that the small training data of Sunnybrook gives our method a disadvantage as there just 15 hearts spanning over three different diseases and one group of normals. Image-driven methods do not suffer from the small training set as they do not need to be trained.

Table 2. Running time in seconds per heart (ED and ES) and relative duality gap of our algorithm after 25 iterations run on an Intel i5 2500K CPU. For RD we canceled any computation taking longer than 12 hours.

Method	Mean
Our	$46_{\pm 27}$
RD	$6109_{\pm 12451}$

(a) Sunnybrook [1]

Method	Mean
Our	$30_{\pm 27}$
RD	$1934_{\pm 7984}$

(b) Lund

	After 25 iterations
Sunnybrook	$0.0014_{\pm 0.0033}$
Lund	$0.000055_{\pm 0.0021}$

(c) Relative duality gap

Table 3. Results for SUNNYBROOK. "?" means not reported in the corresponding paper. "†" means that the result is not directly comparable. Mass and ejection fraction is reported as difference between manual and automatic value.

Method	Dice		LV Mass (g)	LV ejection fraction (%)
	LV endo.	LV epi.		
Our	$0.86_{\pm 0.05}$	$0.92_{\pm 0.02}$	$27.1_{\pm 28.3}$	$12.5_{\pm 8.7}$
Marák et al.	$0.86_{\pm 0.04}$	$0.93_{\pm 0.01}$	$23_{\pm ?}$	$14_{\pm ?}$
Lu et al.	$0.89_{\pm 0.03}$	$0.94_{\pm 0.02}$	$21.6_{\pm 14.6}$	$8.08_{\pm 5.06}$
Wijnhout et al.	$0.89_{\pm 0.03}$	$0.93_{\pm 0.01}$	$28.7_{\pm 18.7}$	$7.02_{\pm 4.78}$
Casta et al.	?	$0.93_{\pm ?}$	†	?
O'Brien et al.	$0.81_{\pm ?}$	$0.91_{\pm ?}$	?	?
Constantinides et al.	$0.89_{\pm 0.04}$	$0.92_{\pm 0.02}$	†	†
Huang et al.	$0.89_{\pm 0.04}$	$0.94_{\pm 0.01}$	?	?
Jolly	$0.88_{\pm 0.04}$	$0.93_{\pm 0.02}$	$31.8_{\pm 17.7}$	$8.35_{\pm 5.78}$

5 Future Work and Limitations

Extending with one more region. It is possible to extend the model to also include papillary muscles in the right ventricle; we need only to introduce one more variable per voxel. If we let $\mu_5 = \mathrm{P}(r_p = 5)$ for this new region and follow the notation in Fig. 1(d) we need only to add one vertex corresponding to the new variable and two edges: one s-t edge with value $\mu_5 - \mu_3$ and one edge going from region 5 to region 3 with ∞ weight. Initial experiments gave worse results for both the right ventricle and myocardium segmentation with the added region. The new region had a tendency to overflow into the septum since this would give region 3 a rounder shape giving a lower regularization cost. We have not yet found a good way of tackling this without relying too heavily on heuristics.

Short- and long-axis images. The LUND data set was manually delineated using both short- and long-axis images. For a number of hearts the most basal slice for the short-axis images containing the left ventricular cavity also cut through to the atrium. For these slices it was hard or even impossible to even manually delineate the left ventricle solely based on information from the short-axis images. When the ground truth was produced, long-axis images were used to properly segment them. It would be desirable for our algorithm to incorporate information from long-axis images as well so we could handle these few slices as well.

Reducing memory usage. In the current implementation we use a standard max-flow implementation [4], but the structure of the graph is highly repetitive. For instance, all geometric interaction terms are equal and they need not be explicitly stored in the graph. Also, if we were to use a pairwise term based on voxel intensity we would just need to save the pairwise terms in one "layer" reducing the memory used by the pairwise terms to 1/4.

6 Concluding Discussion

We have demonstrated that it is possible to apply global optimization techniques for segmentation of cardiac MRI using a sophisticated model of the heart. The model is optimized with a new method which is both fast and memory effective. The added complexity of the model is motivated by improvements in the segmentation results.

Acknowledgments. We thank the Cardiac MR group at the University Hospital of Lund for providing us with the LUND data set and expert delineations. We used Segment [7] to read the DICOM images.

References

1. MICCAI Cardiac MR Left Ventricle Segmentation Challenge (2009), http://smial.sri.utoronto.ca/LV_Challenge/Home.html
2. Boykov, Y., Jolly, M.: Interactive Organ Segmentation Using Graph Cuts. In: Delp, S.L., DiGoia, A.M., Jaramaz, B. (eds.) MICCAI 2000. LNCS, vol. 1935, pp. 276–286. Springer, Heidelberg (2000)
3. Boykov, Y., Kolmogorov, V.: Computing geodesics and minimal surfaces via graph cuts. In: ICCV (2003)
4. Boykov, Y., Kolmogorov, V.: An experimental comparison of min-cut/max-flow algorithms for energy minimization in vision. PAMI (2004)
5. Delong, A., Boykov, Y.: Globally optimal segmentation of multi-region objects. In: ICCV (2009)
6. Grady, L., Jolly, M.: Weights and Topology: A Study of the Effects of Graph Construction on 3D Image Segmentation. In: Metaxas, D., Axel, L., Fichtinger, G., Székely, G. (eds.) MICCAI 2008, Part I. LNCS, vol. 5241, pp. 153–161. Springer, Heidelberg (2008)
7. Heiberg, E., et al.: Design and validation of Segment- freely available software for cardiovascular image analysis. BMC Medical Imaging 10(1), 1 (2010)
8. Kohli, P., Torr, P.: Dynamic graph cuts for efficient inference in markov random fields. PAMI (2007)
9. Kolmogorov, V., Zabih, R.: What energy functions can be minimized via graph cuts? PAMI (2004)
10. Lin, X., Cowan, B., Young, A.: Model-based graph cut method for segmentation of the left ventricle. In: IEEE-EMBS (2006)
11. Lorenzo-Valdés, M., et al.: Segmentation of 4D cardiac MR images using a probabilistic atlas and the EM algorithm. Medical Image Analysis 8(3), 255–265 (2004)
12. Mitchell, S., et al.: Multistage hybrid active appearance model matching: segmentation of left and right ventricles in cardiac MR images. IEEE Transactions on Medical Imaging 20(5), 415–423 (2002)
13. Nesterov, Y.: Introductory Lectures on Convex Optimization. Kluwer Academic Publishers (2004)
14. Paragios, N.: A variational approach for the segmentation of the left ventricle in cardiac image analysis. Int. Journal Computer Vision 50(3), 345–362 (2002)
15. Rother, C., Kolmogorov, V., Lempitsky, V., Szummer, M.: Optimizing binary MRFs via extended roof duality. In: CVPR (2007)
16. Strandmark, P., Kahl, F.: Parallel and Distributed Graph Cuts by Dual Decomposition. In: CVPR (2010)

Analysis of Catheter-Based Registration with Vessel-Radius Weighting of 3D CT Data to 2D X-ray for Cardiac Catheterisation Procedures in a Phantom Study

Michael Truong, Thomas Gordon, Reza Razavi, Graeme Penney, and Kawal S. Rhode

Division of Imaging Sciences and Biomedical Engineering, King's College London, UK
{michael.truong,thomas.gordon,reza.razavi,graeme.penney, kawal.rhode}@kcl.ac.uk

Abstract. X-ray fluoroscopy is routinely used to guide cardiac catheterisations due to its real-time imaging capability and high device visibility, but lacks depth information and poorly visualizes the heart itself. A novel 2D-3D image registration method was developed that can augment 2D fluoroscopy by overlaying 3D CT cardiac images that have excellent soft-tissue information. The method relies on the catheterisation of two vessels during the procedure and globally minimizing a vessel-radius-weighted distance error between the vessel centrelines, segmented from the 3D data, and corresponding catheters reconstructed from biplane X-ray fluoroscopy. Validation of the algorithm was carried out using a glass heart phantom with catheters inserted into combinations of six of its vessels. Results show that registration with the coronary sinus resulted in an average 3D-TRE between 0.55 and 9.1 mm, with the best tested pair being the coronary sinus and descending aorta. The algorithm will be useful for guiding cardiac cauterization procedures and also for co-registration of data for the purposes of biophysical cardiac modelling.

Keywords: 2D-3D image registration, cardiac imaging, image-guided catheterisation, CT, X-ray, weighted absolute orientation.

1 Introduction

X-ray fluoroscopy is routinely used to guide cardiac catheterisations procedures due to its real-time imaging capabilities, high-device visibility, low-cost and widespread availability. However this projective modality provides no depth information and suffers from poor soft-tissue contrast. In catheter-based cardiac procedures, such as percutaneous coronary intervention (PCI), cardiac resynchronisation therapy (CRT), and ablation for atrial fibrillation (AF), the cardiologist must rely on personal expertise to accurately position catheters. Using image-guided approaches, there is scope to reduce procedure time, decrease X-ray exposure, and improve success rates.

Recently, there has been much research to augment X-rayfluoroscopy by overlaying better soft-tissue-contrast 3D information of the heart using 2D-3D image registration [1-8]. A pre-calibrated hybrid X-ray/MR system [1] can achieve registration within an accuracy of 5 mm; however, these systems are not widely

O. Camara et al. (Eds.): STACOM 2011, LNCS 7085, pp. 139–148, 2012.

available outside research environments. Surrogate structures such as fiducial skin markers, visible in both X-ray and the 3D modality, provide another means of registration [2, 3]. However, accuracy may be compromised due to motion between the markers and the heart; this issue may be averted by using the heart itself for registration [4, 5], or by using catheters inserted in the vessels [6-8].

In [6, 7], registration is performed by first projecting the coronary sinus (CS) segmented from CT onto the fluoroscopy, and then matching the centreline of the projected vessel to a CS catheter in 2D. To avoid out-of-plane translation errors associated with projections, [8] performs the registration in 3D with the inclusion of a catheter reconstruction step. The method also includes the use of the descending aorta (DA) to improve accuracy using a global search strategy, but only assesses the accuracy by visual inspection. [6-8] only consider using the CS and/or DA for registration, whereas in clinical interventions, other vessels including the inferior vena cava (IVC), superior vena cava (SVC), ascending aorta (AA) and the pulmonary veins (PVs), are suitable candidates for catheterisation and hence registration.

In this manuscript, the potential use of the IVC, SVC, AA and left upper PV (LUPV), in addition to the CS and DA is explored and analysed for use with the two-catheter registration method described in [8], and the accuracy is quantified using fiducial and anatomical landmarks in a realistic heart phantom.

Furthermore, registering with large vessels such as the DA amplifies registration errors due to the assumption that the catheter lies near the medial line of the vessel, which is not likely to be true [9-11]. The work in [9] indicates that the path of a guidewire inserted into a vessel is relatively reproducible in shape and position. Therefore, registration accuracy can potentially be improved by simulating the catheter path within the vessel using techniques in [10, 11] and assuming that the catheter lies close to this path instead of the vessel's medial line. However, these methods have only been shown to apply where the catheter is well constrained in thin and tortuous vessels, which would not be the case for large vessels that are long and straight such as the DA, IVC and SVC. Therefore, the method presented in this manuscript still matches on the catheter and vessel medial line, but attempts to lessen the errors caused by the inclusion of large vessels by introducing a weight function based on the vessel radius.

2 Methods

The algorithm presented in [8] and extended in this manuscript relies on the catheterisation of two vessels during the interventional procedure and matches on a 3D set of points picked along their centreline$\boldsymbol{V}_{1,i}$ and $\boldsymbol{V}_{2,i}$ from a pre-procedural CT scan of the heart, to a set of 3D-recontructed pointsalong their corresponding catheter$\boldsymbol{C}_{1,i}$ and $\boldsymbol{C}_{2,i}$ from intra-procedural X-ray. A reconstruction step is necessary for the catheters since X-ray is a projective modality. This is done by pre-calibrating and tracking the X-ray system to determine the projection parameters of the two views P_1 and P_2 [1, 8, 12]. According to epipolar geometry, a 2D point $\boldsymbol{p}$ of a catheter in one view (fig 2c) generates an epipolar line $EPL = P_2(P_1)^{+}\boldsymbol{p}$ in the other view that contains its corresponding 2D point $\boldsymbol{q}$ (fig 2d); where P^{+} denotes the Moore-Penrose

pseudo inverse of P. The reconstructed 3D catheter point is at the intersection of the two back projections, $(P_1)^+\boldsymbol{p}$ and $(P_2)^+\boldsymbol{q}$, or at the point closest and equidistant to the back projections if they are skew lines.

Matching requires that the 3D point sets are picked along the curve at a fixed arclength interval Δ and have equal point counts: $m = \#\boldsymbol{V}_1 = \#\boldsymbol{C}_1$, $n = \#\boldsymbol{V}_2 = \#\boldsymbol{C}_2$; where $\#X$ denotes the number of points in X. These curves are then joined together,

$$\begin{matrix} \boldsymbol{V} = \boldsymbol{V}_1 \cup \boldsymbol{V}_2, & \#\boldsymbol{V} = \#\boldsymbol{V}_1 + \#\boldsymbol{V}_2 = m + n \\ \boldsymbol{C} = \boldsymbol{C}_1 \cup \boldsymbol{C}_2, & \#\boldsymbol{C} = \#\boldsymbol{C}_1 + \#\boldsymbol{C}_2 = m + n \end{matrix}. \tag{1}$$

A rigid-body transformation (RBT) T_{reg} made of rotation$R$and translation $\boldsymbol{\delta}$ such that

$$\boldsymbol{V}_i = T_{\text{reg}}\boldsymbol{C}_i + \boldsymbol{e}_i = R\boldsymbol{C}_i + \boldsymbol{\delta} + \boldsymbol{e}_i;\ \forall\, i \in [1, m+n]\,, \tag{2}$$

is found which minimises the vessel-radius-weighted residual error:

$$e = \textstyle\sum_i r_i^{-x}\|\boldsymbol{e}_i\|^2 = \sum_i r_i^{-x}\left\|T_{\text{reg}}\boldsymbol{C}_i - \boldsymbol{V}_i\right\|^2;\ x \in [0, 1, 2, \dots]\,, \tag{3}$$

wherer_i is the radius of the vessel at i, and $x$is a positive integer. By representing the transformation in this form, the problem reduces to that of weighted absolute orientation [13, 14] with no scaling. The CT data can then be registered to the X-ray by first applying the RBT, followed the X-ray view's perspective projection, i.e. PT_{reg}.

Global Search Strategy. As described in [8] and illustrated in fig 1, generally $\#\boldsymbol{V}_1 \neq \#\boldsymbol{C}_1$and $\#\boldsymbol{V}_2 \neq \#\boldsymbol{C}_2$, and the vessel centrelines may not necessarily be picked in the same direction as their catheters. These are accounted for with a global search strategy which finds the best RBT for T_{reg} from a three degree-of-freedom (DOF) search space. The first two DOFs account for the differing number of points between the first vessel and catheter, $M = |\#\boldsymbol{V}_1 - \#\boldsymbol{C}_1| + 1$, and the second, $N = |\#\boldsymbol{V}_2 - \#\boldsymbol{C}_2| + 1$, by finding the subcurves of the centrelines, $\boldsymbol{v}_{1,i}^j$, $\boldsymbol{v}_{2,i}^k$, and catheters $\boldsymbol{c}_{1,i}^j$, $\boldsymbol{c}_{2,i}^k$, of equal point counts: $m = \#\boldsymbol{v}_1^j = \#\boldsymbol{c}_1^j$, $n = \#\boldsymbol{v}_2^k = \#\boldsymbol{c}_2^k$,

$$\begin{matrix} \text{if } \#\boldsymbol{V}_1 < \#\boldsymbol{C}_1\text{:} & \boldsymbol{v}_1^j = \boldsymbol{V}_1, & \boldsymbol{c}_1^j = \boldsymbol{C}_{1,(1:m)+j-1} & m = \#\boldsymbol{V}_1 \\ \text{otherwise:} & \boldsymbol{c}_1^j = \boldsymbol{C}_1, & \boldsymbol{v}_1^j = \boldsymbol{V}_{1,(1:m)+j-1} & m = \#\boldsymbol{C}_1 \end{matrix} \Big\} \forall\, j \in [1, M]\,; \\ \begin{matrix} \text{if } \#\boldsymbol{V}_2 < \#\boldsymbol{C}_2\text{:} & \boldsymbol{v}_2^k = \boldsymbol{V}_2, & \boldsymbol{c}_2^k = \boldsymbol{C}_{2,(1:n)+k-1} & n = \#\boldsymbol{V}_2 \\ \text{otherwise:} & \boldsymbol{c}_2^k = \boldsymbol{C}_2, & \boldsymbol{v}_2^k = \boldsymbol{V}_{2,(1:n)+k-1} & n = \#\boldsymbol{C}_2 \end{matrix} \Big\} \forall\, k \in [1, N]\,. \tag{4}$$

where the superscript indexes the subcurve within the set, and a colon in the subscript denotes a range within the original curve, i.e. its subcurve (see fig 1a).The catheter and vesselsubcurves are then combined together to create a new set of $M \times N$ curves each with $m + n$points similar to eq 1. The catheters are combined as:

$$\boldsymbol{c}^{jk} = \boldsymbol{c}_1^j \cup \boldsymbol{c}_2^k, \quad \forall\, j \in [1, M],\ k \in [1, N]\,. \tag{5}$$

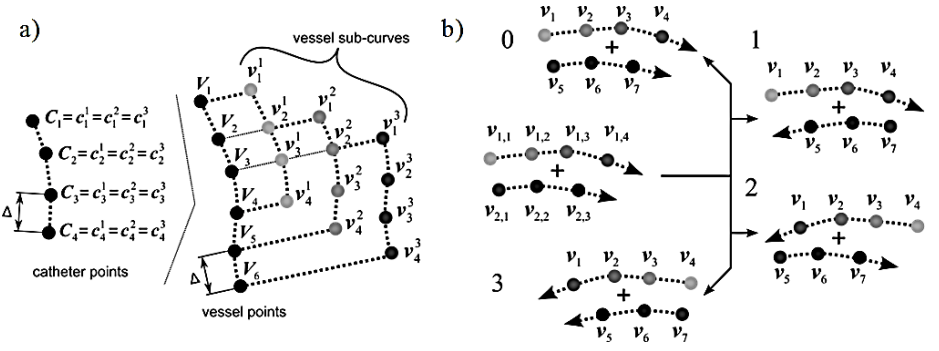

Fig. 1. a) A 4-point catheter and 6-point vessel pair generates 3 unique subcurves from the vessel, and 3 catheter subcurves that are replicas of the original. b) The four ways the vessel centrelines can combine;$Q = 0$: head-to-tail, 1: head-to-head, 2: tail-to-tail, and 3: tail-to-head.

The vessel centrelines are also combined but account for the third DOF, Q, which allows for the centrelines to be picked in any direction relative to their catheter, resulting in set of $M \times N \times 4$ vessel curves, each also of length $m + n$(fig 1b):

$$\boldsymbol{v}^{jkQ} = \begin{cases} \boldsymbol{v}_1^j \cup \boldsymbol{v}_2^k, & Q = 0 \\ \boldsymbol{v}_1^j \cup \text{reverse}(\boldsymbol{v}_2^k), & Q = 1 \\ \text{reverse}(\boldsymbol{v}_1^j) \cup \boldsymbol{v}_2^k, & Q = 2 \\ \text{reverse}(\boldsymbol{v}_1^j) \cup \text{reverse}(\boldsymbol{v}_2^k), & Q = 3 \end{cases}; \forall \begin{cases} j \in [1, M] \\ k \in [1, N] \end{cases}. \tag{6}$$

with $\text{reverse}(\boldsymbol{x})$ reversing the order of the points in the subcurve$\boldsymbol{x}$, i.e. $\boldsymbol{x}_i = \boldsymbol{x}_{\#\boldsymbol{x}-i+1}$.

Subsequently, in the global search strategy an RBT is computed for the $M \times N \times 4$ combinations of subcurves between $\boldsymbol{v}_i^{jkQ}$and $\boldsymbol{c}_i^{jk}$. The RBT that yields the lowest residual error is the one used for registration so that eqs 2 & 3 are replaced with:

$$\begin{aligned} \boldsymbol{v}_i^{jkQ} &= T^{jkQ}\boldsymbol{c}_i^{jk} + \boldsymbol{e}_i^{jk} \\ e^{jkQ} &= \textstyle\sum_i r_i^{-x} \left\| \boldsymbol{e}_i^{jk} \right\|^2; \quad \forall\, j \in [1, M], k \in [1, N], Q \in [0, 3] \\ T_{\text{reg}} &= T^{j'k'Q'} \text{where} j', k', Q' = \text{argmin}_{j,k,Q}\, e^{jkQ} \end{aligned}. \tag{7}$$

2.1 Phantom Experiment

To empirically determine suitable catheter/vessel (C/V) pairs for accurate registration, a phantom experiment was carried out with a glass model of a heart (Farlow's Scientific Glassblowing, Grass Valley, CA, US) (fig 2a). Seven multimodal fiducial markers (Multi-modality radiographic marker, IZI MedicalProducts Corp., Baltimore, MD, US) were placed on the model, followed by a 512×512×384 CT scan (fig 2b) with a 0.68×0.68×1mm^3 voxel resolution (Brilliance iCT, Philips Healthcare, The Netherlands). Catheters were then inserted into the CS, AA, DA, IVC, SVC and

LUPV which were imaged from two biplane views, LAO 30° and PA (fig 2c, d), using a tracked and pre-calibrated X-ray c-arm (AlluraXper FD10, Philips).

The vessel points corresponding to centrelines were manually identified in the CT scan of the phantom, and catheters in the glass heart were manually reconstructed in 3D from the biplane views using epipolar geometry and back projection (fig. 2c, d).Arc-length parameterised natural cubic splines were fitted through the vessel centrelines and catheters and sampled at the interval $\Delta$for use as $\boldsymbol{V}_{1,i}$, $\boldsymbol{V}_{2,i}$, $\boldsymbol{C}_{1,i}$ and $\boldsymbol{C}_{2,i}$ in eq 4 so that number of points in the curve is directly proportional to its length. The vessel's radii was measured at the proximal and distal end and linearly interpolation for use as r_i. The vessels and catheters are summarised in table 2.

To quantify the accuracy of T_{reg} (eq 7) in terms of mean 3D target registration errors (3D-TRE), the seven fiducial markers were used to obtain a gold standard RBT, T_{gs}, between the CT scan and the reconstructed X-ray space, using the method described in [13] without scaling. 17 clinically relevant anatomical landmarks $\boldsymbol{l}_i$were then selected from the CT scan and non-exclusively grouped by the chambers of the heart in which they belong (table 2) to calculate the mean 3D-TRE for the four chambers and for the whole heart:

$$\text{mean 3D-TRE} = \frac{1}{\text{n}}\sum_{i=1}^{n}\left\|T_{\text{gs}}\boldsymbol{l}_i - T_{\text{reg}}\boldsymbol{l}_i\right\| \;\forall\, \boldsymbol{l}_i \in \text{heart or chamber of interest.} \qquad (8)$$

Registration was then carried out using each of the 15 possible two-catheter configurations with the inverse-radius weighting $x = 2$ and sample intervalΔ = 1 mm. Subsequently, the five configurations with the lowest mean 3D-TRE over the whole heart were used to compare the algorithm's accuracy without weighting (x = 0) to weightings inversely proportional to the vessel's cross sectional radius (1), area (2) and volume (3), while fixing Δ =1 mm. These five configurations were also used to test the effects of changes in the sampling interval on the algorithm's accuracy and computing cost by varying Δ between 0.2 and 1.8 mm, centred around the resolution of the CT, while fixing $x = 2$.

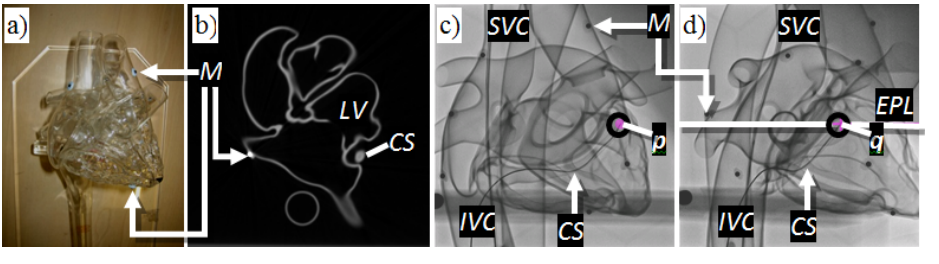

Fig. 2. a) Glass heart model with seven multimodality markers (*labelled M*).b) Four-chamber axial CT slice of the heart.c, d) X-ray LAO 30° and PA views with IVC-to-CS and IVC-to-SVC catheters inserted. A point$\boldsymbol{p}$ from one view generates an epipolar line (EPL) in the other view containing its corresponding point $\boldsymbol{q}$; their back-projections reconstruct the point in 3D.

Table 1. List of the number of points (#) that make up each catheter and vessel centreline, and vessel radii at the distal and proximal ends and mean radius r (mm) is listed. For tapering vessels, i.e. with different distal and proximal radii, the standard deviation is given in brackets.

	#(catheter)	#(vessel)	distal r	proximal r	mean r
CS	70	82	1.0	5.3	2.15 (0.85)
DA	122	183	12.8	11.0	12.7 (0.95)
AA	41	88	12.8	14.3	13.5 (0.44)
IVC	54	201	13.5	13.5	13.5
SVC	55	61	12.0	12.0	12.0
LUPV	24	36	6.0	6.0	6.0

Table 2. Clinically relevant anatomical landmarks categorized by the chambers of the heart

Left atrium (LA)	Right atrium (RA)	Left ventricle (LV)	Right ventricle (RV)
Mid-LA	Mid-RA	Mid-LV	Mid-RV
4 pulmonary veins	Tricuspid valve	Mitral valve	Tricuspid valve
Mitral valve	IVC-RA junction	Mid-aortic valve	Pulmonary valve
Atrial septum	SVC-RA junction	LV apex	Ventricular septum
	Atrial septum	Ventricular septum	

3 Results

Gold standard registration of the seven fiducial markers yielded a fiducial registration error (FRE) of 0.65 mm, which indicates a suitable gold standard since this value is within the CT resolution. With $x = 2$ and $\Delta = 1$ mm, registrations were carried out using each possible two-catheter configuration and their mean 3D-TRE over the whole heart and of each chamber is summarised in table 3. The CS/DA pair yielded the lowest TRE of 0.55 mm over the whole heart. The T_{reg} found with this pair was used to perform the 2D-3D registration of the CT heart phantom onto the X-ray PA view (fig 4a, b). 3D-3D co-registration between the reconstructed catheters and the CT heart phantom can also be visualised for purposes such as biophysical cardiac modelling (fig 4c).

Table 3. Mean 3D-TRE (mm) over four chambers of the heart and of all $\boldsymbol{l}_i$ for the C/V pairs. Lowest five mean 3D-TREs are lightly shaded while the lowest is shaded slightly darker.

vessel pair	CS /DA	CS/AA	CS/IVC	CS/SVC	CS/LUPV	DA/AA	DA/IVC	DA/SVC	DA/LUPV	AA/IVC	AA/SVC	AA/LUPV	IVC/SVC	IVC/LUPV	SVC/LUPV
LA	0.35	2.8	6.0	8.0	5.2	12	20	17	11	21	35	12	42	14	20
RA	0.55	3.9	10	14	7.7	9.6	21	20	16	21	39	18	18	22	35
LV	0.65	3.7	9.0	4.9	7.1	11	23	14	13	17	22	10	63	15	32
RV	0.66	3.9	11	7.7	7.7	8.7	23	17	17	17	30	7.9	49	20	40
all	0.55	3.6	9.1	8.7	6.9	10	22	17	14	19	32	12	43	18	32

Using the five configurations which yielded the lowest mean 3D-TRE to test the sensitivity of the algorithm to variations in x (fig 3a), four had lower TREs when using the vessel-radius-based weighting ($x = 1, 2, 3$) than when not ($x = 0$); the CS/LUPV pair being the exception. When fixing $x = 2$and varying Δbetween 0.2 and 1.8 mm in increments of 0.4 mm, the same four had a maximum percent difference in TRE of 20% or less (fig 3b) while it was 77% for the CS/LUPV configuration. The average computational time for the increasing values of Δ were 1410, 136, 69.7, 34.3 and 24.9 ms (fig 3c). Δ below 0.2 and above 1.8 mm were not considered since these are beyond the resolution of a typical clinical CT scan.

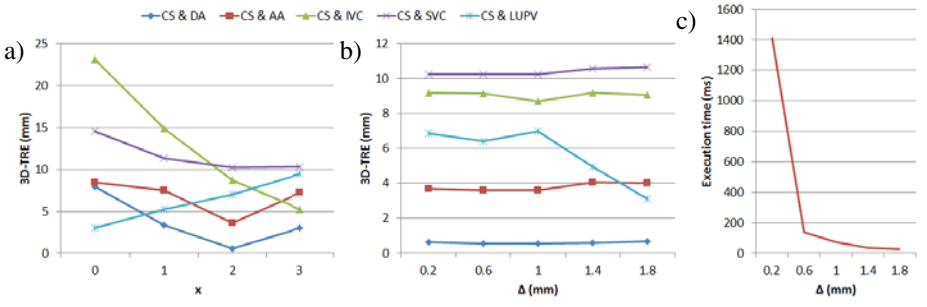

Fig. 3. Mean whole-heart 3D-TRE of best 5 configurations as a function of a) x; b) Δ. c) Computational execution time decreasing significantly with Δ.

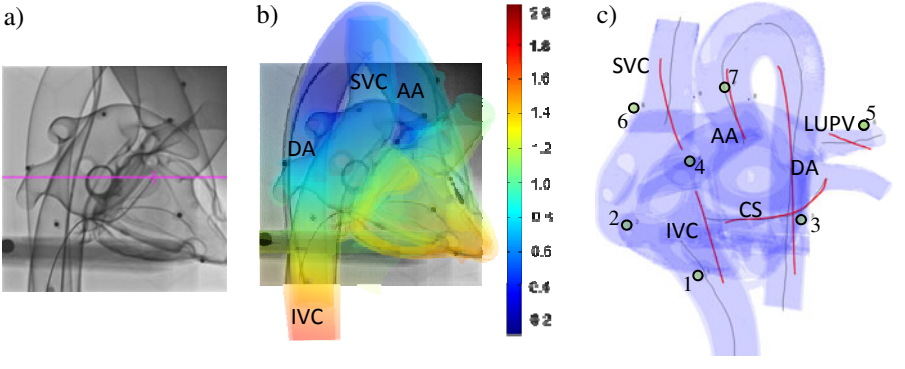

Fig. 4. a) PA X-ray view of glass heart. b)Colour map showing spatial distribution of 3D-TRE over heart phantom (mm) with great vessels (*labelled*) overlaid onto the PA X-ray view. c) 3D view of the glass heart CT scan with registered reconstructed catheters (*thick red lines, labelled*) and medial lines of the vessels(*thin black lines, labelled*) shown. The seven fiducial markers placed around the heart and used to obtain thegold standard registrationare also shown (*circled, numbered*).

4 Discussion and Conclusion

A 2D-3D registration algorithm was developed which can register between pre-procedural 3D cardiac data from CT and intra-procedural fluoroscopy images, which uses the catheters that are placed inside the vessels during the interventions. The approach uses two catheter/vesselpairs and performs registration by matching on points along the vessel centreline to points along its corresponding catheter. A three-DOF global search strategy is used to account for differences in length between the picked catheters and vessels, and in their picking directions.

A phantom experiment was carried out to test this algorithm on 15 different catheter configurations involving the CS, AA, DA, IVC, SVC and LUPV. The accuracy of the algorithm was measured in terms of a mean 3D-TRE over the whole heart against a fiducial-based gold standard with a 0.65 mm FRE. Results show that the TRE was highly dependent on which two catheter/vessel pairs were used and indicates that configurations involving the CS catheter resulted in lower TREs (between 0.55 to 9.1 mm) than those that did not (10 to 43 mm). Furthermore, when using the CS in conjunction with the AA or DA, TREs below the 5-mm clinical tolerance [1] can be achieved at 0.55 and 3.6 mm respectively. The remaining 13 configurations did not yield TREs below the 5-mm tolerance; this is possibly due to a number of reasons. Among the configurations involving combinations of the DA, AA, IVC and SVC, the vessels involved are close to geometrically parallel to each other (fig 4c). Parallel geometries may not be ideal candidates for registration since translations along the parallel vessel direction may result in competitively low residual errors, increasing the probability of a misregistration. All configurations involving the LUPV also resulted in TREs above 5-mm, possibly since the vessel was significantly shorter than the other vessels used for registration (table 1, fig 4c). This may suggest that short catheters are less ideal than long ones for registration since there are fewer points available to minimize the error in eqs 2 and 3.

The assumption that the catheter lies along the medial line of the vessel may not be accurate, especially when registering with great vessels since they provide more room for the catheter to move around (fig 4c, particularly the IVC and SVC).To minimise the loss of accuracy due to this assumption, weighting was used which was a function inversely proportional to the vessel radius. In four out of five configurations involving the CS, using the vessel-radius-weighting resulted in a more accurate registration than without (fig 3a).

Since the size of the search space decreases with increasing Δ, so should the computational cost. Results show that when varying Δ from 0.2 to 1.8 mm, there was a 56-fold decrease in computational time while the maximum difference in accuracy was within 20% for four of five configurations involving the CS (fig 3a,b).

In both sensitivity tests with varying $x$and Δ, the CS/LUPV was the one-in-five outlier. This is possibly due to the two vessels being very close to geometrically parallel while the remaining four were close to perpendicular, and that the LUPV could be too short of a vessel to provide an accurate registration.

While experiment shows that registration with a glass phantom can yield TREs within the 5-mm clinical tolerance, there are several limitations of this approach. With

clinical data, an additional gating step due to cardiac and respiratory motions is needed and will likely decrease the accuracy. The algorithm also assumes that the heart is a rigid-body when at the end-diastole and end-expiration phases. However, the heart undergoes significant motion and deformation throughout the cardiac and respiratory cycles and may not necessarily return to the same shape and size when returning to the same phase. Additionally, the insertion of a rigid catheter into soft-tissue vessel may further cause deformations [9, 10].Both of these issues are likely to add registration errors that are not present when working with a rigid glass heart. The next step in development of this algorithm is to apply it to a cohort clinical study to assess how much of the accuracy is lessened by violations of these assumptions.

In two stages of the algorithm, manual interaction is required: during the segmentation of the vessels, and the epipolar reconstruction of the catheters, prolonging the overall processing time. However, there has been recent research which show promise towards automating these steps [12, 15].It is anticipated that the proposed approach will be suitable for providing image registration for the guidance of cardiac catheterisation procedures or for the off-line fusion of cardiac image data for application in biophysical modelling research.

References

1. Rhode, K.S., Sermesant, M., Brogan, D., Hegde, S., Hipwell, J., Lambiase, P., Rosenthal, E., Bucknall, C., Qureshi, S.A., Gill, J.S., Rezavi, R., Hill, D.L.G.: A system for real-time XMR guided cardiovascular intervention. IEEE Trans. Med. Imag. 24(11), 1428–1440 (2005)
2. Gutiérrez, L.F., de Silva, R., Ozturk, C., Sonmez, M., Stine, A.M., Raval, A.N., Raman, V.K., Sachdev, V., Aviles, R.J., Waclawiw, M.A., McVeigh, E.R., Lederman, R.J.: Technology preview: X-ray fused with magnetic resonance during invasive cardiovascular procedures. Catheter. Cardiovasc. Interv. 70, 773–782 (2007)
3. Rhode, K., Ma, Y., Chandrasena, A., King, A., Gao, G., Chinchapatnam, P., Sermesant, M., Hawkes, D., Schaeffter, T., Gill, J., Razavi, R.: Evaluation of the use of multimodality skin markers for the registration of pre-procedure cardiac MR images and intra-procedure x-ray fluoroscopy images for image guided cardiac electrophysiology procedures. In: Proc. SPIE, vol. 6918 (2008)
4. Ector, J., De Buck, S., Adams, J., Dymarkowski, S., Bogaert, J., Maes, F., Heidbüchel, H.: Cardiac three-dimensional magnetic resonance imaging and fluoroscopy merging: a new approach for electroanatomic mapping to assist catheter ablation. Circulation 112(24), 3769–3776 (2005); Epub. (December 5, 2005)
5. Ector, J., De Buck, S., Huybrechts, W., Nuyens, D., Dymarkowski, S., Bogaert, J., Maes, F., Heidbüchel, H.: Biplane three-dimensional augmented fluoroscopy as single navigation tool for ablation of atrial fibrillation: accuracy and clinical value. Heart Rhythm 5 5(7), 957–964 (2008); Epub. (March 25, 2008)
6. Sra, J., Ratnakumar, S.: Cardiac image registration of the left atrium and pulmonary veins. Heart Rhythm 5(4), 609–617 (2008)
7. Sra, J., Krum, D., Belanger, B., Vaillant, R.: Registration of three-dimensional left atrial computed tomographic images with fluoroscopy. Heart Rhythm 2(9), 1020 (2005)

8. Truong, M.V.N., Aslam, A., Ginks, M., Rinaldi, C.A., Rezavi, R., Penney, G.P., Rhode, K.: 2D-3D Registration of Cardiac Images Using Catheter Constraints. Proc. Cinc., 0605 (2009)
9. Shafer, S., Hoffman, K.R., Noël, P.B., Ionita, C.N., Dmochowski, J.: Evaluation of guidewire path reproducibility. Med. Phys. 35(5), 1884–1892 (2008)
10. Luboz, V., Blazewski, R., Gould, D., Bello, F.: Real-time guide wire simulation in complex vascular models. Vis. Comput. 25, 827–834 (2009)
11. Wang, F., Durratti, L., Samur, E., Spaelter, U., Bleuler, H.: A Computer Based Real-Time Simulation of Interventional Radiology. In: Proc. IEEE-EMBS, vol. 29, pp. 1742–1745 (2007)
12. Ma, Y., King, A.P., Gogin, N., Rinaldi, C.A., Gill, J., Razavi, R., Rhode, K.S.: Real-Time Respiratory Motion Correction for Cardiac Electrophysiology Procedures Using Image-Based Coronary Sinus Catheter Tracking. In: Jiang, T., Navab, N., Pluim, J.P.W., Viergever, M.A. (eds.) MICCAI 2010, Part I. LNCS, vol. 6361, pp. 391–399. Springer, Heidelberg (2010)
13. Horn, B.K.P.: Closed-form solution of absolute orientation using unit quaternions. J. Opt. Soc. Am. A 4, 629–642 (1987)
14. Lissitz, R.W., Schönemann, P.H., Lingoes, J.C.: A solution to the weighted Procrustes problem in which the transformation is in agreement with the loss function. Psychometrika 41(4), 547–550 (1976)
15. Velut, J., Toumoulin, C., Coatrieux, J.L.: 3D coronary structure tracking algorithm with regularization and multiple hypotheses in MRI. In: Proc. ISBI, pp. 37–40 (2010)

Myocardial Contractility and Regional Work throughout the Cardiac Cycle Using FEM and MRI

Vicky Y. Wang[1], Daniel B. Ennis[2], Brett R. Cowan[3], Alistair A. Young[1,3], and Martyn P. Nash[1,4]

[1] Auckland Bioengineering Institute, University of Auckland, New Zealand
{vicky.wang,a.young,martyn.nash}@auckland.ac.nz
[2] Department of Radiological Sciences Diagnostic Cardiovascular Imaging, UCLA
daniel.ennis@ucla.edu
[3] Centre for Advanced MRI, University of Auckland, New Zealand
b.cowan@auckland.ac.nz
[4] Department of Engineering Science, University of Auckland, New Zealand

Abstract. The role of myocardial contractile force in the progression of cardiovascular diseases such as heart failure (HF) has been the focus of many studies. In order to better understand the mechanisms underlying compromised contractility, finite element (FE) modelling of ventricular mechanics is a useful tool. Distributions of active fibre stress during systole were estimated using left ventricular (LV) FE models that incorporated *in vivo* MRI tagging data and concurrent LV endocardial pressure recordings to parameterise a time-varying model of myocardial contraction. For five canine hearts, the calcium dependent contractile stress increased to peaks ranging from 33 kPa to 57 kPa during systole. Regional distributions of fibre stretch, stress, and myocardial work were examined in each case. Using this type of integrative biophysical modelling to compare normal and pathological cases will elucidate the underlying physiological mechanisms of cardiac mechanical dysfunction.

Keywords: Magnetic Resonance Imaging (MRI), Left Ventricular (LV) mechanics, Finite Element Modelling, Active Tension, Regional Work.

1 Introduction

Heart failure (HF) is associated with compromised myocardial contractility [1][2][3]. Even though HF has been the focus of a great deal of medical research, the distributions of myocardial stress, and how they change during HF, are unknown primarily because they cannot be directly measured. Over the past two decades, a variety of studies have reported estimates of myocardial contractile properties based on various data sources.

Guccione and colleagues used a cylindrical model of the LV to quantify the active fibre stress modelled by their deactivation model of cardiac contraction [4]. The maximum isometric tension from the same activation model in sheep with LV aneurysms was estimated in [5] by matching the end systolic cavity volume. A data

O. Camara et al. (Eds.): STACOM 2011, LNCS 7085, pp. 149–159, 2012.

assimilation framework based on clinical and theoretical fibre orientations was proposed by [6] to estimate ventricular myocardial contractility. This methodology used a biventricular model and combined linear elasticity theory to match the measured displacement of 18 random nodes in the model. Recent developments have seen the use of personalised electromechanics models for studying pathological conditions, assisting with treatment planning as well as predicting prognosis for treatment such as cardiac resynchronisation therapy [7][8]. For these two clinical studies, fibre orientation data on HF patients were unavailable, thus canine data were adopted. Due to the large number of parameters involved in these mechanics models and the lack of regional motion data, individualised parameter identification remains challenging [9]. In [8], this issue was addressed by simplifying the passive and active constitutive equations and identifying parameters by matching the LV pressure transient or the recorded pressure-volume loop that could be readily generated by analysing the patient's cine-MR images. A shortcoming of this work was the lack of validation of the systolic motion based on regional ventricular motion data. A study on estimating porcine ventricular tissue contractility was carried out by [10] using MRI and joint state-parameter estimation technique. Regional contractility information was obtained by matching the surface contours of the simulated ES model to the contours segmented directly from the cine MR images. This study was then extended to include displacement information provided by MRI tagging [11]. However, the kinematic data was only limited to the displacement of the tag planes, not the 3D ventricular motion.

In this study, the integrative cardiac FE modelling framework previously proposed by [12][13][14] was extended to estimate the active tension development and regional myocardial work by matching the regional systolic motion to the displacements of sets of material points derived from MRI tagging throughout the cardiac cycle for five normal canine hearts. Distributions of localised mechanical indices were examined.

2 Methods

The LV mechanics models used in this study were derived from individual *in vivo* tagged MRI [15] of five canine hearts (of same breed with similar age and weight), embedded with fibre orientations extracted from the Auckland Dog Heart model [16][17]. This was achieved using previously published techniques for developing integrative subject-specific FE models [12]. The LV mechanics models used nonlinear FE methods to solve the equations governing finite deformation hyperelasticity [18]. The stress–strain (T^{MN}–E_{MN}) relationship used to characterise the myocardial mechanical response is given in Eqs. 1 and 2 [19], and the contraction model used in this study is given in Eq. 3 [20].

$$T^{MN} = \frac{1}{2}\left(\frac{\partial W}{\partial E_{MN}} + \frac{\partial W}{\partial E_{NM}}\right) - p\frac{\partial X_M}{\partial x_k}\frac{\partial X_N}{\partial x_k} + T_a\frac{\partial X_M}{\partial x_1}\frac{\partial X_N}{\partial x_1} \tag{1}$$

where T^{MN} is the 2nd Piola-Kirchhoff stress and E_{MN} is the Green-Lagrange strain tensor. We assume that contractile tension (T_a) is only generated along the axes of the myocytes, hence ∂x_1.

$$\begin{aligned} W &= C_1 \exp(Q) \\ Q &= C_2 E_{ff}^2 + C_3(E_{cc}^2 + E_{rr}^2 + 2E_{cr}E_{rc}) + 2C_4(E_{fc}E_{cf} + E_{fr}E_{rf}) \end{aligned} \tag{2}$$

$$T_a(T_{Ca}, \lambda) = T_{Ca} \times [1 + \beta(\lambda - 1)] \tag{3}$$

where W is the strain energy density, E_{ff}, E_{cc} and E_{rr} represent the strain along the fibre, cross-fibre and radial directions, respectively, C_1-C_4 are the passive material parameters, and T_{Ca} is the time-varying isometric tension at resting sarcomere length, which is modified by a linear function of the fibre (sarcomere) extension ratio (λ) and the constant β = 1.45 [20].

Table 1. Passive myocardial constitutive parameters [21]

Passive Parameters	C_1 (kPa)	C_2	C_3	C_4
Values	2.5	8.6	3.7	25.8

The passive material parameters used for this study (Table 1) were estimated using a combined-subject approach [21] whereby a single set of parameters was tuned to match the displacement information derived from all five sets of tags from the MRI data during diastole in the five hearts. The time-varying contractile tension T_{Ca} (with homogeneous spatial distribution) was quantified using a subject-specific estimation framework that minimised the root-mean-squared-error (RMSE) between the model predicted displacements of a set of 3D material points and those extracted from the MRI tagging data during systole. This is an improvement over our previous work [14], which only considered the match between the measured and predicted LV cavity volumes in the objective function. LV cavity pressures were prescribed based on the concurrent *in vivo* recordings throughout the cardiac cycle. Regional mechanical indices including the fibre stretch, fibre stress (total Cauchy stress) and myocardial work ($Work_i$) at each of the 17 American Heart Association (AHA) regions were also evaluated (Eq. 4, see [22]):

$$Work_i \approx \sum_{t=T_1}^{T_2} \sum_{n \in N_i} \left(\left(E_{ff(n,t)} - E_{ff(n,t-1)} \right) T_{a(n,t)} \; w_{(n)} \sqrt{G_{(n,t)}^{(\xi)}} \right) \tag{4}$$

where i is the AHA region index (1-17), N_i is the set of Gauss points for AHA region i, $[T_1,T_2]$ is the range of time frames analysed (e.g. during ejection), $w_{(n)}$ is the weight at integration point n for the 3D Gaussian quadrature scheme, and $\sqrt{G_{(n,t)}^{(\xi)}}$ is the deformed 3D spatial Jacobian at Gauss point n for time frame t. Note that a

backwards finite difference approximation was used to estimate the (generally smooth) rate of change of fibre strain.

3 Results

The range of values of subject-specific $T_{Ca,max}$ (maximum contractility at ES) for all five cases (Table 2) had a mean±SD of 45 ± 10 kPa. A single value of $T_{Ca,max}$ that best matched the systolic motion of all five animals simultaneously was also determined. This combined-subjects optimal value was then used to evaluate the objective function (RMSE) for each individual animal to assess the sensitivity to this parameter. The individual errors calculated using the combined $T_{Ca,max}$ are listed in the last column of Table 2. On average, a 17% change in the value of $T_{Ca,max}$ altered the RMSE by 5%, thus the combined (generic) value of $T_{Ca,max}$ = 41 kPa fitted the deformations with little additional error in these normal dog hearts. Figure 1 illustrates the estimated T_{Ca} transients along with their recorded pressure traces during systole for all five animals. In each case, T_{Ca} increased rapidly during IVC, and continued to increase during ejection before recovering at a slower rate during IVR.

Table 2. Active myocardial constitutive parameters

Subject-Specific				
Animal	$T_{Ca,max}$ (kPa)	Beta	RMSE (mm)	RMSE (mm) *
0912	55	1.45	2.5	2.7
0917	57	1.45	3.1	3.5
0926	40	1.45	2.5	3.2
1017	33	1.45	2.2	3.1
1024	45	1.45	2.3	2.4
Combined-Subjects				
All	41	1.45	3.0	
*** RMSE evaluated using the parameters estimated using the combined approach**				

To characterise the mechanical function at regional basis, the fibre stretch ratio, total fibre stress, and the myocardial work done during the cardiac cycle (fibre stress-stretch loops) were analysed. Figure 2 illustrates the transmural variations at four locations around the equatorial LV (i.e. anterior, free-wall, posterior and septum). Figure 3 illustrates the transmural variations at four locations down the longitudinal axis of the LV free-wall.

Fibre Stretch Ratio

At the reference state, the fibre stretch ratio was initially 1 (resting length) throughout the whole LV model. During diastole, all fibres were stretched by approximately 10% with little spatial variation (Figures 2 and 3). Following diastole, the fibres continued to

stretch by a small amount during the early stage of IVC before the onset of shortening. Significant fibre shortening occurred during ejection as the blood was ejected out of the LV. There was little transmural variation in fibre stretch ratios in the anterior and free-wall regions of the equatorial LV, but moderate transmural variation was observed in the posterior and septal regions (Figure 2). The most significant transmural variation occurred towards the base and apex of the LV free-wall, whilst the transmural variation was least significant in the mid-ventricle (Figure 3).

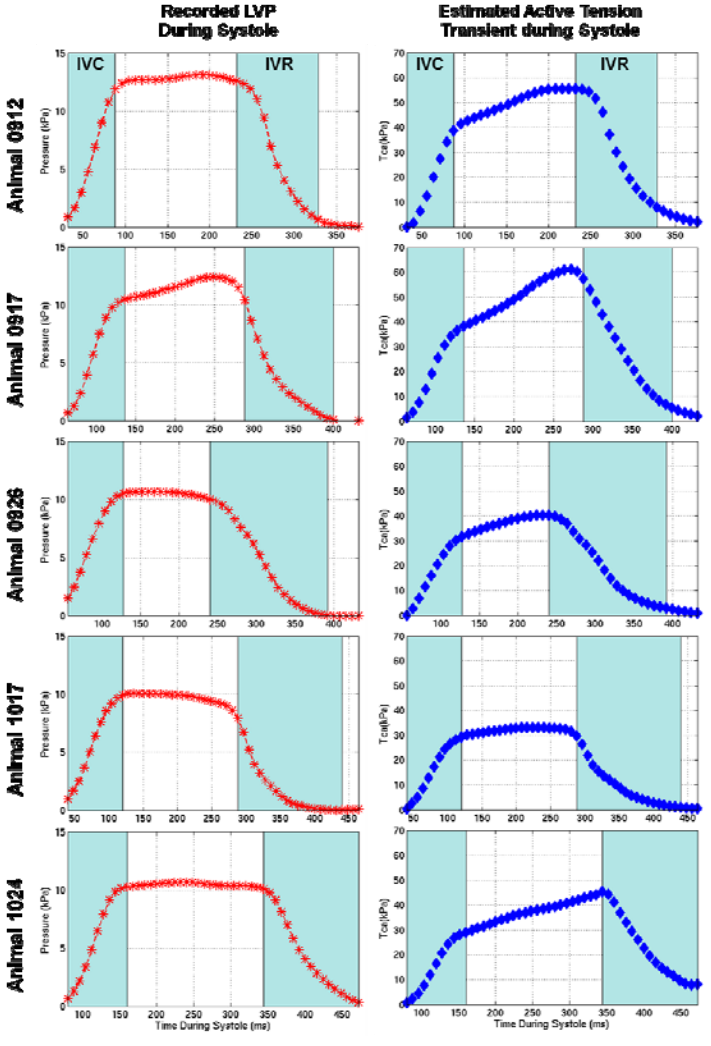

Fig. 1. (Left) Recorded LV cavity pressure traces and (right) *in vivo* T_{Ca} transients during systole for all five animals. The shaded areas indicate IVC and IVR.

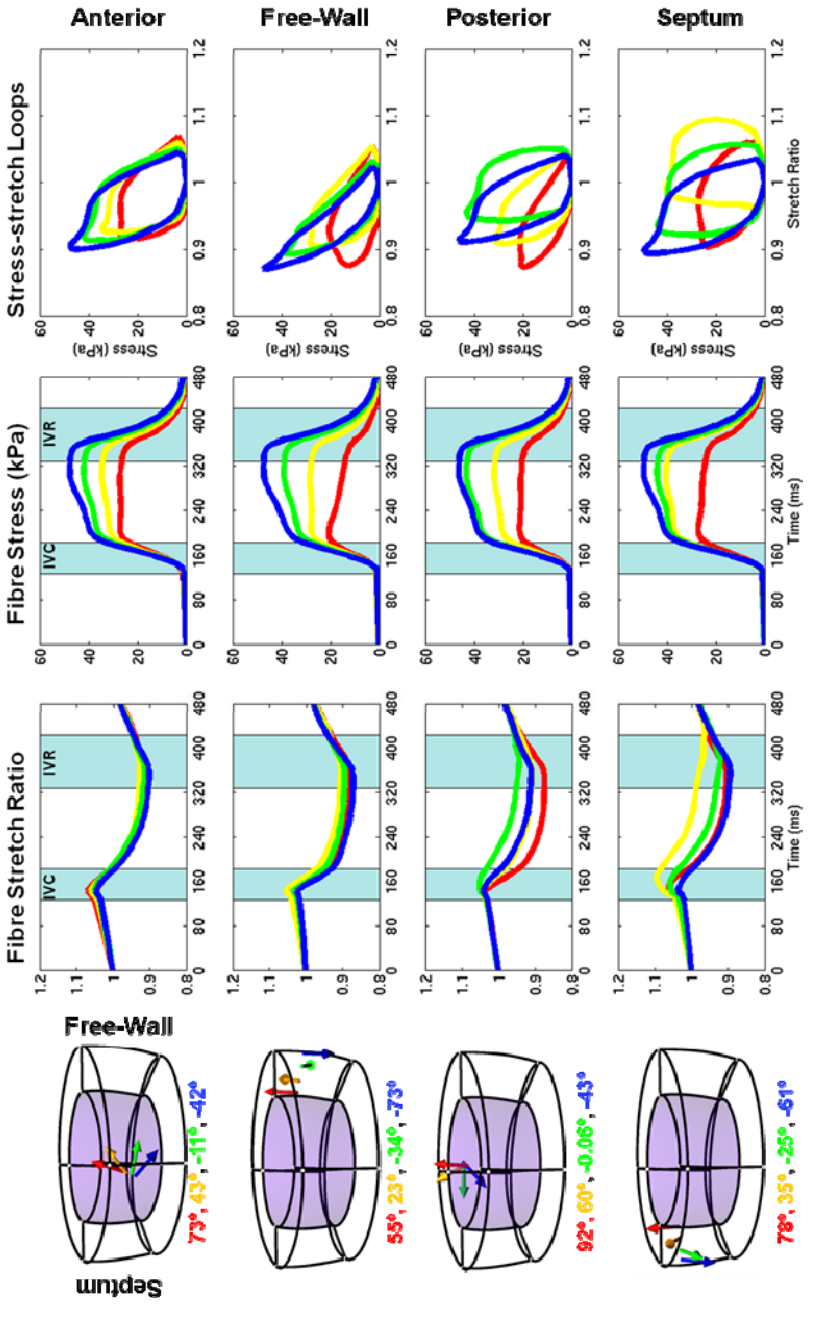

Fig. 2. Fibre stretch ratio (left), fibre stress (centre), and fibre stress-stretch loops in four equatorial regions of the LV model during the cardiac cycle of one animal (Animal 0912), with shading indicating isovolumic contraction (IVC) and isovolumic relaxation (IVR)

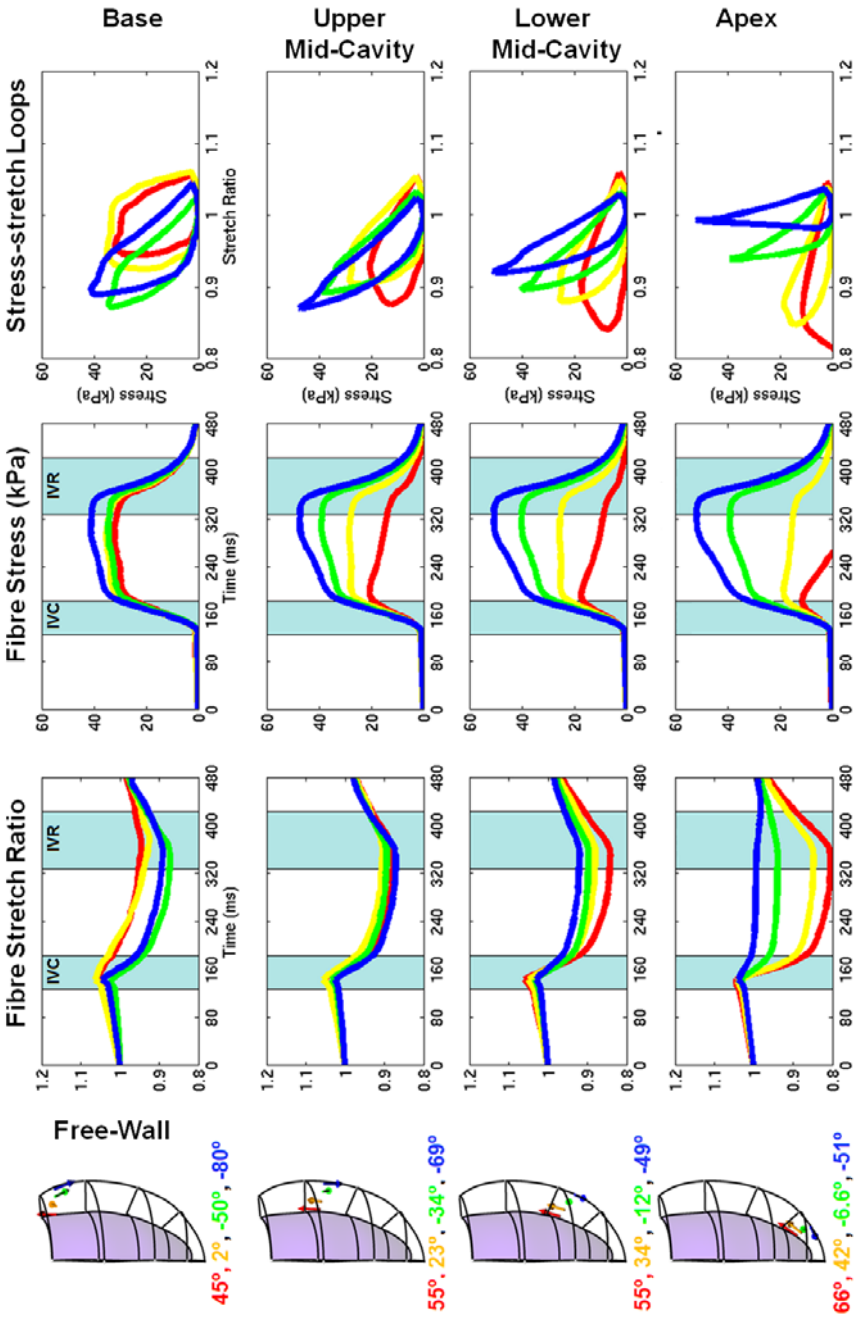

Fig. 3. Fibre stretch ratio (left), fibre stress (centre), and fibre stress-stretch loops in four longitudinal free-wall regions of the LV model during the cardiac cycle of one animal (Animal 0912), with shading indicating IVC and IVR

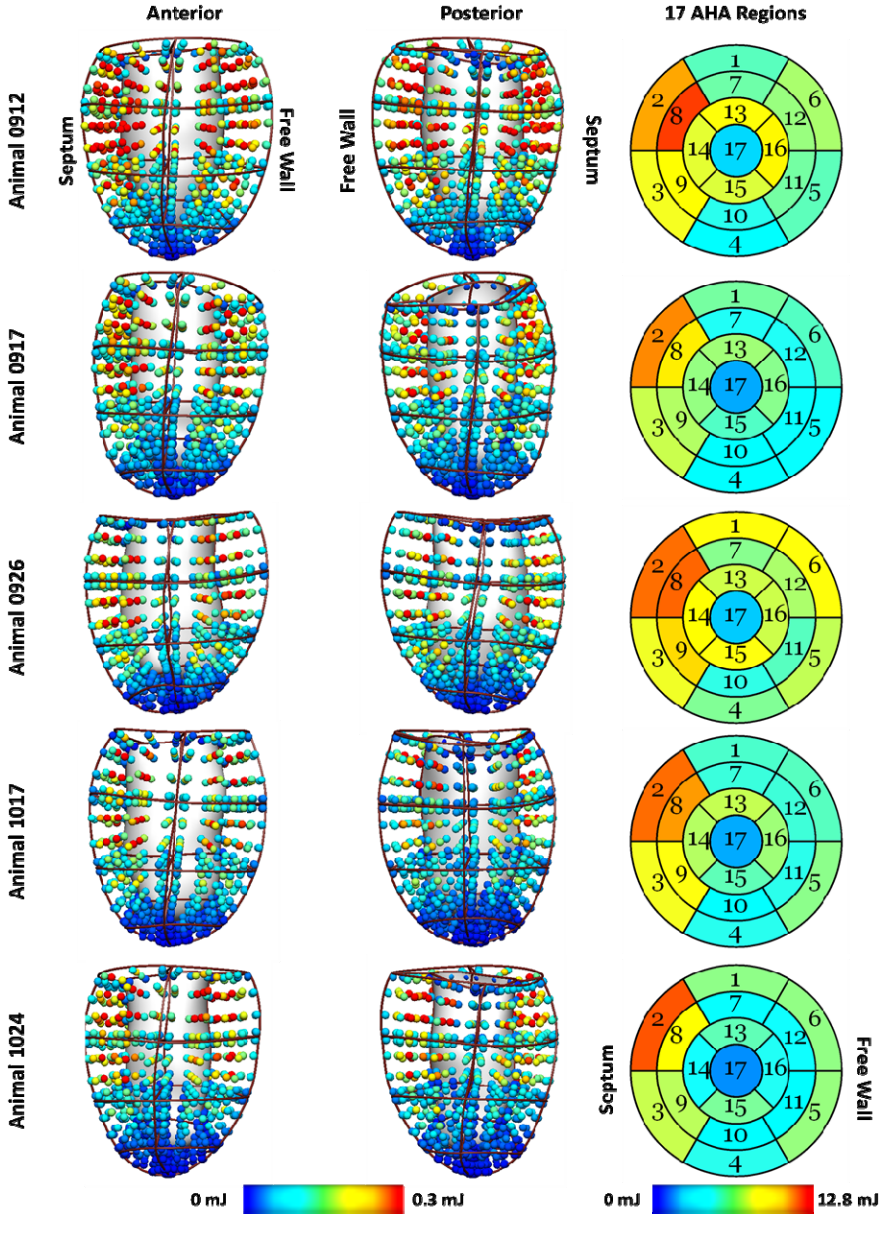

Fig. 4. Anterior (left) and posterior (middle) views of regional distributions of myocardial work evaluated at individual fibres as well as within the 17 AHA regions (right) during contraction

Fibre Stress

Total fibre stress exhibited significant transmural variation during systole with epicardial fibres (Figure 2: blue traces) developing highest stress and endocardial fibres (Figure 2: red traces) developing lowest stress. In addition, the fibres reached their peak stresses at different stages of the cardiac cycle. For example, the epicardial fibre stress was at its maximum at ES whereas the endocardial fibre stress had already achieved its peak by the end of IVC. These transmural and temporal variations were almost consistent among all five animals. On the other hand, the regional variation around the circumference of the LV wall was less distinct. Down the longitudinal-axis of the LV free wall, the endocardial fibre stress exhibited significant variation from base-to-apex, whilst the epicardial fibre stress was comparatively constant (Figure 3). Interestingly, the reversal in the transmural gradient of fibre stretch ratio from base-to-apex was not reflected in the transmural gradients of fibre stress (Figure 3).

Regional Myocardial Work

Figure 4 illustrates anterior (Figure 4: left) and posterior (Figure 4: middle) views of the regional distributions of myocardial work evaluated at individual fibres as well as within each of the 17 AHA regions (Figure 4: right) for each of the five animals during ventricular contraction. In all cases, the myocardial work varied along the long-axis of the LV with the base performing more work than the apex. A transmural variation was also evident but less distinct. Homogenous distributions of myocardial work were generally observed in the lateral and apical regions in contrast to the septal regions of the LV. The peak myocardial work was consistently located at the basal- and mid-anteroseptal regions (region 2 and 8) for all five animals.

4 Discussion and Conclusions

Subject-specific FE models were used to analyse systolic mechanics and to determine the *in vivo* estimates of the time-varying active tension throughout the entire cardiac cycles based on MRI tissue tagging data from five healthy canine LVs. The individual-subject as well as the combined-subjects estimations of T_{Ca_max} at ES were in good agreement with previous studies that have investigated myocardial contractility [4][5][6]. Regional mechanical indices including the time-varying spatial distributions of fibre stretch ratio, fibre stress, and *in vivo* myocardial work were also examined. Integrative modelling of this kind could help to elucidate the underlying pathophysiological basis of ventricular mechanics during HF. To model the mechanical behaviour of failing hearts, heterogeneous distributions of the material properties and activation times will need to be considered to account for the effects of regional pathology and asynchronous contraction. Clinical quantification of these mechanical indices on a patient-specific basis may assist clinicians with the diagnosis and treatment of cardiac dysfunction.

Acknowledgments. V.Y. Wang received funding from the New Zealand Institute of Mathematics & Its Applications (NZIMA) and The University of Auckland. A.A. Young is supported by Award Number R01HL087773 from the National Heart, Lung,

And Blood Institute, USA. M.P. Nash is supported by a James Cook Fellowship administrated by the Royal Society of New Zealand on behalf of the New Zealand Government. We thank Professor McVeigh and Dr Helm from National Institutes of Health and Johns Hopkins University for providing the experimental data.

References

1. Zile, M.R., Brutsaert, D.L.: New concepts in diatsolic dysfunction and diastolic heart failure: Part I: Diagnosis, prognosis, and measurements of diastolic function. Circulation 105, 1387–1393 (2002)
2. Zile, M.R., Brutsaert, D.L.: New concepts in diastolic dysfunction and diastolic heart failure: Part II: Causal mechanisms and treatment. Circulation 105, 1503–1508 (2002)
3. Zile, M.R.: Heart failure with preserved ejection fraction: is this diastolic heart failure? Journal of the American College of Cardiology 41(9), 1519–1522 (2003)
4. Guccione, J.M., McCulloch, A.D.: Mechanics of active contraction in cardiac muscle: Part I - Constitutive relations for fiber stress that describe deactivation. Journal of Biomechanical Engineering 115(1), 72–81 (1993)
5. Walker, J.C., Ratcliffe, M.B., Zhang, P., Wallace, A.W., Edward, B.F., Hsu, W., Saloner, D., Guccione, J.M.: Magnetic resonance imaging-based finite element stress analysis after linear repair of left ventricular aneurysm. American Journal of Physiology - Heart and Circulatory Physiology 289, H692–H700 (2004)
6. Sermesant, M., Moireau, P., Camara, O., Sainte-Marie, J., Andriantsimiavona, R., Cimrman, R., Hill, D.L.G., Chapelle, D., Razavi, R.: Cardiac function estimation from MRI using a heart model and data assimilation: Advances and difficulties. Medical Image Analysis 10, 642–656 (2006)
7. Sermesant, M., Billet, F., Chabiniok, R., Mansi, T., Chinchapatnam, P., Moireau, P., Peyrat, J.-M., Rhode, K., Ginks, M., Lambiase, P., Arridge, S., Delingette, H., Sorine, M., Rinaldi, C.A., Chapelle, D., Razavi, R., Ayache, N.: Personalised Electromechanical Model of the Heart for the Prediction of the Acute Effects of Cardiac Resynchronisation Therapy. In: Ayache, N., Delingette, H., Sermesant, M. (eds.) FIMH 2009. LNCS, vol. 5528, pp. 239–248. Springer, Heidelberg (2009)
8. Niederer, S.A., Plank, G., Chinchapatnam, P., Ginks, M., Lamata, P., Rhode, K.S., Rinaldi, C.A., Razavi, R., Smith, N.P.: Length-dependent tension in the failing heart and the efficacy of cardiac resynchronization therapy. Cardiovascular Research 89(2), 336–343 (2011)
9. Fleureau, J., Garreau, M., Donal, E., Leclercq, C., Hernández, A.: A Hybrid Tissue-Level Model of the Left Ventricle: Application to the Analysis of the Regional Cardiac Function in Heart Failure. In: Ayache, N., Delingette, H., Sermesant, M. (eds.) FIMH 2009. LNCS, vol. 5528, pp. 258–267. Springer, Heidelberg (2009)
10. Chabiniok, R., Moireau, P., Lesault, P., Rahmouni, A., Deux, J., Chapelle, D.: Trials on Tissue Contractility Estimation from Cardiac Cine MRI Using a Biomechanical Heart Model. In: Metaxas, D.N., Axel, L. (eds.) FIMH 2011. LNCS, vol. 6666, pp. 304–312. Springer, Heidelberg (2011)
11. Imperiale, A., Chabiniok, R., Moireau, P., Chapelle, D.: Constitutive Parameter Estimation Methodology Using Tagged-MRI Data. In: Metaxas, D.N., Axel, L. (eds.) FIMH 2011. LNCS, vol. 6666, pp. 409–417. Springer, Heidelberg (2011)

12. Wang, V.Y., Lam, H.I., Ennis, D.B., Young, A.A., Nash, M.P.: Passive Ventricular Mechanics Modelling Using MRI of Structure and Function. In: Metaxas, D., Axel, L., Fichtinger, G., Székely, G. (eds.) MICCAI 2008, Part II. LNCS, vol. 5242, pp. 814–821. Springer, Heidelberg (2008)
13. Wang, V.Y., Lam, H.I., Ennis, D.B., Cowan, B.R., Young, A.A., Nash, M.P.: Modelling passive diastolic mechanics with quantitative MRI of cardiac structure and function. Medical Image Analysis 13(5), 773–784 (2009)
14. Wang, V.Y., Lam, H.I., Ennis, D.B., Cowan, B.R., Young, A.A., Nash, M.P.: Cardiac Active Contraction Parameters Estimated from Magnetic Resonance Imaging. In: Camara, O., Pop, M., Rhode, K., Sermesant, M., Smith, N., Young, A. (eds.) STACOM 2010. LNCS, vol. 6364, pp. 194–203. Springer, Heidelberg (2010)
15. Ennis, D.B.: Assessment of myocardial structure and function using magnetic resonance imaging. PhD thesis, John Hopkins University, USA (2004)
16. Nielsen, P.M.F., Le Grice, I.J., Smaill, B.H., Hunter, P.J.: Mathematical model of geometry and fibrous structure of the heart. American Journal of Physiology - Heart and Circulatory Physiology 260(4), H1365–H1378 (1991)
17. LeGrice, I.J., Smaill, B.H., Chai, L.Z., Edgar, S.G., Gavin, J.B., Hunter, P.J.: Laminar structure of the heart: ventricular myocyte arrangement and connective tissue architecture in the dog. American Journal of Physiology - Heart and Circulatory Physiology 269, H571–H582 (1995)
18. Nash, M.P., Hunter, P.J.: Computational mechanics of the heart. Journal of Elasticity 61, 113–141 (2000)
19. Guccione, J.M., McCulloch, A.D., Waldman, L.K.: Passive material properties of intact ventricular myocardium determined from a cylindrical model. Journal of Biomechanical Engineering 113, 43–55 (1991)
20. Hunter, P.J., McCulloch, A.D., ter Keurs, H.E.D.J.: Modelling the mechanical properties of cardiac muscle. Progress in Biophysics and Molecular Biology 69, 289–331 (1998)
21. Wang, V.Y.: Modelling In Vivo Cardiac Mechanics using MRI and FEM. PhD thesis, The University of Auckland, New Zealand (2011)
22. Niederer, S.A., Smith, N.P.: The role of the Frank-Starling law in the transduction of cellular work to whole organ pump function: a computational modeling analysis. PLoS Computational Biology 5(4), e1000371 (2009)

Variability of the Human Cardiac Laminar Structure

Hervé Lombaert[1,2], Jean-Marc Peyrat[4], Laurent Fanton[3], Farida Cheriet[2], Hervé Delingette[1], Nicholas Ayache[1], Patrick Clarysse[3], Isabelle Magnin[3], and Pierre Croisille[3]

[1] INRIA, Asclepios Team, Sophia-Antipolis, France
[2] École Polytechnique de Montréal, Canada
[3] CREATIS, Université de Lyon, France
[4] Siemens Molecular, Oxford, UK

Abstract. The cardiac fiber architecture has an important role in electrophysiology, in mechanical functions of the heart, and in remodeling processes. The variability of the fibers is the focus of various studies in different species. However, the variability of the laminar sheets is still not well known especially in humans. In this paper, we present preliminary results on a quantitative study on the variability of the human cardiac laminar structure. We show that the laminar structure has a complex variability and we show the possible presence of two populations of laminar sheets. Bimodal distributions of the intersection angle of the third eigenvector of the diffusion tensor have been observed in 10 *ex vivo* healthy human hearts. Additional hearts will complete the study and further characterize the different populations of cardiac laminar sheets.

1 Introduction

The heart is a complex muscle that is composed with myocardial fibers organized as laminar sheets [25,16]. The cardiac fiber structures have an important role in electrophysiology [14] and in mechanical functions [6] of the heart. The understanding of the cardiac fiber architecture is essential for better diagnosis and treatment of many cardiac pathologies. The fibrous nature of the heart has been known for centuries, tracing back to as early as 1694 [28], but has been limited to tedious histological studies [20]. The cardiac fiber structure can now be imaged with diffusion tensor magnetic resonance imaging (DT-MRI) [2,15], however the variability of the fiber structure in humans is still not well known (due to the very limited number and the value of post-mortem healthy human hearts) and is largely speculated from studies on other species (dogs [12,13,11,26,22,21,9], goats [8], and rats [3]). Recently, Lombaert *et al.* [17,18] constructed a statistical atlas of the human cardiac fiber architecture and assessed its variability. The fiber structure is shown to be more stable than the laminar sheet structure. They hypothesized that the higher variability of the laminar sheet could be due to the presence of two or more populations of laminar sheets [11]. Helm *et al.*

O. Camara et al. (Eds.): STACOM 2011, LNCS 7085, pp. 160–167, 2012.

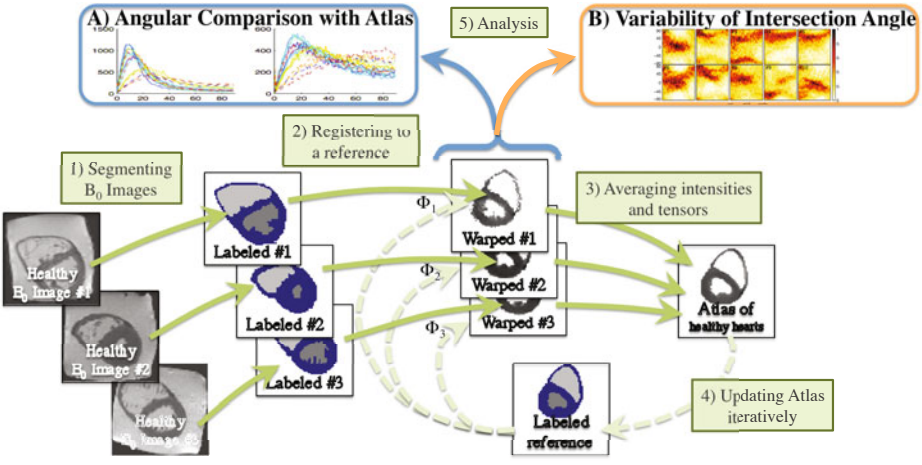

Fig. 1. *Atlas Construction*: *(1)* From the acquired images, the myocardia are segmented. *(2)* Images are then aligned and registered non-rigidly toward a reference image. *(3,4)* The atlas is constructed iteratively by averaging acquired images in the average heart shape. *Variability of the laminar sheets*: *(A)* The directions of the laminar sheet normals are compared with the atlas for each heart, and *(B)* the probability distribution of the intersection angle is analyzed.

studied the variability of the cardiac laminar sheet in [13]. Using 7 canine hearts, they observed a bimodal distribution of intersection angles (i.e., two populations of laminar sheet structure) in most myocardial segments of the left ventricle.

We present here the preliminary results of a study on the variability of the cardiac laminar sheet structure in humans. The methods used to construct and analyze the statistical atlas are briefly described. Next, the results show the angular variability, from the average healthy heart, of the the laminar sheet normal. The complexity of the laminar sheet structure is revealed thereafter by analyzing the distribution of the intersection angle of the laminar sheet normal. The distributions suggest the possible presence of two populations of laminar sheets in several myocardial segments of the left ventricle.

2 Material and Method

2.1 Dataset

The human dataset [7,23] consists of 10 healthy *ex vivo* human hearts acquired during forensic autopsies. The excised hearts were placed in a plastic container and filled with non destructive hydrophilic gel to maintain a diastolic shape. The images have been acquired on a 1.5T MR scanner (Avanto Siemens), all within 24 hours after death and prior to the examination by the pathologist, with a bipolar echo planar imaging using 4 repetitions of 12 gradient images. The diffusion-weighted images, from which are estimated the diffusion tensors, are of

size 128x128x52 with an isotropic resolution of 2 mm. All cases are from extra cardiac sudden deaths, and the hearts are classified as healthy after controlling their weight, wall thickness, and subsequent pathology examination [24].

2.2 Atlas Construction

The statistical atlas is constructed using four steps, all fully described in [17] and summarized here in Fig. 1. Information on the fiber architecture (i.e., any directional data from DT-MRI) is purposely omitted from the registration process in order to avoid introducing any bias in the study of the fiber variability.

Myocardium Segmentation — *Firstly*, the myocardium of each heart is segmented out on the B_0 image of the DT-MRI acquisition. The segmentation method is based on Graph Cuts [4].
Heart Registration — *Secondly*, each myocardium is registered to a reference image using solely the B_0 images and the myocardial masks. The pairwise registrations are performed with the symmetric Log-domain diffeomorphic demons [29,19].
Construction of Healthy Atlas — *Thirdly*, the reference image is deformed toward the morphological average of all hearts by iterating until convergence the pairwise registrations and the heart averaging steps. This atlas construction follows Guimond's *et al.* method [10].
Warping of Diffusion Tensors — *Fourthly*, and last, the resulting deformation fields computed from the registration process are used to warp all tensor fields to the morphological atlas. The diffusion tensors are reoriented using the Finite Strain strategy since it preserves the geometric features [22].

2.3 Statistical Analysis

The diffusion tensor space of symmetric positive definite matrices does not have a vector space structure with the standard Euclidean metric. The Log-Euclidean metric [1] provides a simple and fast framework where first order arithmetic on diffusion tensors has a closed form solution. The average diffusion tensor field, $\overline{\mathbf{D}}$, is computed from the N warped tensor fields $\{\mathbf{D}^{(i)}\}_{i=1\ldots N}$ (with $N = 10$ healthy hearts) using the Fréchet mean:

$$\overline{\mathbf{D}} = \exp\left(\frac{1}{N}\sum_{i=1}^{N}\log(\mathbf{D}^{(i)})\right) \tag{1}$$

The eigendecomposition of the average diffusion tensor $\overline{\mathbf{D}}$ gives the three average eigenvectors $\overline{\mathbf{v}}_{1,2,3}$. The maximal local diffusion, revealed by the primary eigenvector $\mathbf{v}_1$ occurs along the fiber while most of the remaining diffusion occurs within the laminar sheet, where the secondary eigenvector $\mathbf{v}_2$ is thought to lay [12,13,27]. The tertiary eigenvector, $\mathbf{v}_3$, corresponds to the normal of the laminar sheet.

The deviation of the cardiac laminar sheet of each heart is given with the angular difference θ from the direction of laminar sheet normal, $\mathbf{v}_3$, to the direction of the average laminar sheet normal, $\overline{\mathbf{v}}_3$. For instance, for the i^{th} heart, the angular deviation from the average heart is:

$$\theta_3^{(i)} = \arccos\left(\frac{|\mathbf{v}_3^{(i)} \cdot \overline{\mathbf{v}}_3|}{\| \mathbf{v}_3^{(i)} \| \| \overline{\mathbf{v}}_3 \|}\right) \tag{2}$$

The angles are defined between 0° and 90°. The absolute value of the dot product removes the inherent ambiguity in the orientation of the eigenvectors (i.e., $|a \cdot b| = |a \cdot (-b)|$). The variability of the laminar sheet can be measured with the probability distribution of the intersection angle of the third eigenvector (i.e., of the laminar sheet normal). The intersection angle [16] is defined as the projected angle of the laminar sheet normal (in red in the right figure) onto a transverse plane (the vertical transmural plane in green in the right figure). A prolate ellipsoidal model of the heart [20] is fitted to the morphology of the statistical atlas to ease measurements in the prolate ellipsoidal coordinates.

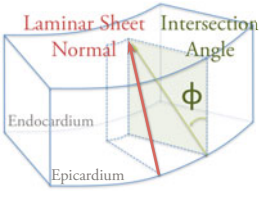

Intersection angle of the 3rd eigenvector in a myocardial section

3 Results

The cardiac laminar sheet was shown [17] to vary more than the fiber direction. In order to understand the higher variability, the distribution of the intersection angle of the laminar sheet normal is estimated in all hearts and in several myocardial segments. The distributions show the presence of possibly two populations of laminar sheets.

3.1 Variability of the Laminar Sheet Normal

The direction of the laminar sheet normal in each heart is compared with the ones of the average healthy heart (i.e., the atlas). The angular differences of the laminar sheet normals, given by Eq. 2 and shown in Fig. 3, present deviations to the average heart in several areas for each heart. The histogram of the angular differences, in Fig. 2, shows an angular peak at $\overline{\theta}_3 = 15.77°$ (the average of the histogram modes in Fig. 2).

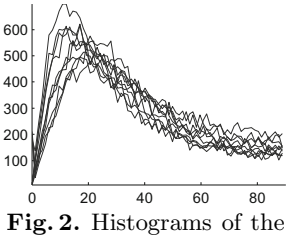

Fig. 2. Histograms of the angular deviation θ_3 (in degrees) for 10 hearts

3.2 Variability of the Intersection Angle

We now study the probability distribution of the intersection angle of the third eigenvector (i.e., the laminar sheet normal). The probability distributions are

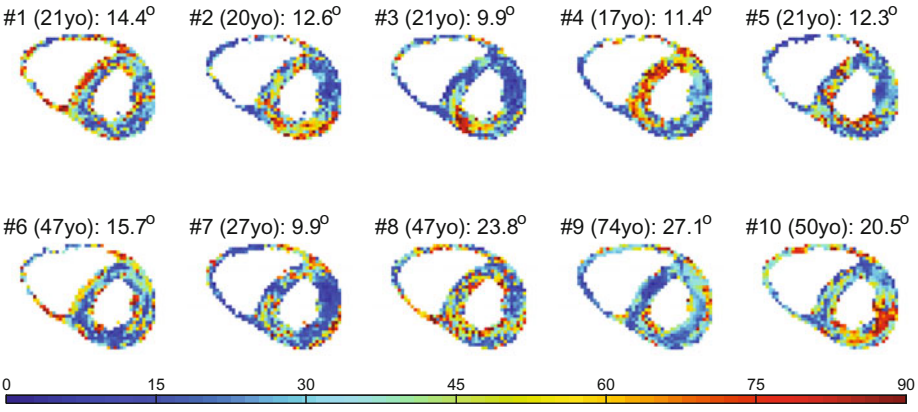

Fig. 3. Deviation, θ_3, of the laminar sheet normal of each heart to the atlas. The coloring is the angular difference in degree.

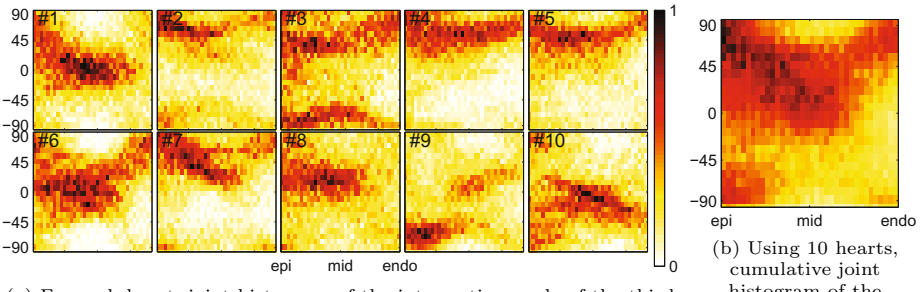

(a) For each heart, joint histogram of the intersection angle of the third eigenvector (i.e., laminar sheet variability)

(b) Using 10 hearts, cumulative joint histogram of the intersection angle.

Fig. 4. Joint histograms showing the distribution of the intersection angle from epicardium *(left side of each histogram)* to endocardium *(right side of each histogram)* for *(a)* each heart, and *(b)* all hearts combined. The x-axis is the transmural distance from epicardium. The y-axis is the distribution of the intersection angles observed at one specific transmural distance (i.e., each column is the histogram of angles for one given distance). Color is the normalized probability distribution.

presented in a joint histograms (Fig. 4) where the angle distribution, on the vertical axis, is plotted against all transmural distances, on the horizontal axis. Each heart appears to have a consistent distribution of laminar sheet normal directions with angles concentrated around a specific mean. Subject #3, #6, #9, and #10 appear to show two populations of laminar sheet normals (i.e., the angles are concentrated along two horizontal curves). The global joint histogram in Fig. 4(b) shows the probability distribution of the intersection angle (i.e., the variability of the laminar sheet normal) among all 10 hearts. Furthermore, the probability distributions in the 17 AHA segments (American Heart Association [5]) provide local statistics across the myocardium. More distinct clusters of laminar sheet structures are visible in Fig. 5, in particular AHA zones 2, 3, 4, 7, 8,

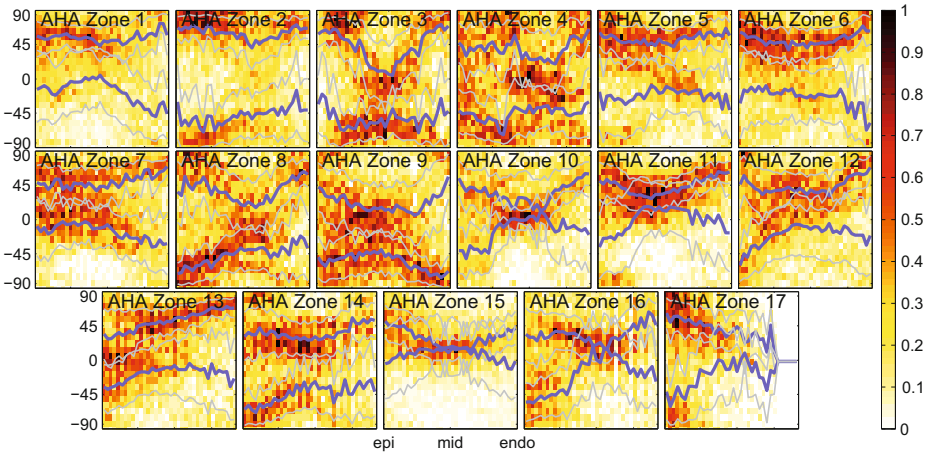

Fig. 5. Joint histograms showing of the distribution of the intersection angle in 17 AHA LV segments. Blue curves (mean angles) are found using GMM (gray lines are the one-standard-deviation envelopes). Two populations of intersection angles are visible in most segments.

9, 12, 13, and 14 show angular distributions concentrated along two horizontal curves. These curves of average angles can be estimated using Gaussian Mixture Models (i.e., for each transmural distance, the intersection angle values are clustered into two Gaussian models). This is illustrated with two blue curves in each joint histogram. Each curves indicates the estimated mean angle of one of the two Gaussian models.

4 Conclusion

In this paper, preliminary results of a study on variability of the human cardiac laminar structure have been presented. The cardiac fiber architecture has an important role in electrophysiology and in mechanical functions of the heart. The variability of the laminar sheets in humans is still not well known. It is thought that there are two populations of laminar sheets. Helm *et al.* [13] observed in 7 canine hearts a bimodal distribution of intersection angles of the third eigenvector (i.e., the laminar sheet normal). We similarly observed a bimodal distribution of intersection angles in human hearts. Our preliminary results within the dataset of 10 hearts suggest the possible presence of two populations of laminar sheets. We will include additional hearts to the study and try to further characterize the different populations of cardiac laminar sheets.

Acknowledgment. The authors wish to acknowledge helpful comments from Leon Axel and the members of the Asclepios Team. The project was supported

financially by the National Science and Engineering Research Council of Canada (NSERC), the Michael Smith Scholarship (CGS-MSFSS), and the EGIDE/INRIA Scholarship.

References

1. Arsigny, V., Fillard, P., Pennec, X., Ayache, N.: Log-Euclidean metrics for fast and simple calculus on diffusion tensors. MRM 56(2), 411–421 (2006)
2. Basser, P.J., Mattiello, J., LeBihan, D.: MR diffusion tensor spectroscopy and imaging. Biophysical Journal 66(1), 259–267 (1994)
3. Bishop, M., Hales, P., Plank, G., Gavaghan, D., Scheider, J., Grau, V.: Comparison of Rule-Based and DTMRI-Derived Fibre Architecture in a Whole Rat Ventricular Computational Model. In: Ayache, N., Delingette, H., Sermesant, M. (eds.) FIMH 2009. LNCS, vol. 5528, pp. 87–96. Springer, Heidelberg (2009)
4. Boykov, Y., Jolly, M.-P.: Interactive Organ Segmentation Using Graph Cuts. In: Delp, S.L., DiGoia, A.M., Jaramaz, B. (eds.) MICCAI 2000. LNCS, vol. 1935, pp. 276–286. Springer, Heidelberg (2000)
5. Cerqueira, M.D., Weissman, N.J., Dilsizian, V., Jacobs, A.K., Kaul, S., Laskey, W.K., Pennell, D.J., Rumberger, J.A., Ryan, T., Verani, M.S.: Standardized Myocardial Segmentation and Nomenclature for Tomographic Imaging of the Heart: A Statement for Healthcare Professionals From the Cardiac Imaging Committee of the Council on Clinical Cardiology of the American Heart Association. Circulation 105(4), 539–542 (2002)
6. Costa, K.D., Holmes, J.W., McCulloch, A.D.: Modelling cardiac mechanical properties in three dimensions. Mathematical, Physical and Engineering Sciences 359(1783), 1233–1250 (2001)
7. Frindel, C., Robini, M., Croisille, P., Zhu, Y.-M.M.: Comparison of regularization methods for human cardiac diffusion tensor MRI. Med. Im. An. 13(3) (2009)
8. Geerts, L., Bovendeerd, P., Nicolay, K., Arts, T.: Characterization of the normal cardiac myofiber field in goat measured with MR-diffusion tensor imaging. Am. J. of Physiology - Heart and Circulatory Physiology 283(1), H139–H145 (2002)
9. Gilbert, S., Benson, A., Li, P., Holden, A.: Visualisation of Dog Myocardial Structure from Diffusion Tensor Magnetic Resonance Imaging: The Paradox of Uniformity and Variability. In: Sachse, F.B., Seemann, G. (eds.) FIHM 2007. LNCS, vol. 4466, pp. 403–412. Springer, Heidelberg (2007)
10. Guimond, A., Meunier, J., Thirion, J.P.: Average Brain Models: A Convergence Study. In: CVIU, pp. 192–210 (2000)
11. Helm, P.A.: A novel technique for quantifying variability of cardiac anatomy: Application to the dyssynchronous failing heart. PhD thesis, Johns Hopkins University (2005)
12. Helm, P.A., Beg, M.F., Miller, M.I., Winslow, R.L.: Measuring and mapping cardiac fiber and laminar architecture using diffusion tensor MR imaging. Annals of the New York Academy of Sciences 1047, 296–307 (2005)
13. Helm, P.A., Tseng, H.-J.J., Younes, L., McVeigh, E.R., Winslow, R.L.: Ex vivo 3D diffusion tensor imaging and quantification of cardiac laminar structure. MRM 54(4), 850–859 (2005)
14. Hooks, D.A., Tomlinson, K.A., Marsden, S.G., LeGrice, I.J., Smaill, B.H., Pullan, A.J., Hunter, P.J.: Cardiac Microstructure: Implications for Electrical Propagation and Defibrillation in the Heart. Circ. Res. 91(4), 331–338 (2002)

15. Hsu, E.W., Henriquez, C.S.: Myocardial fiber orientation mapping using reduced encoding diffusion tensor imaging. Journal of Cardiovascular Magnetic Resonance 3(4), 339–347 (2001)
16. LeGrice, I.J., Smaill, B.H., Chai, L.Z., Edgar, S.G., Gavin, J.B., Hunter, P.J.: Laminar structure of the heart: ventricular myocyte arrangement and connective tissue architecture in the dog. Am. J. of physiology 269(2) (1995)
17. Lombaert, H., Peyrat, J.-M., Croisille, P., Rapacchi, S., Fanton, L., Clarysse, P., Delingette, H., Ayache, N.: Statistical Analysis of the Human Cardiac Fiber Architecture from DT-MRI. In: Metaxas, D.N., Axel, L. (eds.) FIMH 2011. LNCS, vol. 6666, pp. 171–179. Springer, Heidelberg (2011)
18. Lombaert, H., Peyrat, J.-M., Rapacchi, S., Fanton, L., Delingette, H., Croisille, P., Clarysse, P., Ayache, N.: In: ISMRM (2011)
19. Mansi, T., Pennec, X., Sermesant, M., Delingette, H., Ayache, N.: iLogDemons: A Demons-Based registration algorithm for tracking incompressible elastic biological tissues. IJCV, 1–20 (2010)
20. Nielsen, P.M., Le Grice, I.J., Smaill, B.H., Hunter, P.J.: Mathematical model of geometry and fibrous structure of the heart. Am. J. of Physiology, Heart Circulatory Physiology 260(4), H1365–H1378 (1991)
21. Peyrat, J.M.: Comparison of Cardiac Anatomy and Function: Statistics on Fibre Architecture from DT-MRI and Registration of 4D CT Images. PhD thesis, Nice Sophia Antipolis University (2009)
22. Peyrat, J.-M., Sermesant, M., Pennec, X., Delingette, H., Xu, C., McVeigh, E.R., Ayache, N.: A Computational Framework for the Statistical Analysis of Cardiac Diffusion Tensors: Application to a Small Database of Canine Hearts. IEEE TMI 26(11), 1500–1514 (2007)
23. Rapacchi, S., Croisille, P., Pai, V., Grenier, D., Viallon, M., Kellman, P., Mewton, N., Wen, H.: Reducing motion sensitivity in free breathing DWI of the heart with localized Principal Component Analysis. In: ISMRM (2010)
24. Silver, M., Gotlieb, A.I., Schoen, F.R.: Cardiovascular Pathology, 3rd edn. Churchill Livingstone (2001)
25. Streeter, D.D., Spotnitz, H.M., Patel, D.P., Ross, J., Sonnenblick, E.H.: Fiber Orientation in the Canine Left Ventricle during Diastole and Systole. Circ. Res. 24(3), 339–347 (1969)
26. Sundar, H., Shen, D., Biros, G., Litt, H., Davatzikos, C.: Estimating Myocardial Fiber Orientations by Template Warping. In: ISBI, pp. 73–76 (2006)
27. Tseng, W.-Y.Y., Wedeen, V.J., Reese, T.G., Smith, R.N., Halpern, E.F.: Diffusion tensor MRI of myocardial fibers and sheets: correspondence with visible cut-face texture. J. of Mag. Res. Im. 17(1), 31–42 (2003)
28. van Leeuwenhoek, A.: Correspondence with the members of the royal society in london. Letter no 82 (April 1694)
29. Vercauteren, T., Pennec, X., Perchant, A., Ayache, N.: Symmetric Log-Domain Diffeomorphic Registration: A Demons-Based Approach. In: Metaxas, D., Axel, L., Fichtinger, G., Székely, G. (eds.) MICCAI 2008, Part I. LNCS, vol. 5241, pp. 754–761. Springer, Heidelberg (2008)

Polynomial Regression Based Edge Filtering for Left Ventricle Tracking in 3D Echocardiography

Engin Dikici[1] and Fredrik Orderud[2]

[1] Norwegian University of Science and Technology, Trondheim, Norway
Engin.Dikici@ntnu.no
[2] GE Vingmed Ultrasound, Oslo, Norway
Fredrik.Orderud@ge.com

Abstract. Automated detection of endocardial borders in 3D echocardiography is a challenging task. Part of the reason for this is the endocardial boundary leads to alternating edge characteristics that vary over a cardiac cycle. The maximum gradient (MG), step criterion (STEP) and max flow/min cut (MFMC) edge detectors have been previously applied for the endocardial edge detection problem. In this paper, a local polynomial regression based method (LPR) is introduced for filtering the STEP results. For each endocardial model point, (1) the surface is parametrized locally around the point, (2) a polynomial regression is applied on the STEP edges in the parametric domain, and (3) the fitted polynomial is evaluated at the origin of the parametric domain to determine the endocardial edge position. The effectiveness of the introduced method is validated via comparative analyses among the MFMC, STEP, and first & second degree LPR methods.

1 Introduction

3D echocardiography has enabled real-time, non-invasive and low cost acquisition of volumetric images of the LV. The problem of automatic detection and tracking of heart chambers in ultrasound images has received considerable attention lately [1,2]. However, the accurate detection of the endocardial borders remains a challenging task. This is partially due to the trabeculated structure of the endocardial borders, which leads to alternating edge characteristics over a cardiac cycle. Furthermore, the real-time imaging capability of 3D ultrasound requires highly time-efficient algorithms.

One approach for the LV detection is to use a Kalman filter based tracking framework to update a deformable model based on the edge measurements. In an early work by Blake et al., Kalman filtering was used for tracking B-spline models deformed in an affine shape space [3]. In their study, object boundaries were determined by selecting the gradient maxima (MG) of image intensity profiles. Later, this framework was utilized with a principal component analysis based shape space for the LV tracking in 2D ultrasound by Jacob et al.[4,5]. This study employed a local-phase edge detector [6] for the edge measurements, and reported visually enhanced results compared to the maximum gradient method.

O. Camara et al. (Eds.): STACOM 2011, LNCS 7085, pp. 168–177, 2012.

Orderud et al. utilized an extended Kalman filter to track deformable subdivision surfaces in 3D image data sets [2]. The latter work used a step criterion (STEP) [7] for the detection of endocardial edges. More recently, Dikici et al. applied the max flow / min cut algorithm (MFMC) for the detection of endocardial edges in a Kalman tracking framework [8].

Local polynomial regression is a simple and effective method for nonparametric regression. It has been applied for many tasks including the multivariate prediction [9], image filtering [10] and image reconstruction [11]. In this paper, we introduce a novel local polynomial regression based edge filtering approach (LPR) for smoothing the STEP results in a parametric domain. First, the STEP edges are calculated at evenly distributed positions around an endocardial model. Then, the detected STEP edges are filtered by a local polynomial regression using a kernel weighting scheme. The major motivation for this work is to improve the edge detection quality offered by STEP method while still providing a real-time solution. The effectiveness of the introduced method is validated via comparative analyses among the MFMC, STEP, and first & second degree LPR methods.

2 Tracking Framework

The tracking framework is built around a deformable subdivision model parametrized by a set of control vertices with associated displacement direction vectors. Shape and pose deformations are handled by a composite transform $T = T_g(T_l(x_l),\, x_g)$, where local shape deformations $T_l(x_l)$ are obtained by moving control vertices in the subdivision model together with a global transformation $T_g(p_l, x_g)$ that translates, rotates and scales the whole model. This leads to a composite state vector x, consisting of N_g global and N_l local parameters.

A manually constructed Doo-Sabin surface is used as a template for representing the endocardial borders. The control vertices are allowed to move in the surface normal direction to alter the shape. The edge detection is conducted from a set of evenly distributed endocardial surface points.

The tracking framework consists of five separate stages, which will be described briefly in the following subsections (please refer to [2] for further details).

2.1 State Prediction

A *motion model* for predicting the state vector $\overline{x}$ at time time $k+1$ is formulated as:

$$\overline{x}_{k+1} - x_0 = A_1(\hat{x}_k - x_0) + A_2(\hat{x}_{k-1} - x_0), \tag{1}$$

where $\hat{x}_k$ is the estimated state from time-step k, and x_0 is the initial state. Temporal properties like damping and regularization towards x_0 can be adjusted using coefficients in the matrices A_1 and A_2. Prediction uncertainty can similarly be changed by manipulating the process noise covariance matrix used in the associated covariance update equation.

2.2 Evaluation of Tracking Model

A set of surface points p with associated normal vectors n are calculated from the predicted state. Then, the state-space Jacobi matrices relating surface point position changes to state changes are found. The composite deformation model leads to Jacobi matrices including both the global and local derivatives:

$$J_g = \left[\frac{\partial T_g(p_l, x_g)}{\partial x_g}, \frac{\partial T_g(p_l, x_g)}{\partial p_l} J_l \right]. \tag{2}$$

2.3 Edge Measurements

The predicted model is guided towards the target object using edge measurements. Edge detection is conducted in the surface normal direction n_i from each point p_i on the predicted surface (different methods for this part are elaborated in Section-3). The end result is a *normal displacement* value v_i that gives the signed distance between the detected edge $p_{obs,i}$ and the surface point:

$$v_i = n_i^T (p_{obs,i} - p_i). \tag{3}$$

Each normal displacement measurement is coupled with a measurement noise r_i that specifies the spatial uncertainty of the detected edge. Associated measurement vectors h_i for each edge are computed by taking the normal vector projection of the state-space Jacobi matrices:

$$h_i^T = n_i^T J. \tag{4}$$

2.4 Measurement Assimilation

All measurement results are assimilated in an information space with the assumption of uncorrelated measurements. This allows for efficient weighted summation of all measurement results into information vector and matrix with dimensions invariant to the number of measurements:

$$H^T R^{-1} v = \textstyle\sum_i h_i r_i^{-1} v_i, \tag{5}$$

$$H^T R^{-1} H = \textstyle\sum_i h_i r_i^{-1} h_i^T. \tag{6}$$

2.5 Measurement Update

The measurement information is combined with the predicted state to compute an updated state estimate. By using the information filter formulation of the Kalman filter, the updated state estimate $\hat{x}$ for a time step k becomes:

$$\hat{x}_k = \bar{x}_k + \hat{P}_k H^T R^{-1} v_k, \tag{7}$$

where an updated error covariance matrix $\hat{P}_k$ can also be calculated in the information space to avoid inverting large matrices:

$$\hat{P}_k^{-1} = \bar{P}_k^{-1} + H^T R^{-1} H. \tag{8}$$

3 Edge Detection

The edge detection process is performed by first extracting N intensity profiles $(I_1, I_2 \cdots I_N)$ centered around the surface points p_i and oriented in the surface normal directions n_i. The total number of samples in each profile, M, and the distance between consecutive samples are determined empirically. $I_{i,m}$ is used for referring to the intensity value of the i^{th} intensity profile's m^{th} sample. The function L gives the index of the most probable edge in each intensity profile, and is described for the STEP and LPR methods in the following subsections.

3.1 Step Criterion Edge Detector (STEP)

STEP assumes that the intensity profile I_i forms a transition from one intensity plateau to another. It calculates the heights of the two plateaus for each index value, and selects the index with the lowest sum of squared differences between the criteria and the image data. For each profile, the edge index is determined as:

$$L_i = argmin_m \sum_{t=1}^{m} \left(\left(\frac{1}{m} \sum_{j=1}^{m} I_{i,j} \right) - I_{i,t} \right)^2 + \sum_{t=m+1}^{M} \left(\left(\frac{1}{M-m} \sum_{j=m+1}^{M} I_{i,j} \right) - I_{i,t} \right)^2 . \tag{9}$$

If the plateau heights for the determined edge index are similar $(L_i = m \; and \; \frac{1}{m}\sum_{j=1}^{m} I_{i,j} = \frac{1}{M-m}\sum_{j=m+1}^{M} I_{i,j})$, then the edge index is reset to the profile center by $L_i = \frac{M}{2}$. The measurement noise is defined inversely proportional with the height difference between the plateaus.

3.2 Local Polynomial Regression Edge Detector (LPR)

STEP method processes each intensity profile independently, which may cause discontinuous edge measurement over an endocardial model. The discontinuity problem can be resolved by filtering the measurements via local polynomial regression. For applying a local polynomial regression, (1) the local neighborhood for each intensity profile, (2) a weighting function or a *kernel,* and (3) the model degree are needed to be defined.

The distance between the intensity profiles I_i and I_j is defined as the Cartesian distance between their intensity profile centers by $\Gamma_{i,j} = |p_i - p_j|$. The local neighborhood of the i^{th} intensity profile is called K_i, and it includes I_j iff $\Gamma_{i,j} < \lambda$: *kernel radius.* For a notational simplicity, $K_{i,j}$, $K_{i,j}^{(p)}$, and $K_{i,j}^{(l)}$ are used for referring to the i^{th} neighborhood's j^{th} member $(K_{i,j})$, the member's intensity profile center $(K_{i,j}^{(p)})$, and the member's measured STEP edge position $(K_{i,j}^{(l)})$ respectively.

The local coordinate system for K_i can be defined as,

$$e_i = \begin{cases} [1,\, 0,\, 0]^T & if \; n_i \neq [1,\, 0,\, 0]^T \\ [0,\, 1,\, 0]^T & else. \end{cases} \tag{10}$$

$$\boldsymbol{V}_1 = n_i, \quad V_2 = \boldsymbol{V}_1 \times e_i, \quad \boldsymbol{V}_3 = \boldsymbol{V}_1 \times \boldsymbol{V}_2. \tag{11}$$

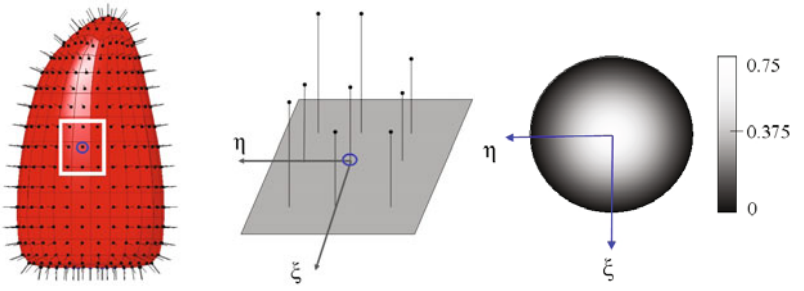

Fig. 1. (Left) An intensity profile and its local neighborhood borders are shown, (middle) the local coordinate system for the selected intensity profile is represented, (right) Epanechnikov quadratic kernel weights are shown

Each member of K_i can be parametrized using ξ and η parameters that can be found by,

$$K_{i,j}^{(\xi)} = \left(K_{i,j}^{(p)} - p_i\right) \cdot \boldsymbol{V}_2, \tag{12}$$

$$K_{i,j}^{(\eta)} = \left(K_{i,j}^{(p)} - p_i\right) \cdot \boldsymbol{V}_3, \tag{13}$$

where $K_{i,j}^{(\xi)}$ and $K_{i,j}^{(\eta)}$ refer to ξ and η parameters of the i^{th} neighborhood's j^{th} member respectively.

The STEP edges can be averaged locally for generating smoother results using $\hat{L}_i = Ave\left(K_{i,j}^{(l)} | j \in \{1, 2 \ldots |K_i|\}\right)$. However, this method might still lead to abrupt discontinuities due to constant weight function. Rather than giving all the points equal weights, we can assign weights that die off smoothly with the distance from the neighborhood center [12]. *Nadaraya–Watson* kernel-weighted average,

$$\hat{L}_i = \frac{\sum_{j=1}^{|K_i|} w_\lambda\left(p_i, K_{i,j}^{(p)}\right) K_{i,j}^{(l)}}{\sum_{j=1}^{|K_i|} w_\lambda\left(p_i, K_{i,j}^{(p)}\right)}, \tag{14}$$

with the *Epanechnikov* quadratic kernel,

$$w_\lambda(p, q) = 0.75\left(1 - \left(\frac{|p-q|}{\lambda}\right)^2\right), \tag{15}$$

can be used for this weighted filtering task *(see Figure 1)*. It can be shown that the Nadara-Watson method solves a weighted least squares problem at each intensity profile by,

$$min_{\beta_0} \sum_{j=1}^{|K_i|} w_\lambda\left(p_i, K_{i,j}^{(p)}\right)\left[K_{i,j}^{(l)} - \beta_0\right]^2, \tag{16}$$

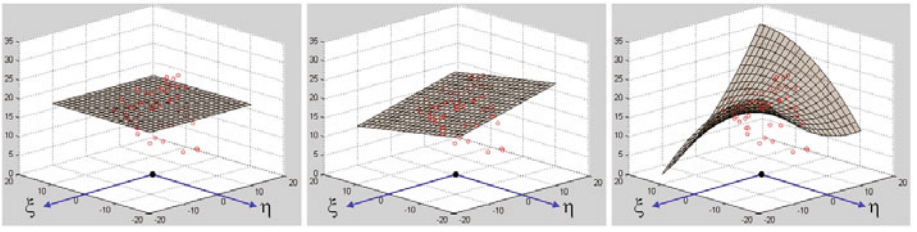

Fig. 2. (Left) 0^{th} degree, (middle) 1^{st} degree - linear, (right) 2^{nd} degree - quadratic planes are fit on the STEP results in the parametric domain

where the estimate is $\hat{L}_i = \beta_0$. Since β_0 is a 0^{th} degree polynomial, the introduced regression is a 0^{th} degree local polynomial regression. This filter might produce high estimation bias due to the fact that a local polynomial regression of degree D only has the bias terms of degree $(D+1)$ and higher (see Appendix). Therefore, a higher degree polynomial regression model should lead to a lower estimation bias, while producing higher estimation variance and computational cost. Accordingly, the model degree should be set considering this tradeoff.

D^{th} degree local polynomial regression plane defined in the parametric coordinates (ξ, η) solves,

$$min_{\beta_0 \ldots \beta_M} \sum_{j=1}^{|K_i|} w_\lambda \left(p_i, K_{i,j}^{(p)}\right) \left[K_{i,j}^{(l)} - \left(\beta_0 + \beta_1 K_{i,j}^{(\xi)} + \beta_2 K_{i,j}^{(\eta)} \ldots \beta_M \left(K_{i,j}^{(\eta)}\right)^D\right)\right]^2. \tag{17}$$

The regression plane needs to be evaluated at the parametric domain's center $(\xi = 0, \eta = 0)$ to determine the filtered edge position. This calculation can be performed using a matrix notation as $\hat{L} = b\,(0,0)\left(B^T W B\right)^{-1} B^T W y$, where

$$b\,(\xi, \eta) = \left[1, \xi, \eta, \xi^2, \eta^2, \xi\eta \ldots \eta^D\right], \tag{18}$$

$$B = \left[b\left(K_{i,1}^{(\xi)}, K_{i,1}^{(\eta)}\right)^T, b\left(K_{i,2}^{(\xi)}, K_{i,2}^{(\eta)}\right)^T \ldots b\left(K_{i,|K_i|}^{(\xi)}, K_{i,|K_i|}^{(\eta)}\right)^T\right]^T, \tag{19}$$

$$y = \left[K_{i,1}^{(l)}, K_{i,2}^{(l)} \ldots K_{i,|K_i|}^{(l)}\right]^T, \tag{20}$$

and W is a $|K_i| \times |K_i|$ diagonal matrix with j^{th} diagonal element $w_\lambda\left(p_i, K_{i,j}^{(p)}\right)$. In Figure 2, 0^{th}, 1^{st} and 2^{nd} degree regression planes are represented for a given STEP data.

4 Results

A set of 17 apical 3D echocardiography recordings, which includes 10 normal cases and 7 cases from patients with heart diseases, was used for the evaluation.

Table 1. Mean surface error *(in mm)* for the ED and ES frames for the first 5 cardiac cycles [ED error - ES error]. The tracker converged after the first cycle; surface error measurements deviated in small amounts in the following cycles.

	Cycle-1	**Cycle-2**	**Cycle-3**	**Cycle-4**	**Cycle-5**
STEP	7.15 − 2.44	2.90 − 2.18	2.95 − 2.19	2.94 − 2.20	2.97 − 2.20
MFMC	5.27 − 2.48	2.43 − 2.46	2.43 − 2.47	2.38 − 2.46	2.42 − 2.45
LPR-1	6.87 − 2.29	2.70 − 2.16	2.61 − 2.17	2.61 − 2.16	2.60 − 2.18
LPR-2	6.86 − 2.30	2.62 − 2.08	2.56 − 2.11	2.57 − 2.07	2.58 − 2.08

The recordings were acquired using a Vivid 7 ultrasound scanner (GE Vingmed Ultrasound, Norway) and a matrix array transducer. Local polynomial regression based edge filtering method was implemented for the 1^{st} (LPR-1) and 2^{nd} degree (LPR-2) polynomials both with $1cm$ kernel radius (λ). MFMC (as introduced in [8]), STEP, LPR-1 and LPR-2 methods were each employed in connection to the existing Kalman tracking framework. 3D meshes were extracted after running the tracker through 3 cardiac cycles for a convergence (see Table 1 for the surface error convergences). The accuracy of the edge detectors were evaluated by comparing the extracted meshes against the verified reference meshes drawn by a medical expert using a semi-automatic segmentation tool (4D AutoLVQ, GE Vingmed Ultrasound, Norway).

A handcrafted Doo-Sabin endocardial model consisting of 20 control points was used as the LV model. Edge measurements were performed in 528 intensity profiles evenly distributed across the endocardial model. Each profile consisted of 30 samples, spaced 1 mm apart.

Table 2 shows Bland-Altman analyses for the LV surface, LV cavity volume, and the associated ejection fraction (EF) agreement. The color coded surface error maps of a sample case are represented in Figure 3 rows (A) and (C).

The tracking framework is implemented in C++, and processed each frame in 7.5 ms with STEP, 78 ms with MFMC, 23.7 ms with LPR-1, and 40.8 ms with LPR-2 when executed on a 2.80 GHz Intel Core 2 Duo CPU.

5 Discussion and Conclusion

We have introduced a local polynomial regression based filtering for the STEP edges. The proposed approach was implemented for the first and second degree polynomial regression models. The method description is provided in a degree-independent fashion; hence the generalization of the method for higher degrees should be an intuitive task. Increasing the degree of regression model lowers the bias component of the mean square error (MSE), while increasing the variance component. Therefore, a proper degree should be selected by considering the bias-variance tradeoff. In a future study, optimal kernel radius and the regression order can be learned from a training data statistically.

A comparative evaluation between the edge detectors showed that both LPR-1 and LPR-2 lead to improved surface and volumetric measurement accuracies over the STEP method. For the ED phase, STEP, LPR-1 and LPR-2 produced $2.94\,mm$, $2.61\,mm$ (12% improvement) and $2.57\,mm$ (13% improvement) mean surface errors. LPR-1 and LPR-2 filters also reduced the LV cavity volume error of the STEP method at the ED phase by 3.73% and 5% respectively. Comparable surface and volumetric measurement improvements were reported for the ES phase (see Table 2).

The control point resolution of the endocardial model is another smoothing factor for the Kalman tracking framework. A higher resolution endocardial model, generated by refining the original model via Doo-Sabin subdivision rules [13], can represent a wider range of deformations. Hence, the effects of edge filtering becomes visually more assessable for the refined model (see Figure 3 rows (B) and (D)). Multiresolution Doo-Sabin surface models with the measurement filtering might also be investigated in a future study.

Acknowledgment. The authors would like to thank Brage Amundsen at the Norwegian University of Science and Technology for providing the 3D echocardiography data sets.

Appendix: Local Polynomial Regression Bias

D^{th} degree local polynomial regression curve for 1D data defined at x_0 as,

$$\hat{f}(x_0) = \left[1, x_0 \dots x_0^D\right] \left(B^T W B\right)^{-1} B^T W y = \sum_{i=1}^{N} l_i(x_0)\, y_i \tag{21}$$

$$E\left[\hat{f}(x_0)\right] = f(x_0) \sum_{i=1}^{N} l_i(x_0) + f^{'}(x_0) \sum_{i=1}^{N} (x_i - x_0)\, l_i(x_0) \cdots \tag{22}$$

Table 2. Columns 1-2: Mean surface error±1.96SD for the ED and ES frames. Columns 3-4: Mean LV cavity volume error±1.96SD for the ED and ES frames. Column 5: Mean EF error±1.96SD.

	ED [mm]	ES [mm]	EDV [%]	ESV [%]	EF [%]
STEP	2.94 ± 1.56	2.20 ± 1.39	-23.01 ± 16.05	-13.03 ± 24.48	-6.05 ± 10.09
MFMC	2.38 ± 1.43	2.46 ± 1.51	-7.44 ± 24.53	12.76 ± 42.92	-8.14 ± 10.50
LPR-1	2.61 ± 1.92	2.16 ± 1.47	-19.28 ± 17.98	-10.54 ± 24.42	-4.98 ± 9.76
LPR-2	2.57 ± 1.95	2.07 ± 1.52	-18.02 ± 19.02	-9.03 ± 24.01	-5.02 ± 8.67

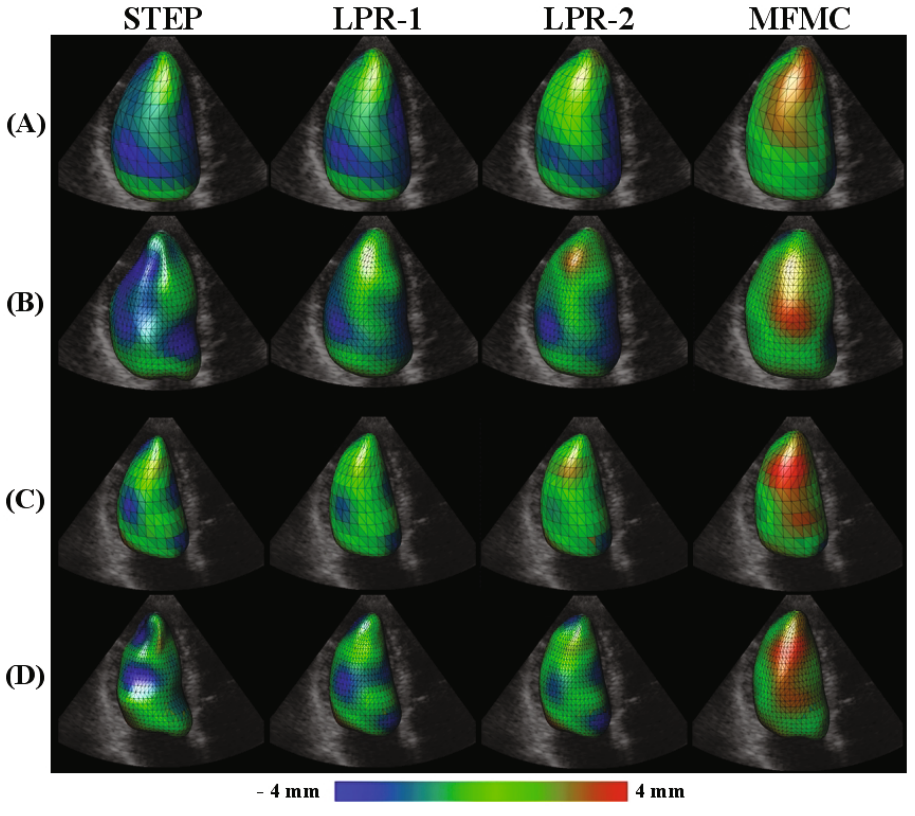

Fig. 3. For a sample case, the signed surface errors for the (A) ED phase of the original model, (B) ED phase of the refined model, (C) ES phase of the original model, and (D) ES phase of the refined model. The original and refined models consist of 20 and 84 control points respectively. *(The original model was used for the surface and volumetric analyses provided in this paper).*

Lemma 1. $\sum_{i=1}^{N} l_i(x_0) = 1$.

Proof. Assume that all $y_i = 1$. Since $l_{i\in\{1,2\ldots N\}}(x_0)$ do not depend on y_i, $\hat{f}(x_0) = \sum_{i=1}^{N} l_i(x_0)\, y_i = \sum_{i=1}^{N} l_i(x_0) = 1$.

Lemma 2. *Define* $b_j(x_0) = \sum_{i=1}^{N} (x_i - x_0)^j\, l_i(x_0)$. *Then,* $b_j(x_0) = 0$ *for all* $j \in \{1, 2 \ldots D\}$.

Proof. Assume that $y_i = (x_i - x_0)^D$. LPR solves

$$min_\beta \left(\sum_{m=0}^{D} C_m x_i^m (-x_0)^{D-m} - \sum_{m=0}^{D} \beta_m(x_0)\, x_i^m \right)^2. \tag{23}$$

where $\beta_m(x_0) = C_m(-x_0)^{D-m}$ minimizes the term. Therefore,

$$\hat{f}(x_0) = \sum_{i=1}^{N} (x_i - x_0)^j l_i(x_0) = \sum_{m=0}^{D} C_m(-x_0)^{D-m} x_0^m = (x_0 - x_0)^D = 0. \quad (24)$$

Due to Lemma-1 and Lemma-2, a local polynomial regression of degree D only has the bias terms of degree $(D+1)$ and higher.

References

1. Yang, L., Georgescu, B., Zheng, Y., Meer, P., Comaniciu, D.: 3d ultrasound tracking of the left ventricles using one-step forward prediction and data fusion of collaborative trackers. In: Proceedings of IEEE Conf. Computer Vision and Pattern Recognition (2008)
2. Orderud, F., Rabben, S.I.: Real-time 3d segmentation of the left ventricle using deformable subdivision surfaces. In: Proceedings of IEEE Conf. Computer Vision and Pattern Recognition (2008)
3. Blake, A., Isard, M.: Active Contours: The Application of Techniques from Graphics, Vision, Control Theory and Statistics to Visual Tracking of Shapes in Motion. Springer-Verlag New York, Inc., Secaucus (1998)
4. Jacob, G., Noble, J.A., Mulet-Parada, M., Blake, A.: Evaluating a robust contour tracker on echocardiographic sequences. Medical Image Analysis 3, 63–75 (1999)
5. Jacob, G., Noble, J.A., Kelion, A.D., Banning, A.P.: Quantitative regional analysis of myocardial wall motion. Ultrasound in Medicine & Biology 27, 773–784 (2001)
6. Venkatesh, S., Owens, R.A.: On the classification of image features. Pattern Recognition Letters 11, 339–349 (1990)
7. Rabben, S.I., Torp, A.H., Støylen, A., Slørdahl, S., Bjørnstad, K., Haugen, B.O., Angelsen, B.: Semiautomatic contour detection in ultrasound m-mode images. Ultrasound in Medicine & Biology 26, 287–296 (2000)
8. Dikici, E., Orderud, F.: Graph-cut based edge detection for kalman filter based left ventricle tracking in 3d+ t echocardiography. In: Proceedings of Computing in Cardiology (2010)
9. Su, L.: Prediction of multivariate chaotic time series with local polynomial fitting. Computers & Mathematics with Applications 59, 737–744 (2010)
10. Palenichka, R.M., Zinterhof, P.: Structure-adaptive filtering based on polynomial regression modeling of image intensity. Journal of Electronic Imaging 10, 521–534 (2001)
11. Takeda, H., Farsiu, S., Milanfar, P.: Kernel regression for image processing and reconstruction. IEEE Transactions on Image Processing 16, 349–366 (2007)
12. Hastie, T., Tibshirani, R., Friedman, J.: The Elements of Statistical Learning: Data Mining, Inference, and Prediction, Corrected edn. Springer, Heidelberg (2003)
13. Doo, D., Sabin, M.: Behaviour of recursive division surfaces near extraordinary points. Computer-Aided Design 10(6), 356–360 (1978)

A Multi-image Graph Cut Approach for Cardiac Image Segmentation and Uncertainty Estimation

Wenzhe Shi[1], Xiahai Zhuang[2], Robin Wolz[1], Duckett Simon[3], KaiPin Tung[1], Haiyan Wang[1], Sebastien Ourselin[2], Philip Edwards[1], Reza Razavi[3], and Daniel Rueckert[1]

[1] Biomedical Image Analysis Group, Department of Computing, Imperial College London
[2] Centre for Medical Image Computing, Department of Computing, University College London
[3] The Rayne Institute, Kings College London

Abstract. Registration and segmentation uncertainty may be important information to convey to a user when automatic image analysis is performed. Uncertainty information may be used to provide additional diagnostic information to traditional analysis of cardiac function. In this paper, we develop a framework for the automatic segmentation of the cardiac anatomy from multiple MR images. We also define the registration and segmentation uncertainty and explore its use for diagnostic purposes. Our framework uses cardiac MR image sequences that are widely available in clinical practice. We improve the performance of the cardiac segmentation algorithms by combining information from multiple MR images using a graph-cut based segmentation. We evaluate this framework on images from 32 subjects: 13 patients with ischemic cardiomyopathy, 14 patients with dilated cardiomyopathy and 5 normal volunteers. Our results indicate that the proposed method is capable of producing segmentation results with very high robustness and high accuracy with minimal user interaction across all subject groups. We also show that registration and segmentation uncertainties are good indicators for segmentation failures as well as good predictors for the functional abnormality of the subject.

1 Introduction

Magnetic Resonance (MR) imaging can be used to visualize the anatomy and function of the heart in detail. The most commonly available MR images of the heart include multiple stacks of short-axis (SA) and long-axis (LA) MR images. These images are typically acquired as cine sequences showing the heart throughout the entire cardiac cycle. Due to the anisotropic resolution of the images (high in-plane resolution but low out-of-plane resolution) and the fact that different

O. Camara et al. (Eds.): STACOM 2011, LNCS 7085, pp. 178–187, 2012.

slices of the stack are acquired during different breath-holds automated segmentation is difficult. On the other hand, 3D volumetric cardiac MR imaging is now becoming feasible [1]. These images have high spatial resolution and are free from inter-slice motion. However, the images have a lower signal-to-noise-ratio and lack of contrast compared to SA and LA MR images. Therefore, combining 3D and cine MR image data, has potential to provide better accuracy and robustness for automated segmentation.

One of the widely recognized technique for cardiac anatomy segmentation is to propagate a pre-constructed atlas to the unseen images using image registration [2,3]. By using a locally affine registration method (LARM), this technique is able to deal with large shape variations of the heart. Another alternative is voxel based segmentation [4,5] The method is able to achieve sub-voxel accuracy but requires a good initialization.

Atlas propagation is widely used either for the initialization for cardiac segmentation [2] or as the primary segmentation method [3]. An important but not yet fully explored aspect of such image segmentation is: How can we quantify and visualize the segmentation uncertainty? This question can be further divided into uncertainty arising from the registration [6,7] and uncertainty about the final segmentation. No matter how robust a segmentation technique is, it is important to have the ability to alert the user if the uncertainty of the segmentation quality is high. High uncertainty can either be a sign of an unreliable segmentation result or of an abnormal cardiac anatomy.

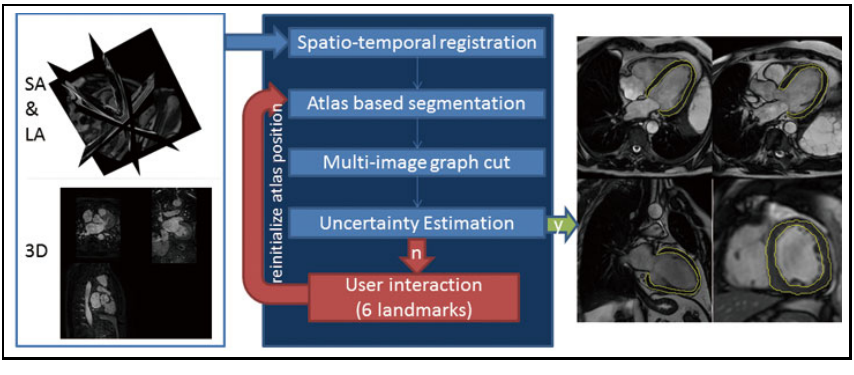

Fig. 1. Work-flow of the automatic segmentation and uncertainty estimation framework

In this paper we extend an automatic image segmentation technique [8] to a framework that simultaneously uses information from multiple (possibly sparsely sampled) cardiac images. The integration of registration- and intensity-based segmentation has shown the ability to achieve both good robustness and accuracy [8]. In the proposed framework shown in Fig.1 we automatically segment the right ventricle, left ventricle and myocardium simultaneously from high-resolution 3D MR images (3D) as well as multiple stacks of SA and LA cine MR images.

Before image segmentation we transform all images into a common spatial and temporal coordinate system and correct the misalignments between inter- and intra- sequences [9]. We first developed a registration scheme that propagates a probabilistic atlas to the subject's coordinate system and then used a multiple component EM (MCEM) estimation algorithm for an initial segmentation. The segmentation is then refined using a multi-image graph cut algorithm.

We also explore the potential of registration and segmentation uncertainty in improving the robustness: If and only if the uncertainty of the segmentation is high, the system will ask the user to input additional landmarks to help better initialize the atlas-to-subject registration. The landmarks include apex, center of mitral valve, center of left ventricle and two right ventricle insertion points. The next section describes the segmentation framework in detail; Section 3 introduces the idea of using uncertainty in the analysis. Finally, section 4 shows results from 32 patients while section 5 summarizes and concludes the paper.

2 Cardiac Segmentation Using Multiple Images

SA and LA cine MR views provide images with high spatial resolution within each slice, but the spatial resolution between slices is poor. Nevertheless, both SA and LA images have high temporal resolution revealing dynamic information about the heart. By contrast, 3D MR images acquired within a single breath-hold provide a static image of the heart with high spatial resolution in all three directions. However, these images are often noisy and provide less good contrast for the myocardium, leading to less accurate delineation. Therefore, we propose to use all three types of MR images within a unified segmentation framework that employs a two-step segmentation technique using registration and intensity-based segmentation.

2.1 Spatio-Temporal Registration

The images we use for each patient consist of stacks of SA and LA images (acquired as cine images) as well as a 3D anatomical end-systolic volume. The LA image stacks consist of four (4CH), three (3CH) and two chamber (2CH) views. Note that, the SA and LA images are acquired during a separate breath-hold for each slice while the 3D anatomical image is acquired in a single breath-hold. Due to potential differences in the position of the heart (e.g. due to respiration) there is usually some spatial misalignment between the images (inter-sequence misalignment) as well as between individual slices of the SA and LA images (intra-sequence misalignment). In addition there is temporal misalignment between the 3D anatomical image and the SA and LA cine images. In order to use multiple images simultaneously, these misalignments must be corrected. The 3D image provides good spatial resolution to serve as target for accurate slice-to-volume registration [9]. In this framework we first register all available LA and SA image sequences to the 3D image using a 1D temporal registration by maximizing normalized mutual information as a similarity measure followed by

a spatial 3D rigid registration using the same similarity measure. The resulting spatio-temporal (4D) transformation corrects both the inter-sequence misalignment and intra-sequence slice shifts so that all images can be transformed to the same spatio-temporal coordinate system, in this case, the coordinate system of the 3D anatomical MR image.

2.2 Atlas Based Segmentation

In [8] image registration was used to propagate an atlas constructed from normal population to subjects. A locally affine registration method (LARM) [3] was used to address the large local shape variability of pathological cardiac anatomy, commonly seen across large populations with pathologies. LARM is integrated into the registration process as an intermediate registration step between a global affine registration and a fully non-rigid registration. Compared to traditional registration schemes, LARM is capable of providing a good initial alignment between the images of patients with pathologies and the atlas constructed from normal subjects.The deformation is defined under the following equation 1:

$$T(X) = \begin{cases} G_i(X) & X \in V_i \\ \sum_{i=1}^{i=n} W_i(X) G_i(X) & \text{otherwise} \end{cases} \quad (1)$$

where $G_i(X)$ is region V_i's estimated affine transformation and W_i is the distance between given X and V_i.

After atlas propagation, We [8] used a two-component Gaussian mixture model for the myocardial tissue modelling infarcted and non-infarcted myocardial tissue while being spatially constrained by the probabilistic atlas [2] propagated.

We extend the above method to multi-image atlas propagation using a combined normalized mutual information similarity measure in which the similarity for each image is weighted by the relative number of voxels in the image.

2.3 Multi-image Graph Cut Refinement

The MCEM algorithm [8] segments the 3D, SA and LA images separately although the atlas is propagated to all images simultaneously. We propose to use an energy function based on Markov Random Fields (MRF) in combination with graph-cuts [5] to refine the segmentation across all images at the same time. 4D graph cuts have recently been used to segment image sequences [10,11]. Here, we have adopted the 4D graph cut approach to utilize information from multiple MR images with different spatial resolution. To differentiate our approach from a 4D graph cut segmentation of image sequences, we refer to it as multi-image graph cut segmentation.

Let I_i be the i-th image of multiple images, segmenting I_i is defined as a process of assigning a label $f_p \in L$ to each voxel $p \in I_i$. An MRF-based energy function can be formulated as:

$$E(f) = \lambda \sum_{p \in I_i} D_p(f_p) + \sum_{\{p,q\} \in N} V_{p,q}^{intra}(f_p, f_q) + \sum_{\{p,q\} \in M} V_{p,q}^{inter}(f_p, f_q) \quad (2)$$

where N and M are a neighborhood of voxels within an image and across different images respectively and f is the labeling of I_i [5]. The data term $D_p(f_p)$ measures the disagreement between the *a-priori* probabilistic model and the observed data. $V_{p,q}(f_p, f_q)$ is a smoothness term penalizing discontinuities of the segmentation in N or M. The parameter λ governs the influence of the data and smoothness terms. We found heuristically that setting $\lambda = 2$ leads to robust results for myocardium segmentation. Two different smoothness terms are chosen respectively for inter image similarity and intra image similarity since they are intuitively distinguished. For intra image similarity continuity in intensity space is enforced. While for inter image similarity comes from overlap between voxels. And continuity in intensity space is neither granted nor meaningful due to different modalities and strong spatial alignment.

To optimize eq. (2), a graph $G =< V, E >$ with a node $v \in V$ for each voxel p is defined on images. Each edge $e \in E$ consists of connections between node v and two terminal nodes F and B (also called source and sink node) as well as connections between neighboring voxels. The terminal nodes F and B represent the two labels describing foreground and background, respectively. By determining a minimum cut on graph G, the desired segmentation can be obtained[5]. The data term $D_p(f_p)$ is estimated using the MCEM segmentation [8] which generates a probability for each class of each voxel.

The smoothness term between neighboring voxels within an image is defined over a cubic neighborhood N by the following equation:

$$V_{p,q}^{intra} = w_{intra} \frac{1}{\ln(1 + (I_p - I_q)^2) + \epsilon} \quad (3)$$

Here I is intensity and ϵ is a small constant value which compensates for noise when I_p is close to I_q. For neighbouring voxels we define $w_{intra} = 1/d$ where d is the distance between two voxels.

For voxels across different images, a different smoothness term is chosen. We define a smoothness term that depends on the degree of overlap between the voxels instead of the intensity similarity to enforce spatial consistency and address the different modalities between images. We use the Dice metric to compute the amount of overlap between images

$$V_{p,q}^{inter} = w_{inter}(2||S_p \cap S_q||)/(||S_p|| \cup ||S_q||) \quad (4)$$

where S_p and S_q are the voxel volumes of voxel p and q and w_{inter} is a constant weight chosen as 2 from extensive experiment. The result of this equation is real number between 0 and 1 due to different voxel size and position of the images. The smoothness term is defined in a neighborhood M where $V_{p,q}^{inter} > 0$.

By using this multi-image graph cut approach, we connect intra-image voxel neighbors according to their intensity similarity and distance and inter-image voxels neighbors according to their spatial overlap. This enables us to segment

multiple images simultaneously and consistently. Finally the energy function is optimized using graph-cuts and multiple labels are achieved at the same time using the expansion and the swap algorithm[5].

3 Uncertainty Definition and Evaluation

3.1 Registration Uncertainty

Given two images, I_{atlas} and I_i (the subject's ith image), we can estimate a transformation $\mathbf{T}$ which maps image I_i to I_{atlas} so that a voxel of $I_i(\mathbf{x})$ correspond to $I_{atlas}(\mathbf{T}(\mathbf{x}))$ and their intensity values should be similar. Using a probabilistic formulation for the image registration problem [6], the uncertainty of a transformation $\mathbf{T}$ at point $\mathbf{x}$ can be modeled by the following equation :

$$uc(\mathbf{T}(\mathbf{x})|(I_i(\mathbf{x}), I_{atlas})) = 1 - \frac{p((I_i(\mathbf{x}), I_{atlas})|\mathbf{T}(\mathbf{x}))p(\mathbf{T}(\mathbf{x}))}{p((I_i(\mathbf{x}), I_{atlas}))} \tag{5}$$

We model the likelihood term, $p((I_i(\mathbf{x}), I_{atlas})|\mathbf{T}(\mathbf{x}))$, as a normal distribution of the intensity difference between transformed I_{atlas} and I_i estimated using an EM algorithm after histogram equalization. Similarly, the prior of the transformation, $p(\mathbf{T}(\mathbf{x}))$, is modeled as a Rician distribution of the Jacobian determinant of the transformation [12]. The distribution is estimated based on the inversion technique proposed in [13]. The Rician distribution is a non-negative and asymmetric distribution which approximates the distribution of the Jacobian determinant well for a given transformation. Finally, $p((I_i(\mathbf{x}), I_{atlas}))$ can be modelled as a constant term.

3.2 Segmentation Uncertainty

The uncertainty of a given label from our 4D graph cut segmentation can be modeled by the following equation:

$$uc(L_j|I_i(\mathbf{x})) = 1 - \frac{p(I_i(\mathbf{x})|L_j)p(L_j)}{p(I_i(\mathbf{x}))} \tag{6}$$

where $p(I_i(\mathbf{x})|L_j)$ is the likelihood that intensity of $I_i(\mathbf{x})$ belongs to L_j as estimated by the segmentation method. $p(I_i(\mathbf{x}))$ is modelled as a constant term and

$$p(L_j) = \frac{1}{log(\delta_j + 1 + \epsilon)} \tag{7}$$

Here ϵ is a small constant value and δ is the interquartile range of the multiple component distribution that represents L_j's intensity distribution from our segmentation method. The interquartile range is chosen because it's a robust statistic that conveys the dispersion of a distribution [6] and corresponds well to the intra-region homogeneity of a segmentation. It is robust in the sense that it provides meaningful information even for non-Gaussian distributions like the ones that can be obtained from the MCEM segmentation.

Table 1. Validation results: The Dice overlap measure for the endocardial segmentation (LV) and epicardial segmentation (LV+MYO) results comparing automatic and manual segmentation. $*$ means that the pair-wise t-test is significant at $p < 0.05$ and $\star$ $p < 0.01$.

Group	Segmentation	Segmentation using SA only [8]	Proposed segmentation
all	endocardial$*$	0.907 ± 0.032	0.920 ± 0.026
	epicardial$*$	0.908 ± 0.028	0.921 ± 0.024
apex	endocardial$\star$	0.837 ± 0.095	0.900 ± 0.059
	epicardial$\star$	0.838 ± 0.079	0.910 ± 0.052
mid	endocardial	0.918 ± 0.028	0.923 ± 0.024
	epicardial	0.920 ± 0.029	0.925 ± 0.021
basal	endocardial $*$	0.894 ± 0.048	0.916 ± 0.041
	epicardial $*$	0.896 ± 0.036	0.917 ± 0.033

3.3 Uncertainty Quantification and User Interaction

For each voxel $\mathbf{x}_i$ in all images, its registration and segmentation uncertainty can be evaluated and visualized using eqs. (5) and (6) respectively. We can further define the registration and segmentation uncertainty of a given region L_j by averaging over the region. The quantification of uncertainty can be used to inform the user about how reliable the segmentation results are.

Based on results from the uncertainty analysis, we can design a system that that detects abnormally high uncertainty. In our analysis we have four failure cases in which the global affine registration fails during the atlas registration. The subsequent segmentations also fail. Myocardial registration uncertainty is a good indicator for failed global affine registration (failed cases 0.86 ± 0.14, successful cases 0.39 ± 0.08 $p < 0.0001$). A combination of registration and segmentation uncertainties is better in terms of classification using linear discriminant analysis (LDA) (failed cases 1.73 ± 0.12, successful cases 1.2 ± 0.08 $p \ll 0.0001$). A good threshold for detecting segmentation failures using the combined registration and segmentation uncertainty is 1.59 derived from LDA with accuracy of 100%.

In the cases that we detect a segmentation failure, the user is asked to define 6 landmarks (apex, center of left ventricle, anterior and inferior insertion points of right ventricle, center of right ventricle and center of basal plane). These landmarks are also defined in the atlas. By introducing knowledge about these additional 6 landmarks, the atlas-to-image registration can be initialized more accurately and all segmentations performed correctly.

4 Results

In this paper we used datasets form 32 subjects. Each dataset consists of short axis (SA), long axis (LA) four (4CH), three (3CH) and two chamber (2CH) cine MR image sequence ($2.2 \times 2.2 \times 10, \mathrm{mm}$, 30 phases) and anatomical 3D MR images ($1.1 \times 1.1 \times 1.1, \mathrm{mm}$, one phase).

Manual segmentations were performed by a cardiologist to extract the myocardium and left ventricle in all images after spatio-temporal registration.

We then compared these to the segmentation results obtained via our previous technique [8] which uses SA MR images only and the proposed technique. Both techniques utilize the landmarks from the user for four patients for which the global affine registration fails. For comparisons between the methods we used the Dice metric, $D = (2||S_a \cap S_b||)/(||S_a|| + ||S_b||)$ where S_a and S_b are respectively the manual label segmentation and automatic label segmentation. The results are summarized in tab.1. The results indicate that our proposed segmentation scheme performed better than the original method especially on the basal and the apex segments. The basal and apex are very difficult to segment using SA MR images only due to the large slice thickness and partial volume. In the proposed approach the segmentation in these region is enhanced by adding information from 3D and LA images.

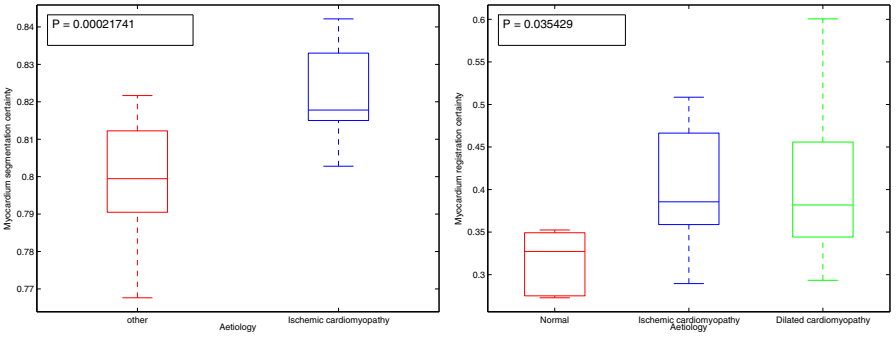

Fig. 2. Left figure shows myocardial segmentation uncertainty and right figure shows myocardial registration uncertainty

Uncertainty is a good indicator for the failure of the global affine registration. However, during our experiment, there is no strong correlation between uncertainty and accuracy of the segmentation if the uncertainty does not rise beyond the threshold used. If the segmentation is considered successful, the uncertainty relates more to abnormality of the patient's cardiac anatomy than the accuracy of the segmentation. This is possibly due to the fact that our segmentation algorithm is designed to segment pathological images well using LARM [3] and MCEM [8]. To examine if the uncertainty correlates to the abnormality of the patients, we assume that segmentation uncertainty which comes from intensity and geometry distribution relates to abnormal intensity like ischemic cardiomyopathy while registration uncertainty which comes from geometry distribution corresponds well to abnormal geometry like dilated cardiomyopathy. Figure.2 shows that myocardial segmentation uncertainty is a very good predictor for separating ischemic cardiomyopathy from the rest of subjects (ischemic subjects 0.82 ± 0.012, other subjects (normal and dealated) 0.80 ± 0.016 $p < 0.001$), meanwhile myocardial registration uncertainty is a good predictor for separating dilated cardiomyopathy from normal subjects (dilated subjects 0.38 ± 0.08,

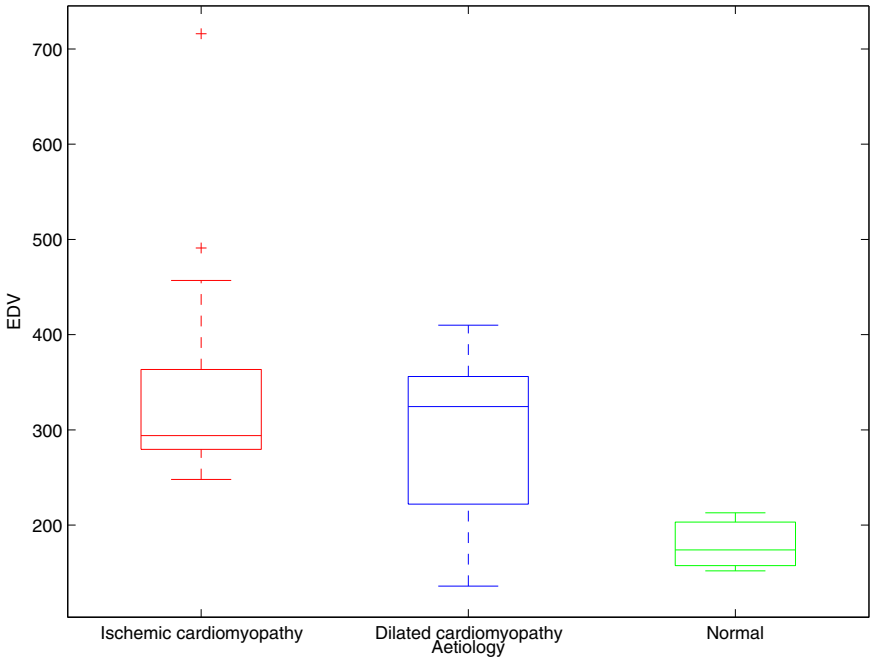

Fig. 3. End Diastolic Volume(EDV) of the subjects from the segmentation, p value between normal and ischemic is 0.025, between normal and dilated is 0.054 and between dilated and ischemic is 0.287

normal subjects 0.33 ± 0.04 $p < 0.05$) but not from ischemic subjects. Compare to EDV Figure 3, uncertainty outperforms EDV by distinguishing ischemic ($p < 0.001$ against $p < 0.05$) from other and separate dilated ($p < 0.05$ against $p > 0.05$) from normal.

5 Conclusion and Future Work

In this paper we present a novel two-step multiple image segmentation framework using three widely available MR image sequences. Using LARM and MCEM we are able to deal with local shape variations as well as infarcted myocardium. The segmentation is performed simultaneously from all images using a multi-image graph cut approach. The accuracy is significantly improved compared to previous segmentation methods by utilizing both intra- and inter-image information Table 1. We finally define a system that detects segmentation failures using registration and segmentation uncertainties.

Cardiac pathology is not always easily detectable in images, e.g. the transposition of vessels, but likely to be detected by registration and segmentation

uncertainty. Since we can define uncertainty for every part of the cardiac anatomy, it is desirable to investigate if the relationship between uncertainty and abnormality could help to detect these pathologies automatically.

References

1. Uribe, S., Muthurangu, V., et al.: Whole-heart cine MRI using real-time respiratory self-gating. Magnetic Resonance in Medicine 57(3), 606–613 (2007)
2. Lorenzo-Valdés, M., Sanchez-Ortiz, G., Rueckert, D., et al.: Segmentation of 4D cardiac MR images using a probabilistic atlas and the EM algorithm. Medical Image Analysis 8(3), 255–265 (2004)
3. Zhuang, X., Rhode, K., Ourselin, S., et al.: A Registration-Based Propagation Framework for Automatic Whole Heart Segmentation of Cardiac MRI. IEEE Transactions on Medical Imaging, 1612–1625 (2010)
4. Zhang, Y., Brady, M., Smith, S.: Segmentation of brain MR images through a hidden Markov random field model and the expectation-maximization algorithm. IEEE Transactions on Medical Imaging 20(1), 45–57 (2001)
5. Boykov, Y., Veksler, O., Zabih, R.: Fast approximate energy minimization via graph cuts. IEEE Transactions on Pattern Analysis and Machine Intelligence, 1222–1239 (2001)
6. Risholm, P., Pieper, S., Samset, E., Wells III, W.M.: Summarizing and Visualizing Uncertainty in Non-rigid Registration. In: Jiang, T., Navab, N., Pluim, J.P.W., Viergever, M.A. (eds.) MICCAI 2010, Part II. LNCS, vol. 6362, pp. 554–561. Springer, Heidelberg (2010)
7. Kybic, J.: Bootstrap resampling for image registration uncertainty estimation without ground truth. IEEE Transactions on Image Processing 19(1), 64–73 (2009)
8. Shi, W., Zhuang, X., Wang, H., Duckett, S., Oregan, D., Edwards, P., Ourselin, S., Rueckert, D.: Automatic Segmentation of Different Pathologies from Cardiac Cine MRI Using Registration and Multiple Component EM Estimation. In: Metaxas, D.N., Axel, L. (eds.) FIMH 2011. LNCS, vol. 6666, pp. 163–170. Springer, Heidelberg (2011)
9. Chandler, A., Razavi, R., et al.: Correction of misaligned slices in multi-slice MR cardiac examinations by using slice-to-volume registration. In: 3rd IEEE International Symposium on Biomedical Imaging: Nano to Macro, pp. 474–477. IEEE (2006)
10. Linguraru, M.G., Pura, J.A., Chowdhury, A.S., Summers, R.M.: Multi-organ Segmentation from Multi-phase Abdominal CT via 4D Graphs Using Enhancement, Shape and Location Optimization. In: Jiang, T., Navab, N., Pluim, J.P.W., Viergever, M.A. (eds.) MICCAI 2010, Part III. LNCS, vol. 6363, pp. 89–96. Springer, Heidelberg (2010)
11. Wolz, R., Heckemann, R., Aljabar, P., et al.: Measurement of hippocampal atrophy using 4D graph-cut segmentation: Application to ADNI. NeuroImage (2010)
12. Rohlfing, T., Maurer Jr., C., Bluemke, D., Jacobs, M.: Volume-preserving nonrigid registration of MR breast images using free-form deformation with an incompressibility constraint. IEEE Transactions on Medical Imaging 22(6), 730–741 (2003)
13. Koay, C., Basser, P.: Analytically exact correction scheme for signal extraction from noisy magnitude MR signals. Journal of Magnetic Resonance 179(2), 317–322 (2006)

Toward Clinically-Feasible Noninvasive Electrophysiological Imaging: Investigating the Impact of Local Anatomical Details

Azar Rahimi, Hongda Mao, Pengcheng Shi, and Linwei Wang

Computational Biomedicine Labratory
Rochester Institute of Technology, Rochester, New York, USA

Abstract. Noninvasive Cardiac electrophysiological (EP) imaging aims to compute cardiac electrical dynamics from body surface potential. Anatomical data acquisition and processing computations, to reconstruct detailed geometry of heart and torso, are complex and time consuming tasks that are incompatible with clinical requirements. Our ultimate goal is to improve noninvasive EP imaging techniques toward clinical feasibility by investigating the minimum anatomical information. As the first step toward this goal, in this study we investigate the impact of local geometrical details on cardiac EP imaging. It is known that, global geometrical factors such as size, position and orientation of heart are important in noninvasive electrocardiography problem; but the effect of local geometrical details is unknown and it is difficult to accurately capture. We hypothesize that, as long as global geometrical parameters are captured, local details of realistic cardiac geometry do not significantly impact diagnostic effectiveness of cardiac EP imaging. We verify this hypothesis by developing simple geometrical model instead of realistic heart that enables us to measure local anatomical error, and applying it in EP imaging for detection of myocardial infarction. The results computed based on simple geometrical model are comparable to that of the realistic heart geometry. Thus, it confirms our hypothesis that discarding local geometrical details does not affect diagnostic cardiac EP imaging. The findings of this study pave the road for further studies on tomographic input data processing toward clinical feasibility.

Keywords: Cardiac electrophysiology, Simplified geometry of heart.

1 Introduction

Noninvasive cardiac electrophysiological (EP) imaging aims to combine body surface potential (BSP) and image-derived anatomical information to computationally reconstruct cardiac electrical dynamics. Decades of research on cardiac EP imaging resulted in methods that are able to reconstruct EP details either on heart surface [1,2,3] or transmurally through myocardium [4,5]. Different phases of state-of-the-art noninvasive cardiac EP imaging techniques [1-5] are presented

O. Camara et al. (Eds.): STACOM 2011, LNCS 7085, pp. 188–197, 2012.

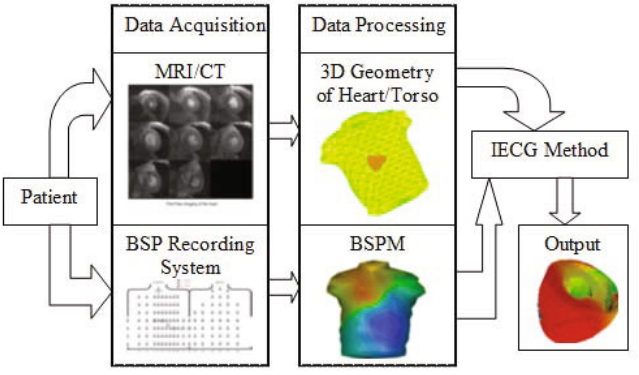

Fig. 1. Diagram of state-of-the-art cardiac electrophysiological methods

in Figure 1. Common input data to all of these state-of-the-art methods include large number of high quality tomographic images to reconstruct detaild 3D geometry of heart and torso and body surface potential (BSP) maps.

Detailed 3D heart/torso geometry reconstruction puts high demand on high-quality tomographic data. As a result, the tomographic data mainly used for noninvasive cardiac EP imaging are magnetic resonance (MR) and computed tomography (CT) images and more commonly available imaging tools such as ultrasound have not been exploited for the detailed 3D geometry reconstruction due to lower images quality. Furthermore, varying quality and artifacts of obtained CT/MR images have direct effect on detailed 3D geometry reconstruction. On the other hand, generating detailed realistic geometry of heart and torso volumes requires complex and most oftenly non-automatic image processing such as segmentation and surface mesh generation [6]. Thus, tomographic data processing step is a challenging, time-consuming and complex task that demands expertise and high level of user intervention and can not be fulfilled in clinics.

To be feasibile clinical routins, noninvasive cardiac EP methods have to be inexpensive, fast and easy with reproducible diagnostic results. Our research addresses this problem by investigating the minimum tomographic data required for diagnostic cardiac EP imaging. We start by asking this question: "what are the minimum geometrical details needed for diagnostic cardiac EP imaging?" Although several studies [7] have shown that global geometrical features such as size, orientation and position of heart with respect to torso are very critical in reconstruction of cardiac electrical potential, impacts of local anatomical details such as heart surface irregularities or errors caused by segmentation are unclear. How these local geometrical details affect cardiac EP imaging is the main focus of this study. In order to do so, we develop simple geometrical model for heart and apply it in noninvasive EP imaging of myocardial infarction to evaluate the impact of discarding local geometrical details. The findings of this study will further enable us to develop an adaptive geometrical modeling framework for

cardiac EP imaging that incorporates anatomical information based on available images quality and quantity and clinical needs as well.

2 Optimization of 3D Geometry Reconstruction

Detailed 3D geometry reconstruction needs complex processing including the segmentation of tomographic images. Varying quality of tomographic images makes this task more challenging that demands high level of user intervention and expertise and may introduce ambiguos input error to the system. This input error and its effects should be determined and investigated. In this study, we assess the impact of local geometrical details (e.g segmentation error, heart surface irregularities) on noninvasive cardiac electrophysiological imaging.

Cardiac Simplified Geometry: To evaluate the impact of local geometrical details on cardiac EP imaging, we propose a simple geometrical model for heart that only employs patient's heart size, position and orientation with respect to torso while ignores local details of the heart. In this model, left ventricle epicardium and endocardium are represented by two concentric circles at short axis and an ellipsoid at long axis according to equation 1.

$$R_{Lendo}^2 = (\varepsilon - \varepsilon_0)^2 + (\eta - \eta_0)^2 + a^2(\zeta - \zeta_0)^2 \tag{1}$$

where $\varepsilon - \eta$ plane is considered as the heart short axis and ζ is related to the long axis, $(\varepsilon, \eta, \zeta)$ represents coordinates of the left ventricle, $(\varepsilon_0, \eta_0, \zeta_0)$ represents center of the left ventricle, R_{Lendo} is the radius of left ventricle endocardium (inner circle radius), and ellipticity of the shape is described by parameter a. Left ventricle epicardium would be modeled with the same formulation as the left ventricle endocardium only with different radius, called R_{Lepi}, which is larger than R_{Lendo}. It has been experimentally shown that this model of left ventricle can better represent its geometry compared to other geometrical models [8]. The required parameters are radius of the two circles, which determine the left ventricle wall thickness and would be obtained from the base slice MR image. The center of these two concentric circles is placed at the center of the left ventricle. This model and its corresponding 3D reconstruction of the left ventricle is shown in Figure 2.

Right ventricle endocardium is modeled using two intersecting circles at short axis and a parabola at long axis according to [9]. The following equation represents a shape which is a circle in $\varepsilon - \eta$ plane and a parabola in ζ direction perpendicular to $\varepsilon - \eta$ plane.

$$\zeta = \zeta_0 + a[(\varepsilon - \varepsilon_0)^2 + (\eta - \eta_0)^2] \tag{2}$$

Similarly, $(\varepsilon, \eta, \zeta)$ represents surface coordinates of this shape, $(\varepsilon_0, \eta_0, \zeta_0)$ is the center of this geometrical shape and a is a scaling factor which refers to the elongation of the shape in ζ direction.

It should be noted that the distance between these two intersecting circles changes along the long axis such that the center of the circle representing free

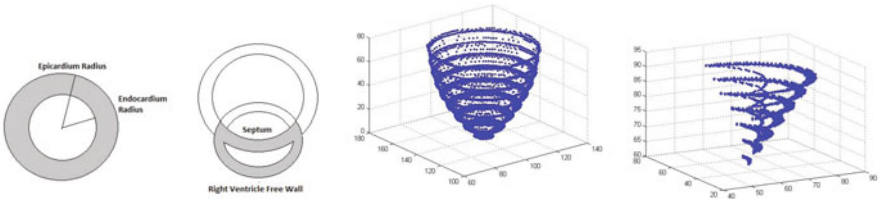

Fig. 2. (a) Left ventricle, and (b) right ventricle simplified geometry model in short axis. 3D reconstruction of (c) left ventricle, and (d) right ventricle.

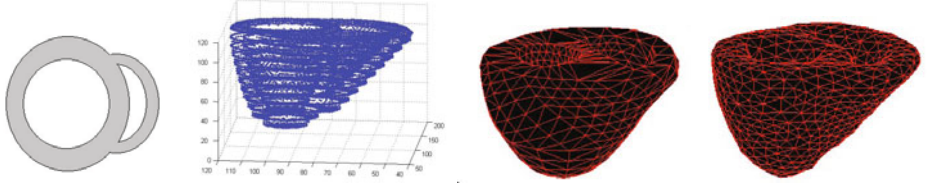

Fig. 3. (a) Simplified geometry of heart in short axis, (b) 3D reconstruction of the heart. Surface mesh of cadiac (c) realistic geometry, and (d) simplified geometry.

wall of the right ventricle moves toward the center of the circle representing the septum. This is automatically controlled by a ceofficient that decreases the distance between to circles center gradually along the long axis from the base to the apex. Figure 2b and 2d clarify the geometrical model used for right ventricle surface mesh generation. The grey area represents the right ventricle myocardium in $\varepsilon - \eta$ plane. By integrating the right ventricle and the left ventricle, simplified heart volume would be constructed as presented in Figure 3.

It is worth mentioning that by applying the simplified geometry of heart there is no need for manual segmentation of MRI slices. The simplified geometry enables us to reconstruct 3D geometry of heart by only eight parameters including center of the left ventricle, radii of the left ventricle endocardium and epicardium (representng left ventricle wall thickness), and center of the right ventricle, radii of the right ventricle epicardium and endocardium (representing right ventricle wall thickness), and lentgh of left ventricle and right ventricle. To obtain these 8 parameters, only the base and the apex slices of cardiac MR image series are required for user intervention.

Torso Geometry Customization: After generation of 3D heart geometry, torso geometry would be constructed followed by adjustment of heart into torso according to subject's heart orientation and position. Surface mesh of torso can be reconstructed using electrodes' positions on body surface that are used for recording body surface potentials. High resolution electrode arrays employed in different BSPM models can sufficiently represent torso surface without using

tomographic images [10]. Position and orientation of patient's heart with respect to torso would be obtained from MRI metadata. The subject's heart size is reflected in the parameters used for generating the simplified geometry such as left and right ventricle wall thicknesses as well as parameter a which controls elongation of the ventricles along the long axis. Customization of the simplified heart geometry would ensure correct location and orientation of the heart relative to torso. Correct position of the heart would be achieved by finding the location of left ventricle center on the short axis base slice MRI and translating the origin of$\{\varepsilon, \eta, \zeta\}$coordinate system to that location. Rotation of $\{\varepsilon, \eta, \zeta\}$ coordinate system to the subject's coordinate system corrects the orientation of the heart as well. Figure 4a shows the subject-specifiec heart/torso model used in our experiments.

3 Results

To assess the impact of discarding local geometrical details, we apply the simplified geometry model of heart to noninvasive cardiac EP imaging in simulated myocardial infarction (MI).

Experiments are conducted on synthesized and real data with MI condition. Heart and torso geometry models provided by [11] are used to generate synthesized MI data set. The cardiac simplified geometry is constructed based on the realistic canine heart geometry as presented in Figure 3c and 3d. The torso geometry is also shown in Figure 4a. In order to measure impact of local geometrical details, we ensure that global geometrical parameters are preserved as explained in section 2.2. Experiments are conducted on 88 synthesized cases with MI of different sizes and locations in the left ventricle for both realistic and simplified heart geometries. Simulation of each MI condition is performed on the cardiac realistic geometry, using Aliev–Panfilov model [12] for TMP activity and quasi-static electromagnetism for the bioelectric field of BSP. Next, the simulated BSP is corrupted with 20-dB white gaussian noise. Without any prior knowledge about the infarct size and location, the inverse step estimates the cardiac transmembrane potential (TMP) based on the noisy BSP for the simplified and realistic heart geometries according to the inverse EP method described in [13]. In this way, identical BSP is provided to the inverse EP imaging technique with the simplified and realistic heart geometries; hence the only factor affecting the output would be discarding local details of heart geometry. In addition to synthesized cases, cardiac simplified geometry of one post-MI patient (case 2 provided through 2007 PhysioNet/Computers in Cardiology Challenge [14]) is generated and corresponding TMP is estimated based on the provided BSP.

Geometrical Error Measurment: To quantify the geometrical error introduced in input using the cardiac simplified geometry, difference of two volumes (heart simplified geometry and realistic one) is calculated. This difference is simply obtained by finding non-overlapping area of realistic and simplified heart volumes. The difference of realistic heart geometry and simplified geometry for the base

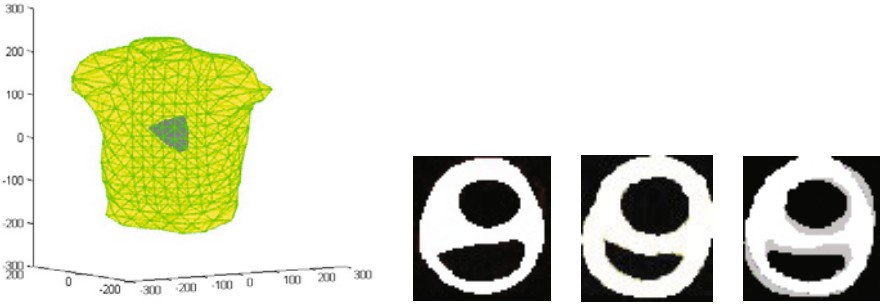

Fig. 4. (a) Torso surface mesh with heart mesh free points. The base slice of (b) realistic heart geometry, and (c) simplified heart geometry. (d) The difference of two geometries' base slices.

slice is shown in Figure 4d, where the non-overlapping area is highlighted by grey. Since our TMP estimation method is formed on meshfree points representation of the heart, the geometrical error is calculated based on the number of meshfree points residing in the difference volume. The number of meshfree points located in the difference volumes for heart geometries provided by [11] and [14] are 12.42% and 14.23% respectively.

Infarct quantification: Experimental studies have shown that TMP characteristics of infarct scar change such as action potential duration (APD) and depolarization rate [15], regardless of the EP imaging technique used for TMP estimation. Therefore in this study, infarct quantification parameters including infarct center (CE) and size (IS) are calculated based on the abnormality in activation time (AT) and APD of TMP dynamics to quantitatively evaluate the impact of simplified geometry application to cardiac EP imaging. AT and repolarization time are extracted from maximum first derivative of TMP upstroke and maximum second derivative of TMP downstroke respectively [16]. Difference between repolarization time and AT shows APD. Infarct center represents the center of infarcted meshfree points and infarct size is obtained by dividing the number of infarcted meshfree points by the total number of meshfree points. Overlap between the detected infarct scar and true infarct scar determines the precision, sensitivity and specificity of infarct identification.

S*ynthesized cases*: These experiments on 88 different cases have infarct size ranging from less than 10% to 60% of the left ventricle distributed in different locations. Cardiac transmembrane potential dynamics for realistic and simplified geometries are computed, with the difference of local anatomical details measured above as the only factor affecting cardiac EP imaging. Figure 5 presents the simulated volumetric TMP dynamics of simplified heart for normal case and estimated TMP for a heart with MI in 4 time instances; delayed excitation is visible in the infarct area. The true (green points) and estimated (red points)

infarct extents for this example are shown in Figure 6a. The precision and specificity are degraded from 0.45 to 0.34 and 0.97 to 0.95, respectively while the sensitivity is improved to 0.53. Table 1 summarizes the quantitative comparison of infarct parameters for simplified and realistic geometries.

Table 1. Comparison of Infarct Parameters for the Cardiac Simplified and Realistic Geometries. ISD (CED) is the difference of simulated and estimated IS (CE).

IS	CED	ISD	Precision	Sensitivity	Specificity
Simplified Geometry					
0%-10%	11.86±6.8	0.05±0.03	0.23±0.12	0.41±0.15	0.94±0.02
10%-20%	5.48±2.18	0.02±0.04	0.42±0.13	0.47±0.08	0.94±0.02
20%-30%	4.21±1.42	0.01±0.06	0.52±0.17	0.45±0.12	0.94±0.03
>30%	3.15±2.19	0.01±0.03	0.83±0.13	0.42±0.11	0.97±0.02
Realistic Geometry					
0%-10%	9.87±7.24	0.03±0.03	0.55±0.04	0.27±0.01	0.97±0.03
10%-20%	10.84±7.92	0.05±0.03	0.52±0.04	0.31±0.09	0.96±0.04
20%-30%	7.98±6.11	0.11±0.02	0.66±0.07	0.28±0.03	0.96±0.02
>30%	7.53±3.42	0.22±0.03	0.88±0.05	0.29±0.02	0.98±0.01

The minimum infarct size detectable using cardiac simplified geometry is 5%. However, better results are obtained based on CED and ISD for infarct with larger sizes. The center and size of myocardial infarct are not negatively affected by replacement of detailed geometry of heart with the simplified geometry. Sensitivity of the estimation using simplified geometry outperforms the one using realistic geometry; it may be due to regular shape of simplified geometry. However, the precision and specificity of the simplified geometry are degraded compared to realistic geometry.

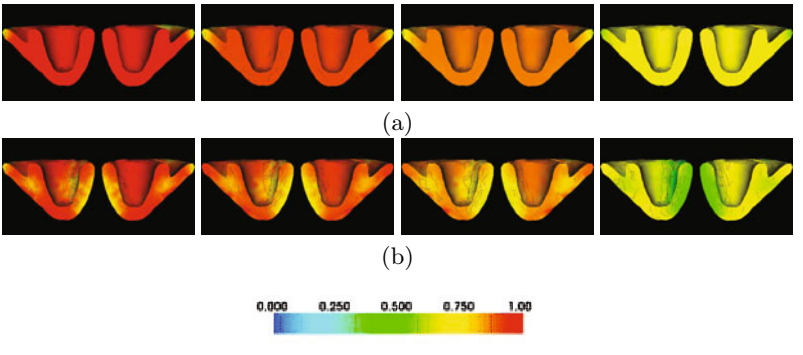

Fig. 5. Volumetric TMP dynamics (a) simulated normal results, (b) estimated results using the simplified geometry in 4 times instances from 10 ms to 130 ms

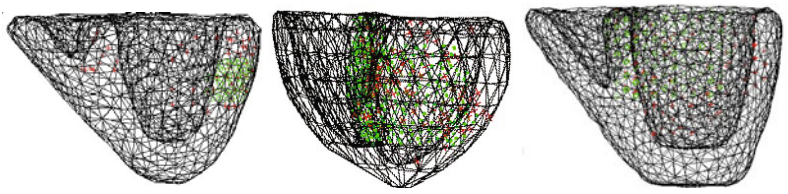

(a) (b) (c)

Fig. 6. (a)Estimated and true infarct extent for one synthesized case presented in figure 5. Estimated infarct for post-MI patient in (b) realistic heart, (c) simplified heart. Estimated infarct area is shown by red points while the green points represent the ground truth infarct extent.

Real case: Figure 6b and 6c show the infarct extent of post-MI patient estimated using realistic and simplified heart. Red points represent estimated infarct area inside the heart while green points represent the ground truth infarct extent. In the simplified geometry the infarct area is correctly identified with overestimation at inferolateral mid-cavity. Replacing the realistic heart with simplified one decreases the specificity from 0.76 to 0.5 and increases the sensitivity from 0.25 to 0.37 . However, more experiments on real cases are required for valid conclusion.

4 Conclusion

To be able to use the state-of-the-art EP methods in clinical applications, the anatomical data aquisition and processing should be fast, easy and inexpensive. As the begining step toward clinically-feasible cardiac EP imaging, we investigated the impact of local geometrical details on cardiac EP imaging by developing cardiac simplified geometry. The cardiac simplified geometry proposed here describes the 3D geometry of heart with minimum tomographic information as input. The results do not show significant change in terms of infarct extent and infarct center compared to the results of realistic geometry. The smallest infarct size detected using simplified geometry is 5%; however, increasing the infarct size improves the results. Therefore, the experiment results preliminarily confirm our hypothesis that local geometrical details of heart do not have critical effects on diagnostic EP imaging of myocardial infarction cases as long as global geometrical details are preserved. This would allow application of the simplified geometry in cardiac EP imaging which in addition eliminates MR image segmentation phase, reduces the user intervention and expedites geometry reconstruction as well. In addition, personalized cardiac simplified geometry generation only requires two slices of MR images; the images quality does not have significant effect on geometry reconstruction as long as the center of ventricles and wall thicknesses can be extracted. Thus, using simplified geometry enables us to employ other imaging modalities such as ultrasound in cardiac EP imaging.

In this study, only one geometry is used to generate the synthesized data set; In the future work, furthur experiments would be performed on different heart

geometries to provide statistically significant results. In addition, the findings of our study are restricted to the EP technique [5] utilized for TMP estimation; to be able to generalize the findings of this study to other EP methods, we will also employ cardiac simplified geometry to other EP techniques [1,4]. It is worth mentioning that cardiac EP imaging methods [1-4], disregard other cardiac anatomical structures such as purkinje fibers and papillary muscles for TMP estimation. The EP technique [5], used in this study, follows that assumption as well. Based on our preliminary study, we focus on investigating the impact of cardiac simplified geometry on diagnosis and quantification of infarct scar. Since different error measures are required for diagnostic effectiveness comparison of cardiac simplified geometry on other cardiac pathological conditions, it would be considered in our future works.

References

1. Rudy, Y., Messinger-Rapport, B.: Inverse Problem of Electrocardiography: Solutions in terms of Epicardial Potentials. Criti. Rev. Biomed. Eng. 16, 215–268 (1988)
2. Dawoud, F., Wagner, G., Moody, G., Horacek, B.M.: Using Inverse Electrocardiography to Image Myocardial Infarction. J. Electrocardiography 41(6), 630–635 (2008)
3. Pullan, A.J., Cheng, L.K., Nash, M.P., Bradley, C.P., Paterson, D.J.: Noninvasive Electrical Imaging of the Heart: Theory and Model Development. J. Biomed. Eng. 29, 817–836 (2001)
4. He, B., Wu, D.: Imaging and Visualization of 3-D Cardiac Electric Activity. IEEE Trans. on Info. Tech. in Biomed. 5(3), 181–186 (2001)
5. Wang, L., Zhang, H., Wong, K.C.L., Liu, H., Shi, P.: Noninvasive Volumetric Imaging of Cardiac Electrophysiology. In: IEEE Conf. on Computer Vision and Pattern Recognition, pp. 2176–2183 (2009)
6. Petitjean, C., Dacher, J.N.: A Review of Segmentation Methods in Short Axis Cardiac MR Images. Med. Image Anal. 15(2), 169–184 (2010)
7. Rapport, B.J., Rudy, Y.: The Inverse Problem in Electrocardiography: a Model Study of the Effects of Geometry and Conductivity Parameters on the Reconstruction of Epicardial Pontetials. IEEE Trans. Biomed. Eng. 33(7), 667–675 (1986)
8. Czegledy, F., Aebischer, N., Smith, D., Katz, J.: A Mathematical Description Of The Right Ventricular Free Muscle Wall Geometry And Mass. Eng. Med. and Biology Society 13, 2313–2314 (1991)
9. Wise, R.G., Huang, C.L., Al-Shafei, A.I., Carpenter, T.A., Hall, L.D.: Geometrical Models of Left Ventricular Contraction from MRI of the Normal and Spontaneously Hypertensive Rat Heart. Physics in Med. and Bio. 44(10), 2657–2676 (1999)
10. Wang, L., Wong, K.C.L., Zhang, H., Liu, H., Shi, P.: How Much Geometrical Detail Do We Need in Cardiac Electrophysiological Imaging? A Generic Heart-Torso Representation for Fast Subject-Specific Customization. In: Camara, O., Pop, M., Rhode, K., Sermesant, M., Smith, N., Young, A. (eds.) STACOM 2010. LNCS, vol. 6364, pp. 232–241. Springer, Heidelberg (2010)
11. Nash, M.: Mechanics and Material Properties of the Heart using an Anatomically Accurate Mathematical Model. Auckland University (1998)
12. Aliev, R.R., Panfilov, A.V.: A simple two-variable model of cardiac excitation. Chaos, Solitions Fractals 7(3), 293–301 (1996)

13. Wang, L., Zhang, H., Wong, K., Liu, H., Shi, P.: Physiological-modelconstrained noninvasive reconstruction of volumetric myocardial transmembrane potentials. IEEE Trans. Biomed. Eng. 57(2), 296–315 (2010)
14. Goldberger, A.L., Amaral, L.A.N., Glass, L.: Physiobank, physiotoolkit, and physionet components of a new research resource for complex physiological signals. Cric. 101, e215–e220 (2000)
15. Miller, W.T., Geselowitz, D.B.: Simulation studies of the electrocardiogram. II. Ischemia and infarction. Circ. Res. 43, 315–323 (1978)
16. Efimov, I.R., Huang, T.D., Rendt, J.M., Salama, G.: Optical mapping of repolarization and refractoriness from intact heart. Circ. Res. 90, 1469–1480 (1994)

A 3D+Time Spatio-temporal Model for Joint Segmentation and Registration of Sparse Cardiac Cine MR Image Stacks

An Elen[1,⋆], Jeroen Hermans[1], Hadewich Hermans[2], Frederik Maes[1], and Paul Suetens[1,⋆⋆]

Katholieke Universiteit Leuven
[1]Medical Image Computing, Dept. of Electrical Engineering (ESAT)
[2]Clinical Cardiology, Belgium
an.elen@uz.kuleuven.ac.be

Abstract. We previously developed a hybrid spatio-temporal method for the segmentation of the left ventricle in 2D+time magnetic resonance (MR) image sequences and here extend this model-based approach towards 3D+time sparse stacks of cine MR images with random orientation. The presented method combines an explicit landmark based statistical geometric model of the inter-subject variability at the end-diastolic and end-systolic time frames with an implicit geometric model that constraints the intra-subject frame-to-frame temporal deformations through deterministic non-rigid image registration of adjacent frames. This hybrid model is driven by both local and global intensity similarity, resulting in a combined spatio-temporal segmentation and registration approach. The advantage of our hybrid model is that the segmentation of all image slices and of the whole sequence can be performed at once, guided by shape and intensity information of all time frames. In addition, prior shape and intensity knowledge are incorporated in order to cope with ambiguity in the images, while keeping training requirements limited.

1 Introduction

Assessment of left ventricular function from 3D+time cine cardiac magnetic resonance (MR) images requires segmentation of the myocardial wall of the left ventricle (LV) in all short-axis (SA) and long-axis (LA) slices of these time series images. In clinical practice, such segmentation is often performed manually, which is labor intensive and susceptible to observer variability, for which reason it is often limited to the end-diastolic (ED) and end-systolic (ES) frames only. Several automatic and semi-automatic model-based methods for LV segmentation from cardiac MR images have been proposed.

Explicit landmark based statistical shape and appearance models (such as active shape models (ASM) [1]) learn realistic shapes and shape variations as

⋆ Research assistant of the Research Foundation - Flanders (FWO - Vlaanderen).
⋆⋆ IBBT-K.U.Leuven Future Health Department.

O. Camara et al. (Eds.): STACOM 2011, LNCS 7085, pp. 198–206, 2012.

well as local or global intensity models from a data set of (manually) segmented training images. These landmark based models can generate good segmentation results, even in ambiguous image regions, because of the prior knowledge that is incorporated in the statistical shape model. These methods have been extended towards the segmentation of deforming objects in dynamic image sequences by modeling all landmarks in all image frames together as one large feature vector [2]. But this implicitly assumes that all image sequences consist of the same number of frames and the need for a sufficiently large number of completely (and likely largely manually) segmented training image sequences makes the training quite labor intensive. Landmark based methods have also been extended towards the segmentation of sparse 3D MR image stacks of SA and LA slices. Some methods assume that the slices of all stacks image identical LV regions [3], which is not always the case in clinical practice. Alternative methods combine a 3D shape model with a simplified intensity model of the global characteristics of the intensities of e.g. the blood pool, myocardium and background [4], not requiring correspondence of the image slices. Methods with localized and spatially variant intensity models such as ASM may, however, capture more knowledge.

Alternatively, shape information can be encoded implicitly in the form of an annotated gray scale image or template that is non-rigidly deformed or registered towards the image to be segmented using a suitable similarity measure and deformation regularizer. Such registration based approach has been used to segment entire image sequences by propagating segmentations from one initially segmented frame to all others after frame-to-frame registration [5] or by registration of the entire 2D or 3D image sequence with an atlas or pre-segmented image sequence [6]. This approach is typically well suited for capturing small and smooth frame-to-frame deformations, provided that sufficient registration clues are present. However, inaccuracies in the frame-to-frame registrations will accumulate during propagation, especially in regions where registration clues are absent or ambiguous (e.g. the papillary muscle at ED vs. ES) or where contrast varies between frames (e.g. at the interface of LV and pericardium).

The benefits and limitations of explicit landmark based and implicit registration based approaches for the segmentation of image sequences are thus largely complementary. Hence, we proposed a 2D+t hybrid method that integrates explicit landmark based and implicit image registration based representations in a unified framework, thus combining the advantages of both models [7]. This resulted in a spatio-temporal model that performs joint segmentation and registration of all frames in the image sequence combined. In the proposed approach, explicit statistical shape and intensity models were constructed for selected frames (in casu ED and ES) only, strongly reducing the need for tedious manual delineation during training. These models were explicitly (for ED and ES) and implicitly (for all other frames) used to guide the segmentation of all image frames simultaneously through non-rigid image registration. While the method in [7] considers 2D+t joint registration and segmentation, we here extend this hybrid method towards sparse 3D+time MR image sequences, consisting of a sparse set of (i.e. limited number of) randomly oriented SA and LA slices with

SA inter-slice distances of approximately 1cm. The main focus of this paper is on the methodological concept of our method. Evaluation on two data sets of 70 image sequences shows that joint 3D+time segmentation and registration of all frames of all SA and LA slices combined performs better than segmentation of each frame individually due to the spatio-temporal integration of all available information.

2 Methods

The proposed hybrid model combines a statistical landmark based model, that captures inter-subject shape and intensity variability, with a deterministic registration based model, that captures the intra-subject temporal variation. Consistency between both models is assured by the used shape representation. The resulting model consists of four components: (1) frame-specific statistical landmark based shape models that are constructed for some selected key frames only (in casu ED and ES) to limit training requirements; (2) statistical local image appearance models constructed for each landmark separately on these selected frames that guide their segmentation on all frames; (3) frame-to-frame non-rigid image registration parameterized by the landmark locations and driven by global intensity similarity between consecutive frames; and (4) a temporal smoothness penalty imposed on the registration.

2.1 Shape Representation

We consider a 3D+time cardiac cine MRI data set to consist of separate 2D+time image slices that together define the 3D shape of the LV endo- and epicardial surface at each time frame $f \in \{1, 2, \cdots, F\}$. These surfaces are represented by a set $\mathbf{q}^f = [\mathbf{q}_1^f, \mathbf{q}_2^f, \cdots, \mathbf{q}_C^f]^T$ of C corresponding control points (CPs) $\mathbf{q}_c^f = [q_{x,c}^f, q_{y,c}^f, q_{z,c}^f]^T$, that is defined as a standardized sampling of the 3D LV endo- and epicardial surfaces (Fig. 1). All the CPs of one time frame are organized in a mesh, that completely represents the 3D surface (Fig. 1c), with mesh lines perpendicular to and mesh lines in plane with the central axis of the LV. As the CPs do not necessarily coincide with the image planes, a second set of points $\mathbf{v}^{f,s}$, i.e. the in-plane landmarks (LMs) $\mathbf{v}_l^{f,s} = [v_{x,l}^{f,s}, v_{y,l}^{f,s}]^T$ for each slice s, is defined as the intersection of the mesh lines with the image planes (Fig. 1d). As all landmarks coincide with the image planes, they will be used to define the position of intensity profiles and to guide in-plane registrations.

2.2 Model Component 1: Shape Model

A 3D shape model is statistically learned for the ED and ES frames separately from relative CP positioning of the training data, after global Procrustes alignment to remove differences in pose and scale. Independent component analysis (ICA) is used to construct the modes of variation, as this was found to perform better than traditional principal component analysis (PCA) [7]. A new shape

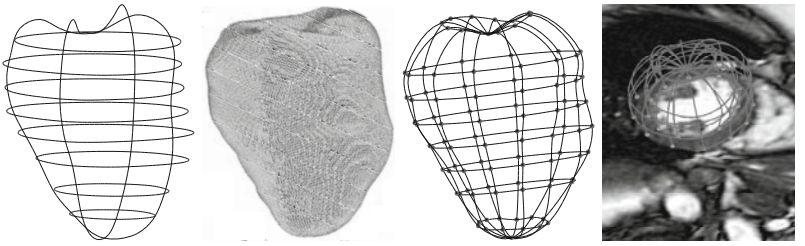

Fig. 1. CP and LM definition for the epicardial surface of one 3D training image. (a) Manual segmentations. (b) 3D surface fitted through the manual segmentations. (c) Standardized sampling of the surface, yielding the CPs (gray) with interpolation lines. The mesh lines perpendicular to the central axis are used to define the LMs in the LA slices and the mesh lines in plane with the central axis to define the LMs in the SA slices. (d) Definition of the LMs (light gray dots) in one SA slice.

$\mathbf{q}^f$ is thus defined as $\mathbf{q}^f = \mathbf{T}(\overline{\mathbf{q}^f} + \sum_{k=1}^{K^f} b_k^f \cdot \boldsymbol{\Phi}_k^f)$, with $\mathbf{T}$ the global alignment transformation, $\mathbf{b}^f$ the model parameters, $\boldsymbol{\Phi}^f$ the modes of shape variation and K^f the retained number of modes of variation. The shape cost is then defined as the squared Mahalanobis distance of the current shape $\mathbf{q}^f$ to the training shapes: $C_S^f(\mathbf{b}^f) = \left(\mathbf{T}^{-1}\mathbf{q}^f - \overline{\mathbf{q}^f}\right)^T (\mathbf{S}^f)^{-1} \left(\mathbf{T}^{-1}\mathbf{q}^f - \overline{\mathbf{q}^f}\right) = \sum_{k=1}^{K^f} \frac{\left(b_k^f\right)^2}{\lambda_k^f}$, for $f \in \{f_{ED}, f_{ES}\}$, with $\overline{\mathbf{q}^f}$ the mean and $\mathbf{S}^f$ the covariance matrix of the globally aligned training shapes and $\boldsymbol{\lambda}^f$ the variance of the model parameters.

2.3 Model Component 2: Local Appearance Model

We construct statistical local intensity appearance models, capturing the variability of the intensity (or derived) features within a local region around each LM l of the ED and ES frames independently. To this end, training LMs are defined by the intersection of image planes, that are sufficiently close to the current LM, with the same mesh line of the shape model as LM l. Kernel PCA (KPCA) was used to construct the local appearance models, as this was found to perform best [7]. Based on these models, the local intensity cost $C_{LI}^f(\mathbf{b}^f)$ (with $f \in \{f_{ED}, f_{ES}\}$) is calculated for each LM l of the ED or ES image stack as the squared Mahalanobis distance of the feature vector around the current LM l from the ones of the training set, in the higher dimensional feature space of KPCA, expressed by [8]: $C_{LI}^f(\mathbf{b}^f) = \sum_{l=1}^{N} \sum_{k=1}^{M^f} \frac{\left((\boldsymbol{\alpha}_k^{f,l})^T \mathbf{K}^{f,l}(\mathbf{b}^f)\right)^2}{\lambda_k^{f,l}}$, with $\mathbf{K}^{f,l}(\mathbf{b}^f)$ the kernel vector of the landmark considered and $\boldsymbol{\alpha}_k^{f,l}$ and $\lambda_k^{f,l}$ $(k = 1, \ldots, M^f)$ the M^f eigenvectors and eigenvalues of the training kernel matrix $\mathbf{K}_{train}^{f,l}$ of LM l in frame f. For all other frames of the entire image sequence, for which no explicit training data are assumed to be available, we define the local intensity cost $C_{LI}^f(\mathbf{q}^f)$ as the linearly weighted sum of the intensity costs of the landmarks in that frame f according to the corresponding ES and ED intensity models [7].

2.4 Model Component 3: Global Intensity Similarity

We incorporate global intensity similarity between different frames in the segmentation process by reformulating the landmark based segmentation of multiple frames simultaneously as a non-rigid registration problem. The registration transformation $F^{f,f-1,s}$ between frames f and f-1 of slice s is defined as the thin-plate spline (TPS) warp of corresponding landmarks $\mathbf{v}^{f,s}$ in frame f onto $\mathbf{v}^{f-1,s}$ in frame f-1, smoothly extrapolating the correspondences defined by the landmarks towards the whole image domain. All registrations are calculated in-plane, slice by slice. We thus neglect the out-of-plane motion, but assume this to be small between consecutive time frames and, moreover, to be practically unmeasurable due to the sparseness of the data. We here chose mutual information (MI) [9] as similarity measure S to assess the quality of the registration and thus the agreement between the landmarks on each set of neighboring frames is given by

$$C_{GI}^{f}(\mathbf{q}^{f-1}, \mathbf{q}^{f}, \mathbf{q}^{f+1}) = -\sum_{s}(S(\mathbf{I}^{f,s}, \mathbf{I}^{f-1\to f,s}(\mathbf{q}^{f-1}, \mathbf{q}^{f})) + S(\mathbf{I}^{f,s}, \mathbf{I}^{f+1\to f,s}(\mathbf{q}^{f+1}, \mathbf{q}^{f}))). \quad (1)$$

with $\mathbf{I}^{f-1\to f,s}(\mathbf{q}^{f-1}, \mathbf{q}^{f})$ image slice $\mathbf{I}^{f-1,s}$ warped to $\mathbf{I}^{f,s}$ using a TPS deformation based upon corresponding landmark locations $\mathbf{v}^{f-1,s}$ and $\mathbf{v}^{f,s}$ which are defined by $\mathbf{q}^{f-1}$ and $\mathbf{q}^{f}$ respectively. $\mathbf{I}^{f+1\to f,s}(\mathbf{q}^{f}, \mathbf{q}^{f+1})$ is similarly defined. Denoting the joint and marginal intensity probability distributions of $\mathbf{I}^{f,s}$ and $\mathbf{I}^{f-1\to f,s}$ by $p^{f,f-1,s}(a,b)$, $p^{f-1,s}(a)$ and $p^{f,s}(b)$ (with a and b intensity values), the mutual information between both images is given by

$$S(\mathbf{I}^{f,s}, \mathbf{I}^{f-1\to f,s}) = \sum_{a}\sum_{b} p^{f,f-1,s}(a,b) \cdot \log \frac{p^{f,f-1,s}(a,b)}{p^{f-1,s}(a) \cdot p^{f,s}(b)}, . \quad (2)$$

As we only assume frame-to-frame similarity within or near the object of interest itself (in casu the LV) and not in its background [9], computation of the mutual information in Eq. 2 is restricted to a ROI.

2.5 Model Component 4: Temporal Regularization

We regularize the propagation of shape information by constraining the shape changes of the CPs between consecutive time frames f-1, f and f+1 by the spatiotemporal smoothness penalty

$$C_{R}^{f}(\mathbf{q}^{f-1}, \mathbf{q}^{f}, \mathbf{q}^{f+1}) = |\mathbf{q}^{f+1} - \mathbf{q}^{f}| + |\mathbf{q}^{f-1} - 2\mathbf{q}^{f} + \mathbf{q}^{f+1}|. \quad (3)$$

Although ad hoc, this temporal regularization captures the intuitive expectations of inter-frame landmark motion. Specifically, inter-frame landmark motion is expected to be small and smooth which is reflected by penalizing large first order and second order derivatives of landmark locations respectively. Obviously, other spatial regularization terms are possible, including statistically learned deformation models (increasing the amount of training data required).

2.6 Hybrid Model

We combine the individual models described above to guide the joint segmentation of all frames in an image sequence by statistically learned and through landmark correspondence propagated shape and intensity knowledge. Hence, the quality of the simultaneous segmentation of all F frames is expressed as a global cost function that balances the four model components by a weighted sum of cost terms:

$$C(\mathbf{Q}) = C_S^{f_{ED}}(\mathbf{b}^{f_{ED}}) + C_S^{f_{ES}}(\mathbf{b}^{f_{ES}}) + \gamma_2 \left(C_{LI}^{f_{ED}}(\mathbf{b}^{f_{ED}}) + C_{LI}^{f_{ES}}(\mathbf{b}^{f_{ES}}) \right) + \sum_{f=2}^{F-1} \left(\gamma_1 C_R^f(\mathbf{q}^{f-1}, \mathbf{q}^f, \mathbf{q}^{f+1}) + \gamma_2 C_{LI}^f(\mathbf{q}^f) + \gamma_3 C_{GI}^f(\mathbf{q}^{f-1}, \mathbf{q}^f, \mathbf{q}^{f+1}) \right), \quad (4)$$

with $\mathbf{Q} = [\mathbf{T}, \mathbf{b}^{f_{ED}}, \mathbf{b}^{f_{ES}}, \mathbf{q}^{f \notin \{f_{ED}, f_{ES}\}}]$ the set of parameters to be determined and γ_1, γ_2 and γ_3 suitably chosen weighing factors. $\mathbf{T}$ represents the parameters of the global geometric alignment between the model and the image data, while $\mathbf{b}^{f_{ED}}$ and $\mathbf{b}^{f_{ES}}$ are the ICA model parameters of the ED and ES shape models respectively. In addition, $\mathbf{q}^{f \notin \{f_{ED}, f_{ES}\}}$ are the landmark locations in the other image frames for which no shape model was trained. The joint segmentation and registration amounts to the minimization of Eq. 4 w.r.t. $\mathbf{Q}$: $\mathbf{Q}_{opt} = \text{argmin}_{\mathbf{Q}} C(\mathbf{Q})$. This minimization is performed for all parameters simultaneously using a conjugate gradient approach with analytically determined derivatives.

3 Experimental Evaluation

A first data set of 70 3D+time MR image sequences was obtained in one clinical center, from patients with valve stenosis. A second data set consisted of 70 randomly selected 3D+time MR image sequences from the DETERMINE (Defibrillators to Reduce Risk by Magnetic Resonance Imaging Evaluation) cohort [10], which were acquired at multiple sites using a range of different scanner types and manufacturers. The images consist of 2 (data set 1) or 2 to 6 (data set 2) LA slices and on average 12 SA slices and 26 time frames. Manually supervised contours of the 4D LV segmentation were provided through expert analysis. Possible breath hold related misalignments between different LA and SA slices were corrected using the method of [11].

We evaluate the proposed 3D hybrid method with a leave-one-out experiment. After construction of the ED and ES shape and intensity models, the results of separate ED and ES ASM segmentation is compared to the segmentation results for these frames obtained with the method proposed. In both experiments (ASM and method proposed), the mean shape is used for initialization purposes along with manually obtained pose and scale parameters $\mathbf{T}$. More principled initialization approaches are imaginable but are not considered in this work.

Moreover, as a temporary simplification, the global alignment parameters **T** were kept fixed during model fitting.

To evaluate the fitted shapes, segmentations for each SA and LA image slice interpolating the from the shape derived LMs are compared with manual ground truth segmentations. The remaining mean radial point-to-point errors ϵ for each endo- and epicardial contour in each image slice and on each frame separately are reported in pixel units in Fig. 2 for the initialization and after both experiments.

The largest segmentation errors were obtained for the LA slices with a median of 2.3 times the pixel size for both data sets, after application of our hybrid method (Fig. 2). For the SA slices, segmentation results are best in the mid-ventricular region with median errors of respectively 1.42 and 1.57 times the pixel size for data sets 1 and 2.

A statistically significant difference was found between the segmentation errors of the initialization, Experiment 1 and Experiment 2, showing that the registration based coupling improves segmentation of ED and ES over individual segmentation of each frame separately using the same statistical shape and intensity models, as knowledge of the separate time frames becomes available for the entire image sequence. This is illustrated in Fig. 3, showing the ED and ES frame of 3 SA and 1 LA slice of a selected patient of data set 2, with the resulting segmentations of Experiments 1 and 2 and the manual segmentations.

The maximal segmentation errors are higher for data set 2, due to its higher shape and intensity variability, as the images were acquired in different clinical centers, from patients with different pathologies. This is disadvantageous for statistical modeling, as a sufficiently large and representative training data set is assumed to be available.

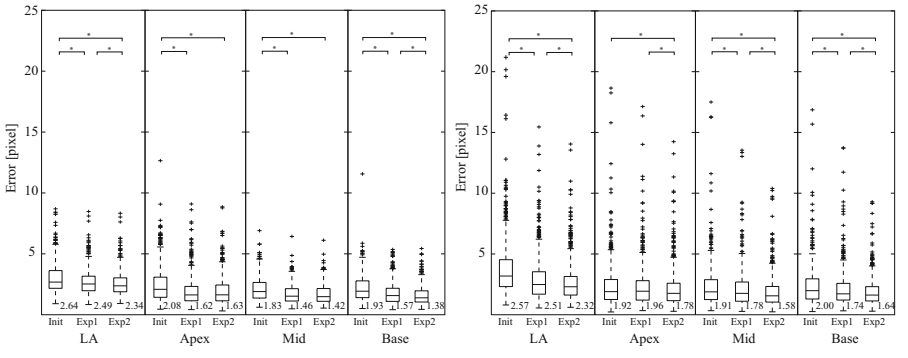

(a) Data set 1 (b) Data set 2

Fig. 2. Segmentation errors ϵ per contour for the initialization (Init) and after fitting of our hybrid model without (Exp1) and with (Exp2) the registration component enabled. The errors are given for all LA slices (LA), and for the apical (Apex), mid (Mid) and basal (Base) SA slices separately. Statistically different values are indicated above the graph: $^*p < 0.05$.

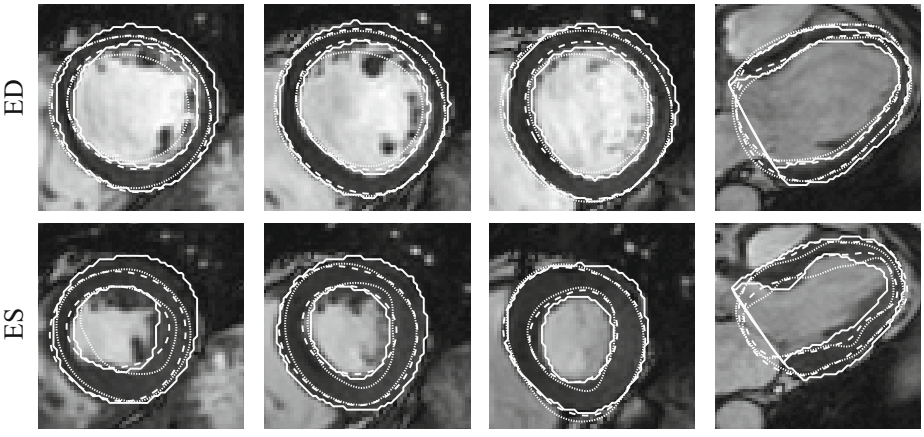

Fig. 3. ED and ES frame of 3 SA and 1 LA slice of a selected patient, with the resulting segmentations of Experiments 1 (dotted) and 2 (dashed) and the ground truth manual segmentations (full).

4 Discussion and Conclusion

We propose a hybrid spatio-temporal segmentation+registration approach for 3D+time image sequences. The method combines statistical global shape and local intensity models of only a few selected time frames with simultaneous frame-to-frame non-rigid registration. Segmentation clues are passed in both directions to guide the segmentation of all frames simultaneously using all available intensity and shape information. Hence, our hybrid model allows the use of prior knowledge, necessary for the segmentation of ambiguous image regions, in all time frames, while keeping training requirements within bounds. It was shown that the simultaneous registration improves landmark-based segmentation. The different orientations of the slices and the sparseness of the entire image stack was taken into account by defining a set of in-plane landmarks to guide the intensity models, next to the shape-defining control points. The focus of this work was on the theoretical concept of the 3D hybrid model. The presented framework was intentionally kept as general as possible, allowing easy adaptation of individual components, such as the used intensity features, number of control points etc. Alternative model choices may improve the segmentation results. E.g. the large LA segmentation errors may be explained by large local errors near the apex and base, due to the current control point mesh definition with limited apical and basal sampling. Hence, segmentation performance may be improved by a more sophisticated definition of the underlying 3D interpolation mesh, a more robust optimization procedure, alternative local intensity features, etc.

The proposed hybrid segmentation and registration method can as well be used to segment entire image sequences, based on statistically learned shape and intensity models of only a few selected frames, as previously shown for 2D+time MR sequences [7].

References

1. Cootes, T.F., Taylor, C.J., Cooper, D., Graham, J.: Active shape models - their training and application. Computer Vision and Image Understanding 61(1), 38–59 (1995)
2. Hamarneh, G., Gustavsson, T.: Deformable spatio-temporal shape models: extending active shape models to 2D+time. Image Vision Computing 22, 461–470 (2004)
3. Oost, C.R., Lelieveldt, B., Üzümcü, M., Lamb, H.J., Reiber, J.H.C., Sonka, M.: Multi-view Active Appearance Models: Application to X-Ray LV Angiography and Cardiac MRI. In: Taylor, C.J., Noble, J.A. (eds.) IPMI 2003. LNCS, vol. 2732, pp. 234–245. Springer, Heidelberg (2003)
4. van Assen, H.C., Danilouchkine, M.G., Frangi, A.F., Ordás, S., Westenberg, J.J.M., Reiber, J.H.C., Lelieveldt, B.P.F.: SPASM: A 3D-ASM for segmentation of sparse and arbitrarily oriented cardiac MRI data. Medical Image Analysis 10(2), 286–303 (2006)
5. Hautvast, G., Lobregt, S., Breeuwer, M., Gerritsen, F.: Automatic contour propagation in cine cardiac magnetic resonance images. IEEE Transactions on Medical Imaging 25(11), 1472–1482 (2006)
6. Perperidis, D., Mohiaddin, R., Edwards, P., Rueckert, D.: Segmentation of cardiac MR and CT image sequences using model based registration of a 4D statistical model. Progress in Biomedical Optics and Imaging 8(1), D5121 (2007)
7. Elen, A., Bogaert, J., Maes, F., Suetens, P.: A spatio-temporal model-for joint segmentation and registration of cardiac cine MR images. Submitted to Medical Image Analysis (2011)
8. Cremers, D.: Statistical shape knowledge in variational image segmentation. PhD thesis, Universität Mannheim (2002)
9. Maes, F., Collignon, A., Vandermeulen, D., Marchal, G., Suetens, P.: Multimodality image registration by maximization of mutual information. IEEE Transactions on Medical Imaging 16(2), 187–198 (1997)
10. Kadish, A.H., Bello, D., Finn, J.P., Bonow, R.O., Schaechter, A., Subacius, H., Albert, C., Daubert, J.P., Fonseca, C.G., Goldberger, J.J.: Rationale and design for the defibrillators to reduce risk by magnetic resonance imaging evaluation (DETERMINE) trial. Journal of Cardiovascular Electrophysiology 20(9), 982–987 (2009)
11. Elen, A., Hermans, J., Ganame, J., Loeckx, D., Bogaert, J., Maes, F., Suetens, P.: Automatic 3-D breath-hold related motion correction of dynamic multislice MRI. IEEE Transactions on Medical Imaging 29(3), 868–878 (2010)

Statistical Atlas of Human Cardiac Fibers: Comparison with Abnormal Hearts

Hervé Lombaert[1,2], Jean-Marc Peyrat[4], Laurent Fanton[3], Farida Cheriet[2], Hervé Delingette[1], Nicholas Ayache[1], Patrick Clarysse[3], Isabelle Magnin[3], and Pierre Croisille[3]

[1] INRIA, Asclepios Team, Sophia-Antipolis, France
[2] École Polytechnique de Montréal, Canada
[3] CREATIS, Université de Lyon, France
[4] Siemens Molecular, Oxford, UK

Abstract. Criteria of normality of the cardiac fibers are important in cardiomyopathies. In this paper, we investigate the differences in the cardiac fiber structures between 10 hearts classified as healthy and 6 hearts classified as abnormal, and determine if properties of the cardiac fiber structures can be discriminants for abnormality. We compare the variability of the fiber directions from abnormal hearts to an atlas of healthy hearts. The human atlas of the cardiac fiber structures is built with an automated framework based on symmetric Log-domain diffeomorphic demons. We study the angular variability of the different fiber structures. Our preliminary results might suggest that a higher variability of the fiber structure directions could possibly characterize abnormality of a heart.

1 Introduction

Cardiovascular diseases are by far the number one killer in the US with over 930,000 deaths annually and 71 millions, more than a fifth of the population, live with a form of cardiovascular disease [20]. The characterization of the consequences lead by specific cardiopathies is essential to a better diagnosis and a better treatment of these diseases. Among the possible causes, the differences in the cardiac fiber architecture could be an promising topic. The heart is composed of myocardial fibers organized in a complex laminar structure [18,10], and the cardiac fiber structures have an important role in electrophysiology [8], in mechanical functions [4], and in remodeling [23] of the heart. Changes in the fiber structures are for instance inherent in myocardial hypertrophy [9,19,6]. Myocardial disarray, or disorganisation of the fibers, is also still the focus of contentious studies [2]. The question of normality of the cardiac fiber structures arises when trying to assess the role of myocardial disarray in cardiomyopathies. In this paper, we try to assess whether there is a difference in the cardiac fiber structures between hearts classified as normal and hearts considered as abnormal.

The directions of the fiber structures and their variability can be measured with Diffusion Tensor Imaging (DT-MRI). A human atlas of the cardiac fiber

O. Camara et al. (Eds.): STACOM 2011, LNCS 7085, pp. 207–213, 2012.

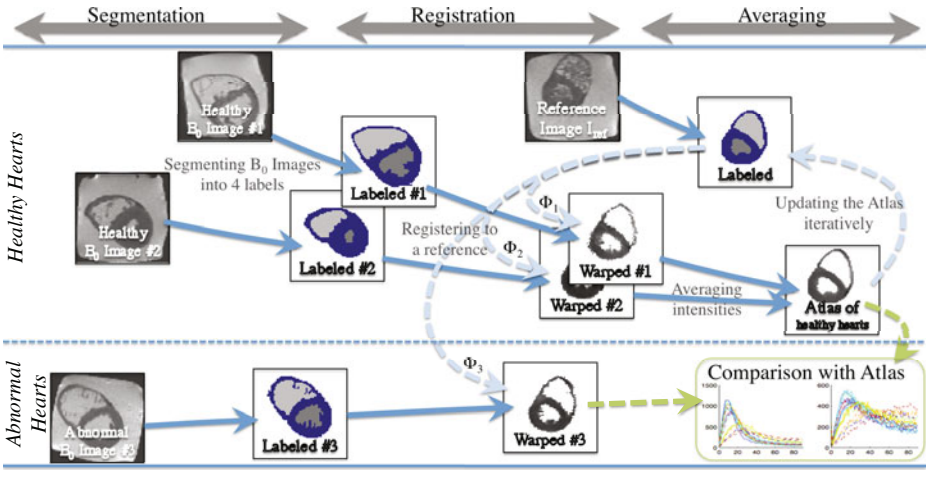

Fig. 1. *Construction of the healthy atlas*: The myocardia are segmented. Images are then aligned and registered non-rigidly toward a reference image. The atlas is constructed iteratively by averaging acquired images in the average heart shape. *Comparison with the atlas*: Abnormal hearts are registered to the average healthy heart. The cardiac fiber structures of each abnormal heart are compared with the structures of the average healthy heart.

structures from DT-MRI [12,13] has recently been built with 10 healthy *ex vivo* hearts. We register 6 *ex vivo* hearts classified as abnormal to the atlas of healthy hearts and analyze the angular differences between the fiber structure directions of the abnormal hearts and the ones of the average healthy heart. The statistical study shows that the directions of the cardiac fiber structures vary more in abnormal hearts than in healthy hearts. The preliminary results might suggest that a higher variability of the fiber structure directions could possibly characterize abnormality.

2 Material and Method

2.1 Dataset

The human dataset [5,16] consists of 10 healthy and 6 abnormal *ex vivo* human hearts acquired during forensic autopsies. All cases are from extra cardiac sudden deaths. However, the true nature of deaths is not available. The images have been acquired on a 1.5T MR scanner (Avanto Siemens), all within 24 hours after death and prior to the examination by the pathologist, with a bipolar echo planar imaging using 4 repetitions of 12 gradient images. The diffusion-weighted images, from which are estimated the diffusion tensors, are of size 128x128x52 with an isotropic resolution of 2 mm. Criteria of abnormality [17] are based on the heart weight (with given permitted weight limits within the 95% percentile),

the septal thickness (with a maximal thickness defined at 12 mm for women and 14 mm for men), and on subsequent pathology examination.

2.2 Registration of Abnormal Hearts

The atlas of diffusion tensors is constructed using the automated framework described in [12]. The method is summarized in Fig. 1 and has four steps. The myocardium is segmented [3] and its mask is used to guide the nonrigid pairwise registration [21,22,14]. All hearts are registered to an initial reference image, which is updated toward the morphological average of all hearts [7]. Once the transformations of all hearts toward the average cardiac shape are computed, the diffusion tensors are warped [15] to the morphological atlas.

The processing of abnormal hearts is performed within the same framework [12]. Firstly, the myocardia of the abnormal hearts are segmented using a minimal user interaction. Secondly, their masks are registered to the newly computed average healthy heart. The diffusion tensors are warped accordingly to the shape of the average healthy heart.

2.3 Comparison with Abnormal Hearts

The diffusion tensors fields from all hearts, $\{\mathbf{D}^{(i)}\}_{i=1\ldots N}$ (with $N = 10$ healthy + 6 abnormal hearts), are warped to the morphological average of the healthy hearts (i.e., in a common reference). The Log-Euclidean metric [1] is used to compute efficiently the average diffusion tensor of the healthy hearts (hearts #1 to #10) with the Fréchet mean, $\overline{\mathbf{D}} = \exp\left(\frac{1}{10}\sum_{i=1}^{10}\log(\mathbf{D}^{(i)})\right)$.

The eigendecomposition of the diffusion tensor matrix $\overline{\mathbf{D}}$ gives the principal directions $\mathbf{v}_{1,2,3}$ describing the fiber structures. More precisely, the first eigenvector $\mathbf{v}_1$ gives the fiber orientation, the second eigenvector $\mathbf{v}_2$ is believed to lie within the laminar sheet and to be perpendicular to the fiber, and the third eigenvector $\mathbf{v}_3$ is assumed to give the normal of the laminar sheet.

The abnormal hearts are compared with the average healthy heart by measuring the angular deviations of the fiber structures of each heart with the average heart. The angle θ between the direction of an eigenvector $\mathbf{v}_j$ of the i^{th} heart and the direction of the corresponding average eigenvector $\overline{\mathbf{v}}_j$ is defined between 0° and 90° with:

$$\theta_j^{(i)} = \arccos\left(\frac{|\mathbf{v}_j^{(i)} \cdot \overline{\mathbf{v}}_j|}{\| \mathbf{v}_j^{(i)} \| \| \overline{\mathbf{v}}_j \|}\right) \tag{1}$$

The absolute value of the dot product removes the inherent ambiguity in the orientation of the eigenvectors (i.e., $|a \cdot b| = |a \cdot (-b)|$).

3 Results

We study the deviation of the fiber structures of each heart (healthy and abnormal) to the average structures of the healthy hearts (i.e., to the atlas). The

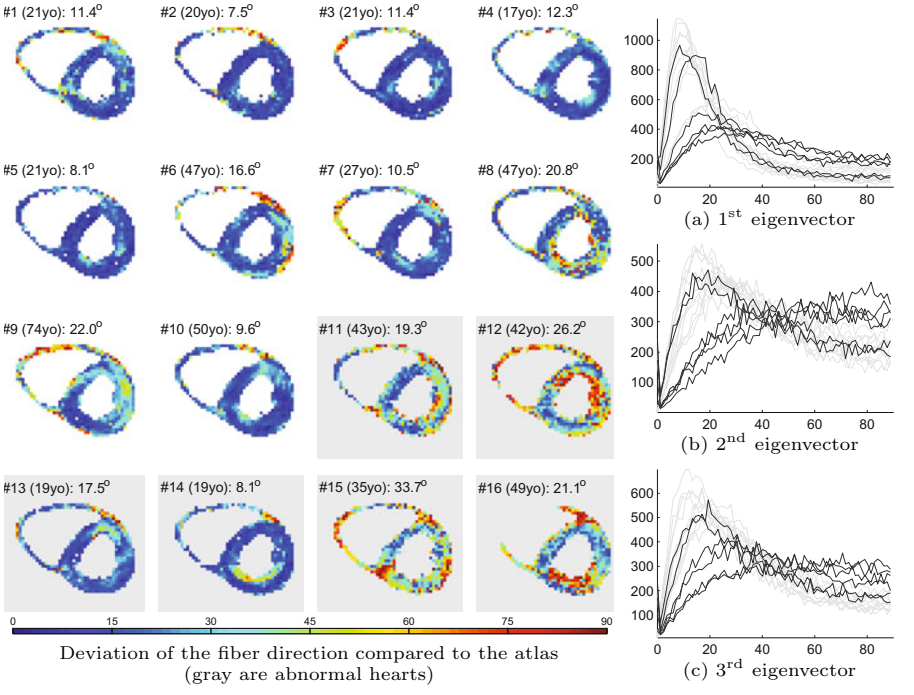

Fig. 2. *(Left)* Deviation of the fiber direction of each heart to the atlas of healthy hearts. Coloring is the angular difference in degree. Abnormal hearts are with gray background. The age of each subject is provided in each sub figure. *(Right)* Histograms of the angular variability (in degrees) of *(a)* the 1st eigenvector, *(b)* 2nd eigenvector, and *(c)* 3rd eigenvector (abnormal hearts in dark lines, healthy hearts in light lines).

structures in the healthy hearts are, as expected, very similar to the atlas. The histograms of the angular differences of the first, second, and third eigenvectors of the healthy hearts to the atlas (gray curves in Fig. 2) show average modes of respectively (i.e., the curves are peaking at) $\overline{\theta}_1 = 13.03°$, $\overline{\theta}_2 = 21.76°$, and $\overline{\theta}_3 = 15.77°$. Abnormal hearts show by contrast fiber structures that have larger deviations to the atlas of healthy hearts. The histograms of the angular differences of structures show higher modes in abnormal hearts (black in Fig. 2), with a deviation of $\overline{\theta}_1 = 20.96°$ for the fibers (i.e., first eigenvector) and of $\overline{\theta}_2 = 48.21°$ and $\overline{\theta}_3 = 34.36°$ for the laminar sheets (i.e., second and third eigenvector). The visualization of the angular difference in a slice of each heart shows large discrepancies in the left ventricle with localized high-variability areas for patient #12, #15, and #16 (shown in the sub-figures of Fig. 2 with gray backgrounds). This is again confirmed when visualizing the angular difference of the second and third eigenvectors (i.e., the laminar sheets). It is to note that the registration of the right ventricle (which exhibited a very small volume) failed for the last patient (#16). The patients #13 and #14, even if classified as abnormal,

presented consistently very small deviations to the average fiber structures of the healthy atlas (Fig. 2).

4 Discussion and Conclusion

The question whether the variability of the cardiac fiber structures is a marker to normality or abnormality is relevant to the study of many cardiomyopathies, including left ventricular hypertrophy or myocardial disarray. In this paper, we compared the structural changes between a population of abnormal hearts and of healthy hearts. It was shown that the three eigenvectors of the diffusion tensors have measurable differences between abnormal hearts and healthy hearts. When compared to an atlas of healthy hearts, the fibers of abnormal hearts showed an angular difference of 20.96°, while the fibers of healthy hearts showed less deviation with 13.03°. The laminar sheets also showed a greater deviation and a greater variability in abnormal hearts than in healthy hearts. Even though the laminar sheet is known to be more variable than the fiber structure in humans [12], the difference in both populations is non negligible (deviation of the laminar sheet normal of 34.36° in abnormal hearts compared to 15.77° in healthy hearts). The abnormal hearts also experience a large fiber angle difference around trabeculae areas. A localized study might reveal the origin of such large deviance.

Nonetheless, two outliers are present (hearts #13 and #14 as shown in Fig. 2). They were initially classified as abnormal even though their cardiac fiber structures are very similar to the average healthy heart (deviation of 17° and 8°). We hold the attention on the age of both subjects, both very young (19 years old). Furthermore, the modes in healthy hearts, i.e., the peaks of the histograms in Fig. 2(a), also show that the cardiac fibers are less variable in younger subjects than in older subjects. Age is thought to have an impact in the fiber structure of skeletal muscles [11]. No study has yet been performed in cardiac muscles. For that matter, the mode of the angular differences of the first eigenvector (i.e., the fiber direction) was plotted against the age of each subject (Fig. 3). The correlation factor between age and fiber variability is 0.73 when considering only the 10 healthy hearts (with a low p-value of 0.016). When considering only the abnormal hearts, the correlation factor is higher at 0.86 (with a p-value of 0.029). The estimated least-square fit lines of both population are overlaid in Fig. 3. Before hypothesizing that the variability of the fiber directions increases faster with age in abnormal hearts, many unknown parameters should be considered firstly (for instance, the distinction between primitive hypertrophy or secondary hypertrophy, known to occur in old subjects, is here unknown).

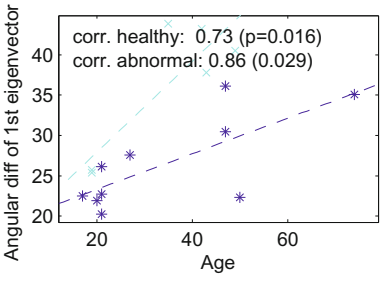

Fig. 3. Possible correlation between the age and the fiber variability (healthy hearts in blue with a correlation factor $\rho = 0.73$, abnormal in cyan with $\rho = 0.86$)

In conclusion, our study comparing a population of abnormal hearts and of healthy hearts showed that there are observable differences in the fiber directions in both populations. Abnormal hearts have fiber directions that are more variable and that are on average 20.96° different from the average healthy heart. Future studies will include additional hearts in order to further study these preliminary findings.

Acknowledgment. The authors wish to acknowledge the members of the Asclepios Team. The project was supported financially by the National Science and Engineering Research Council of Canada (NSERC), the Michael Smith Scholarship (CGS-MSFSS), and the EGIDE/INRIA Scholarship.

References

1. Arsigny, V., Fillard, P., Pennec, X., Ayache, N.: Log-Euclidean metrics for fast and simple calculus on diffusion tensors. Magnetic Resonance in Medicine 56(2), 411–421 (2006)
2. Becker, A.E., Caruso, G.: Myocardial disarray. a critical review. British Heart Journal 47(6), 527–538 (1982)
3. Boykov, Y., Jolly, M.-P.: Interactive Organ Segmentation Using Graph Cuts. In: Delp, S.L., DiGoia, A.M., Jaramaz, B. (eds.) MICCAI 2000. LNCS, vol. 1935, pp. 276–286. Springer, Heidelberg (2000)
4. Costa, K.D., Holmes, J.W., Mcculloch, A.D.: Modelling cardiac mechanical properties in three dimensions. Mathematical, Physical and Engineering Sciences 359(1783), 1233–1250 (2001)
5. Frindel, C., Robini, M., Croisille, P., Zhu, Y.-M.M.: Comparison of regularization methods for human cardiac diffusion tensor MRI. Med. Im. An. 13(3) (2009)
6. Grajek, S., Lesiak, M., Pyda, M., Zajac, M., Paradowski, S., Kaczmarek, E.: Hypertrophy or hyperplasia in cardiac muscle. post-mortem human morphometric study. European Heart Journal 14(1), 40–47 (1993)
7. Guimond, A., Meunier, J., Thirion, J.P.: Average Brain Models: A Convergence Study. In: Computer Vision and Image Understanding, pp. 192–210 (2000)
8. Hooks, D.A., Tomlinson, K.A., Marsden, S.G., LeGrice, I.J., Smaill, B.H., Pullan, A.J., Hunter, P.J.: Cardiac Microstructure: Implications for Electrical Propagation and Defibrillation in the Heart. Circulation Research 91(4), 331–338 (2002)
9. Karsner, H.T., Saphir, O., Todd, T.W.: The state of the cardiac muscle in hypertrophy and atrophy. The American Journal of Pathology 1(4) (July 1925)
10. LeGrice, I.J., Smaill, B.H., Chai, L.Z., Edgar, S.G., Gavin, J.B., Hunter, P.J.: Laminar structure of the heart: ventricular myocyte arrangement and connective tissue architecture in the dog.. The American Journal of Physiology 269(2) (1995)
11. Lexell, J., Taylor, C.C.: Variability in muscle fibre areas in whole human quadriceps muscle: effects of increasing age. Journal of Anatomy 174, 239–249 (1991)
12. Lombaert, H., Peyrat, J.-M., Croisille, P., Rapacchi, S., Fanton, L., Clarysse, P., Delingette, H., Ayache, N.: Statistical Analysis of the Human Cardiac Fiber Architecture from DT-MRI. In: Metaxas, D.N., Axel, L. (eds.) FIMH 2011. LNCS, vol. 6666, pp. 171–179. Springer, Heidelberg (2011)
13. Lombaert, H., Peyrat, J.-M., Rapacchi, S., Fanton, L., Delingette, H., Croisille, P., Clarysse, P., Ayache, N.: In: ISMRM (2011)

14. Mansi, T., Pennec, X., Sermesant, M., Delingette, H., Ayache, N.: iLogDemons: A Demons-Based registration algorithm for tracking incompressible elastic biological tissues. International Journal of Computer Vision, 1–20 (2010)
15. Peyrat, J.-M., Sermesant, M., Pennec, X., Delingette, H., Xu, C., McVeigh, E.R., Ayache, N.: A Computational Framework for the Statistical Analysis of Cardiac Diffusion Tensors: Application to a Small Database of Canine Hearts. IEEE Transactions on Medical Imaging 26(11), 1500–1514 (2007)
16. Rapacchi, S., Croisille, P., Pai, V., Grenier, D., Viallon, M., Kellman, P., Mewton, N., Wen, H.: Reducing motion sensitivity in free breathing DWI of the heart with localized Principal Component Analysis. In: ISMRM (2010)
17. Silver, M., Gotlieb, A.I., Schoen, F.R.: Cardiovascular Pathology, 3rd edn. Churchill Livingstone (2001)
18. Streeter, D.D., Spotnitz, H.M., Patel, D.P., Ross, J., Sonnenblick, E.H.: Fiber Orientation in the Canine Left Ventricle during Diastole and Systole. Circulatory Research 24(3), 339–347 (1969)
19. Tezuka, F.: Muscle fiber orientation in normal and hypertrophied hearts. The Tohoku Journal of Experimental Medicine 117(3), 289–297 (1975)
20. Thom, T., Haase, N., Rosamond, W., Howard, V.J., Rumsfeld, J., Manolio, T., Zheng, Z.-J., Flegal, K., Odonnell, C., Kittner, S., Lloyd-Jones, D., Goff, D.C., Hong, Y.: Heart disease and stroke statistics–2006 update. Circulation 113, 85–151 (2006)
21. Vercauteren, T., Pennec, X., Perchant, A., Ayache, N.: Symmetric Log-Domain Diffeomorphic Registration: A Demons-Based Approach. In: Metaxas, D., Axel, L., Fichtinger, G., Székely, G. (eds.) MICCAI 2008, Part I. LNCS, vol. 5241, pp. 754–761. Springer, Heidelberg (2008)
22. Vercauteren, T., Pennec, X., Perchant, A., Ayache, N.: Diffeomorphic demons: efficient non-parametric image registration. NeuroImage 45(1), S61–S72 (2009)
23. Wu, M.-T., Tseng, W.-Y.I., Su, M.-Y.M., Liu, C.-P., Chiou, K.-R., Wedeen, V.J., Reese, T.G., Yang, C.-F.: Diffusion Tensor Magnetic Resonance Imaging Mapping the Fiber Architecture Remodeling in Human Myocardium After Infarction: Correlation With Viability and Wall Motion. Circulation 114(10), 1036–1045 (2006)

Maximum Likelihood Correction of Shape Bias Arising from Imaging Protocol: Application to Cardiac MRI

Pau Medrano-Gracia[1], David A. Bluemke[4], Brett R. Cowan[1], J. Paul Finn[2], Carissa G. Fonseca[2], João A.C. Lima[3], Avan Suinesiaputra[1], and Alistair A. Young[1]

[1] Auckland Bioengineering Institute
University of Auckland, New Zealand
{p.medrano,b.cowan,a.suinesiaputra,a.young}@auckland.ac.nz
http://www.abi.auckland.ac.nz, http://www.cardiacatlas.org
[2] Diagnostic CardioVascular Imaging
University of California, Los ngeles, USA
{cfonseca,pfinn}@mednet.ucla.edu
http://dcvi.radsci.ucla.edu
[3] The Donald W. Reynolds Cardiovascular Clinical Research Center
The Johns Hopkins University, USA
jlima@jhmi.edu
http://www.reynolds.jhmi.edu
[4] NIH Clinical Center, USA
bluemked@mail.nih.gov
http://clinicalcenter.nih.gov

Abstract. To establish a fair comparison between shape models derived from different imaging protocols, a mapping correcting local bias must be applied. In this paper, a multi-dimensional statistical model has been investigated to correct the systematic differences between Steady-State Free Precession (SSFP) and Gradient Recalled Echo (GRE) cardiac MRI protocols. This statistical model makes use of the Maximum Likelihood (ML) approach to estimate the local parameters of the respective GRE and SSFP distributions. Once those parameters are known, a local mapping can be applied. We applied this method to 46 normal volunteers who were imaged with both protocols. The SSFP model was estimated from the corresponding GRE model and validation was performed with leave-one-out experiments. The error was examined in both the local model parameters and the clinically important global mass and volume estimates. Results showed that the systematic bias around the apex and papillary muscles could be locally corrected and that the mapping also provided a global correction in cavity volume (average error of 0.4 ± 12.4 ml) and myocardial mass (-1.2 ± 11.1 g).

Keywords: Statistical Model, Cardiac Magnetic Resonance Imaging (MRI), Finite Element Modelling, Steady-State Free Precession (SSFP), Gradient Recalled Echo (GRE), Protocol Correction.

O. Camara et al. (Eds.): STACOM 2011, LNCS 7085, pp. 214–223, 2012.

1 Introduction

It is often necessary to compare two shape representations arising from different imaging protocols, for example as imaging hardware or acquisition parameters are refined and developed over time. However, the difference in imaging protocols may lead to regional bias in the shape estimate which must be removed before any statistical shape comparisons can be made. In the field of cardiac Magnetic Resonance Imaging, GRE (Gradient Recalled Echo, also known as FGRE or FLASH) was the clinical standard until 2001. Since then, SSFP (Steady-State Free Precession) emerged as the new standard protocol for Cardiac MRI given its advantages in terms of signal quality and acquisition time.

Typically, SSFP results in larger estimates of left ventricular cavity volume and smaller estimates of left ventricular (LV) mass than GRE [1]. However, the effect of imaging protocol on statistical shape representations is unknown. In the Cardiac Atlas Project [2], approximately 2500 GRE cases have been contributed as part of the MESA study [3]. In order to compare statistical shape models between this cohort and others obtained using the SSFP protocol, a shape mapping must be generated which corrects for bias between the two protocols. Other approaches, not necessarily in these 2 protocols, are also presented in the literature: see [4] for an intensity inter-scanner correction, [5] for a review of various methods for PET/MRI and [6] for a comparison between PET-MRAC and PET-CTAC in the torso.

To our knowledge, this is the first attempt at mapping the protocol effect across a population of shape models. This is of key importance for we intend to compare large populations using algorithms that can automatically detect regional abnormalities in patients regardless of the imaging protocol in which they were acquired (see for example [7]). It is also important to ensure that any local mapping not only corrects local bias, but also corrects differences in clinical indices of global function, including mass and volume, which have previously been noted in the literature [1]. Since the mapping is derived on the local parameters only, it is not obvious whether the global functional indices will also be corrected. Volume and mass were not included in the optimisation of the local mapping, but must also be validated for clinical application.

This paper derives such a mapping from 46 patients scanned in both GRE and SSFP modalities. The shape model used in this paper is described in detail in [8]. Section 2 describes the methodology of our approach, Section 3 explains the experimentation and validation in terms of leave-one-out experiments as well as volume and mass, and conclusions are discussed in Section 4.

2 Methods

The image dataset consisted of 50 normal volunteers who were scanned with both GRE and SSFP protocols on a Siemens 1.5 T scannner. Four patients were excluded due to inconsistent images arising from breath-holding artefacts. The demographics are summarised in Table 1. Finite Element (FE) shape models of

the LV were then fitted by experts using a standardised interactive procedure [8]. Each model was generated independently using its own coordinate system. Thus, even though each patient must have had the same *patient coordinates*, the *model coordinates* were expressed in different reference systems (see Figure 1).

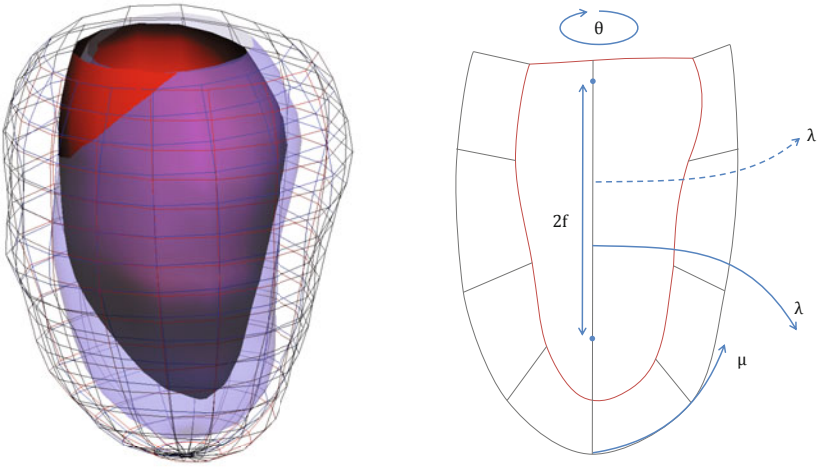

Fig. 1. On the left (A), 3D SSFP model (blue) superimposed to the GRE model (red) in *model coordinates* for example-case no. 25 (ED). On the right (B), prolate spheroidal coordinate system: focal length (f), radial parameter (λ), hyperboloidal parameter (μ) and azimuthal angle (θ) [8].

Table 1. Age and sex distribution of the 46 cases analysed

	Number	Age ($\mu \pm \sigma$)
Male	26	42.5 ± 11.7
Female	20	37.3 ± 13.9
Total	46	40.2 ± 12.9

The FE models were represented by 215 Bzier parameters (in 16 elements both for the endocardial and epicardial surfaces) in the prolate spheroidal coordinate system [9], as can be seen in Figure 1-B. The Bzier parameters were statistically modelled in GRE and SSFP space and a global mapping was derived through the Maximum Likelihood (ML) parameters of their probability distributions.

The first step to determine the systematic differences was to align the GRE and SSFP model coordinate systems for each patient so that we could then

compare the parameters in the same reference. This was achieved by means of rigid body alignment of the SSFP model to GRE coordinates. In Figure 4-A the average difference between GRE and SSFP surfaces is presented. The most significant regional differences appear in the apical endocardium and around the papillary muscles. Also some differences arise in the basal plane. These regional differences are physically reasonable since GRE contrast is dependent on blood flow to a greater extent than SSFP, leading to possible differences in regions where apical trabeculation or papillary muscles disrupt the local blood flow [1].

Once the models were aligned in a common reference system (GRE's), the statistical distributions of the model parameters were examined. Anderson-Darling's test for normality [10] reported that 88% of the parameter distributions could have been drawn from a Gaussian distribution with a critical level of 5%. A Gaussian approximation was therefore employed for all cases. The parameters of the Gaussian distributions were estimated by means of ML. An example of these distributions is shown in Figure 2.

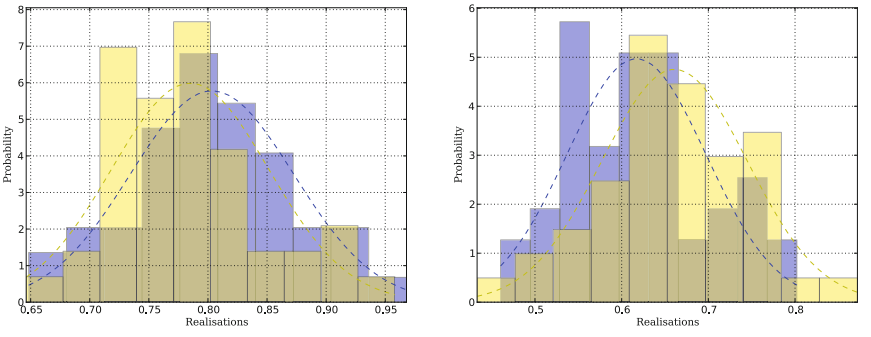

Fig. 2. Sample distributions of the values for parameters' numbers $j = 21$ and $j = 110$ of the FE models (out of $M = 215$ parameters). The blue distribution corresponds to the GRE protocol and the yellow one to SSFP. The histograms have been approximated by Gaussian distributions $\mathcal{N}(\mu_j^{GRE}, \sigma_j^{GRE})$ and $\mathcal{N}(\mu_j^{SSFP'}, \sigma_j^{SSFP'})$ respectively.

In Figure 3 we formalise the different signals that we have used throughout our experiments. For each one of the parameters $j = 1, \ldots, M$, and each patient $n = 1, ..., 46$, let $GRE_j(n)$ be the GRE samples, $SSFP_j(n)$ the SSFP samples, $SSFP'_j(n)$ the aligned SSFP samples in the GRE coordinate system and $\widehat{SSFP}_j(n)$ the estimated SSFP samples from the GRE models. Therefore, we define T_j as the mapping derived for each parameter which is applied to $GRE_j(n)$ as per equation 1.

$$\widehat{SSFP}_j(n) \equiv T_j(GRE_j(n)) = \left(\frac{GRE_j(n) - \mu_j^{GRE}}{\sigma_j^{GRE}} \right) \sigma_j^{SSFP'} + \mu_j^{SSFP'} \qquad (1)$$

Given the four Gaussian-distribution parameters (mean and standard deviation of GRE and of SSFP, namely $\mathcal{N}(\mu_j^{GRE}, \sigma_j^{GRE})$ and $\mathcal{N}(\mu_j^{SSFP'}, \sigma_j^{SSFP'})$

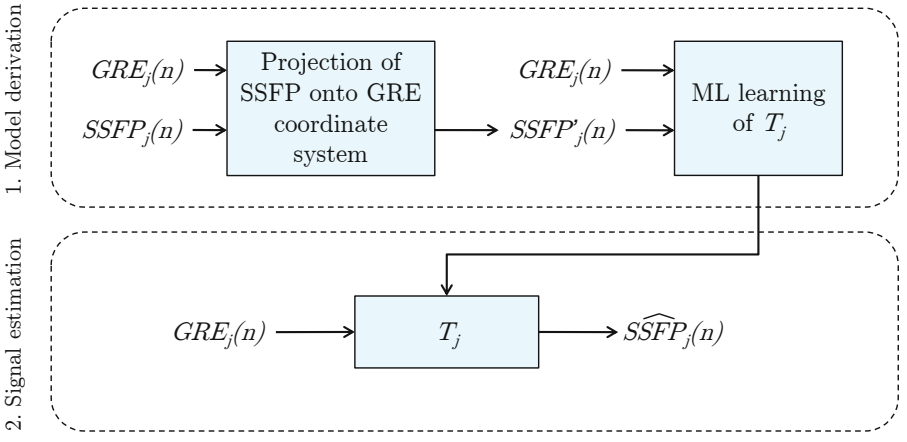

Fig. 3. Signal model for the GRE-SSFP correction mapping

respectively), we can estimate any parametric value $\widehat{SSFP}_j(n)$ from its corresponding $GRE_j(n)$ with equation 1, which may be understood as a form of linear regression.

Estimating the correct mass and volume of the LV is of crucial importance in the diagnosis of a number of cardiovascular diseases [1]. Any local correction of shape parameters must also correct global clinical indices of mass and volume. Therefore, in Section 3, we validated our statistical model through the mass and volumes of the resulting models.

3 Results

Validation was performed in two steps. Firstly, leave-one-out ($L1$) experiments were run to test the predictive power of the models by training the ML parameters with $N-1$ cases, leaving one out at a time. Secondly, we trained the algorithm with all the available cases ($L0$). In both cases, we computed the volume of the resulting models. This was done to ensure that the local mapping also corrects the global discrepancy previously noted in mass and volume.

Thus, using the model described in Section 2, the SSFP parameters were estimated from their corresponding GRE distributions for each parameter. Figure 4-B shows that the transformation $T(L0)$ has corrected the regional bias present in the uncorrected shape parameters.

The initial error (expressed as $\log_{10}|\mu| \pm \log_{10}\sigma^{-1}$) in normalised radial shape coordinate (average value of $\lambda = 0.67$ for $SSFP'$ models) between the original GRE and $SSFP'$ models was of -2.38 ± 0.96. In the $L1$ experiments, the error between estimated and actual SSFP values went down to -4.32 ± 1.02, and in $L0$, it was of -5.88 ± 0.98.

Table 2. Volume comparison of the original volumes versus the leave-one-out ($L1$) and estimated volumes from all cases ($L0$). The error in volume is computed using the SSFP volume as the reference.

Cavity vol. ED (ml)	GRE	$SSFP$	$\widehat{SSFP}_{L1}$	$\widehat{SSFP}_{L0}$
Mean (μ)	126.2	134.8	135.6	135.1
Std. deviation (σ)	27.0	28.4	29.0	28.8
Error mean	−8.6	–	0.9	0.4
Error std. deviation	12.4	–	12.9	12.4

Cavity vol. ES (ml)	GRE	$SSFP$	$\widehat{SSFP}_{L1}$	$\widehat{SSFP}_{L0}$
Mean (μ)	52.8	53.5	54.3	54.0
Std. deviation (σ)	12.6	13.8	13.4	13.0
Error mean	−0.6	–	0.9	0.5
Error std. deviation	8.2	–	8.8	8.3

LV mass ED (g)	GRE	$SSFP$	$\widehat{SSFP}_{L1}$	$\widehat{SSFP}_{L0}$
Mean (μ)	145.3	132.3	130.9	131.1
Std. deviation (σ)	33.1	32.1	30.7	30.7
Error mean	12.34	–	−1.2	−1.2
Error std. deviation	10.16	–	11.1	11.1

Table 2 reports the mean and standard deviation of the computed volumes for these experiments. The table is structured in 2 vertical sections: the original volumes ($GRE, SSFP$) and the validation volumes from the leave-one-out experiments ($L1$) and the corrected ones ($L0$) using all available cases. The volume is provided for the endocardial cavity of the LV at ED, ES and the estimated mass through the myocardial volume at ED. The error in volume was calculated using the SSFP models as a reference since this is the most accurate of the available measures.

Results show that the corrected volumes from the GRE signal ($L0$) follow the SSFP ones very closely with an average bias of ≤ 0.5 ml in the cavity and of -1.2 g in the LV mass. This is also evident in the Bland-Altman plots [11] in Figure 5 which show how the cloud of points move toward zero after the correction whilst preserving the intrinsic variance of the GRE population. Also, the close agreement of the leave-one-out volumes ($L1$) portray the robustness and the goodness of the predictive power of the algorithm.

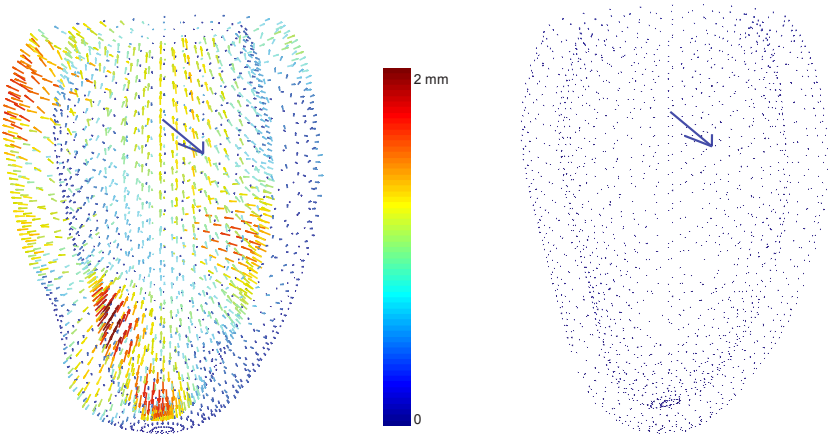

(A) (B)

Fig. 4. On the left (A), average difference between the GRE and $SSFP$ models before the mapping and on the right (B), average difference between the estimated $\widehat{SSFP}_{L0}$ models and the $SSFP$. The arrow points toward the RV and the colour indicates the Euclidean norm of the 3D vector for the same point distribution sampled from the LV FE models.

4 Conclusions and Future Work

In this work, we provided a methodology for mapping FE models derived from GRE and SSFP images. This methodology is applicable to other protocols as well since it is not limited to any particularities found in the present acquisition sequences. The uncorrected and corrected differences in mass and volume were similar to those reported (in a different patient group) using simple linear regression of global indices [1]. The uncorrected difference in mass and volume is similar to expected changes due to disease and treatment [12]. Our method can therefore be used to correct both local and global functional indices.

In the future, we plan to use this mapping to remove the protocol-induced bias and statistically compare models from different patient populations irrespective of their acquisition sequence. This is of key importance in moving forward toward the automatic detection of regional abnormalities.

A limitation of the current work is that the mapping was learnt using data from normal volunteers. It is not known whether the transformation derived from this normal dataset set will show the same degree of robustness when applied to patients with disease, such as, hypertensive hypertrophy where the wall becomes greatly thickened, or heart failure, where the ventricle becomes more spherical and the wall thins out. The transformation may primarily reflect the difference between the SSFP and GRE protocols and remain relatively invariant with disease, or it may have some dependence on ventricular geometry. A further

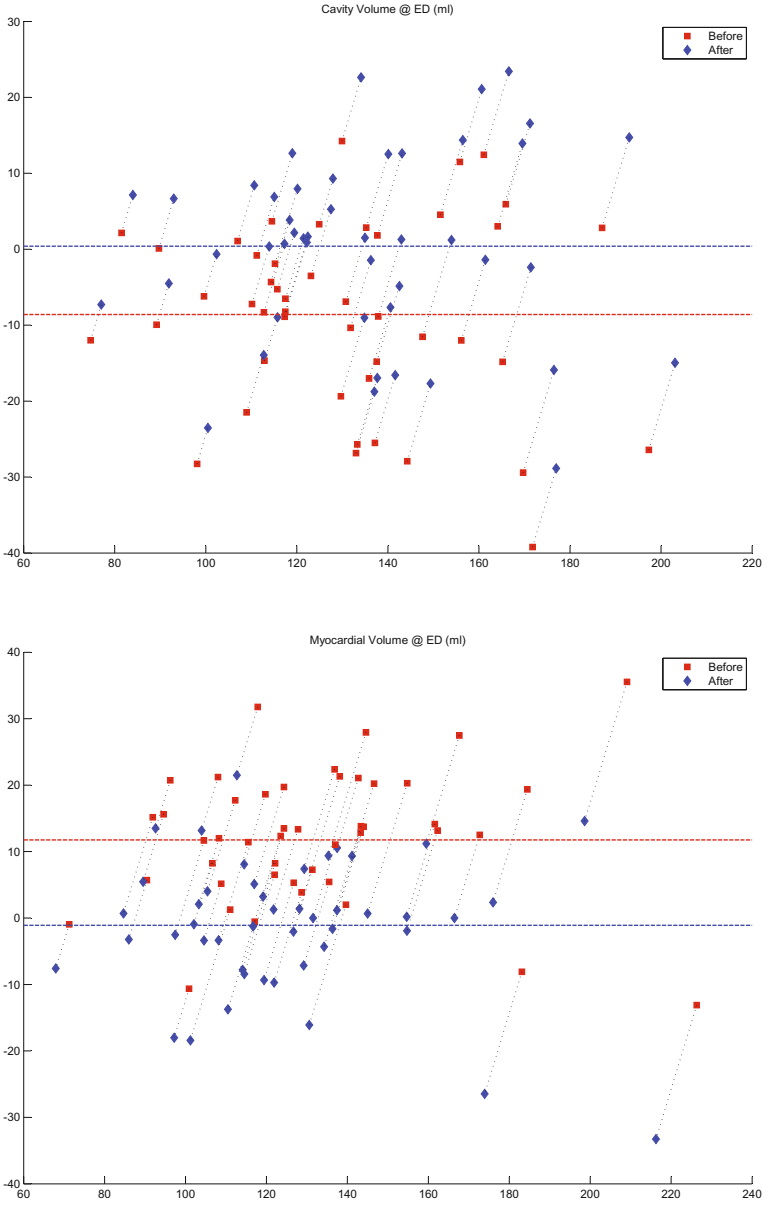

Fig. 5. Bland-Altman plots of the difference between the volumes of GRE and $SSFP$ before correction (red) and between $\widehat{SSFP}_{L0}$ and $SSFP$ after correction (blue). The plots show the endocardial cavity volume (top) and the myocardial volume (bottom), both at ED. The values for each case are connected by a dotted line. The dashed horizontal levels indicate the mean values for both data clouds.

question relates to the known increase in wall thickness that occurs with slow moving blood with GRE imaging in heart failure where the ventricle has very poor function and this effect may be accentuated. These topics should be the subject of further research.

Another area of interest could be to target the bias at the image level, well before the models are derived.

Acknowledgements. The project described was supported by Award Number R01HL087773 from the National Heart, Lung, and Blood Institute. The content is solely the responsibility of the authors and does not necessarily represent the official views of the National Heart, Lung, and Blood Institute or the National Institutes of Health.

We would also like to thank the reviewers for their insightful remarks and comments.

References

1. Malayeri, A.A., Johnson, W.C., Macedo, R., Bathon, J., Lima, J.A.C., Bluemke, D.A.: Cardiac cine MRI: Quantification of the relationship between fast gradient echo and steady-state free precession for determination of myocardial mass and volumes. Journal of Magnetic Resonance Imaging 28(1), 60 (2008)
2. Fonseca, C.G., Backhaus, M., Bluemke, D.A., Britten, R., Chung, J.D., Cowan, B.R., Dinov, I., Finn, J.P., Hunter, P.J., Kadish, A.H., Lee, D.C., Lima, J.A.C., Medrano-Gracia, P., Shivkumar, K., Tao, W., Young, A.A.: The Cardiac Atlas Project – An Imaging Database for Computational Modeling and Statistical Atlases of the Heart. Bioinformatics (in press, 2011)
3. Bild, D., Bluemke, D., Burke, G., Detrano, R., Diez Roux, A., Folsom, A., Greenland, P., et al.: Multi-Ethnic Study of Atherosclerosis: objectives and design. American Journal of Epidemiology 156(9), 871 (2002)
4. Sled, J.G., Zijdenbos, A.P., Evans, A.C.: A nonparametric method for automatic correction of intensity nonuniformity in MRI data. IEEE Transactions on Medical Imaging 17(1), 87–97 (1998)
5. Hofmann, M., Steinke, F., Scheel, V., Charpiat, G., Farquhar, J., Aschoff, P., Brady, M., Scholkopf, B., Pichler, B.J.: MRI-based attenuation correction for PET/MRI: a novel approach combining pattern recognition and atlas registration. Journal of Nuclear Medicine 49(11), 1875 (2008)
6. Beyer, T., Weigert, M., Quick, H., Pietrzyk, U., Vogt, F., Palm, C., Antoch, G., Müller, S., Bockisch, A.: MR-based attenuation correction for torso-PET/MR imaging: pitfalls in mapping MR to CT data. European Journal of Nuclear Medicine and Molecular Imaging 35(6), 1142–1146 (2008)
7. Medrano-Gracia, P., Backhaus, M., Bluemke, D.A., Chung, J.D., Cowan, B.R., Finn, J.P., Fonseca, C.G., Hunter, P.J., Kadish, A.H., Lee, D.C., Lima, J.A.C., Shivkumar, K., Tao, W., Young, A.A.: The Cardiac Atlas Project: Rationale, Design and Preliminary Results. Journal of Cardiovascular Magnetic Resonance 13(suppl. 1), O72 (2011)
8. Young, A.A., Cowan, B.R., Thrupp, S.F., Hedley, W.J., Dell'Italia, L.J.: Left Ventricular Mass and Volume: Fast Calculation with Guide-Point Modeling on MR Images. Radiology 216(2), 597 (2000)

9. Nielsen, P.M., Le Grice, I., Smaill, B.H., Hunter, P.J.: Mathematical model of geometry and fibrous structure of the heart. American Journal of Physiology- Heart and Circulatory Physiology 260(4), H1365 (1991)
10. Stephens, M.A.: EDF statistics for goodness of fit and some comparisons. Journal of the American Statistical Association 69(347), 730–737 (1974)
11. Bland, J.M., Altman, D.G.: Statistical methods for assessing agreement between two methods of clinical measurement. Lancet 1(8476), 307–310 (1986)
12. Cowan, B., Young, A., Anderson, C., Doughty, R., Krittayaphong, R., Lonn, E., Marwick, T., Reid, C., Sanderson, J., Schmieder, R., et al.: Left ventricular mass and volume with telmisartan, ramipril, or combination in patients with previous atherosclerotic events or with diabetes mellitus (from the ONgoing Telmisartan Alone and in Combination With Ramipril Global Endpoint Trial [ONTARGET]). The American Journal of Cardiology 104(11), 1484–1489 (2009)

Volumetric Modeling Electromechanics of the Heart

Hongda Mao[1], Linwei Wang[1], Ken C.L. Wong[2],
Huafeng Liu[3], and Pengcheng Shi[1]

[1] Computational Biomedicine Laboratory, Rochester Institute of Technology, USA
[2] ASCLEPIOS Research Project, INRIA Sophia Antipolis, France
[3] State Key Laboratory of Modern Optical Instrumentation
ZhengJiang University, China

Abstract. Heart is an electromechanical coupled organ, thus it is important to integrate electrical and mechanical functions when building a computational model of the heart. The existing models either treat electrical and mechanical functions separately, or follow a so-called "one-way" electromechanical coupling. However, electrical and mechanical functions of the heart are depended on each other, and realistic simulation results can only be achieved when such coupled relationship is considered. In this paper, we propose a generic model to simulate electromechanics of the heart that takes both electromechanical coupling and mechanoelectrical feedback into account. The model contains four components: cardiac electrophysiological model, electromechanical coupling, cardiac mechanics model and mechanoelectrical feedback. We report numerical simulations of a cube to provide an insight of the electromechanical coupled behavior of our model. Experiments have also been performed on a biventricular heart which present physiological plausible values, such as transmembrane potential (TMP) maps and strain maps.

1 Introduction

Cardiovascular disease remains the leading cause of death in the developed countries. Computational modeling of heart activities provides a powerful tool for understanding the mechanisms behind healthy and aberrant heart behaviors. That's why the modeling of electromechanical activities of the heart has been an active research area [1,2,3,4]. Due to the electromechanical coupled property of the heart, a complete computational heart model should contain four components: cardiac electrophysiological model, electromechanical coupling, cardiac mechanics model and mechanoelectrical feedback [4]. Cardiac electrophysiology model details the spatiotemporal dynamics of electrical wave propagation. Electromechanical coupling determines active contraction stresses resulting from electrical activation. Cardiac mechanics model describes attributions of the myocardium and the deformation related to the active contraction stresses. Cardiac mechanoelectrical feedback depicts the effect of mechanical activity to cardiac electrophysiology.

O. Camara et al. (Eds.): STACOM 2011, LNCS 7085, pp. 224–233, 2012.

Table 1. Comparison of cardiac computational models, "√" means the model contains this component, "×" means the model does not contain this component

Components / Models	Cardiac electrophysiological model	Electromechanical coupling	Cardiac mechanics model	Mechanoelectrical feedback
[5]	√	×	×	×
[7,9,8]	√	√	√	×
[1]	√	√	√	√
Proposed	√	√	√	√

However, most of existing models do not contain all the four components. On one hand, a variety of models composed of a cardiac electrophysiological model have been widely used in personalized cardiac electrophysiology (EP) simulation and recovery [5,6]. The drawback of these models is electrical activity of the heart is solved separately from mechanical activity, since the heart is assumed to be static. On the other hand, a so-called "one-way" electromechanical coupling models are popularly used in cardiac electromechanical modeling [7,8] and motion tracking [7,9]. In these works, electrical activity is first determined by the solution of a cardiac electrophysiological model and then be treated as an input for mechanical activity. Although the effect of electromechanical coupling is considered, the effect of mechanoelectrical feedback was ignored. In [1], the authors proposed an integrated heart model that included both electromechanical coupling and mechanoelectrical feedback. They found that the heart deformation contributed significantly to the dynamics of electrical wave propagation. However, the assumption of isotropic and homogeneous myocardium material properties limited its application in clinical environment. What's more, the simulations were performed only in two dimensional space. More recently, some more complex models coupled a cellular electrophysiology model and an active mechanics model for cardiac electromechanics simulation were proposed [2,3]. However, it is not practical to measure ion concentrations in clinical environment. In this paper, we mainly focus on models in tissue level. A detailed component comparison among existing computational heart models is listed in table 1.

In this paper, we propose an electromechanical coupled model for volumetric simulation electromechanical activities of the heart under the assumption that the myocardium is both anisotropic and inhomogeneous. The model includes all the aforementioned four components. To demonstrate its ability of modeling electromechanical coupled behavior, a simulation is performed on a cube with myocardial material properties. We also present simulation results of a biventricular heart, which provide us with physiological plausible values, such as TMP maps and strain maps.

The structure of this paper is as follows: in section 2, we detail the four components of the proposed electromechanical coupled model, and also give a description of numerical implementation. In section 3, we present experimental results of a cube and a biventricular heart. After having a discussion in section 4, the paper ends with a brief conclusion in section 5.

2 Methodology

2.1 Cardiac Electrophysiological Model

Although there are various electrophysiological models from cellular level to organ level [4], we have selected the monodomain two-variable Aliev-Panfilov model [10] to keep a balance of computational feasibility and physiological plausibility. The model has been widely used in cardiac EP simulation [7] and cardiac EP imaging [5].

$$\begin{cases} \frac{\partial u}{\partial t} = \bigtriangledown \cdot (\mathbf{D} \bigtriangledown u) + su(u-a)(1-u) - uv \\ \frac{\partial v}{\partial t} = -e(v + su(u-a-1)) \end{cases} \tag{1}$$

where the variable u stands for normalized TMP, and v is a recovery current variable. $\mathbf{D}$ is the conductivity tensor reflecting the anisotropic properties of the myocardium tissue. Parameters a, e, and s are constants determine the shape of TMP.

2.2 Electromechanical Coupling

The electromechanical coupling component determines the active contraction stresses resulting in electrical activation. Many active contraction models have been proposed in the literature, from realistic complex cellular models [11] to ordinary differential equation (ODE) based phenomenological model [7,1]. To keep a balance of computational feasibility and physiological plausibility, we have selected the ODE-based phenomenological model from [7]

$$\dot{\sigma_c} + \sigma_c = u\sigma_0 \tag{2}$$

where σ_c is a scalar related to active contraction stress, and $\dot{\sigma_c}$ is the time derivative of σ_c. σ_0 controls the magnitude of active stress. u is the normalized TMP from cardiac electrophysiological model. Through equation (2), electrical activity is coupled to mechanical activity. Further, we can get the contraction Cauchy stress tensor $\boldsymbol{\sigma}$ by :

$$\boldsymbol{\sigma} = -\sigma_c f \otimes f \tag{3}$$

where f is the fiber orientation of a point inside the computational domain, and $\otimes$ represents the tensor product.

2.3 Cardiac Mechanics Model

Cardiac mechanics model describes the material properties of the myocardium, which relates the active stresses generated by electromechanical coupling with the resulted heart deformation through equation (6). Since the length of a single cardiac cell changes up to 20% during a heart beat [1], the mechanical analysis

should follow finite deformation elasticity theory. With the assumption that the myocardium is elastic, we can establish the stress-strain relation by Hooke's Law:

$$\mathbf{S} = \mathbf{C}\epsilon \tag{4}$$

Here $\mathbf{S}$ is the second Piola-Kirchhoff stress tensor and ϵ the Green-Lagrangian strain tensor. $\mathbf{C}$ is the stiffness matrix accounts for the materials properties of the tissue, which refers to Young's modulus and Poisson's ratio in this paper.

2.4 Mechanoelectrical Feedback

Many previous works assumed the effect of mechanical activity to electrical activity can be ignored [9,5,8]. However, electrical activity and mechanical activity are depending on each other, realistic simulation results can only be achieved when their inter-depended relationship is considered. Experimental and clinical research has demonstrated that mechanical activity of the heart affects cardiac electrophysiology [3]. Mechanical activity affects cardiac electrophysiology mainly in two ways: firstly, the position of electrical source inside the myocardium will be changed while the geometry of the heart changes; secondly, stretch-activated ion channels in the cell membrane will be activated when the heart deforms [3,12]. In the paper, we only consider the effect of heart motion to the electrical source position. The reason are twofold: first, it is not practical to measure ion concentrations in clinical environment; second, we want our model to be solved efficiently and to have fewer parameters. Following this mechanoelectrical feedback, cardiac electrophysiological model will be solved in updated deformed geometry. Finally, we can modify the original electrophysiological model in equation (1) as follows

$$\begin{cases} \frac{\partial u}{\partial t} = \bigtriangledown \cdot (\mathbf{D}(\mathbf{E}) \bigtriangledown u) + su(u-a)(1-u) - uv \\ \frac{\partial v}{\partial t} = -e(v + su(u-a-1)) \end{cases} \tag{5}$$

$$\begin{cases} \frac{\partial u}{\partial t} = \bigtriangledown \cdot (\mathbf{D}(\mathbf{F}) \bigtriangledown u) + su(u-a)(1-u) - uv \\ \frac{\partial v}{\partial t} = -e(v + su(u-a-1)) \end{cases} \tag{6}$$

The variable $\mathbf{E}$ is deformation gradient tensor. The conductivity tensor $\mathbf{D}$ is depended on $\mathbf{E}$, thus mechanoelectrical feedback is naturally introduced into the model.

2.5 Numerical Implementation

Using principle of virtual work, we can put the above four components into the same framework by using total-Lagrangian formulation, whose matrix formulation can be represented as follows:

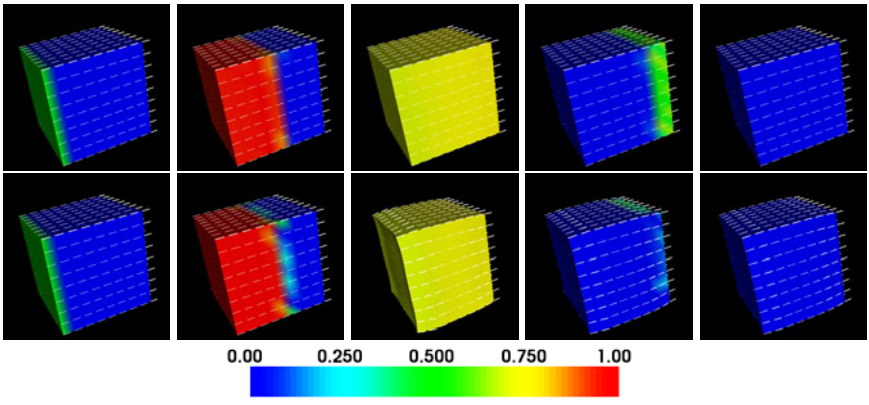

Fig. 1. Comparison of static EP simulation and electromechanics simulation. Top row: static EP simulation with electrophysiological model introduced in section 2.1; Bottom row: electromechanics simulation with proposed model. Left to right with time: 0ms, 13ms, 110ms, 140ms, and 148ms (white lines are fiber directions, the color indicates normalized TMP value).

$$ {}^{t}\mathbf{M}^{t+\Delta t}\ddot{U} + {}^{t}\mathbf{C}^{t+\Delta t}\dot{U} + ({}^{t}\mathbf{K} + {}^{t}\mathbf{K}_b)\Delta U = {}^{t+\Delta t}R + {}^{t}R_b - {}^{t}R_I \tag{7} $$

Variables with superscript t are measured at time t, and variables with superscript $t + \Delta t$ are measured at time $t + \Delta t$. With ${}^{t}\mathbf{M}$ the mass matrix, ${}^{t}\mathbf{C}$ is the damping matrix, ${}^{t}\mathbf{K}$ the stiffness matrix, ${}^{t}\mathbf{K}_b$ the stiffness matrix from boundary conditions, and ${}^{t+\Delta t}\ddot{U}$, ${}^{t+\Delta t}\dot{U}$, ΔU are acceleration, velocity and incremental displacement vectors. The matrix ${}^{t+\Delta t}R$ is active force from electromechanical coupling, and matrix ${}^{t}R_b$ is external forces from boundary conditions. ${}^{t}R_I$ is an internal term. By using Newmark method for time integration, the only unknown in equation (7) is incremental displacement ΔU, and the equation can be solved by Newton's method [13].

3 Experimental Results

To show the importance of integrating electrical and mechanical activities within the same model, we have made a comparison between static EP simulation by a cardiac electrophysiological model and electromechanics simulation by the proposed model. Experiments have been performed on a cube with myocardium properties and a biventricular heart.

3.1 A Cube

A cube with size 60mm*60mm*60mm has been used to emulate a piece of heart muscle as listed in Fig. 1. By using meshfree method [14], the cube is represented by 729 unstructured points. The electrical propagation wave is initialized

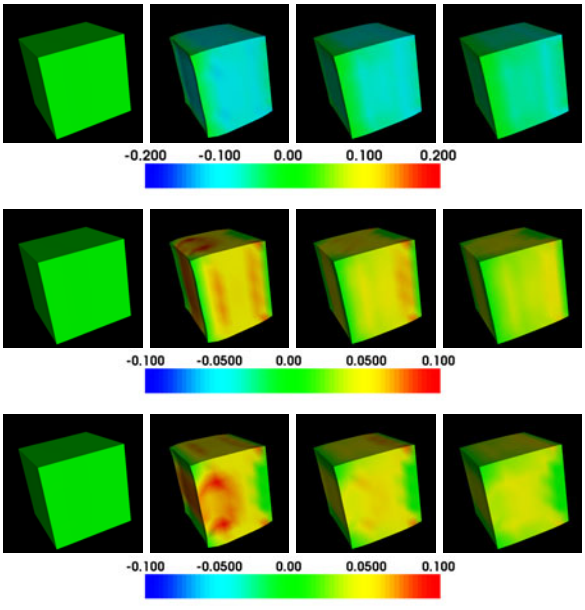

Fig. 2. Strain maps of electromechanics simulation. From top to bottom: strain map along fiber, fiber cross direction, fiber cross direction. Negative and positive values indicate contraction and extension respectively. Left to right with time: 13ms, 110ms, 140ms, and 148ms.

from the left face of the cube, and then propagates through the whole object. Moreover, the right face of the cube is fixed to emulate the constraints from myocardium. One cycle of 200ms is simulated.

Fig. 1 depicts the comparison between static EP simulation and electromechanics simulation. The top row shows the spatiotemporal dynamics of TMP propagation with static geometry. The bottom row exhibits spatiotemporal dynamics of TMP propagation and the corresponding deformation caused by electromechanical coupling. Through comparison, we find that action potential duration (APD) of electromechanics simulation is shorter than that of static EP simulation. Obviously, the difference of APD between these two simulations reflects the effect of mechanoelectrical feedback. Electrical wave propagation induces active stresses, which cause the cube shortening along the fiber direction, and thus shortens the time between the cube depolarization and repolarization. This result is consistent with findings in [15], in which the authors found heart motion can shorten APD through a two dimensional heart simulation.

To verify the mechanical behavior of the cube, we provide strain maps in Fig. 2. As expected, the values along the fiber direction are almost negative due to the cube contraction, which is showed in the top row. The values along fiber cross directions are positive due to the extension, which are listed in the bottom two rows.

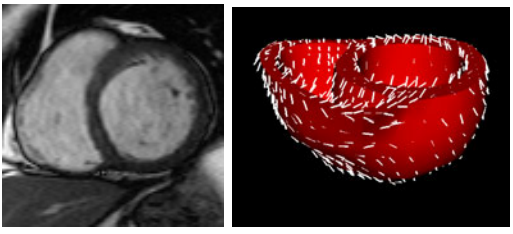

(a) (b)

Fig. 3. A biventricular model of heart from MRI. (a) MRI image. (b)Heart geometry along with fiber directions.

3.2 A Biventricular Heart

To show the physiological plausibility of our model, electromechanics simulation has been performed on a biventricular heart. The geometry of the heart is extracted from MRI images, which can be publicly downloaded [16], as showed in Fig. 3 (a). After image segmentation slice by slice, a three dimensional surface mesh of the heart can be built. By using meshfree method, the biventricular heart is represented by 2017 meshfree points surrounded by the surface mesh. Fiber direction of each point is mapped from the Auckland heart [17]. The biventricular heart with fiber directions is listed in Fig.3 (b). Since realistic Purkinje network of this heart is not available, we have selected points on the endocardium and within segments 1, 8, 9 and 15 as initial activation sites (according to American Heart Association suggestion, we have divided the left-ventricular myocardium into 17 segments [18]). Two boundary conditions have been taken into account for describing the following two phenomena: first, the apex of the myocardium is almost still during the heart cycle; second, the base is constrained by the myocardium and the arteries.

Again, a comparison of static EP simulation and electromechanics simulation is listed in (a) and (b) of Fig. 4, in which the color reflects the normalized TMP value. As we can see, the pattens of TMP propagation for both simulations are almost the same before the heart repolarization. However, electromechanics simulation repolarizes faster than static EP simulation as showed in the figures at 144ms. This is consistent with the findings in the work [15]. The authors compared two ECG signals mapped from a two-dimensional static heart and dynamic heart respectively, and found the T-wave of the dynamic heart had a left-side shift. Since T-wave represents ventricular repolarization period, this is the same as to say the APD of the biventricular heart is shortened.

For a normal heart, the fiber directions in the myocardium are typically perpendicular to the radial direction. As a result, circumferential strain value is typically negative during the heart contraction, and positive during the heart extension, while the values of radial strain are opposite. In Fig.4, we list radial and circumferential strain in (c) and (d), the color reflects strain value. In this simulation, we find circumferential strain values are always positive at the top

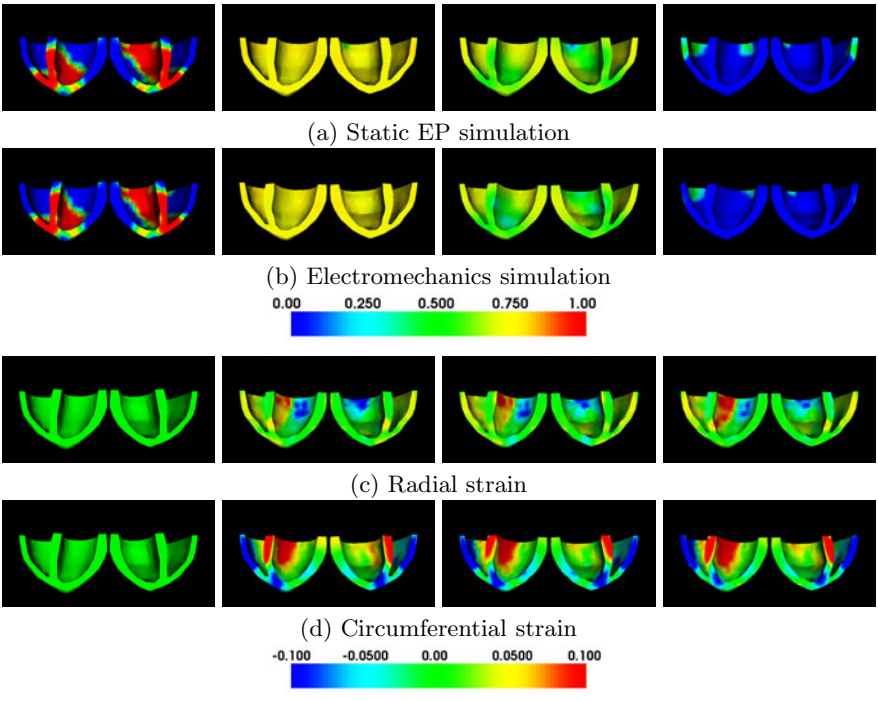

Fig. 4. Simulation on real biventricular model. Left to right with time: 9ms, 100ms, 126ms and 144ms.

of the septum, which may be not realistic. The possible reason is that we did not include a physiological model to control the blood pressure within the left and right ventricles.

4 Discussion

The main advantage of the proposed model is it integrates both electrical and mechanical activities. Through the experiments, we have found that APD of the proposed is shorter than that of a static heart model due to the effect of mechanoelectrical feedback. As a result, the proposed model is supposed to be better describe the behaviors of the heart. We believe our model should be useful in cardiac EP simulation and cardiac deformation recovery.

However, there are still several ways for us to improve our model. First, our model is a generic model, the parameters of the model are all from literature [10,7], thus it only can simulate normal heart behaviors at this time. The simulation results can not be compared with subject-specific data. Actually, personalizing the parameters of the model will be our future work. One possible solution is to recover the parameters from clinical measurements through inverse problems.

For example, we can build a three dimensional mapping between TMP dynamics and body surface potential maps, and then recover the TMP dynamics and corresponding parameters through data assimilation [5]. Second, each component model may not be the best model to describe the heart behaviors. For example, some nonlinear mechanical models are said to be better for describing the heart behavior [9]. Finding the best model for each component is underway. Third, we have simplified the effect of mechanoelectrical feedback by only considering the effect of heart deformation to the position of electrical source. The realistic mechanoelectrical feedback simulation can only be achieved through models include the contribution of stretch-activated channels (SACs) [3,12]. However, this kind of models usually contain a lot of parameters and are much more complex than phenomenal models used in the paper. For clinical usage, computational heart models need to have fewer parameters and be low computational cost. This is the reason why when did not consider the models describing the mechanism of SACs. To keep a balance of physiological plausibility and computational cost of the models will be our ongoing work. Fourth, there is no knowledge of ventricular blood pressure of the current used MRI data. A potential solution for this issue is to introduce a blood pressure control model [8] into our model.

5 Conclusion

In this paper, we presented an electromechanical coupled model and detailed each component of the model. To demonstrate the electromechanical coupled property of the model, we have performed numerical simulations on a cube and a biventricular heart. Compared to static EP simulation, simulation results of the proposed model presented the effect of mechanoelectrical feedback that shortens the APD due to the contraction of the objects during electrical wave propagation.

References

1. Nash, M., Panfilov, A.: Electromechanical model of excitable tissue to study reentrant cardiac arrhythmias. Progress in Biophysics and Molecular Biology 85, 501–522 (2004)
2. Goktepe, S., Kuhl, E.: Electromechanics of the heart: a unified approach to the strongly coupled excitation-contraction problem. Computational Mechanics 45, 227–243 (2010)
3. Traynova, N., Constantino, J., Gurev, V.: Models of stretch-activated ventricular arrhythmias. Journal of Electrocardiology 43, 479–485 (2010)
4. Kerckhoffs, R., Healy, S., Usyk, T., Mcculloch, A.: Computational methods for cardiac electromechanics. Proceedings of IEEE 94, 769–783 (2006)
5. Wang, L., Zhang, H., Wong, K., Liu, H., Shi, P.: Physiological-model-constrained noninvasive reconstruction of volumetric myocardial transmembrane potentials. IEEE Transaction on Biomedical Engineering 57, 296–315 (2010)

6. Plank, G., Romero, D., Sebastian, R., Wong, K.C.L., Zhang, H., Ayache, N., Frangi, A.F., Shi, P., Smith, N.P., Camara, G.A.W.O., Sermesant, M., Lamata, P., Wang, L., Pop, M., Relan, J., Craene, M.D., Delingette, H., Liu, H., Niederer, S., Pashaei, A.: Inter-model consistency and complementarity: Learning from ex-vivo imaging and electrophysiological data towards an integrated understanding of cardiac physiology. Progress in Biophysics and Molecular Biology (accepted, 2011)
7. Sermesant, M., Delingette, H., Ayache, N.: An electromechanical model of the heart for image analysis and simulation. IEEE Transactions on Medical Imaging 25, 612–625 (2006)
8. Chapelle, D., Fernández, M.A., Gerbeau, J.-F., Moireau, P., Sainte-Marie, J., Zemzemi, N.: Numerical Simulation of the Electromechanical Activity of the Heart. In: Ayache, N., Delingette, H., Sermesant, M. (eds.) FIMH 2009. LNCS, vol. 5528, pp. 357–365. Springer, Heidelberg (2009)
9. Wong, K.C.L., Wang, L., Zhang, H., Shi, P.: Physiological Fusion of Functional and Structural Data for Cardiac Deformation Recovery. In: Jiang, T., Navab, N., Pluim, J.P.W., Viergever, M.A. (eds.) MICCAI 2010. LNCS, vol. 6361, pp. 159–166. Springer, Heidelberg (2010)
10. Aliev, R., Panfilov, A.: A simple two-variable model of cardiac excitation. Chaos, Solitions Fractals 7(3), 293–301 (1996)
11. Niederer, S., Smith, N.: An improved numerical method for strong coupling of excitation and contraction models in the heart. Progress in Biophysics and Molecular Biology 96, 90–111 (2008)
12. Rudy, Y., Ackerman, M., Bers, D., Clancy, C., Houser, S., London, B., McCulloch, A., Przywara, D., Rasmusson, R., Solaro, R., Trayanova, N., Wagoner, D., Varro, A., Weiss, J., Lathrop, D.: Systems approach to understanding electromechanical activity in the human heart: a national heart, lung, and blood institute workshop summary. Circulation 118, 1202–1211 (2008)
13. Bathe, K.: Finite element procedures. Prentice Hall, Englewood Cliffs (1996)
14. Dolbow, J., Belytschko, T.: An tntroduction to programming the meshless element free galerkin method. Archives of Computational Methods in Engineering 5(3), 207–241 (1998)
15. Smith, N., Buist, M., Pullan, A.: Altered t wave dynamics in a contracting cardiac model. The Journal of Cardiovascular Electrophysiology 14, 203–209 (2003)
16. Physionet/computers in cardiology challenge 2007: electrocardiographic imaging of myocardial infarction, vol.2 (2007), http://www.physionet.org/challenge/2007
17. Nash, M.: Mechanics and material properties of the heart using an anatomically accurate mathematical model, vol.2, Ph.D dissertation, University of Auckland
18. Cerqueira, M., Weissman, N., Dilsizian, V., Jacobs, A., Kaul, S., Laskey, W., Pennell, D., Rumbergen, J., Ryan, T., Verani, M.: Standardized myocardial segmentation and nomenclature for tomographic imaging of the heart: a statment for healthcare professionals from the cardiac imaging committee of the council on clinical cardiology of the american heart association. Circulation 105, 539–542 (2002)

Matching Sparse Sets of Cardiac Image Cross-Sections Using Large Deformation Diffeomorphic Metric Mapping Algorithm

Siamak Ardekani[1], Aastha Jain[1], Saurabh Jain[1], Theodore P. Abraham[2], Maria R. Abraham[2], Stefan Zimmerman[2], Raimond L. Winslow[3], Michael I. Miller[1,3], and Laurent Younes[1,3]

[1] Center for Imaging Sciences, Johns Hopkins University, USA
sardekani@jhu.edu
[2] Johns Hopkins University Medical Institutions, USA
[3] Institute for Computational Medicine, Johns Hopkins University, USA

Abstract. The purpose of this study is to illustrate the application of large deformation diffeomorphic metric mapping to perform registration among sparsely sampled cardiac magnetic resonance imaging (MRI) data. To evaluate the performance of this method, we use two sets of data: 1) contours that are generated from sparsely sampled left ventricular sections and extracted from short axis cardiac MRI of patients with hypertrophic cardiomyopathy and 2) left ventricular surface mesh that is generated from higher resolution cardiac computed tomography image. We present two different discrepancy criteria, one based on a measure that is embedded in the dual of a reproducing kernel Hilbert space of functions for curves and the other is based on a geometric soft matching distance between a surface and a curve.

1 Introduction

Cardiac disease is often associated with remodeling, which is a process by which mechanical, neurohormonal, and genetic factors alter ventricular size, shape, and function. Because ventricular shape and function are influenced by this remodeling, metrics related to the shape and motion may be used as an early indicator of disturbances in myocardial organization that occur during disease progress and may have great value in risk prediction and treatment evaluation. Assessing regional differences in left ventricular (LV) shape and motion at the population level requires establishing anatomical correspondence using registration-based techniques. In this process, transformations that deform a reference heart shape to assume the shape of an individual heart characterize shape variation and allow for statistical comparison of patient groups.

Cardiac magnetic resonance imaging (MRI) is a non-invasive imaging modality that provides detailed quantitative data about cardiac function and geometry. Its main advantage is the ability to acquire functional and anatomical images in any plane and direction using different contrast and magnetic field gradient

O. Camara et al. (Eds.): STACOM 2011, LNCS 7085, pp. 234–243, 2012.

mechanisms. However, in routine clinical studies, cardiac MRI data are usually collected with relatively low through-plane resolution that is not optimum for using standard image intensity-based registration methods. Several methods have been proposed that rely on fitting a smooth surface to the segmented contours using either shape-based interpolation or Hermite basis functions in the spheroidal prolate coordinate systems [3], [10], [7]. This may produce artifacts in the registration process, because it is difficult to separate shape differences that were truly present in the original (sparse) data from those that were induced by the interpolation process. In this paper, we develop methods that directly register shapes of interest within a single framework, using methods that are referred to as large deformation diffeomorphic metric mapping (LDDMM) for matching curves and surfaces [4], [8], [9], [2], [5]. The advantage of these algorithms is to compute transformations that are smooth and one to one with smooth inverse (diffeomorphic) that preserves connectivity and topology, therefore enabling one to study local variations.

The main objective of this work is to adapt these algorithms to the registration of sparsely sampled cardiac MR volumes, and to study their feasibility. We consider two specific problems, namely the registration between two sparsely sampled MR images, and the registration between a full LV template represented as a triangulated surface and a sparsely sampled image. This will be illustrated with cardiac MR images of patients with hypertrophic cardiomyopathy and a template surface mesh that has been constructed from high-resolution computed tomography (CT) images.

2 Method

2.1 Subjects

All human studies were approved by the Institutional Review Board for human investigation. Cardiac MR data were selected from a set of patients (n = 5, 4 females, mean age of 50.4 ± 15.24 years) who were diagnosed with familial cardiomyopathy. The in-plane resolution was approximately ∼1.4 mm × 1.4 mm and thickness was of 8 mm with 2 mm gap.

2.2 Preprocessing

Segmentation. From the MRI data, epicardial and endocardial contours were isolated using *Segment* [6], which is a semi-automatic freely available software.

Breath Hold Correction. Differences in expiration level due to the cardiac MRI acquisition at separate breath-holds can lead to the misalignment of short axis (SA) image slices. We implemented an Euclidean distance-based matching approach to estimate an optimum 2D within-slice translation that corrects for breath-hold related motion. To drive the matching algorithm, we used contour points from 3 different perpendicular planes: short axis, horizontal long axis (HLA), and vertical long axis (VLA). Let S_{SA} represent a set of endocardial

and epicardial points in a particular slice at SA plane, and $S_{SA\cap LA}$ represent a set of endocardial and epicardial points from the LA planes that are located on the intersection lines between these planes and the SA plane. The goal is to seek an optimum in-plane translation that minimizes the cost function

$$e(\Pi) = \sum_{p \in S_{SA\cap LA}} d^2(T(p, \Pi), S_{SA}) \ , \tag{1}$$

where d is the Euclidean norm and $T(p, \Pi)$ represents space translation of point sets in p with respect to $\Pi = (\pi_x, \pi_y)$ which is a vector of two parameters for translation in the (x, y) plane.

Rigid Alignment. Before performing nonrigid matching, we roughly aligned and scaled the objects (curves and surfaces) by orienting the long axis of LV geometry along the z axis, translating the centroid of LV geometry to the center of the coordinate system, aligning the line that connects mid-ventricular insertion points (place where right ventricle connects to the left ventricle) with the y axis, and normalizing the variance of curve (vertex) points.

Template Surface. The template surface is a triangulation of a binary volume, that was obtained using shape averaging in a previous study [1], in which the shape average was obtained from intensity CT images from 25 subjects. We refer to [1] for details. The triangulation used the image-to-mesh conversion method provided in the ParaView software (`http://www.paraview.org/`), and a triangulated surface mesh with 61262 vertices was generated from the CT-based intensity template.

2.3 Registration Methods

We now discuss two approaches that perform nonrigid alignment on sparse cross-sectional data. We start with a curve-based approach that takes as input two families of segmented cross-sections and computes a 3D registration between them. We will then describe an algorithm that aligns a full three-dimensional template, represented as a triangulated surface, to a family of cross-sectional segmentations.

To be more specific, we introduce some notation to describe cross-sectional segmentations. They can be seen as families of plane curves, taking the form

$$\Gamma = \{\gamma_k, k = 1, \ldots, N\} \ , \tag{2}$$

where each γ_k is a curve included in one of the cross-sections, all parametrized over a fixed interval, $I = [0, 1]$. Choosing a coordinate frame (x, y, z) where z represents the long-axis coordinate, this means that all points in γ_k share the same z coordinate, denoted by z_k. Even if N is typically larger than the total number of cross-sectional images, because there are several curves per section, the possible number of different z_k coincides with the number of cross-sections.

Nonrigid Alignment between Segmentations. Our first registration method takes as input two families of curves, $\Gamma^{(0)}$ and $\Gamma^{(1)}$, represented as in (2), possibly with different values of N, and finds an optimal transformation, say ϕ, such that $\phi(\Gamma^{(0)}) \simeq \Gamma^{(1)}$, where $\phi(\Gamma^{(0)})$ is the family of curves obtained by applying the transformation ϕ to each of the curves that constitute $\Gamma^{(0)}$.

Because we cannot assume that $\Gamma^{(0)}$ and $\Gamma^{(1)}$ contain the same number of curves, or even the same number of cross-sections, we use a variant of the current-based curve matching algorithm described in [4], and minimize an objective function taking the form

$$E(\Gamma, \alpha) = \int_0^1 F(\Gamma(t), \alpha(t))dt + \frac{1}{\sigma^2} D(\Gamma(1), \Gamma^{(1)})^2 \, . \tag{3}$$

We now describe the terms involved in this expression. The variables, Γ and α, are time dependent. At time t, $\Gamma(t)$ is a deformation of the template family of curves, $\Gamma^{(0)}$ taking the form $\Gamma(t) = \{\gamma_k(t, \cdot), k = 1, \ldots, N\}$; $\alpha(t)$ represent a family of functions $\alpha(t) = \{\alpha_k(t, \cdot), k = 1, \ldots, N\}$, such that $\alpha_k(t, \cdot)$ takes values in $\mathbb{R}^3$; Γ and α are linked by the evolution equation

$$\frac{d}{dt}\gamma_k(t, v) = \sum_{l=1}^{N} \int K(\gamma_k(t, v), \gamma_l(t, u))\alpha_l(t, u)du \, . \tag{4}$$

with $\gamma_k(0, v) = \gamma_k^{(0)}(v)$, where K is a reproducing kernel that we specify below. The deformation cost function, F, is defined by

$$F(\Gamma(t), \alpha(t)) = \sum_{k,l=1}^{N} \int \int \alpha_k(t, u)^T K(\gamma_k(t, u), \gamma_l(t, v))\alpha_l(t, v)dudv \, .$$

The data-attachment term, D, is a norm measuring the discrepancy between the families of curves $\Gamma(1)$ (deformed template at time $t = 1$) and $\Gamma^{(1)}$ (target). This norm is defined via a mathematical construction that embeds families of curves into a Hilbert space of linear forms over vector fields, and we refer the reader to [4,11] for details.

Finally, $(p, p') \mapsto K(p, p')$ is a smoothing kernel function, whose presence ensures that curves evolve via (4) without creating singularities, self-intersection or topological changes. It is defined over all p, p' in $\mathbb{R}^3$, and differs from kernels used in [4] and subsequent works in order to ensure that cross-sections have a uniform long-axis motion over time, so that they remain planar. This leads to modeling K as a 3 by 3 diagonal matrix given by $K(p, p') = \mathrm{diag}(g(\|p - p'\|), g(\|p - p'\|), g(z - z'))$ with $g(t) = \exp(-t^2/2a^2)$ for some parameter a (where z and z' are the long-axis coordinates of p and p'). Doing so ensures that the velocity of γ_k in (4) has a long-axis component that only depends on the third coordinate, so that γ_k has a uniform motion in the long axis direction.

Surface to Curves Registration. Our second algorithm matches a template defined as a closed surface, $S^{(0)}$ (delimiting the left ventricle), to a collection

of curves, which will be denoted by $\Gamma^{(1)}$ as above. The approach is similar and minimizes an objective function taking the form

$$E(S,\alpha) = \int_0^1 F(S(t),\alpha(t))dt + \frac{1}{\sigma^2} D(S(1),\Gamma^{(1)})^2 \ . \tag{5}$$

where S and α depend on time. Here S is an evolving surface, parametrized over $S^{(0)}$, with $S(0,p) = p$ for all $p \in S^{(0)}$, and $\alpha(t,\cdot)$ is a function defined over $S^{(0)}$ with values in $\mathbb{R}^d$. The evolution equation now takes the form

$$\frac{d}{dt}S(t,q) = \int_{S^{(0)}} K(S(t,q),S(t,p))\alpha(t,p)ds(p) \ . \tag{6}$$

(where $ds(p)$ denotes the area form over $S^{(0)}$). The deformation cost is given by

$$F(S(t),\alpha(t)) = \int_{S^{(0)}}\int_{S^{(0)}} \alpha(t,p)^T K(S(t,p),S(t,q))\alpha(t,q)ds(p)ds(q) \ .$$

and the kernel K is now chosen isotropic, such that $K(p,p') = g(\|p-p'\|)\mathrm{Id}_{\mathbb{R}^3}$ with g as above. Finally, the data-attachment term, D, computes the sum of the integrals of the squared distances between each point in each curve in $\Gamma^{(1)}$ and the deformed surface $S(1)$, so that, assuming N curves in $\Gamma^{(1)}$,

$$D(S(1),\Gamma^{(1)})^2 = \sum_{k=1}^{N} \int \mathrm{dist}(\gamma_k^{(1)}(u),S(1))^2 \|\dot{\gamma}_k^{(1)}(u)\| du \ . \tag{7}$$

To simplify the computation of derivatives, we slightly relax this expression in our implementation, defining, for a point $x \in \mathbb{R}^3$ and a surface S,

$$\mathrm{dist}_T(x,S) = \inf_{\eta_x} \left(\int_S \eta_x(p)\|x-p\|^2 ds(p) - T\int_S \eta_x(p)\log\eta_x(p)ds(p) \right) \tag{8}$$

where $T > 0$ is a small relaxation constant and the infimum is over all positive functions η_x defined over S. The optimal η_x is given by

$$\eta_x^*(p) = \frac{e^{-\|x-p\|^2/T}}{\int_S e^{-\|x-p\|^2/T} ds(p)}, \tag{9}$$

which gives an alternate expression of dist_T which does not involve an infimum. It is easy to show that, if x has a unique closest point on S, $\mathrm{dist}_T(x,S)$ converges to $\mathrm{dist}(x,S)$ when T tends to 0. Our implementation uses dist_T instead of dist in (7), with a small value of T, using the variational expression in (8) (therefore adding the η functions as auxiliary variables) rather than the more complex explicit expression derived from (9).

Measure of Robustness. To evaluate the robustness of our nonrigid alignment algorithms, we set up four experiments: 1) we matched the high resolution triangulated surface mesh template to the endo and epicardial contours (complete curve set) that were extracted from the cardiac MR images of 5 subjects,

then 2) we generated an incomplete curve set by randomly removing contours from one of the cross-section image planes in each of the cardiac MR image sets and repeated the surface to curve matching; 3) we conducted the same procedure for the curve to curve matching by first generating a set of curves that were 10 mm apart using the same high resolution CT image template and match these template curves to the curves that were obtained from the MRI dataset, and finally 4) we matched the template curves to the set of curves with the removed planes. For experiments 3 and 4, in addition to the deformed template curves, we used equation (4) to estimate the transformation that deformed vertices in the surface template, therefore for each experiment a set of deformed surface templates were generated. To evaluate the robustness of surface-to-curve and curve-to-curve matching methods, a closest-distance measure between the removed curve points and the center of triangulated faces from the deformed template was calculated.

3 Results

Figures 1(a) and 1(b) illustrate the results of the breath-hold correction algorithm to correct SA slice-to-slice misalignment. Note that despite severe misalignment, the algorithm was mostly able to recover the overall 3D geometry of left ventricle as presented by the contours of LA planes.

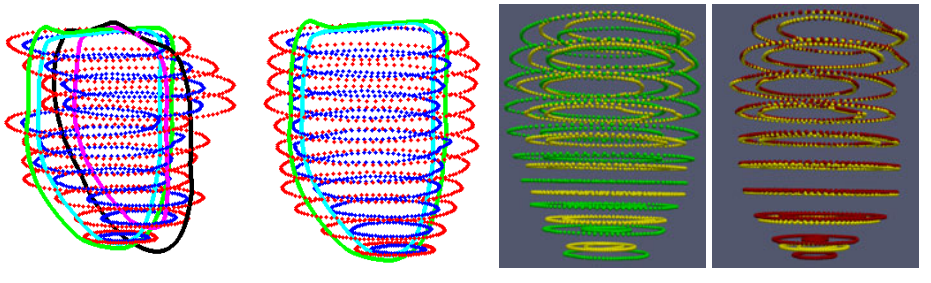

Fig. 1. *(a-b)*: Correction of slice-to-slice misalignment in SA view due to breath-holding motion.*(a)*: Before correction. *(b)*: After correction. Note that endocardial and epicardial contours from two perpendicular planes have been used to align short axis slices (Blue and red : endocardial and epicardial surfaces from SA view, Cyan and green: endocardial and epicardial contours from vertical long axis view, Pink and black: endocardial and epicardial contours from horizontal long axis view. *(c-d)* Curve-to-curve matching using LDDMM. *(c)*: LV epicardial contours from 2 different subjects. *(c)*: LV contours before curve matching (green: template contours, yellow: target contours). *(d)*: LV contours after deforming template subject contours (red) to match target subject (yellow).

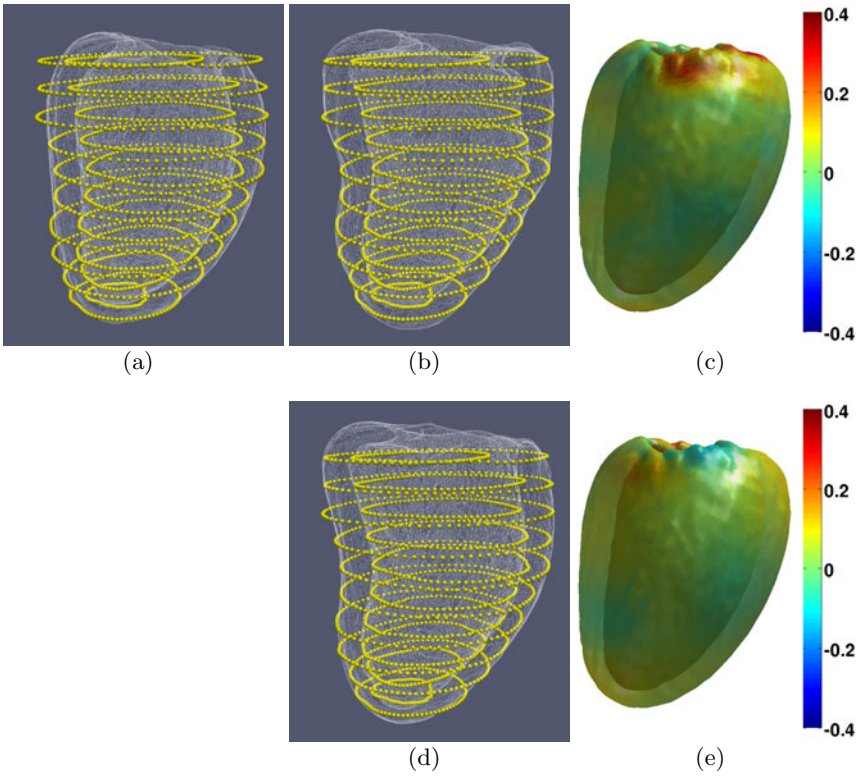

Fig. 2. Surface-to-curve matching using distance-based LDDMM. *(a)*: Surface template with target contours. *(b)*: After registration. *(c)*: Map of the surface area ratio of triangulated faces in deformed template relative to template superimposed on template mesh (scale is based on log_{10}). *(d)*: After registration using projection of gradients on the first 24 eigenvectors of smoothing kernel. *(e)*: same as *(c)* but for the deformation estimated from *(d)*. Grey wireframe represents high resolution triangulated mesh template. Yellow contours are representing LV epicardial and endocardial regions from the MRI cross-sections.

Visual assessment of the curve-matching method described in section 2.3 indicates that this method can successfully register two LV geometries despite limited volume sampling (figures 1(c) and 1(d)). Note that, as explained in section 2.3, the specific choice of kernel configuration ensured that the curves have remained planar.

Figure 2(b) demonstrates the result of matching of a high-resolution triangulated surface mesh to the LV cross-section contours using the approach described in section 2.3. A careful examination of the result indicates that the surface mesh has been fully deformed to assume the shape of LV contours. However, this matching has resulted in the introduction of artificially large curvature

variation on the deformed surface. To remedy this problem and increase the robustness of the method, we have slightly modified the approach by projecting the gradient of the objective function on the principal directions (first eigenvectors) of the smoothing kernel. The result has been shown in Figure 2(d). It is clear that by projecting the gradient, we were able to reduce curvature variation, while preserving matching accuracy. Regional surface area expansion or shrinkage can be examined by estimating the determinant of the Jacobian matrix from the transformation that matches the template to the target object. Figures 2(c) and 2(e) show the determinant of the Jacobian maps that were calculated for the surface-to-curve matching, with and without eigen-projection, respectively. Examination of the maps indicates an overall smooth transformation, except for a small region with a relatively high area expansion on the base of the left ventricle in the non-projected matching. However, projecting the gradient of the objective function on the principal directions of the smoothing kernel resulted in a more uniform transformation.

Table 1 summarizes the distance error for different experiments. All the surface-to-curve experiments are based on eigen-projection using the largest 24 principal directions. While, due to the limited data size, it would be difficult to draw any conclusion, it appears that curve-to-curve matching and surface-to-curve matching are both performing equally well. However, surface-to-curve matching is more robust with respect to missing data.

Table 1. Distance Error (mm): I) Distance error associated with the matching of the surface template to the complete curve set, measured from the removed cross-sectional curves to the deformed surface template. II) Distance error associated with the matching of the surface template to the incomplete curve set, measured from the removed cross-sectional curves to the deformed surface template. III) Repeating case (I) with the curve to curve matching. IV) Repeating case (II) with the curve to curve matching. V) Pre-registration distance between the complete curve set and surface template. VI) Surface to curve matching error estimated by using the entire curve set as opposed to using curves from a single cross section (case I) VII) Curve to curve matching error estimated by the complete curve set.

subjects	I	II	III	IV	V	VI	VII
1	0.88	1.79	1.34	6.94	3.35	1.47	1.08
2	1.79	2.10	0.90	3.89	3.29	1.85	1.24
3	1.27	3.34	1.60	3.72	3.09	1.42	1.10
4	1.69	3.61	2.04	4.73	3.42	1.98	1.32
5	2.74	3.10	0.95	2.28	3.03	2.03	0.98
Mean(SD)	1.67(0.70)	2.79(0.80)	1.37(0.47)	4.31(1.71)	3.24(0.17)	1.75(0.29)	1.15(0.14)

4 Discussion

In this study we have presented the application of LDDMM to match cardiac MR cross-sections. In particular, LDDMM surface-to-curve matching can be used to

deform a high-resolution triangulated surface mesh to match cardiac MR cross-sections with low out-of-plane resolution. This algorithm does not require the selection of same number of points (for curves) and vertices (for surfaces) and does not rely on a predefined geometric model; it therefore eliminates the need to specify an arbitrary correspondence between points and surfaces. This can be extremely useful considering that there are only very few unique cardiac anatomic landmarks that could be easily identified.

LDDMM surface-to-curve matching permitted regions with sharp curvature to be matched accurately. However, due to the limited number of contours, this enhanced accuracy resulted in overfitting, and an artificially large curvature variation while transitioning form one cross-section to another on the cardiac surface of the deformed high resolution triangulated mesh. Projecting the gradient of the objective function onto the space defined by the principal directions of smoothing kernel captures geometrical scales that are relatively larger, therefore maintaining the accuracy of registration while reducing the large curvature variation.

LDDMM curve-to-curve matching provides an alternative to the surface-to-curve matching, allowing for the comparison of MR images without the intervention of a surface template. However, this method is more sensitive to the variations in landmark spacing and geometry coverage as demonstrated by larger distance error while matching data with missing cross-sections. Therefore to achieve superior performance, it would be critical to have two sets of curves that represent similar geometry coverage. Furthermore, to enhance the quality of curve-to-curve matching, we have included constraints to enforce uniform deformation of points in curves, that belong to the same cross-section, along the through-plane direction.

In conclusion, methods that have been presented here provide potentially valuable tools to perform a quantitative analysis of cardiac shape and motion using sparsely sampled ventricular geometry. Particularly, this would be useful while integrating information from several imaging modalities that are collected at different spatial scales.

Acknowledgments. This research was supported by the Cardiovascular Research Grid Project R24HL085343.

References

1. Ardekani, S., Weiss, R.G., Lardo, A.C., George, R.T., Lima, J.A., Wu, K.C., Miller, M.I., Winslow, R.L., Younes, L.: Computational method for identifying and quantifying shape features of human left ventricular remodeling. Ann. Biomed. Eng. 37, 1043–1054 (2009)
2. Durrleman, S., Pennec, X., Trouv, A., Ayache, N.: Statistical models of sets of curves and surfaces based on currents. Medical Image Analysis 13(5), 793–808 (2009); includes Special Section on the 12th International Conference on Medical Imaging and Computer Assisted Intervention, http://www.sciencedirect.com/science/article/pii/S1361841509000620

3. Frangi, A.F., Rueckert, D., Schnabel, J.A., Niessen, W.J.: Automatic construction of multiple-object three-dimensional statistical shape models: application to cardiac modeling. IEEE Transactions on Medical Imaging 21(9), 1151–1166 (2002)
4. Glaunes, J., Qiu, A., Miller, M.I., Younes, L.: Large Deformation Diffeomorphic Metric Curve Mapping. Int. J. Comput. Vis. 80, 317–336 (2008)
5. Gorbunova, V., Durrleman, S., Lo, P., Pennec, X., De Bruijne, M.: Curve-and Surface-based Registration of Lung CT images via Currents, vol. 10, pp. 15–25. Citeseer (2009), http://www.lungworkshop.org/2009/proc2009/15.pdf
6. Heiberg, E., Sjogren, J., Ugander, M., Carlsson, M., Engblom, H., Arheden, H.: Design and validation of Segment–freely available software for cardiovascular image analysis. BMC Med. Imaging 10, 1 (2010)
7. Myronenko, A., Song, X.: Point set registration: Coherent point drift. IEEE Transactions on Pattern Analysis and Machine Intelligence 32(12), 2262–2275 (2010)
8. Vaillant, M., Glaunes, J.: Surface matching via currents. Inf. Process. Med. Imaging 19, 381–392 (2005)
9. Vaillant, M., Qiu, A., Glaunes, J., Miller, M.I.: Diffeomorphic metric surface mapping in subregion of the superior temporal gyrus. Neuroimage 34, 1149–1159 (2007)
10. Wang, V.Y., Lam, H., Ennis, D.B., Cowan, B.R., Young, A.A., Nash, M.P.: Modelling passive diastolic mechanics with quantitative MRI of cardiac structure and function. Medical Image Analysis 13(5), 773–784 (2009); includes Special Section on the 12th International Conference on Medical Imaging and Computer Assisted Intervention, http://www.sciencedirect.com/science/article/pii/S1361841509000619
11. Younes, L.: Shapes and Diffeomorphisms. Springer, Heidelberg (2010)

VURTIGO: Visualization Platform for Real-Time, MRI-Guided Cardiac Electroanatomic Mapping

Perry E. Radau[1], Stefan Pintilie[1], Roey Flor[1], Labonny Biswas[1], Samuel O. Oduneye[1,2], Venkat Ramanan[1], Kevan A. Anderson[1,2], and Graham A. Wright[1,2]

[1] Imaging Research, Sunnybrook Health Sciences Centre
[2] Medical Biophysics, University of Toronto

Abstract. Guidance of electrophysiological (EP) procedures by magnetic resonance imaging (MRI) has significant advantages over x-ray fluoroscopy. Display of electroanatomic mapping (EAM) during an intervention fused with a prior MR volume and DE-MRI derived tissue classification should improve the accuracy of cardiac resynchronization therapy (CRT) for ventricular arrhythmias. Improved accuracy in the spatial localization of recorded EP points will produce an EAM to constrain and customize patient-specific cardiac electroanatomic models being developed for understanding the patterns of arrhythmogenic slow conduction zones causing reentry circuits and treatment planning. The Vurtigo software presented here is a four dimensional (3D+time) real-time visualization application for guiding interventions capable of displaying prior volumes, real-time MRI scan planes, EAM (voltage or activation times), segmented models, and tracked catheters. This paper will describe the architecture and features of Vurtigo followed by the application example of guiding percutaneous cardiac electroanatomic mapping in porcine models.

1 Introduction

Magnetic resonance imaging (MRI) has been used primarily as a diagnostic tool in clinical practice and has recently been applied to the guidance of interventional procedures with the development of rapid imaging acquisition protocols. In practice, real-time MR imaging refers to the acquisition and reconstruction of images in less than one heart cycle [1]. Guidance by real-time MRI is attractive compared with x-ray fluoroscopy, because MRI has better soft tissue contrast and is capable of displaying ischemic, infarcted or arrhythmogenic tissue that impacts interventional decisions to target isthmuses of infarct tissue that form slow conduction regions[16]. Furthermore, MRI is not a source of harmful radiation which is a concern for long procedures under x-ray fluoroscopy[2]. Physiological, clinical and modelling evidence suggest that the isthmus size that generates reentry circuits is 1-2mm [18,17,21,19,20] which we hypothesize is of the order of targeting accuracy achievable for our MR-guided, real-time interventional EP platform, Vurtigo.

O. Camara et al. (Eds.): STACOM 2011, LNCS 7085, pp. 244–253, 2012.

The Vurtigo software [22] presented in this paper is designed to enhance the use of real-time computer imaging for therapeutic interventions. The Vurtigo platform has an open-source (modified BSD) license, although it permits proprietary plugins. Frameworks for various image-guided applications such as surgery [4], and specifically for MRI-guided, percutaneous cardiovascular interventions [5] have been previously described. There are a number of 2D and 3D visualization applications for MRI such as the Slicer[6] project. However, Slicer was designed to perform a wide range of tasks from real-time tracking of interventional equipment to post-processing, segmentation, registration and analysis of data. Vurtigo is focused on features that are useful in a EP interventional setting, and designed to achieve the performance and stability for real-time updates. This project represents an attractive alternative, and is open-source, cross-platform and portable to a variety of systems outside of the original communication system.

Vurtigo provides a roadmap, or 3D visual context, for the 2D real-time images using a volume acquired just before real-time scanning begins. The preoperative volume, real-time image(s) and actively tracked catheters are acquired in the same coordinate system and can be rendered together in proper spatial alignment. By comparison, using the prevalent commercial CARTO XP system (Biosense Webster, Diamond Bar, CA) an EAM is acquired under fluoroscopic (2D) guidance. This is subsequently aligned with a previously acquired MR/CT volume by manually selecting anatomical landmarks for spatial registration and then post-processing to correct for errors associated with cardiac, respiratory or patient torso motion.[14,15,16] Vurtigo allows importing an existing EAM dataset or composing it from tracked catheter EP recordings, and then fusing the EAM with a prior MR volume and tissue classification map. These features will be demonstrated by data from several experimental interventions with porcine models of myocardial infarct and ventricular tachycardia.

2 Architecture

This section of the paper will discuss both Vurtigo and the communication system connecting it to the MRI scanner.

2.1 Communication System Design

The communication system is composed of several pieces of software that communicate over TCP/IP sockets, (Fig. 1(a)). The central piece is the Geometry Server that serves a storage location for the most recent information, including images, image plane orientations, physiological data, and catheter information. Multiple clients can send and receive information to the server simultaneously, and all server data will remain synchronized. Between the MRI scanner and the Geometry Server is RTHawk [7]. RTHawk is both a 2D viewer and a real-time MRI scan control system, allowing customizable real-time image sequences. The communication system has been tested on GE 1.5 T Signa Excite 12.0 and 14.0 systems, and is theoretically compatible with all RTHawk-supported MRI systems.

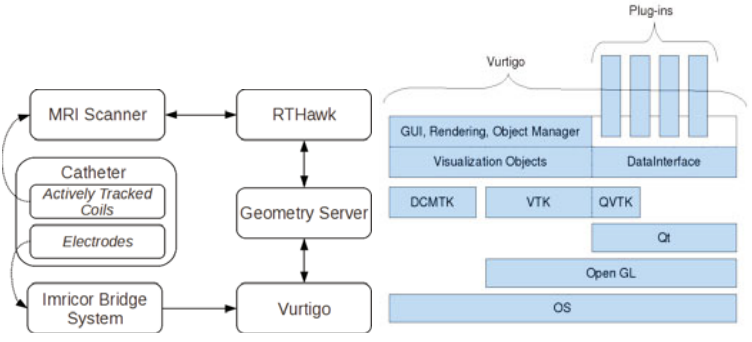

(a) Pipeline (b) Software Architecture

Fig. 1. Design. a) Communication pipeline. Vurtigo is able to passively receive information from the MRI scanner or actively prescribe the scan. EP catheter recordings are via the Imricor bridge system. b) Software components and libraries.

Vurtigo and any other client applications connect directly to the Geometry Server and as such are independent of MRI scanner architecture. Vurtigo can passively read the scan plane orientation from the server, or drive the location of the scan plane. The latency of communication, from sending an image from RTHawk through the Geometry Server to display in Vurtigo was measured: 46 $\pm$ 11 ms (empty scene) or 64 $\pm$ 14 ms (typical EP application scene including two views, contours, and 480 EP points). Currently a work in progress, we have integrated Vurtigo into the RTHawk application and measured latencies an order of magnitude smaller: 5.6 $\pm$ 7.3 ms (empty scene) or 6.3 $\pm$ 7.7 ms (typical EP scene). The latency statistics were measured with $\geq$ 60,000 samples, by execution on a computer having an Intel®quad-core i7 2.8 GHz, 8 GB RAM, and NVIDIA®GTX 470 graphics. The unmeasured latency of communication from the scanner acquisition board to the RTHawk application (raw data client) is $\sim$3 ms.

2.2 Vurtigo Design

Vurtigo was designed and written from the beginning to provide real-time visualization for image guided interventions, and has an open-source license, (download available from www.vurtigo.ca). The architecture is illustrated in Fig. 1(b).

Vurtigo was written in C++ and uses cross-platform libraries, including Qt [9], VTK [8], DICOM Toolkit (DCMTK) [10], Insight Toolkit [11], and CUDA Toolkit [12]. CMake [13] is used as the build system. The application has been compiled on WinXP, Ubuntu Linux and MacOSX 10.6, and in principle should be compatible with most variants.

Vurtigo's plugin design provides a modular and easily extensible framework for developers, making it easy to implement desired features without advanced knowledge of VTK. The application can be conceptually separated into the core and plug-ins. The core comprises the Graphical User Interface (GUI) as well as

storage and rendering of a dynamic set of *objects*, e.g. an MRI volume, a transformation matrix, or a tracked device. Plug-ins add functionality by adding, removing, and editing these objects or enabling object interaction. Plugins can also extend Vurtigo's object framework to define new object types. Vurtigo provides developers considerable design flexibility. For example, a plug-in can provide a user interface that will be loaded dynamically. The plug-ins may be threaded, although care must be taken to track the threads internally to the plug-in. As a consequence of the modular design, plug-in developers need not be concerned with rendering updates, external objects or plug-in states, or the memory management of objects.

3 Features

3.1 Core Features

While many of Vurtigo's features are written as plug-ins, the core manages rendering and dynamic object management. Objects in the core are of two different types, those that can be rendered (e.g. 3D voxel volumes or polygonal meshes), and those that represent the state of another object (e.g. transformation matrix, colour map). There is no software-imposed limit on the number of objects that can be simultaneously loaded into Vurtigo. The software has been designed such that if an object were loaded but not rendered, then it will not have an impact on processing resources. The capacity for loaded objects, however, will be restricted by the memory (RAM) of the computer. Vurtigo on a Intel Core2 Duo laptop with 2GB RAM was able to operate normally with five volumes loaded (8 bit gray levels, matrix $512 \times 512 \times 60$). Rendering loaded objects will impact Vurtigo's execution speed depending on the object type and rendering quality.

3.2 Visualization

The MRI scanner obtains real-time updates for one or two 2D planes, depending on the pulse sequence configuration. The two scan planes are completely independent and each can have a different orientation, position, and field of view (FOV). Vurtigo can display and update these real-time planes and within a prior volume visualization. If there are other real-time image sources then Vurtigo can render those images in the same 3D context. Breath-hold MRI pulse sequences can produce high-quality 3D or 4D (3D+time) datasets. After export of these files in Digital Imaging and Communications in Medicine (DICOM) format, Vurtigo can read them with accompanying meta-data describing the image and its orientation. Vurtigo has three display techniques for this content: 3-Plane, Composite, and Maximum Intensity Projection (MIP).

Rendering a set of three orthogonal planes that cut the volume and may slide along each axis or be tilted is the fastest. The 3-Plane view is texture-mapped and renders quickly even while the planes are being manipulated. A stack of DICOM slices can also be rendered as a volume by ray tracing, and opacity is determined by voxel intensity. A Maximum Intensity Projection (MIP), a type

of ray tracing that emphasizes the high intensity regions of the volume, can also be displayed. 4D volumes can be rendered and played in a loop to show cardiac motion. Hardware-accelerated rendering by CUDA compatible graphics processing units is utilized where available, increasing frame rates by a factor of 10.

All the visual objects including 2D planes, 3D volumes, 4D volumes or catheter devices that are loaded into Vurtigo are oriented and positioned in a global 3D coordinate system, and any number of these can be displayed simultaneously in their correct relative positions. The options for multiple render windows, object visibility settings, and overlay provide the means for intuitive visual comparison of MRI volumes, real-time planes, catheters, and EP mesh surfaces. An example is Fig. 2(a).

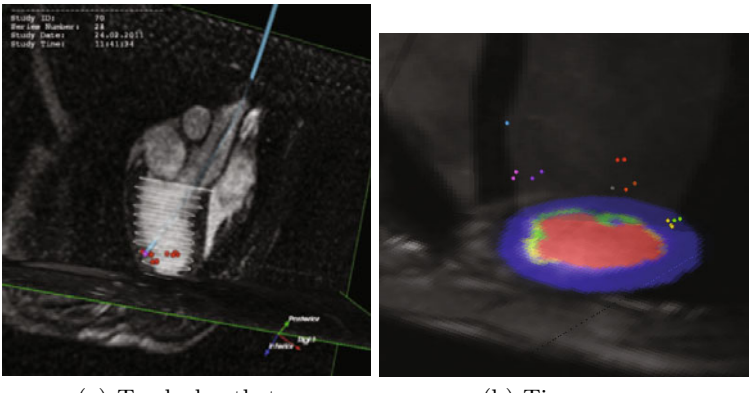

(a) Tracked catheter (b) Tissue map

Fig. 2. a)Tracked EP catheter (blue) having three microcoils fused with EP recordings (red), a prior cine MR and associated endocardial surface contours (white). b) Tissue classification map from DE-MRI fused with prior cine SSFP MR volume showing blood (red), healthy myocardium (blue), infarct (green) and heterogeneous tissue (yellow). Points are EP catheter recording locations with separate colour coding by activation time.

3.3 Interactive and Automated 2D Plane Control

Vurtigo can remotely control the MRI scan plane prescription if RTHawk is placed in read mode. Vurtigo has both a *drive mode* and a *passive mode*. In passive mode it will listen for and render new information from the scanner. In drive mode the Vurtigo interface allows the user to move the plane to a new position or orientation in the 3D view to actively change the position of the scan plane. The scanner will acquire an image at the requested position and then pass the new image back to be rendered by Vurtigo. This way of moving scan planes is more intuitive since it has the advantage that once a prior 3D volume is loaded, or a catheter tip is located, those objects can be used as a guide

to determine where the plane should be positioned. Automated prescription of real-time and/or prior roadmap planes to follow the catheter tip has also been implemented in Vurtigo.

4 Methods for EP Interventions

4.1 Active Tracking of Catheters

Catheters can be actively tracked in the MR using microcoils placed on the catheter which are sensitive to a small region in their vicinity. The location of a microcoil can be determined using a non-selective (or weakly selective) RF pulse and acquiring projections in three orthogonal directions. A centroid-based peak detection is usually used to determine the location of the microcoil in three dimensions [23].

Tracking was done with a projection (TR of 12 ms) along each direction and a tracking field of view (FOV) of 40 cm to give a true tracking rate of approximately 28 frames per second (fps) and a resolution of 1.6 mm. Active detuning of the surface coil was used to avoid coupling with the catheter coils, and requires less time ($\sim$3 ms) than the shortest TR using for imaging/tracking. The accuracy of tracking was measured in a water bath to be $\leq$2 mm, but requires further validation in-vivo.[24]

The signal in the coil is susceptible to the orientation of the catheter microcoils with respect to the main magnetic field. Additionally, tracking projections are poor when there are magnetic susceptibility differences between the catheter and tissues or materials near the microcoil. These could result in double peaks or other artifacts in the projection [25]. These are the main sources of errors in our tracking procedures. Peak offsets due to off-resonance frequencies are not an issue in practice due to the higher bandwidths (125 KHz) in our acquisition.

The tracking sequence is sensitive to off-resonance frequencies; these may be due to field inhomogeneities in the main magnetic field and variations in the local magnetic susceptibility. The field inhomogeneities were minimized by a pre-scan with a prescribed shim volume over the heart. We used higher bandwidths (125KHz) for the acquisition to give a 488 Hz bandwidth per pixel, so that any remaining centre frequency offset has negligible effect on positioning.

Depending on the number and location of tracked coils, Vurtigo is able to display the device's tip, the tip and direction, or a spline indicating the catheter's shape. With Vurtigo in drive mode, prior volume image planes can be attached to a tracked location on or near the catheter tip to follow its movement.

4.2 EP Recordings and EAM Generation

EP interventional procedures usually use two catheters. A mapping catheter is used to map the surface electrophysiological signals. A pacing catheter is used to pace the heart slightly above its natural rate. In our EP interventions, anywhere from one to three microcoils on a mapping catheter are tracked as it is maneuvered in the LV, as well as one microcoil on the pacing catheter placed in the RV that provides programmed stimulation.[26]

EP measurements were performed using a prototype Bridge EP Recording System with two Vision MR conditional catheters (Imricor Medical Systems, Burnsville, MN). A porcine model of myocardial infarct was used for experimental EP recordings, with three of six subjects completing the entire procedure (catheter insertion, recording, removal) successfully.

MR-guided activation EP data was post-processed by Vurtigo to generate voltage amplitude maps or isochronal maps of local activation time (LAT). Each EP recording is matched to the simultaneously captured catheter position data with cardiac diastolic gating of both datasets (approximately 200ms window).

After labelling each recording point with the EP data (voltage or LAT), the data is mapped to a LV endocardial surface mesh that was automatically segmented by an in-house MATLAB®(Mathworks) post-processing algorithm [27] from the diastolic phase of the prior cine SSFP volume, (Fig. 3). Each mesh vertex is assigned the weighted average of the EP values of the recorded points (eg. voltage or LAT) located within a 10 mm (user defined) area of effect. The weightings are calculated by the inverse squared distance between the vertex and the EP recording locations, with the weight sum normalized to one. The vertices are coloured by a lookup table which maps the scalar values to RGB colours, and there is linear interpolation of colour between the vertices of each mesh triangle. This method improves upon conventional EAM by ensuring that the map has an anatomical shape rather than the best fit mesh derived from asymmetrically sampled EP recording locations that often has an irregular shape.[26]

Validation of the spatial and temporal fusion is a work in progress. For fusion of prior cine volumes with catheter locations, the catheter points were filtered to match the cardiac phase (diastole). A limiting factor is the temporal resolution (50 ms) of the prior cine volume. Therefore an estimate of the synchronization error would be approximately 65 ms, due to cine temporal resolution and variation in communication latency, assuming regular cardiac rhythm. The spatial error would correspond to the displacement of the cardiac wall over this time interval, though diastolic motion is slow. Additional spatial registration errors that require estimation and/or compensation are gross patient motion between the time of prior volume acquisition and the intervention, and the cycle-to-cycle variation due to cardiac and respiratory motion.

4.3 MR Imaging

MR imaging was performed on a 1.5 T CV/i scanner (GE Healthcare, Milwaukee, WI, USA) using a 5" surface coil. For real-time imaging, spoiled gradient echo images (128x128 pixel, 30 cm FOV, 2.3 mm resolution) were continuously acquired with a 6.8 ms TR for a true frame rate of about 9 fps. Prior volume cine SSFP parameters: 256×256 pixels, TR 3.7-4.7 ms, 20 phases, 19-23 cm FOV. During in-vivo experiments catheter tracking positions were rendered with the prior volume. Tracking was occasionally alternated with 2D real-time scan planes to observe the current state, albeit with lower resolution and smaller FOV than the prior volume images. Rendering the volume, the real-time planes and the catheters in a fused visualization improves the interventionalist's ability to navigate with respect to the patient's anatomy.

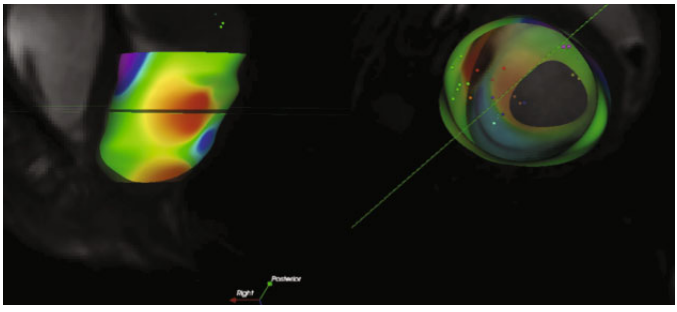

Fig. 3. Long (left) and short axis (right) views of the LV endocardial surface segmented from the prior MR volume in a fused display. Surface colour coding represents an LAT map obtained from an EP recording catheter.

One or more prior MR volumes were also acquired to provide detailed visualization of anatomy (cine SSFP series) or infarct. (Infarct was determined by a novel late Gadolinium enhanced (LGE) MRI series, multi-contrast delayed enhancement (MCDE) [28] with imaging parameters: SAX, 256×256 mm, 4-4.3 ms TR, 20 phases, 22-23 cm FOV.) Automatic segmentation and classification of MCDE provides maps that indicate healthy, infarcted and heterogeneous tissue. The latter has been shown to be predictive of arrhythmia events (inducibility of VT, appropriate activation of an implanted intracardiac defibrillator), and may provide an additional target for cardiac resynchronization therapy [29]. Vurtigo has the capability of fusing the tissue map with the anatomy and EP catheter information, either by same-day imaging or post-processing with landmark registration, (Fig. 2(b)).

5 Conclusions

Vurtigo is a cross-platform, freely available, open-source application, that provides advanced visualization for image-guided interventions, and has a vital role in supporting our image-guided, in-vivo EP experiments. Several new features are works in progress at this time including real-time calculation of EP data (voltage and LAT maps) from tracked EP recording catheters, and the implementation of improved signal processing and motion correction of EP data points. Further validation of the registration and synchronization accuracy, especially in-vivo, is required to assess the fusion errors of catheter locations and imaging. Work is in progress to analyse the correspondence of tissue heterogeneity from MR and slow conduction zones from electroanatomic mapping, before and after RF ablation therapy.

Acknowledgements. The authors would like to thank the Canadian Foundation for Innovation and Canadian Institutes of Health Research for their support.

References

1. Nayak, K.S., Hu, B.S.: The future of real-time cardiac magnetic resonance imaging. Curr. Cardiol. Rep. 7(1), 45–51 (2005)
2. Ladd, M.E., Quick, H.H., Debatin, J.F.: Interventional MRA and intravascular imaging. J. Magn. Reson. Imaging 12(4), 534–546 (2000)
3. Pintilie, S., Biswas, L., Anderson, K.A., Wright, G.A., Radau, P.: Visualization Software for Real-time Image-guided Therapeutics in Cardiovascular Interventions. In: MICCAI: Cardiac Interventional Imaging and Biophysical Modeling Workshop (2009)
4. Gary, K., Ibanez, L., Aylward, S., Gobbi, D., Blake, M., Cleary, K.: IGSTK: An Open Source Software Toolkit for Image-Guided Surgery. IEEE Computer, 46–53 (2006)
5. Guttman, M., et al.: Real-time accelerated interactive MRI with adaptive sense and unfold. Magn. Reson. Med. 50, 315–321 (2003)
6. 3D Slicer, http://www.slicer.org/
7. Santos, J.M., Cunningham, C.H., Lustig, M., Hargreaves, B.A., Hu, B.S., Nishimura, D.G., Pauly, J.M.: Single Breath-Hold Whole-Heart MRA Using Variable-Density Spirals at 3T. Magn. Reson. Med. 55, 371–379 (2006)
8. Schroeder, W., Martin, K., Lorensen, B.: Visualization Toolkit: An Object-Oriented Approach to 3D Graphics, 4th edn. (2006)
9. Blanchette, J., Summerfield, M.: C++ GUI Programming with Qt 4, 2nd edn. (2008)
10. DCMTK - DICOM Toolkit, http://dicom.offis.de/dcmtk
11. Ibanez, L., Schroeder, W., Ng, L., Cates, J.: ITK Software Guide. ITK Version 2.4 (2005)
12. CUDA Toolkit, http://www.nvidia.com/object/cuda_home.html
13. Martin, K., Hoffmann, B.: Mastering CMake, 4th edn. (2008)
14. Desjardins, B., Crawford, T., Good, E., Oral, H., Chugh, A., Pelosi, F., Morady, F., Bogun, F.: Infarct architecture and characteristics on delayed enhanced magnetic resonance imaging and electroanatomic mapping in patients with postinfarction ventricular arrhythmia. Heart Rhythm 6(5), 644–651 (2009); Epub. (February 14, 2009)
15. Dickfeld, T., Tian, J., Ahmad, G., Jimenez, A., Turgeman, A., Kuk, R., Peters, M., Saliaris, A., Saba, M., Shorofsky, S., Jeudy, J.: MRI-Guided ventricular tachycardia ablation: integration of late gadolinium-enhanced 3D scar in patients with implantable cardioverter-defibrillators. Circ. Arrhythm. Electrophysiol. 4(2), 172–184 (2011); Epub. (January 26, 2011)
16. Wijnmaalen, A.P., van der Geest, R.J., van Huls van Taxis, C.F., Siebelink, H.M., Kroft, L.J., Bax, J.J., Reiber, J.H., Schalij, M.J., Zeppenfeld, K.: Head-to-head comparison of contrast-enhanced magnetic resonance imaging and electroanatomical voltage mapping to assess post-infarct scar characteristics in patients with ventricular tachycardias: real-time image integration and reversed registration. Eur. Heart J. 32(1), 104–114 (2011); Epub. (September 23, 2010)
17. de Chillou, C., Lacroix, D., Klug, D., Magnin-Poull, I., Marqui, C., Messier, M., Andronache, M., Kouakam, C., Sadoul, N., Chen, J., Aliot, E., Kacet, S.: Isthmus characteristics of reentrant ventricular tachycardia after myocardial infarction. Circulation 105(6), 726–731 (2002)
18. Stevenson, W.G., Khan, H., Sager, P., Saxon, L.A., Middlekauff, H.R., Natterson, P.D., Wiener, I.: Identification of reentry circuit sites during catheter mapping and radiofrequency ablation of ventricular tachycardia late after myocardial infarction. Circulation 88(4 Pt 1), 1647–1670 (1993)

19. Janse, M.J., Wit, A.L.: Electrophysiological mechanisms of ventricular arrhythmias resulting from myocardial ischemia and infarction. Physiol. Rev. 69(4), 1049–1169 (1989)
20. Kleber, A.G., Rudy, Y.: Basic mechanisms of cardiac impulse propagation and associated arrhythmias. Physiol. Rev. 84(2), 431–488 (2004)
21. Bub, G., Shrier, A.: Propagation through heterogeneous substrates in simple excitable media model. Chaos 12(3), 747–753 (2002)
22. Pintilie, S., Biswas, L., Oduneye, S.O., Anderson, K.A., Wright, G.A., Radau, P.: Visualization platform for real-time, MRI-guided cardiac interventions. In: Proceedings 19th Scientific Meeting, ISMRM, Montreal, May 7-13, p. 6887 (2011)
23. Dumoulin, C.L., Souza, S.P., Darrow, R.D.: Real-time position monitoring of invasive devices using magnetic resonance. Magn. Reson. Med. 29, 411–415 (1993)
24. Ramanan, V., Oduneye, S.O., Biswas, L., Pintilie, S., Wright, G.A.: Accurate catheter tip tracking for MR-Guided EP procedures using realtime active detuning. In: Proceedings 19th Scientific Meeting, ISMRM, Montreal, May 7-13 (2011)
25. Dumoulin, C.L., Mallozzi, R.P., Darrow, R.D., Schmidt, E.J.: Phase-field dithering for active catheter tracking. Magn. Reson. Med. 63, 1398–1403 (2010)
26. Oduneye, S.O., Biswas, L., Pintilie, S., Ramanan, V., Barry, J., Zeidan Shwiri, T., Kadmon, E., Crystal, E., Wright, G.A.: MR-Guided endocardial local activation time map during programmed stimulation. In: Proceedings 19th Scientific Meeting, ISMRM, Montreal, May 7-13, p. 3888 (2011)
27. Lu, Y., Radau, P., Connelly, K.A., Dick, A.J., Wright, G.A.: Segmentation of Left Ventricle in Cardiac Cine MRI: An Automatic Image-Driven Method. In: Ayache, N., Delingette, H., Sermesant, M. (eds.) FIMH 2009. LNCS, vol. 5528, pp. 339–347. Springer, Heidelberg (2009)
28. Detsky, J.S., Paul, G.A., Dick, A.J., Wright, G.A.: Reproducible classification of infarct heterogeneity using fuzzy clustering on multicontrast delayed enhancement magnetic resonance images. IEEE Trans. Med. Imaging 28(10), 1606–1614 (2009)
29. Roes, S.D., Borleffs, C.J., van der Geest, R.J., Westenberg, J.J., Marsan, N.A., Kaandorp, T.A., Reiber, J.H., Zeppenfeld, K., Lamb, H.J., de Roos, A., Schalij, M.J., Bax, J.J.: Infarct tissue heterogeneity assessed with contrast-enhanced MRI predicts spontaneous ventricular arrhythmia in patients with ischemic cardiomyopathy and implantable cardioverter-defibrillator. Circ. Cardiovasc. Imaging 2(3), 183–190 (2009); Epub. (March 23, 2009)

Validation of a Novel Method for the Automatic Segmentation of Left Atrial Scar from Delayed-Enhancement Magnetic Resonance

Rashed Karim[1], Aruna Arujuna[1,2], Alex Brazier[1], Jaswinder Gill[1,2], C. Aldo Rinaldi[1,2], Michael Cooklin[1,2], Mark O'Neill[1,2], Reza Razavi[1,2], Tobias Schaeffter[1], Daniel Rueckert[3], and Kawal S. Rhode[1]

[1] Division of Imaging Sciences and Biomedical Engineering, King's College London, UK
[2] Department of Cardiology, Guy's and St. Thomas' Hospitals NHS Trust, London, UK
[3] Department of Computing, Imperial College London, London, UK
{rashed.karim,aruna.arujuna,alex.brazier,tobias.schaeffter, kawal.rhode}@kcl.ac.uk, {jaswinder.gill,aldo.rinaldi, mark.oneill}@gstt.nhs.uk, d.rueckert@imperial.ac.uk

Abstract. Delayed-enhancement magnetic resonance imaging is an effective technique for imaging left atrial (LA) scars both pre- and post- radio-frequency ablation for the treatment of atrial fibrillation. Existing techniques for LA scar segmentation require expert manual interaction, making them tedious and prone to high observer variability. In this paper, a novel automatic segmentation algorithm for segmenting LA scar was validated using digital phantoms and clinical data from 11 patients. The performance of the approach was compared to the two leading semi-automatic techniques and the ground truth of manual segmentations by 2 expert observers. The novel approach was shown to be accurate in terms of Dice coefficient, robust to typical image intensity variability, and much faster in terms of execution time.

Keywords: Cardiac MRI, atrial fibrillation, scar segmentation, graph-cuts, Markov random fields.

1 Introduction

Atrial fibrillation (AF) affects approximately 2.2 million people in the USA. One of the most common catheter laboratory procedures is catheter-based radio-frequency ablation (RFA) that can provide a cure for AF by electrically isolation of the pulmonary veins (PVs). With a success rate of 50-80%, the assessment of the LA substrate in terms of scarring becomes important. Gadolinium delayed enhancement (DE) magnetic resonance imaging (MRI) has been shown effective for LA scar imaging [1,2]. Quantification of the DE-MRI has been proposed using thresholding techniques for either endocardial surface-based segmentation [3] or volumetric segmentation [2]. Such quantification has been shown to predict likely response to RFA in clinical studies [4,5]. It will also be critical for applying cardiac biophysical models of AF for patient selection and RFA planning [6].

O. Camara et al. (Eds.): STACOM 2011, LNCS 7085, pp. 254–262, 2012.

Existing techniques [2,3] for LA scar segmentation require expert user interaction making them tedious and prone to high inter- and intra-observer variability. In this paper, we evaluated an automatic LA scar segmentation algorithm [11] based on a probabilistic tissue intensity model of DE-MRI data. The algorithm employs a Markov random field (MRF)-based energy formulation that is solved using graph-cuts. We validated the automatic method using digital phantoms and 11 patient data and compared the performance to expert manual segmentations and semi-automatic approaches in [2,3].

2 Methods

2.1 Automatic Segmentation of Atrial Lesions

Segmentation Framework: The segmentation approach [13] is based on a MRF-based energy formulation solved using graph-cuts [9]. Segmentation of scars from DE-MRI images can be described as assigning a label $f_p \in \{0,1\}$ to every voxel p in the image I. The MRF-based energy function over a neighborhood of voxels N and labeling f:

$$E(f) = \lambda \sum_{p \in P} D_p(f_p) - \sum_{\{p,q\} \in N} V_{(p,q)}(f_p, f_q). \quad (1)$$

The weighting term λ weights the influence of the energy terms. The intensity energy D_p measures the disagreement between the *a prior* probabilistic model and the observed data, and $V_{(p,q)}$ is a smoothness term within a tissue class that penalizes any discontinuities between voxel pairs $\{p, q\}$. The scar segmentation problem is solved by minimization of the energy function described in Eq. 1. To optimize Eq. 1 with graph cuts, a graph $G = \langle V, E \rangle$ with a node $v \in V$ for each voxel p is defined on I. The edges $e \in E$ consists of connections between neighbouring voxels. The terminal nodes S and H of the graph represent labels for scar and non-scar (i.e. healthy) tissues. By determining an S-H cut on G, the desired segmentation is obtained.

Tissue Priors: The intensity priors for the scar and non-scar tissue classes are modeled using Gaussian distributions. As scar tissue normally borders with a multitude of tissues, a multi-modal intensity distribution is necessary and this is accomplished using a mixture of Gaussian distributions. Given segmentations of the LA endocardium from the an atomical images is available, regions of blood pool, atrial wall and pericardium can be approximated. This is accomplished by obtaining regions within fixed distances from the LA endocardium using a distance transform. It is important to note that the non-scar tissue Gaussian mixture model is obtained from the image to be segmented (i.e. unseen image).

The intensity model for scar is built from training data. These are DE-MRI images with manually segmented scars with some regions of blood pool and pericardium outlined. To derive an intensity distribution model for scar tissues, a Gaussian density function is used:

$$p(I|f_p = 1) = \frac{1}{\sqrt{2\pi\sigma^2}} \exp\left[-\frac{1}{2}\left(\frac{r-\mu}{\sigma}\right)^2\right] \quad (2)$$

where r is the ratio of DE-MRI signal of scar tissue to interfacing tissues with mean μ and variance σ. The parameters μ and σ are derived from training images which are expert hand-segmentations of scars in DE-MRI. The ratio r for each voxel in the unseen image is determined as the ratio of its intensity to mean blood pool and myocardium intensity. Finally, to ensure continuity and smoothness within voxels of a tissue class through the $V_{(p,q)}$ term of the MRF energy function, neighboring voxels sharing similar intensities incur an exponentially high cost if they are classified into different tissue classes:

$$V(p,q) = \exp\left[-\frac{1}{2}\left(\frac{|I_p - I_q|}{\sigma}\right)^2\right]. \tag{3}$$

2.2 Validation of the Automatic Algorithm

The automatic algorithm was evaluated on both digital phantoms and patient MRI data.

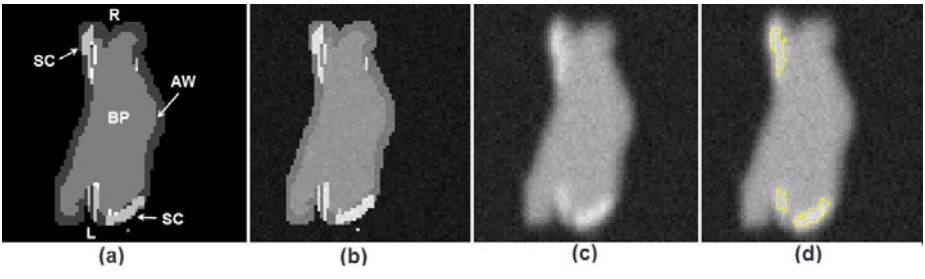

Fig. 1. (a) The phantom template showing the anatomical regions in a 2D slice (BP-blood pool, AW – atrial wall, SC - hand-drawn scar, R-right side, L-left side). (b) Grey-level intensities randomly sampled from the respective Gaussian distributions. (c) The final phantom obtained following anisotropic blurring with Gaussian white noise. (d) Detection of scars on the phantom by the algorithm.

Digital Phantom Validation: Due to the variability between observers in manual segmentations, it is difficult to establish the ground-truth for scar in DE-MRI. For this reason, a digitally synthesized phantom was used for validation of the novel segmentation approach. The construction of the phantom *template* begins with the LA geometry obtained from one particular patient. From the contour of the LA, a signed distance map is applied such that each voxel inside and outside the LA is assigned its minimum Euclidean distance to the contour. This allows the creation of a phantom atrial epicardial wall with a 1.25 mm thickness which is in agreement with the average human left atrial wall thickness [10]. Voxels inside the LA contour constitute the blood pool. Phantom scars are then drawn by hand inside the left atrial wall region. Each region of scar is geometrically unique. Fig. 1 shows an example. The grey-level intensities assigned to each region (atrial wall, blood pool and background) in the phantom template are obtained from Gaussian distributions. These distributions are measured from patient DE-MRI data. For our purposes, we obtained the mean intensity and variance of blood pool, atrial wall and background from our patient cohort. For

scar, however, its intensity Gaussian is obtained by varying the scar to blood pool mean intensity ratio. This simulates the typical variability seen in DE-MRI data that is caused by selecting different inversion times, the goal of which is to null the healthy myocardium and blood-pool as much as possible. It is this ratio that has a direct and important effect on the quality of segmentation.

Finally, to simulate partial volume effect and anisotropic voxel sizes in DE-MRI, where the in-plane resolution is normally higher than the through-plane resolution, an anisotropic blur is applied with a kernel size of 2 mm in the through-plane direction and 1 mm in the in-plane direction. Note that the image resolution of the phantom is set to $1.3\times1.3\times2$ mm^3.

Clinical Data Validation: 11 patients with paroxysmal AF were recruited into the study under a local ethics committee approved protocol. The patients underwent RFA circumferential ablation to achieve isolation of the PVs. At 6 months post-ablation, the patients underwent MRI (1.5T Achieva, Philips Healthcare, The Netherlands). The MR examination included (a) a 3D magnetic resonance angiography (MRA) scan with whole-heart coverage, reconstructed to 1mm^3 isotropic resolution, following injection of a Gd-DTPA contrast agent; (b) a 3D respiratory-navigated and cardiac-gated, balanced steady state free precession (bSSFP) acquisition with whole-heart coverage, reconstructed to 1.3mm^3 isotropic resolution; and (c) 20 minutes after contrast injection, the delayed enhancement scan, which was a 3D respiratory-navigated and cardiac-gated, inversion recovery turbo field echo with whole LA coverage, reconstructed to $1.3\times1.3\times2$mm^3 resolution.

The best quality anatomical scan was selected from either the bSSFP or MRA scans and the endocardial boundary of the LA was segmented using an automatic approach based on a statistical shape model [7]. The automatic segmentation was verified by a clinical expert and manual corrections were made whenever required to achieve a high-fidelity result. The anatomical images were registered to the DE images using initialization by the DICOM header data, followed by affine registration [8]. Thereby the endocardial LA boundary was defined in the DE images.

3 Results

3.1 Digital Phantom

A series of experiments was conducted with the digital phantoms to test the accuracy and robustness of the automatic algorithm. Using grey level intensities measured from real DE-MRI scans, the scar to blood pool (SC-BP) ratio was varied in each set of experiments (see Table 1).

Table 1. The grey-level intensities (mean and standard deviation) used for the phantom experiments obtained using measurements from real DE-MRI scans. Note that the grey-level intenisty for scar is varied by varying its ratio to the blood-pool.

Background	Atrial wall (AW)	Blood-pool (BP)	Scar (SC)	SC:BP	BP:AW
30 (20)	117 (20)	140 (15)	154-420 (50)	1.1 – 3.0 (0.35)	1.2

The SC-BP ratio ranged between 1.1 to 3.0 in increments of 0.1, based on the range found in real DE-MRI scans. Note that this ratio is normally above 1.3 in high quality DE-MRI images. In the first set of experiments, the scar model was trained on a specific SC-BP ratio band by randomly generating 30 phantoms for our training set. The segmentation algorithm was then tested against 30 randomly generated unseen phantom instances *for each* SC-BP ratio, i.e. 1.1 to 3.0. Note that the scar and LA geometry in these phantoms remain unchanged with the intensity distributions randomly sampled. The mean Dice coefficients of similarity with the known ground truth for scar was computed. Fig. 3 shows results from these experiments.

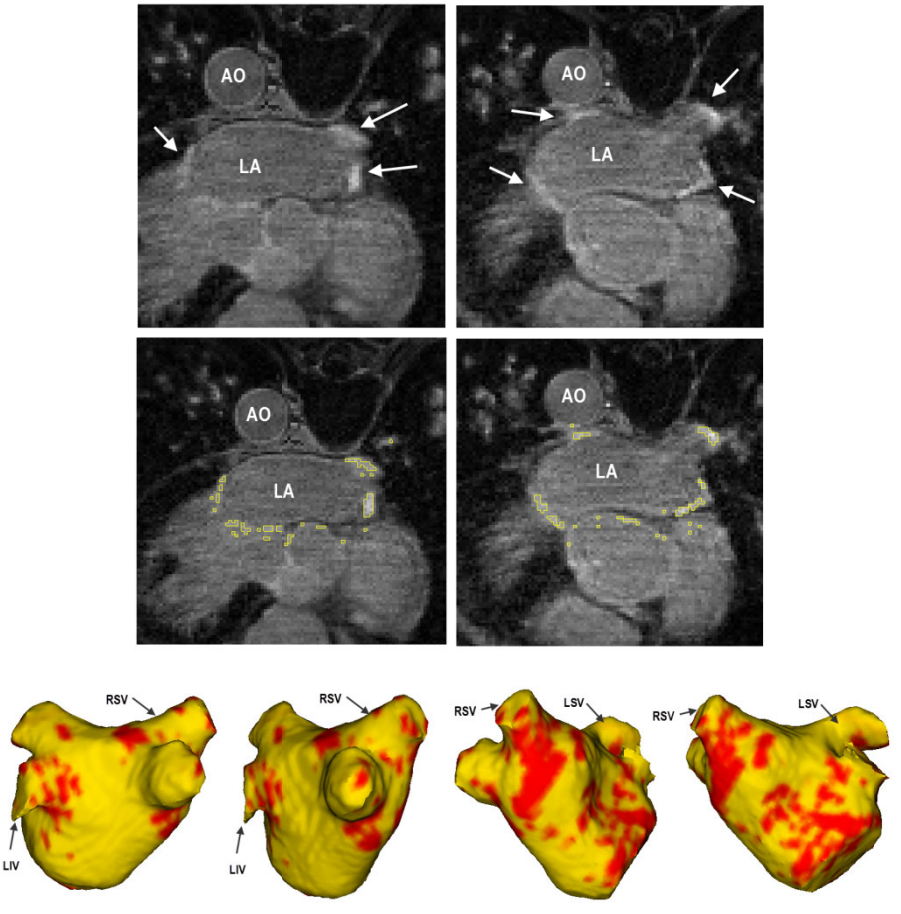

Fig. 2. The data shown is from a single patient. Original DE-MRI slices (top row). Areas of enhancement are indicated by arrows. The segmentation obtained from the algorithm on these slices (middle row). The surface shell given in four different orientations showing segmented regions. Abbreviations: LA – left atrium, AO – aorta, RSV – right superior vein, LIV – left inferior vein, LSV – left superior vein.

In a separate set of experiments, the robustness of the algorithm was tested by constructing three new phantoms, each with new and unique scar geometry. However, the algorithm was trained separately only on its best-performing SC-BP bands: 1.5-1.8 and 1.8-2.1. The Dice coefficient with ground truth is reported for each training band in Fig. 4. In the final set of experiments, the algorithm was tested on phantoms that have a randomly varying SC-BP ratio within the 1.1 – 3.0 range. 100 random phantoms were generated and run on two separately trained models. The mean Dice coefficients were 0.847 (0.004) and 0.749 (0.002) for training bands 1.5-1.8 and 1.8-2.1, respectively.

The phantom tests reveal that the algorithm performs consistently within its training band zone (Fig. 3). The consistency increases when images have good scar clarity (high SC-BP). The algorithm also demonstrated that it is robust to differing scar geometries and SC-BP ratios (when SC-BP > 1.5).

3.2 Clinical Data

In these set of experiments, the algorithm was evaluated against expert manual segmentations and two different semi-automatic techniques [3, 5]. All experiments were run on a 2.8 Ghz PC. The automatic algorithm was trained using the leave-one-out principle. The pre-processing (LA segmentation and registration) was the same for each approach, i.e. automatic, semi-automatic and manual, and took typically 5 minutes. The automatic algorithm completed the segmentation process for each DE image in typically 30 seconds whereas the semi-automatic approach in [3] took 5 minutes, whilst the technique in [5] took 7 minutes. Manual segmentation of the scars took typically 45 minutes per observer. See Fig. 2 for results on a single patient data.

Here we describe how the semi-automatic approaches in both [3] and [5] were implemented. The semi-automatic approach in [3] employs a maximum intensity projection (MIP) followed by thresholding for mapping scar onto the segmented 3D LA shell. The scar information is thus only available on the shell's 2D surface. As the automatic and manual segmentations generate volumetric segmentations, a MIP was performed to project the segmentation information to the 2D surface shell. The consequence of this step is loss of volumetric information, but is an essential step for allowing comparison with the semi-automatic approach. Note that the thresholding step for the semi-automatic approach was obtained from an expert-observer. For the semi-automatic approach in [5], a first step is to acquire the atrial wall which was accomplished by applying a signed distance transform on the segmented LA's contour. The approximate wall was then automtically obtained as 1 pixel inside and outside the LA contour. Scar is defined in [5] as 2-4 standard deviations from the lower mean of the bi-modal intensity histogram of the atrial wall. The selection of this threshold cut-off was based on an expert observer. The segmentation is then projected onto the LA surface shell. We compared all segmentations by computing the Dice coefficient on the LA surface shell (see Table 2).

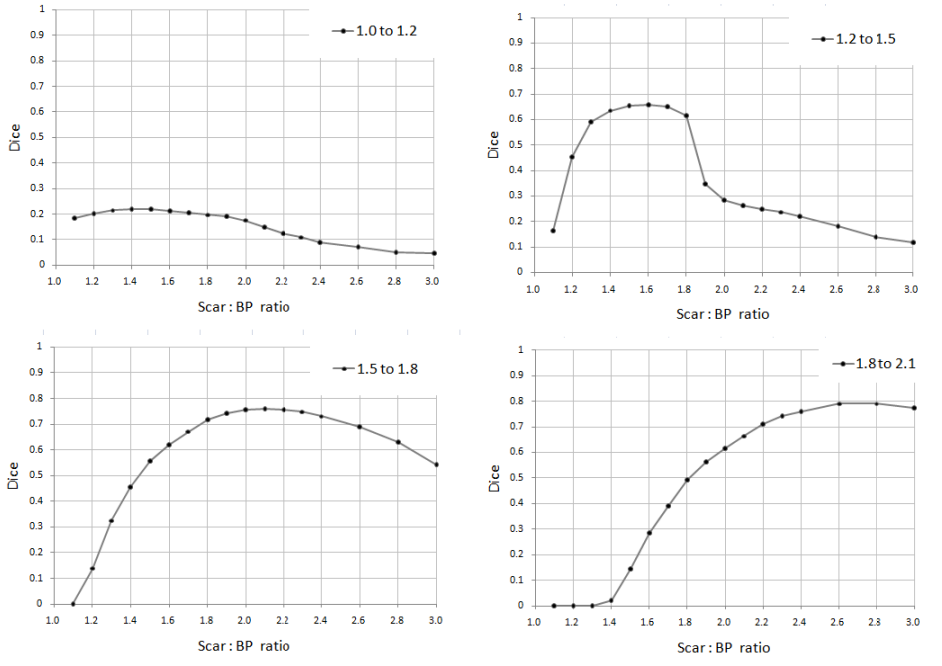

Fig. 3. The mean Dice coefficients against ground truth obtained with the scar model trained on a separate SC-BP ratio band, clock-wise from left: 1.0 - 1.2, 1.2 - 1.5, 1.8 - 2.1 and 1.5 - 1.8. Note that the error bars for each point are omitted as they are less than 0.05 standard deviations in all cases.

The Dice comparing the segmentation MIPs (Table 2(A)) showed that the segmentation outputs from the automatic and expert-operated semi-automatic methods

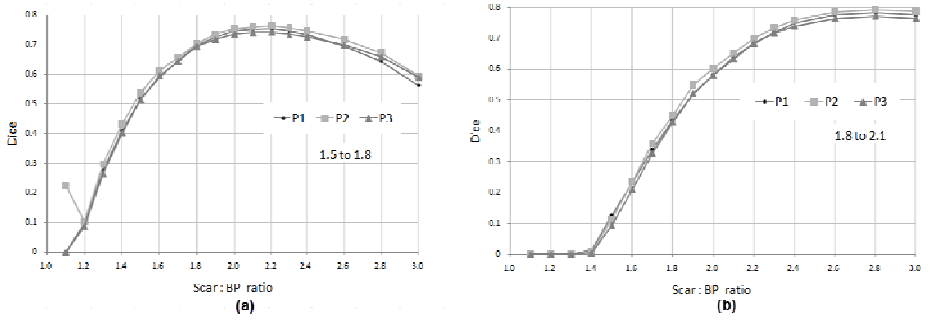

Fig. 4. The mean Dice-coefficients against ground truth in three different phantoms (P1, P2 & P3) each with unique scar geometry and tested with 30 random instances per SC-BP ratio: (a) with scar-model trained on SC-BP band 1.5 - 1.8 (b) with scar model trained on SC-BP band 1.8 - 2.1. Note that error bars for each point are omitted as they are less than 0.01 in all cases.

compared well with good Dice overlaps (means 0.72 and 0.54). The agreement between the expert observers was evaluated and some degree of variability was found (mean Dice = 0.4 in Table 2(B)) owing to the challenging and laborious task of manual segmentation. In addition to this, it was found that the observers were often reluctant to repeatedly change the width of the tip of the brush used to mark regions of scar in the images. This would make the task of manual segmentation even more laborious. As a result, the extent of scar was sometimes exaggerated in some regions. Finally, we compared segmentations from the automatic algorithm to the expert segmentations, this time *not* the Dice on the segmentation MIPs but on the volumetric images, and found a reasonable overlap (mean Dice = 0.5 in Table 2(C)).

Table 2. (A) The Dice comparing the MIPs of segmentations from the automatic algorithm to the output from semi-automatic algorithms 1 and 2 in [3] and [5] respectively. (B) comparison of expert segmentations from the two observers. (C) comparison of automatic algorithm with expert observers.

A

	semi-1	semi-2
P1	0.6	0.6
P2	0.7	0.5
P3	0.7	0.5
P4	0.7	0.6
P5	0.8	0.6
P6	0.6	0.4
P7	0.7	0.6
P8	0.9	0.4
P9	0.8	0.5
P10	0.7	0.7
P11	0.2	0.1
Mean	0.72	0.54

B

Patients	(OB1 / OB2)
P1	0.4
P2	0.1
P3	0.2
P4	0.4
P5	0.5
P6	0.5
P7	0.3
P8	0.3
P9	0.3
P10	0.4
P11	0.4
Mean	0.4

C

Patients	OB-1	OB-2
P1	0.6	0.5
P2	0.4	0.5
P3	0.5	0.4
P4	0.1	0.5
P5	0.6	0.5
P6	0.6	0.5
P7	0.6	0.4
P8	0.5	0.4
P9	0.6	0.4
P10	0.8	0.4
P11	0.7	0.6
Mean	0.5	0.5

4 Discussion and Conclusion

In this paper, a novel fully automatic technique for segmenting scars in the LA using DE-MRI has been validated using digital phantoms and patient MRI data. A quantitative evaluation with digital phantoms showed that the algorithm was robust to variability in image intensities and accurate as measured by Dice coefficient. The algorithm was also tested on clinical data. It approximated the scars in the images well and this was evaluated by comparing its results with those of two existing well established semi-automatic techniques. In addition to this, they were compared against expert segmentations from two observers. The degree of agreement between observers was shown to be low. The automatic method produced a considerable time-saving over using manual segmentation (30 seconds vs. 45 minutes) and some saving over the using semi-automatic method (30 seconds vs. 5/7 minutes). A major advantage is that the algorithm is automatic requiring no expert user supervision.

It is envisaged that user-independent lesion segmentation with low computational cost will allow for standardization of DE-MRI as a marker of cardiac injury. Future work will focus on improved training of the probabilistic intensity model and validation using a larger patient cohort with more expert segmentations per data set.

References

[1] Peters, D.C., et al.: Detection of pulmonary vein and left atrial scar after catheter ablation with three-dimensional navigator-gated delayed enhancement MR imaging: initial experience. Radiology 243(3), 690–695 (2007)

[2] McGann, C.J., et al.: New magnetic resonance imaging-based method for defining the extent of left atrial wall injury after the ablation of atrial fibrillation. J. Am. Coll. Cardiol. 52(15), 1263–1271 (2008)

[3] Knowles, B.R., et al.: 3-D visualization of acute RF ablation lesions using MRI for the simultaneous determination of the patterns of necrosis and edema. IEEE Trans. Biomed. Eng. 57(6), 1467–1475 (2010)

[4] Reddy, V.Y., et al.: Arrhythmia recurrence after atrial fibrillation ablation: Can magnetic resonance imaging identify gaps in atrial ablation lines? Journal of Cardiovascular Electrophysiology 19(4), 434–437 (2008)

[5] Oakes, R.S., et al.: Detection and quantification of left atrial structural remodeling with delayed-enhancement magnetic resonance imaging in patients with atrial fibrillation. Circulation 119(13), 1758–1767 (2009)

[6] Reumann, M., et al.: Preventive ablation strategies in a biophysical model of atrial fibrillation based on realistic anatomical data. IEEE Trans. Biomed. Eng. 55(2 Pt 1), 399–406 (2008)

[7] Peters, J., Ecabert, O., Meyer, C., Schramm, H., Kneser, R., Groth, A., Weese, J.: Automatic Whole Heart Segmentation in Static Magnetic Resonance Image Volumes. In: Ayache, N., Ourselin, S., Maeder, A. (eds.) MICCAI 2007, Part II. LNCS, vol. 4792, pp. 402–410. Springer, Heidelberg (2007)

[8] Schnabel, J.A., Rueckert, D., Quist, M., Blackall, J.M., Castellano-Smith, A.D., Hartkens, T., Penney, G.P., Hall, W.A., Liu, H., Truwit, C.L., Gerritsen, F.A., Hill, D.L.G., Hawkes, D.J.: A Generic Framework for Non-rigid Registration Based on Non-uniform Multi-level Free-Form Deformations. In: Niessen, W.J., Viergever, M.A. (eds.) MICCAI 2001. LNCS, vol. 2208, pp. 573–581. Springer, Heidelberg (2001)

[9] Boykov, Y., Veksler, O., Zabih, R.: Fast approximate energy minimization via graph cuts. IEEE Transactions on Pattern Analysis and Machine Intelligence 23(11), 1222–1239 (2002)

[10] Hall, B., Jeevanantham, V., Simon, R.: Variation in left atrial transmural wall thickness at sites commonly targeted for ablation of atrial fibrillation. J. Interv. Card. Eletrophysiol. 17(2) (2006)

[11] Karim, R., Arujuna, A., Brazier, A., Gill, J., Rinaldi, C.A., O'Neill, M., Razavi, R., Schaeffter, T., Rueckert, D., Rhode, K.S.: Automatic Segmentation of Left Atrial Scar from Delayed-Enhancement Magnetic Resonance Imaging. In: Metaxas, D.N., Axel, L. (eds.) FIMH 2011. LNCS, vol. 6666, pp. 63–70. Springer, Heidelberg (2011)

Cardiac Motion Estimation Using Covariant Derivatives and Helmholtz Decomposition

Alessandro Becciu[1], Remco Duits[1,2], Bart J. Janssen[2], Luc M.J. Florack[1,2], and Hans C. van Assen[1]

[1] Dept. of Biomedical Engineering, Eindhoven University of Technology, Netherlands
http://bmia.bmt.tue.nl
[2] Dept. of Mathematics, Eindhoven University of Technology, Netherlands

Abstract. Quantification of cardiac function is important for the assessment of abnormalities and response to therapy. We present a method to reconstruct dense cardiac motion from sparse features in tagging MRI, decomposed into solenoidal and irrotational parts using multi-scale Helmholtz decomposition. Reconstruction is based on energy minimization using covariant derivatives exploiting prior knowledge about the motion field. The method is tested on cardiac motion images. Experiments on phantom data show that both covariant derivatives and multi-scale Helmholtz decomposition improve motion field reconstruction.

Keywords: Cardiac function, MRI tagging, multi-scale, Helmholtz decomposition, covariant derivatives.

1 Introduction

MRI tagging admits detailed noninvasive intramural assessment of myocardial motion, quantification of which may help in (early) diagnosis of cardiac abnormalities such as ischemia and myocardial infarction.

Motion extraction may be based on the optic flow constraint equation (OFCE), originally developed for scalar images [1,2], which can be adapted to MRI tagging and extended to multiple scales [3]. Alternatively, feature tracking based on "demons" has been proposed in which certain features are preserved [4]. Multi-scale feature tracking with dense flow field reconstruction from a sparse set of anchor point velocities has been proposed for scalar sequences [5], but not for MRI tagging.

Kohlberger et al. [6] and Corpetti et al. [7] already exploited the Helmholtz decomposition to study the behavior of fluid flows. Cuzol et al. [8] did so for the characterization of fluid flows by a map of vortex and source particles, whereas we use it for separate regularization of the the irrotational and solenoidal parts of the flow field based on covariant derivatives and gauge fields. Furthermore, our algorithm aims at tracking cardiac motion, whereas Cuzol et al. applied their method to meteorological data, airplane wings, and brain data. Based on [4], Mansi et al. proposed a nonrigid registration algorithm incorporating tissue incompressibility, and applied it to cardiac 3D cardiac MR tagging and cardiac

O. Camara et al. (Eds.): STACOM 2011, LNCS 7085, pp. 263–273, 2012.

cine MRI [9]. An incompressibility constraint is not desired in our approach, as in 2D incompressibility does not apply, and due to through-plane motion. Furthermore, during systole myocardial volume is reduced by approximately 8%, because blood is squeezed out.

Many optic flow methods are based on the brightness constancy assumption without taking into account the physical properties of the data. The motivation to embed the Helmholtz decomposition in our method is the fact that the cardiac motion consists of a combination of rotation and contraction. Such a combination can be well characterized by div-curl regularizers. Moreover, from a clinical point of view, solenoidal and irrotational parts of the vector field may be analyzed independently to reveal and quantify abnormal deformation in the tissue. The novelty of our contribution is threefold:

(i) we propose a multi-scale variational feature tracking and dense flow field reconstruction method for MRI tagging;
(ii) we separate motion into *independently regularized* solenoidal and irrotational components using Helmholtz decomposition [10];
(iii) we extend standard Tikhonov regularization by incorporating *covariant derivatives* biased by a "gauge field".

Performance is assessed quantitatively on two phantoms, and on MRI tagging data obtained from a healthy volunteer and a patient with myocardial infarcts. For a schematic overview of our method, see Fig. 1.

2 Multi-scale Feature-Based Tracking Using Optical Flow

2.1 Image Data Set and Preprocessing

MR tags are artificial periodic intensity patterns, obtained by spatial modulation of magnetization (SPAMM) [11], cf. Fig. 2(a). Current methods for analysing MRI tagging images are optical flow [12,13], finite element models [14], nonrigid

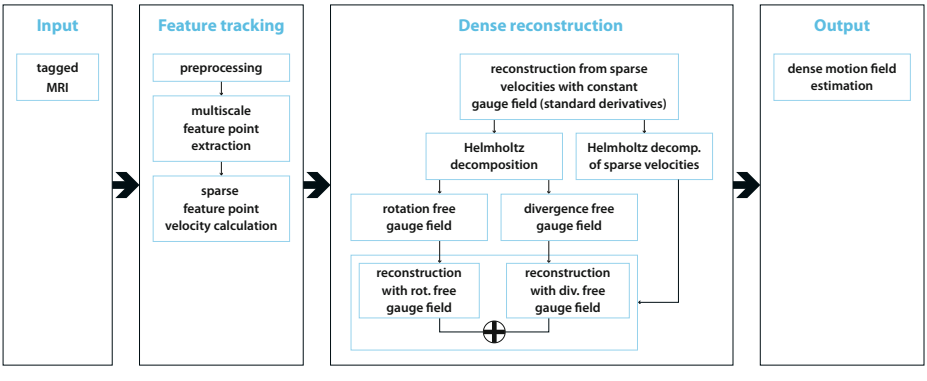

Fig. 1. Schematic overview of our method

registration [15], stripe following [16,17], and Fourier methods, such as (3D) HARP [18,19], sine wave modeling [20], and Gabor filtering [21]. The constant brightness assumption underlying some techniques is not applicable to MRI tagging due to T_1 relaxation (causing tag fading). Other methods are limited in that they are based on sparse landmark sets degrading resolution. For a review of MRI motion analysis protocols, see [22].

We extract discontinuity-free sine phase images using Gabor filters [23], cf. Fig. 2(b). Horizontal and vertical tags are combined into a grid, cf. Fig. 2(c).

2.2 Calculation of Sparse Velocity Features

At a critical point the spatial gradient—obtained using Gaussian derivatives at scale $s>0$—vanishes, $\nabla I(\mathbf{x}, s, t) = 0$. From this one can infer subpixel estimates of its position $\mathbf{x}$ at time t as a function of scale s [24]. A label $q = 1, \ldots, N_B$ identifies a critical point. Given s, tracking relies on the implicit constraint

$$\nabla I(\mathbf{x}_s^q(t), s, t) = 0\,, \tag{1}$$

in which $I(\mathbf{x}_s^q(t), s, t)$ represents the intensity at $\mathbf{x}_s^q(t) = \mathbf{x}_s^q(0) + \int_0^t \dot{\mathbf{x}}_s^q(\tau)d\tau$. By partitioning the time interval $[0, T]$ into discrete intervals labeled by t_k, with $k = 1, \ldots, K$, $t_0 = 0$, $t_K = T$, this yields a sparse set of velocities $\widetilde{\mathbf{v}}(\mathbf{x}_s^q(t_k)) = \dot{\mathbf{x}}_s^q(t_k) = \mathbf{v}(\mathbf{x}_s^q(t_k), t_k)$. Differentiation of (1) with respect to t yields [24]

$$\widetilde{\mathbf{v}}(\mathbf{x}_s^q(t_k)) = \begin{bmatrix}\widetilde{u}(\mathbf{x}_s^q(t))\\ \widetilde{v}(\mathbf{x}_s^q(t))\end{bmatrix} = \begin{bmatrix}u(\mathbf{x}_s^q(t), t)\\ v(\mathbf{x}_s^q(t), t)\end{bmatrix} = -(H(\mathbf{x}_s^q, s, t))^{-1}\frac{\partial(\nabla I(\mathbf{x}_s^q, s, t))}{\partial t} \tag{2}$$

where H represents the spatial Hessian matrix of image I. In the remainder of this article we will denote the velocity vectors at the critical points as

$$\mathbf{d}_q^k := \begin{pmatrix} d_q^{k,1}\\ d_q^{k,2}\end{pmatrix} := \begin{pmatrix}\widetilde{u}(\mathbf{x}_s^q(t_k))\\ \widetilde{v}(\mathbf{x}_s^q(t_k))\end{pmatrix}\,. \tag{3}$$

Velocities are necessarily retrieved at a certain scale. The most appropriate scale may vary from point to point. The slope of the tangent vector along a critical path $s \mapsto (\mathbf{x}_s^q(t), s)$ in scale space (t fixed) provides a measure for its spatial stability. Hence for each critical path q at fixed time $t \geq 0$ we choose the highest scale s_q such that the slope of the tangent vector along the critical path is below a certain a priori angle ϑ with respect to the scale direction [24].

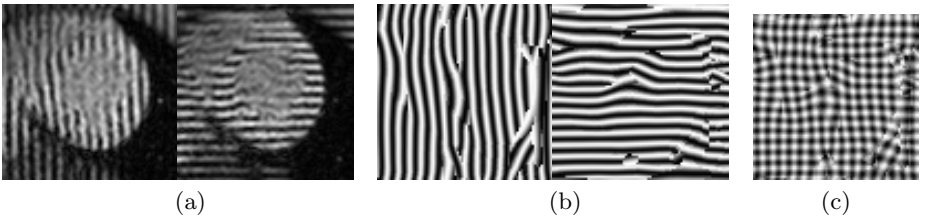

(a) (b) (c)

Fig. 2. (a) Tagged short axis views of a left ventricle. (b) Sine-phase images. (c) Sum of sine-phase images. Images are 80×80 pixels with pixel size of 1.36×1.36 mm^2.

3 Vector Field Decomposition

The cardiac muscle exhibits twistings and contractions, suggesting a Helmholtz decomposition [10]. Given a bounded domain $\Omega \subseteq \mathbb{R}^3$ and a vector field $\mathbf{v} \in \mathbf{C}^0(\overline{\Omega}) \bigcap \mathbf{C}^1(\Omega)$, functions $\Phi, \mathbf{A} \in \mathbf{C}^1(\overline{\Omega})$ exist such that

$$\mathbf{v} = \nabla\Phi + \nabla \times \mathbf{A} \quad \text{and} \quad \nabla \cdot \mathbf{A} = 0\,. \tag{4}$$

The functions Φ and $\mathbf{A}$ are the so-called *scalar potential* and *vector potential*, and $\nabla\Phi$ and $\nabla \times \mathbf{A}$ represent the *irrotational* and *solenoidal* components of $\mathbf{v}$. However in our cardiac MRI tagging application we consider $\Omega \subset \mathbb{R}^2$, and in $\mathbb{R}^2$ one does not have an outer product. We therefore need the following definition.

Definition 1. *In terms of Euclidean coordinates we define the rotation of a 2D-vector vector field and of a 2D-scalar field, respectively, as*

$$\operatorname{rot} \mathbf{v} = \partial_x v^2 - \partial_y v^1 \quad \textit{resp.} \quad \widetilde{\operatorname{rot}}\, f = \begin{pmatrix} \partial_y f \\ -\partial_x f \end{pmatrix}. \tag{5}$$

3D Helmholtz decomposition is extended to 2D by applying (5) consistently. To obtain explicit formulas, we approximate[1] a solution to the Poisson equation [25] on Ω:

$$\Delta\boldsymbol{\xi} = \mathbf{v} \tag{6}$$

viz.

$$\boldsymbol{\xi}(\mathbf{x}) = \int_{\Omega} G^{2D}(\mathbf{x} - \mathbf{x}')\mathbf{v}(\mathbf{x}')\mathrm{d}\mathbf{x}' \tag{7}$$

where

$$G^{2D}(\mathbf{x} - \mathbf{x}') = \frac{1}{2\pi} \ln \|(\mathbf{x} - \mathbf{x}')\| \ . \tag{8}$$

is the so-called Green's function of the two-variables Poisson equation. Moreover, $\boldsymbol{\xi}$ satisfies $\Delta\boldsymbol{\xi} = \nabla(\nabla \cdot \boldsymbol{\xi}) - \widetilde{\operatorname{rot}}\,(\operatorname{rot}\boldsymbol{\xi})$. From this and (6) we obtain

$$\mathbf{v} = \nabla\Phi + \widetilde{\operatorname{rot}}\, A\,, \tag{9}$$

cf. (4), with $\Phi = \nabla \cdot \boldsymbol{\xi}$ and $A = -\operatorname{rot}\boldsymbol{\xi}$. However, this decomposition is not unique. The decomposition is unique if we subtract the harmonic infilling $\boldsymbol{\psi}$ from the original vector field [26]. Hence

$$\widetilde{\mathbf{v}} = \mathbf{v} - \boldsymbol{\psi} \tag{10}$$

vanishes at the boundaries. Our aim is a dense reconstruction of $\widetilde{\mathbf{v}}$ and its unique Helmholtz decomposition from the sparse evidence represented by (3).

[1] If $\Omega = \mathbb{R}^2$ it is an exact solution.

3.1 Multi-scale Helmholtz Decomposition of the Optical Flow Field

Instead of using standard derivatives in (7–10), the Green's function can be differentiated by convolution with derivatives of a Gaussian kernel. This introduces a scale parameter $s = \frac{1}{2}\sigma^2$, and simultaneously removes the singularity at the origin. The first order Gaussian derivatives of the Green's function are:

$$\partial_{x^i} G_s^{2D}(\mathbf{x}) = \frac{1}{2\pi} \frac{x^i \left(1 - \exp(-\frac{x^2+y^2}{4s})\right)}{x^2+y^2} \,. \tag{11}$$

By combining (7–10) and (11) one obtains

$$\tilde{\mathbf{v}}_s := \text{grad}\,(\partial_{x^1} G_s^{2D} * \tilde{v}^1 + \partial_{x^2} G_s^{2D} * \tilde{v}^2) - \widetilde{\text{rot}}\,(-\partial_{x^2} G_s^{2D} * \tilde{v}^1 + \partial_{x^1} G_s^{2D} * \tilde{v}^2) \tag{12}$$

where $*$ denotes convolution. We note that the effective kernel operators can be pre-computed *analytically* [26]. The original vector field (at scale s) is given by

$$\mathbf{v}_s = \widetilde{\mathbf{v}}_s + \boldsymbol{\psi} \,. \tag{13}$$

3.2 Experiments on the Decomposition of the Vector Field

To assess the accuracy of the irrotational and solenoidal components, and of the recomposed vector field (12–13), a ground-truth phantom was created for a multi-scale Helmholtz decomposition (Fig. 3 top row)

$$\mathbf{v}_s := G_s * \mathbf{v}_0 = -2\gamma \begin{pmatrix} \partial_x \phi_{s+\gamma} \\ \partial_y \phi_{s+\gamma} \end{pmatrix} - 2\gamma \begin{pmatrix} -\partial_y \phi_{s+\gamma} \\ \partial_x \phi_{s+\gamma} \end{pmatrix}, \tag{14}$$

with $(x, y) \in [-1, 1] \times [-1, 1]$, $s > 0$, $\gamma = 0.02$ fixed, where ϕ_s denotes the Gaussian kernel. Computations were performed at scale $s = 1$ on a uniform 101×101 grid with spatial step size 0.02, and evaluated using the average angular error (AAE) [27]. Comparing the recomposed vector field $\mathbf{v}_{s=1}$ to the original vector field $\mathbf{v}_0$ yields AAE $= 0.40°$, confirming the visual similarity of the original and recomposed vector fields (see Fig. 3). Comparing $\mathbf{v}_{s=1}$ numerically computed using the exact effective kernels [26, Thm 4.4] to the true $\mathbf{v}_{s=1}$ vector field at the same scale, yields negligible angular error (AEE $= 0.0043°$).

3.3 Covariant Derivatives and Reconstruction

The covariant derivative of a function $f : \Omega \to \mathbb{R}$ with respect to an a priori *gauge function* $h : \Omega \to \mathbb{R}$ is defined as

$$D_{x^i}^h f(x, y) = \partial_{x^i} f(x, y) - \frac{\partial_{x^i} h(x, y)}{h(x, y)} f(x, y) \tag{15}$$

where $(x^1, x^2) = (x, y) \in \Omega \subset \mathbb{R}^2$ and $h(x, y) \neq 0$. Tikhonov regularization by regular derivatives ($h(x, y) =$ constant) suffers from the drawback that at areas where only few features are present the solution tends towards a constant.

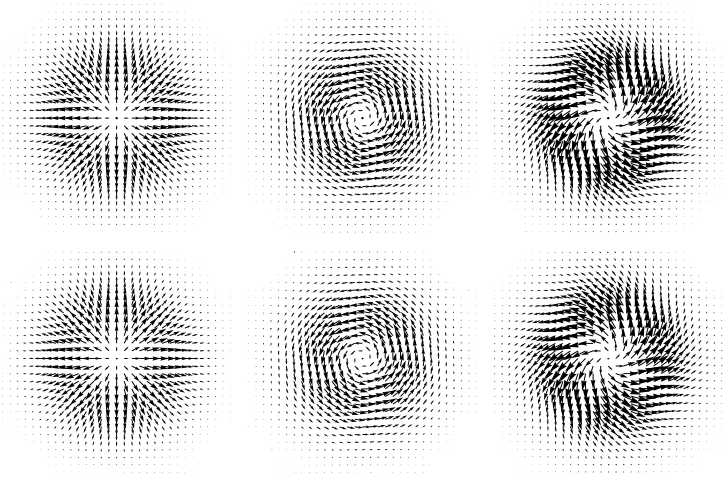

Fig. 3. Top row: ground truth Helmholtz decomposition of the phantom field $\mathbf{v}_{s=0}$, cf. (14). Bottom row: output $\mathbf{v}_{s=1}$ of the Helmholtz decomposition algorithm, cf. (13). Left to right: divergence free, rotation free, full field.

The use of covariant derivatives drives the solution towards the a priori gauge function instead ("background field"). We construct the gauge function as the solution of a sparse velocity reconstruction using Tikhonov regularization with *standard derivatives*, and subsequently refine the reconstruction using *covariant derivatives* instead. The refinement is less biased towards constant velocities and moreover it employs the features *twice*, both in the data- and regularization term. For details, cf. [26].

3.4 Feature Based Optic Flow Equation with Covariant Derivatives and Helmholtz Decomposition (CDHD)

We aim to retrieve $\mathbf{v}^k$ at time-step k, by minimizing the energy functional

$$\mathcal{E}^{\lambda,\mathbf{h}^k,\mathbf{d}^k}(\mathbf{v}^k) = \mathcal{E}^{\mathbf{h}^k}_{\text{reg}}(\mathbf{v}^k) + \mathcal{E}^{\mathbf{d}^k}_{\text{data}}(\mathbf{v}^k) =$$
$$\sum_{q=1}^{N_B} w_q^k \sum_{j=1}^{2} |(\phi_{s_q} * v^{k,j})(\mathbf{x}_q) - d_q^{k,j}|^2 + \lambda \int_\Omega \sum_{i=1}^{2}\sum_{j=1}^{2} |D_{x^i}^{h^{k,j}} v^{k,j}(\mathbf{x})|^2 \, \mathrm{d}\mathbf{x} \tag{16}$$

where $w_q^k \in \mathbb{R}^+$ is a weight factor, $\lambda > 0$ provides balance between regularization and the data term, q enumerates the extremal branches. Index $j \in \{1, 2\}$ indicates the vertical and horizontal component of the field and $x^i \in \{x, y\}$. Moreover, $\phi_k^q(\mathbf{x}) := \phi_{s_q}(\mathbf{x} - \mathbf{x}_q)$ denotes the Gaussian kernel centered around $\mathbf{x}_q$ with scale $s_q > 0$ and the sparse velocity components $d_q^{k,j}$ in (3) are derived by solving (2). Minimization of (16) was carried out by exact solutions of the discrete Euler Lagrange equations [26].

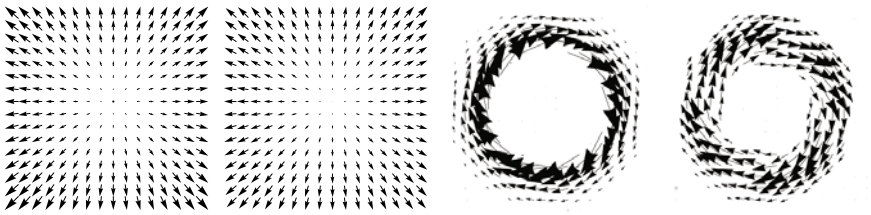

Fig. 4. Phantom 1 frame 5: ground truth (a), reconstructed vector field (b). Phantom 2 frame 3: ground truth (c) and reconstructed vector field (d). Arrows are magnified.

To reconstruct the rotation-free and divergence-free components of a vector field separately, we include the multi-scale Helmholtz decomposition in (16). To this end we also decompose the sparse velocities into divergence-free and rotation-free components: $\mathbf{d}^k = \mathbf{d}^k_{df} + \mathbf{d}^k_{rf}$. Namely, we reconstruct the velocity field by a regularization with standard derivatives at very small $0 < \lambda \ll 1$, to obtain a regularized velocity field that (nearly) satisfies the hard constraints (as $0 < \lambda \ll 1$). Then we apply a multi-scale Helmholtz decomposition on this field and we extract its divergence-free and rotation-free parts at the position $\mathbf{x}_q$ and scale s_q of interest (we use pre-computed exact analytic kernels [26, Thm 4.4]).

Hence, to calculate a dense motion field, we minimize (16) separately over solenoidal (df) and irrotational (rf) parts,

$$\mathbf{v}^k = \underset{\mathbf{v}}{\operatorname{argmin}}\ \mathcal{E}^{\lambda_1, \mathbf{h}^k_{\mathrm{rf}}, \mathbf{d}^k_{\mathrm{rf}}}(\mathbf{v}) + \underset{\mathbf{w}}{\operatorname{argmin}}\ \mathcal{E}^{\lambda_2, \mathbf{h}^k_{\mathrm{df}}, \mathbf{d}^k_{\mathrm{df}}}(\mathbf{w}). \tag{17}$$

4 Experiments and Results

Our method was evaluated on two different ground truth phantoms. Phantom 1 consists of 19 time-frames (99×99 pixels) of an irrotational pattern (Fig. 4(a)). Phantom 2 [28] has 13 frames (93×93 pixels) and shows non-rigid rotation (Fig. 4(c)). The analytic function for phantom 1 is $v^i(x, y, t) = \frac{(x^i - l)(m - 2n \cdot t)}{(l + (m - n \cdot t)t}$, $l = 50$, $m = 5$, and $n = 0.25$. In both phantoms the motion vanishes at the boundaries. We index our parameters as follows. The smoothness in the dense flow field reconstruction is controlled by λ_1, and η_1 denotes the interpolation parameter between covariant and standard derivatives, both of the rotation-free part. The parameters for the divergence-free part are λ_2 and η_2. Parameter η governs the influence of the covariant derivative by taking the η (sign-preserving) power of the gauge function; $D^{h^\eta} f = \partial_{x^i} f - \eta \cdot \frac{\partial_{x^i} h}{h} f$.

Increasing $\lambda \in \{10^{-2}, 10^{-1}, 1, 10, 100, 10^3, 10^4, 10^5, 10^6\}$ increases the smoothness of the reconstructed motion field. We choose λ such that the AAE and the L2 norm error w.r.t. the ground truth is minimized.

Table 1. Performance of our method using different reconstructions on phantom 1

Reconstruction Methodology ↓	AAE	L2 Norm	parameter
Conventional Derivatives	$1.26° \pm 1.11°$	$4.2 \times 10^{-2} \pm 0.04$	$\lambda = 10^{-2}$
Covariant Derivatives	$1.20° \pm 1.01°$	$3.6 \times 10^{-2} \pm 0.03$	$\lambda = 10^2$, $\eta = 0.7$
Covariant Derivatives and Helmholtz Decomposition	$0.97° \pm 0.62°$	$3.3 \times 10^{-2} \pm 0.03$	$\lambda_1 = 10^{-2}$, $\lambda_2 = 10^2$ $\eta_1 = 0.9$, $\eta_2 = 0.5$

Table 2. Performance of our method using different reconstructions on phantom 2

Reconstruction Methodology ↓	AAE	L2 Norm	parameter
Conventional Derivatives	$8.05° \pm 9.09°$	0.21 ± 0.26	$\lambda = 1$
Covariant Derivatives	$7.30° \pm 9.81°$	0.19 ± 0.25	$\lambda = 10$, $\eta = 0.9$
Covariant Derivatives and Helmholtz Decomposition	$6.68° \pm 9.48°$	0.16 ± 0.24	$\lambda_1 = 10^2$, $\lambda_2 = 10^3$ $\eta_1 = 0.5$, $\eta_2 = 0.7$

Table 3. Performance comparison with other optic flow methods on phantom 2

Method ↓	AAE	L2 Norm	parameter
Horn & Schunck [1]	$5.78°$	0.16	$\lambda = 0.5$
Lucas & Kanade [2]	$5.08°$	0.22	$\lambda = 0.01$
Conventional Derivatives	$5.33°$	0.14	$\lambda = 1$
Covariant Derivatives and Helmholtz Decomposition	$3.84°$	0.11	$\lambda_1 = 10^2$, $\lambda_2 = 10^3$ $\eta_1 = 0.5$, $\eta_2 = 0.9$

When reconstructing based on CDHD, λ_2 and λ_1 were fixed for phantoms 1 and 2 respectively and the other λ component was optimized. Once the λ_i parameter is tuned, parameter $\eta_i \in \{0.5, 0.7, 0.9, 1., 1.1, 1.3\}$, $i = 1, 2$ is investigated, which governs the influence of the gauge field in the velocity field reconstruction. The outcome of the optic flow method based on conventional derivatives of time frame k is used as the gauge field to reconstruct the motion field at time k. This is only one of the possible gauge field choices. For the reconstruction based on CDHD, η_2 and η_1 are fixed for phantoms 1 and 2 respectively. The other η_i are selected such that the AAE is minimized (see Tables 1, 2, 3).

The error measurements during algorithm evaluation are an average over three subsequent frames. Tables 1 and 2 show the performance of our optic flow method, using multi-scale maxima as feature points only, based on the AAE and the L2 norm, comparing standard derivatives, covariant derivatives, and CDHD respectively. For both phantoms, one frame of the retrieved motion fields together with their ground truths is shown in Fig. 4. Table 3 shows a comparison of our methods with Horn & Schunk [1] and Lucas & Kanade [2] on phantom 2. For a fair comparison, we included more features (maxima, minima and saddle points) in our method to get a less sparse set of velocity vectors $\mathbf{d}_q^k$ before dense field reconstruction. This led to a slightly different optimal value for η_2 for CDHD. For the Horn & Schunk method, $\lambda \in \{0.05, 0.5, 5, 50, 500\}$ was also optimized for best performance. In our implementation of the Lucas and Kanade algorithm, the eigenvalues of the motion matrix were thresholded, using $\lambda \in \{0.1, 0.05, 0.01, 0.005, 0.001\}$ as the threshold, which was optimized (Tab. 3).

We compared the motion fields extracted from a healthy volunteer and a patient, who suffered a number of small infarctions. Systolic tagged MR images

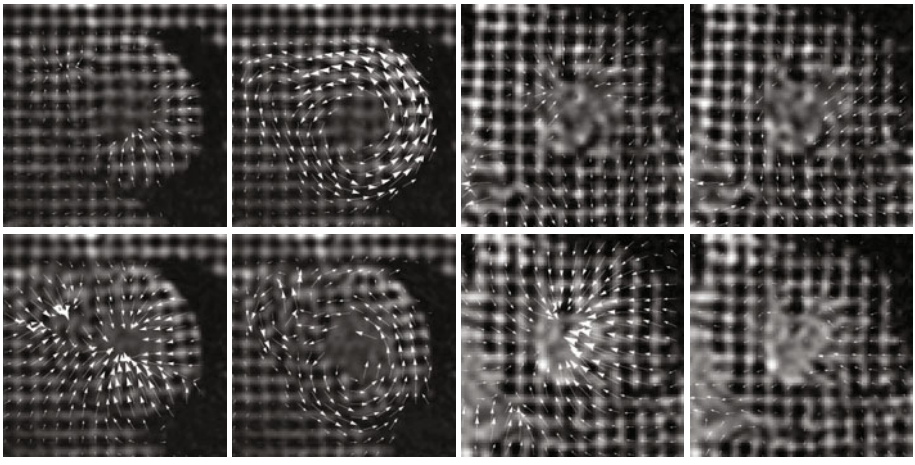

Fig. 5. Rotation-free (a,c) and divergence-free (b,d) parts of true cardiac motion fields for a healthy volunteer (a,b) and the patient (c,d), frames 3 (top) and 6 (bottom). Note that the patient lacks rotational motion (div-free part) in both frames, whereas the rotation-free part is affected locally.

were acquired; 11 frames, pixel size of $1.2 \times 1.2mm^2$, slice thickness of $8mm$. In Fig. 5 the rotation-free (a,c) and divergence-free (b,d) parts of boths hearts are shown. At early systole, the healthy heart shows little contraction and a strong rotation (Fig. 5(a,b), top). Later, the contribution of both parts becomes comparable (Fig. 5(a,b), bottom). The infarcted heart lacks rotation in both frames (Fig. 5(d)), leaving contraction only (Fig. 5(c)).

5 Discussion and Conclusion

Multi-scale Helmholtz decomposition allows assessment of irrotational and solenoidal motion separately. We have shown that extending Tikhonov regularization by incorporating a gauge field based on multi-scale covariant derivatives improves dense motion field reconstruction. The proposed approach outperforms similar techniques that use regular derivatives and without Helmholtz decomposition, and outperforms other optic flow methods. The influence of noise is reduced by scale selection based on the slope of the tangent vector along each critical path in scale space [24], thus providing also a measure for spatial stability of each critical point. Furthermore, the Gabor filters remove the influence of noise outside their frequency band. Inclusion of more features than maxima only improves motion field reconstruction. Application to tagged MR images showed its potential for diagnostics. Currently, we are evaluating our technique on a large population.

References

1. Horn, B.K.P., Shunck, B.G.: Determining optical flow. AI 17, 185–203 (1981)
2. Lucas, B., Kanade, T.: An iterative image registration technique with application to stereo vision. In: DARPA, Image Process, vol. 21, pp. 85–117 (1981)
3. Florack, L., van Assen, H.: Dense multiscale motion extraction from cardiac cine MR tagging using HARP technology. In: ICCV Workshop on MMBIA (2007)
4. Thirion, J.: Image matching as a diffusion process: an analogy with Maxwell's demons. Med. Imag. Anal. 2(3), 243–260 (1998)
5. Janssen, B., Florack, L., Duits, R., ter Haar Romeny, B.: Optic Flow from Multiscale Dynamic Anchor Point Attributes. In: Campilho, A., Kamel, M.S. (eds.) ICIAR 2006. LNCS, vol. 4141, pp. 767–779. Springer, Heidelberg (2006)
6. Kohlberger, T., Mémin, E., Schnörr, C.: Variational Dense Motion Estimation Using the Helmholtz Decomposition. In: Griffin, L.D., Lillholm, M. (eds.) Scale-Space 2003. LNCS, vol. 2695, pp. 432–448. Springer, Heidelberg (2003)
7. Corpetti, T., Mémin, E., Pérez, P.: Dense estimation of fluid flows. IEEE Trans. Pattern Anal. Mach. Intell. 24(3), 365–380 (2002)
8. Cuzol, A., Hellier, P., Mémin, E.: A low dimensional fluid motion estimator. IJCV 75, 329–349 (2007), doi:10.1007/s11263-007-0037-0
9. Mansi, T., Pennec, X., Sermesant, M., Delingette, H., Ayache, N.: iLogDemons: A demons-based registration algorithm for tracking incompressible elastic biological tissues. IJCV 92(1), 92–111 (2011)
10. von Helmholtz, H.: Üeber integrale der hydrodynamischen Gleichungen, welche den Wirbelbewegungen entsprechen. Crelles J. 55(25) (1858)
11. Axel, L., Dougherty, L.: MR imaging of motion with spatial modulation of magnetization. Radiology 171(3), 841–845 (1989)
12. Prince, J.L., McVeigh, E.R.: Motion estimation from tagged MR image sequences. IEEE Trans. Med. Imaging 11(2), 238–249 (1992)
13. Gupta, S.N., Prince, J.L.: On Variable Brightness Optical Flow for Tagged MRI. In: Proc. of 14th Int. Conf., IPMI 1995. Kluwer, Dordrecht (1995)
14. Young, A.A.: Model tags: direct three–dimensional tracking of heart wall motion from tagged magnetic resonance images. Med. Image Anal. 3(4), 361–372 (1999)
15. Chandrashekara, R., Mohiaddin, R., Rueckert, D.: Analysis of myocardial motion in tagged mr images using nonrigid image registration. In: Proc. of SPIE, vol. 4684, pp. 1168–1179 (2002)
16. Amini, A., Chen, Y., Elayyadi, M., Radeva, P.: Tag surface reconstruction and tracking of myocardial beads from spamm-mri with parametric b-spline surfaces. IEEE Trans. Med. Imaging 20(2), 94–103 (2001)
17. Axel, L., Chen, T., Manglik, T.: Dense Myocardium Deformation Estimation for 2D Tagged MRI. In: Frangi, A.F., Radeva, P., Santos, A., Hernandez, M. (eds.) FIMH 2005. LNCS, vol. 3504, pp. 446–456. Springer, Heidelberg (2005)
18. Osman, N.F., Kerwin, W.S., McVeigh, E.R., Prince, J.L.: Cardiac motion tracking using CINE harmonic phase (HARP). Magnetic Resonance Imaging, MRM 42(6), 1048–1060 (1999)
19. Pan, L., Prince, J.L., Lima, J.A.C., Osman, N.F.: Fast tracking of cardiac motion using 3D–HARP. IEEE Trans. Biomed. Eng. 52(8), 1425–1435 (2005)
20. Arts, T., Prinzen, F.W., Delhaas, T., Milles, J.R., Rossi, A.C., Clarysse, P.: Mapping displacement and deformation of the heart with local sine-wave modeling. IEEE Trans. Med. Imaging 29(5), 1114–1123 (2010)

21. Chen, T., Wang, X., Chung, S., Metaxas, D., Axel, L.: Automated 3d motion tracking using gabor filter bank, robust point matching, and deformable models. IEEE Trans. Med. Imaging 29(1), 1–11 (2010)
22. Ozturk, C., Derbyshire, J.A., McVeigh, E.R.: Estimating motion from MRI data. Proc. of the IEEE 91(10), 1627–1648 (2003)
23. Gabor, D.: Theory of communication. J. IEE 93(26), 429–457 (1946)
24. Florack, L., Kuijper, A.: The topological structure of scale-space images. JMIV 12(1), 65–79 (2000)
25. Dassios, G., Lindell, I.: Uniqueness and reconstruction for the anisotropic Helmholtz decomposition. J. Phys. Math. Gen. 35, 5139–5146 (2002)
26. Duits, R., Janssen, B.J., Becciu, A., van Assen, H.C.: A variational approach to cardiac motion estimation based on covariant derivatives and multi-scale helmholtz decomposition. Quarterly of Applied Mathematics (accepted)
27. Barron, J., Fleet, D., Beauchemin, S.: Performance of optical flow techniques. IJCV 12(1), 43–77 (1994)
28. Young, A.A., Axel, L., Dougherty, L., Bogen, D.K., Parenteau, C.S.: Validation of tagging with mr imaging to estimate material deformation. Radiology 188(1), 101–108 (1993)

Temporal Diffeomorphic Motion Analysis from Echocardiographic Sequences by Using Intensity Transitivity Consistency

Zhijun Zhang[1], David J. Sahn[1,2], and Xubo Song[1]

[1] Department of Biomedical Engineering
[2] Department of Pediatric Cardiology
Oregon Health and Science University
20000 NW Walker Road, Beaverton, OR 97006, USA
{zhangzhi,songx,sahn}@ohsu.edu

Abstract. Quantitative motion analysis from echocardiography is an important yet challenging problem. We develop a motion estimation algorithm for echocardiographic sequences based on diffeomorphic image registration in which the velocity field is spatiotemporally smooth. The novelty of this work is that we propose a functional of the velocity field which minimizes the intensity consistency error of the local unwarped frames. The consistency error is measured as the sum of squared difference of the four frames evolving to any time point between the two inner frames of them. The estimated spatiotemporal transformation has maximum local transitivity consistency. We validate our method by using simulated images with known ground truth and real ultrasound datasets, experiment results indicate that our motion estimation method is more accurate than other methods.

1 Introduction

Quantitative analysis of cardiac deformation and motion is important for studying architecture of heart and illness related to ischemia or infarct [1]. Echocardiography (echo) is the most widely used cardiac imaging tools because it is non-ionizing, real-time, cost-effective and convenient. With the development of the new transducer array technology, 3D echo now provides real-time images of the whole heart [2]. However, due to the low signal-noise-ratio, general methods for motion estimation do not work well on echo images. In addition, the 4D (3D+t) data is acquired with a compromise that both the spatial and temporal resolutions are reduced comparing to 2D+t sequences. As a result, 3D motion analysis from echo sequences remains a challenging problem.

Motion estimation from cardiac imaging falls into two categories: model based methods and intensity based methods. Various deformable models have been proposed for use of cardiac motion tracking and segmentation [3]. Papademetrics *et al.* [4] used a finite element model whose deformation between frames is estimated from the tracked features from the segmented myocardium surfaces.

O. Camara et al. (Eds.): STACOM 2011, LNCS 7085, pp. 274–284, 2012.

Wang *et al.* [5] tracked myocardial surface points by maximizing the likelihood of a combined surface and a two-steps motion prediction model. Both the initial myocardial surface detector and the motion prediction model need to be learned in advance. Comparing to model based methods, intensity based methods estimate motion directly from voxel intensity. They have the important advantage that there is no requirement of prior knowledge and the result is not limited by the accuracy of feature extraction method. We focus our work on intensity based approach. Methods directly applying the nonrigid registration algorithms sequentially to estimate motion have been proposed in [6,7,8]. However, these methods separate the motion estimation problem into a series of independent image registrations, the temporal continuity of motion is not taken into account. Temporal smoothness is very important in cardiac motion estimation since the particle trajectory of the myocardium is continuous. Consideration of the temporal smoothness will reduce the particle motion irregularity. Temporal smoothness have been reinforced in various ways in current motion estimation methods. Methods using spatiotemporal models have been proposed in [9,10,11]. Carbayo *et al.* [9] proposed a spatiotemporal deformation model for cardiac motion estimation by using 2D+t B-spline, the parameters of the model are estimated by optimizing a similarity metric between the transformed reference frame and the following frames. Metz *et al.* [10] proposed a generic nD+t B-spline deformation model with the option of temporal periodicity. Bertrand *et al.* [11] proposed a 3D+t B-spline model in which each control point coordinate varying with time is a function in form of a sum of periodic harmonic functions. Particle trajectory constraint such as polynomial modeling has been used to regularize the spatiotemporal motion smoothness [12]. Properties of symmetry and transitivity have been used to constrain the spatial transformation [13,14]. Sundar *et al.* [13] used an inverse consistent registration energy and a temporal consistent energy term to make the transformation spatiotemporally smooth. Skrinjar *et al.* [14] used transformation transitivity property of three consecutive frames to make that the composition of transformation from second frame to the third frame with that from first frame to the second frame equals to the transformation from first frame to the third frame. Diffeomorphic image registration has been proposed to estimate the spatial transformation which is implicitly smooth and invertible [15,16,17]. In this method, the spatial transformation is considered as the end point of an evolution process with a smooth velocity field and the spatial displacement field is considered as the integral of the velocity field over time. This method is physically plausible for cardiac motion analysis since the particle motion between sequence is continuous in velocity. Khan *et al.* [18] extended the method to solve the motion estimation problem by minimizing a variational energy of the velocity field in form of a summed dissimilarity function between the reference image and the unwarped image frames. De Craene *et al.* [19] used a smooth and invertible spatiotemporal transformation which is the Euler integral of a velocity field defined by a series of 3D B-spline functions. The B-spline parameters are optimized by minimizing the summed image difference between the reference frame to each of the unwarped following frames. In a following

work [20], the velocity field is defined as a 3D+t spatiotemporal B-spline model to reduce the number of control parameters in temporal direction.

The above methods only constrain the reference image to have the smallest error with the unwarped following frames on time points of each frames, we propose a novel method to enforce the intensity consistency of the velocity field on each time points including those within frames. We propose a diffeomorphic variational motion estimation method in which the optimal velocity field is obtained by making the frames local to a time points evolving to this time point along the flow to have maximal intensity transitivity consistency. Experimental results shows motion estimated by using our method is more accurate and more temporally smooth than other methods.

2 Method

2.1 Parameterized Diffeomorphic Registration

We define a flow $\boldsymbol{\phi}(\mathbf{x},t), t \in [0,T], \mathbf{x} \in \Omega \subset R^d (d = 2,3)$ with its smooth velocity field $\boldsymbol{v}(\mathbf{x},t)$ by using the differential equation of $\frac{d\boldsymbol{\phi}}{dt} = \boldsymbol{v}(\mathbf{x},t)$. It has been proven in [21] that if $\boldsymbol{v}(\mathbf{x},t)$ is smooth with a differential operator L in a Sobolev space V, then the transformation $\boldsymbol{\phi}(\mathbf{x},t)$ defines a group of diffeomorphisms with t varying from 0 to T. The diffeomorphic image registration is stated as a variational problem, that given two images I_0 and I_1, to find an optimal velocity field $\hat{\boldsymbol{v}}$ which minimizes an energy functional consisting of a measurement of SSD between the pull-back images of $I_0(\boldsymbol{\phi}_{t,0}(\mathbf{x}))$ and $I_1(\boldsymbol{\phi}_{t,T}(\mathbf{x}))$ at each time point t and a distance metric between transformations $\boldsymbol{\phi}(\mathbf{x},0)$ and $\boldsymbol{\phi}(\mathbf{x},T)$:

$$\hat{\boldsymbol{v}} = arg \inf_{\boldsymbol{v}\in V} \lambda \int_0^T ||\boldsymbol{v}(\mathbf{x},t)||_V^2 dt + \int_0^T \int_\Omega (I_0(\boldsymbol{\phi}_{t,0}(\mathbf{x})) - I_1(\boldsymbol{\phi}_{t,T}(\mathbf{x})))^2 d\mathbf{x}dt, \quad (1)$$

with λ being the weight to balance these two energies, $\boldsymbol{\phi}_{t,0}(\mathbf{x})$ and $\boldsymbol{\phi}_{t,T}(\mathbf{x})$ being the transformations from time t to 0 and from t to T.

The direct solution for the dense velocity field function is expensive. Alternatively, a parameterized representation of the velocity field is used like [17], where the velocity field continuous in time is represented as a series of B-spline functions on discrete time points. The transformation can be expressed as the forward Euler integral of velocity field by assuming that the velocity is piecewise constant within a time step. The B-spline function is defined as $\boldsymbol{v}(\mathbf{x},t_k) = \sum \mathbf{c}_{i;k}\boldsymbol{\beta}(\mathbf{x}-\mathbf{x}_i)$, with $\mathbf{c}_{i;k}$ being the B-spline control vectors located on a uniform grid of $\mathbf{x}_i$ at t_k, $\boldsymbol{\beta}(\mathbf{x}-\mathbf{x}_i)$ being the B-spline kernel function which is the tensor product of the 1-D B-spline functions. Denote $\boldsymbol{\phi}_k = \boldsymbol{\phi}(\mathbf{x},t_k)$ the transformation from t_0 to t_k, because the velocity is piecewise constant within a time step, we have $\boldsymbol{\phi}_k = \boldsymbol{\phi}_{k-1} + \boldsymbol{v}(\boldsymbol{\phi}_{k-1},t_{k-1})\Delta t = (\boldsymbol{Id} + \boldsymbol{v}_{k-1}\Delta t) \circ \boldsymbol{\phi}_{k-1}$, with $\Delta t = T/N_t$ being the length of a time step, $\boldsymbol{\phi}_0(\mathbf{x}) = \mathbf{x}$, $k = 1,2,...,N_t$, with N_t being the total number of time steps of the discretized velocity field. The second term in Eqn.(1) will be discretized as $\sum_k \int (I_0(\boldsymbol{\phi}_{k,0}) - I_1(\boldsymbol{\phi}_{k,N_t}))^2 d\mathbf{x}$, which is a sum of SSD metrics of the pull back image $I_0(\boldsymbol{\phi}_{k,0})$ and $I_1(\boldsymbol{\phi}_{k,N_t})$ at each $t_k (k = 0,1,...,N_t)$. The forward transformation $\boldsymbol{\phi}_{k,N_t}$ from t_k to t_{N_t} can be

represented as $\boldsymbol{\phi}_{k,N_t} = (\boldsymbol{Id}+\boldsymbol{v}_{N_{t-1}}\Delta t)\circ...\circ(\boldsymbol{Id}+\boldsymbol{v}_k\Delta t)$, and by considering the reverse motion whose velocity is $-\boldsymbol{v}(\mathbf{x},t)$ at each time, the backward transformation from time t_k to t_0 can be represented as $\boldsymbol{\phi}_{k,0} = (\boldsymbol{Id}-\boldsymbol{v}_1\Delta t)\circ...\circ(\boldsymbol{Id}-\boldsymbol{v}_k\Delta t)$. The registration energy functional Eqn.(1) is then parameterized as a function of a group of parameters $\mathbf{c}_{i;k}$ and it can be optimized by using a gradient based method [17].

2.2 Diffeomorphic Image Sequence Registration

We use n_s time steps between each two consecutive frames. For convenience of illustration, we explain our method by using $n_s = 2$ as an example, but the idea is the same when other integers are used. Fig.(1) shows the principle of intensity transitivity consistency along the particle trajectories at a time point. Assume that we have an image sequence and a point $\mathbf{x}$ in a virtual plane I_v at t_{2k+1} moves through four consecutive frames $I_{k-1}, I_k, I_{k+1}, I_{k+2}$. We use the notation $\boldsymbol{\phi}_{2k+1,2k}$ as the transformation which maps $\mathbf{x}$ from t_{2k+1} to t_{2k}, then the trajectories of point $\mathbf{x}$ in the four nearest frames in time are $\boldsymbol{\phi}_{2k+1,2k}(\mathbf{x})$, $\boldsymbol{\phi}_{2k+1,2k+2}(\mathbf{x})$, $\boldsymbol{\phi}_{2k+1,2k-2}(\mathbf{x})$,$\boldsymbol{\phi}_{2k+1,2k+4}(\mathbf{x})$. Their intensity values of $I_k(\boldsymbol{\phi}_{2k+1,2k})$, $I_{k+1}(\boldsymbol{\phi}_{2k+1,2k+2})$, $I_{k-1}(\boldsymbol{\phi}_{2k+1,2k-2})$, $I_{k+2}(\boldsymbol{\phi}_{2k+1,2k+4})$ should be identical since they are from the same particle trajectory and their intensity should be preserved. Theoretically the point $\mathbf{x}$ at t_{2k+1} can be replaced by any time point along the trajectory and the four frames can be extended to all image frames in the sequences. In real implementation we will consider up to four frames as a compromise of intensity consistency context and computational efficiency. At one hand, considering consistency between two frames before and after a time point will give us enough temporal constraint for the transformation; on the other hand, consideration of far away frames will bring correspondence ambiguity due to the speckle decorrelation [23]. Then we define an SSD energy term to measure the image errors as: $E_{ssd}(2k+1) = \int (I_k(\boldsymbol{\phi}_{2k+1,2k}) - I_{k+1}(\boldsymbol{\phi}_{2k+1,2k+2}))^2 + (I_{k-1}(\boldsymbol{\phi}_{2k+1,2k-2}) - I_{k+1}(\boldsymbol{\phi}_{2k+1,2k+2}))^2 + (I_k(\boldsymbol{\phi}_{2k+1,2k}) - I_{k+2}(\boldsymbol{\phi}_{2k+1,2k+4}))^2$. We call this function as transitivity consistency error at time point t_{2k+1} since this function measures that how consistent the intensity values of local frames under a velocity field is. The optimal velocity field will be estimated by minimizing a variational energy:

$$\hat{\boldsymbol{v}} = arg \inf_{\boldsymbol{v}\in V} \lambda \int_0^T ||\boldsymbol{v}(\mathbf{x},t)||_V^2 dt + \sum_{k=1}^{(N_f-1)*n_s} E_{ssd}(t_k), \tag{2}$$

The first term regularizes the velocity field to make it spatiotemporally smooth and the second term assures that the optimized velocity field minimizes the local transitivity consistency at all time points t_k.

We use an adaptive scheme to choose the value of n_s. It is initialized as 2. The B-spline parameters during optimization is checked at each iteration to make sure that the transformation between each two time points, that is $\boldsymbol{Id} + \boldsymbol{v}_k\Delta t$, is a diffeomorphism [22]. If the condition is broken due to large deformation between two frames, the number of n_s will be doubled to tolerate larger deformation while keeping the transformation between time points to be diffeomorphic.

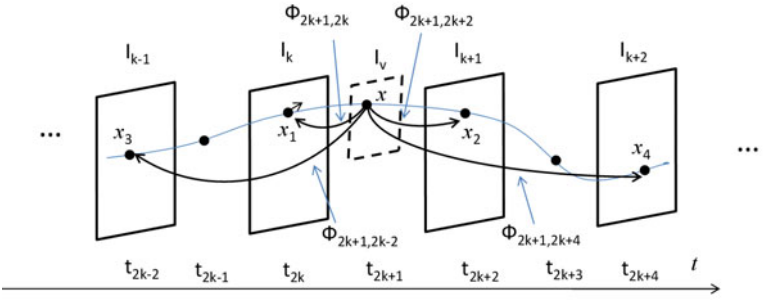

Fig. 1. The intensity of a point along the particle trajectory should be preserved. We use two time steps between each two frames as an example. The optimal velocity field should minimize the difference of evolving image $I_k(\boldsymbol{\phi}_{2k+1,2k})$, $I_{k+1}(\boldsymbol{\phi}_{2k+1,2k+2})$, $I_{k-1}(\boldsymbol{\phi}_{2k+1,2k-2})$,$I_{k+2}(\boldsymbol{\phi}_{2k+1,2k+4})$ at time point t_{2k+1}.

2.3 Regularization

In order to assure the $\boldsymbol{\phi}(\mathbf{x},t)$ to be diffeomorphic, we need to define $\mathbf{v}(x,t)$ to be spatiotemporally smooth under a differential operator L. The linear operator we choose is: $L = \nabla^2\boldsymbol{v} + w_t\frac{d\boldsymbol{v}}{dt}$, with $\nabla^2(\cdot)$ being a Laplacian operator and w_t a constant weight. In the discrete time form of velocity field, the time integral of the norm in V space of Eqn.(2) will be approximated by: $E_{reg} = \sum_{k=1}^{N_t}\sum_{\mathbf{x}}(\nabla^2\boldsymbol{v}_k)^2 + w_t\sum_{k=2}^{N_t}\sum_{\mathbf{x}}|\boldsymbol{v}_k(\mathbf{x}+\boldsymbol{v}_{k-1}\Delta t) - \boldsymbol{v}_{k-1}|^2$, with $\boldsymbol{v}_k = \boldsymbol{v}(\mathbf{x},t_k)$. The first term makes the velocity field spatially smooth, we denote it as E_{sr}. The second term keeps the particle velocity smooth and it is denoted as E_{tr}. The overall effect is to keep the velocity field spatiotemporally smooth.

2.4 Optimization

We use a steepest descent method to optimize the parameterized function. The derivative of the total registration energy with respect to the transformation parameters will be calculated analytically.

Due to the fact that the transitivity consistency error at each time point t_k is made up of the SSD functions of three pair of local frames, the derivative of the second term in Eqn.(2) with respect to the B-spline parameters is equalized to calculate derivatives of SSD functions of three separate two image registrations at each t_k with respect to the B-spline parameters and then add the gradient together. Suppose we have two images I_0 and I_1, we want to estimate the derivative of SSD energy term $E_{0,1}(j) = \int_\Omega(I_0(\boldsymbol{\phi}_{j,0}(\mathbf{x})) - I_1(\boldsymbol{\phi}_{j,N_1}(\mathbf{x})))^2 d\boldsymbol{x}$ at each t_j with respect to a series of discrete velocity field B-spline parameters $\boldsymbol{v}_k(0 \le k \le N_1)$, with N_1 being the total number of time steps. We know from Sec.(2.1) that $\boldsymbol{\phi}_{j,N_1}$ is only affected by the velocity field $\boldsymbol{v}_k$ with $j \le k \le N_1 - 1$ and $\boldsymbol{\phi}_{j,0}$ is only related to $-\boldsymbol{v}_k$ with $1 \le k \le j$. If we denote $c_{i,m;k}$ as the mth $(m = x, y, z)$

component of the ith B-spline parameter of $\boldsymbol{v}_k$, the derivative of $E_{0,1}(j)$ with respect to $c_{i,m;k}$ is:

$$\frac{\partial E_{0,1}(j)}{\partial c_{i,m;k}} = \sum_{\Omega'}(I_1(\boldsymbol{\phi}_{j,N_1}) - I_0(\boldsymbol{\phi}_{j,0}))\nabla_m I_1(\boldsymbol{\phi}_{j,N_1})\frac{\partial \boldsymbol{\phi}_{j,N_1}}{\partial c_{i,m;k}}, (j \le k \le N_1 - 1),$$

$$\frac{\partial E_{0,1}(j)}{\partial c_{i,m;k}} = \sum_{\Omega'}(I_0(\boldsymbol{\phi}_{j,0}) - I_1(\boldsymbol{\phi}_{j,N_1}))\nabla_m I_0(\boldsymbol{\phi}_{j,0})\frac{\partial \boldsymbol{\phi}_{j,0}}{\partial c_{i,m;k}}, (1 \le k \le j), \tag{3}$$

with Ω' being the local support of the B-spline kernel function, $\nabla_m(\cdot)$ being the mth component of the image gradient, $\frac{\partial \boldsymbol{\phi}_{j,N_1}}{\partial c_{i,m;k}}$ and $\frac{\partial \boldsymbol{\phi}_{j,0}}{\partial c_{i,m;k}}$ being the derivative of the concatenated B-spline function with respect to the B-spline parameters which are calculated using chain rule [17,19]. By replacing image pair of I_0 and I_1 with the three pairs of images used in intensity transitivity consistency error at each t_k, we can get the derivative of the total similarity metric with respect to the velocity field parameters.

For the derivative of the spatial and temporal regularization energies with respect to $c_{i,m;k}$, we have:

$$\frac{\partial E_{sr}}{\partial c_{i,m;k}} = \sum_{\mathbf{x}\in\Omega'} \boldsymbol{\beta}_m^{''}(\mathbf{x} - \mathbf{x}_i), \tag{4}$$

with $\boldsymbol{\beta}_m^{''}(\cdot)$ being the second derivative of the B-spline function with respect to mth component. Considering that the displacement between two time step is small, we have:

$$\frac{\partial E_{tr}}{\partial c_{i,m;k}} \approx w_t \sum_{\mathbf{x}\in\Omega'} (2 * v_{i,m;k} - v_{i,m;k-1} - v_{i,m;k+1})\boldsymbol{\beta}(\mathbf{x} - \mathbf{x}_i). \tag{5}$$

The registration energy can be optimized by starting from initial position and descending along the negative gradient direction at each iteration until there is no significant decrease.

2.5 Implementation

In our implementation, we use a series of B-spline transformations with grid spacing of 10 in each dimension to represent the velocity field. The values of λ and w_t are set to be 0.1 and 0.005. The algorithm is implemented with Matlab under a windows XP 64 bit system on a machine with 2.13GHz CPU and 6GB RAM. For 2D image sequence of 11 frames with frame size of 274×192, it takes 20 minutes to estimate the motion, for a 3D sequence of 16 frames with frame size of $104 \times 112 \times 104$ the computing time is about 5 hours.

3 Experiment and Data

We use simulated and real ultrasound sequences to validate the proposed method. In the simulated data experiment, a longitudinal view of a diastolic left ventricle (LV) image with size of 274×192 is used as the reference image. This

frame is then deformed with a series of continuous displacement field functions. The deformations are symmetrical along the long axis of the LV to simulate the myocardial contraction effect along radial and longitudinal directions. The displacement functions are in form of: $f_x(i) = a_x sin\frac{\pi(x-x_c)}{2r_d} sin(\frac{i\pi}{N_f})$ and $f_y(i) = a_y sin\frac{\pi(y-y_{apex})}{2(y_{base}-y_{apex})}(sin(\frac{i\pi}{N_f}+\frac{\pi}{16}) - sin\frac{\pi}{16})$, with x_c, r_d the axis center coordinate and the average axial radius of LV, y_{apex} and y_{base} the height of base and apex planes, N_f and i the number of frames and the frame index, and a_x, a_y are the magnitudes of displacement fields which are the largest shift in axial and longitudinal directions. An image sequence with $N_f + 1$ frames is generated when i varies from 0 to N_f to simulate the cardiac motion in one cycle from diastolic to systolic and then back.

Three sequences with 11 frames each are simulated with multiplicative speckle noise of variance 0.06, 0.08 and 0.10 added to each frames. The magnitude parameter a_x and a_y used are 5 and 15 respectively. The reference frame and the $6th$ frame with speckle noise variance 0.10 are shown together with the ground truth displacement field in Fig.(2).

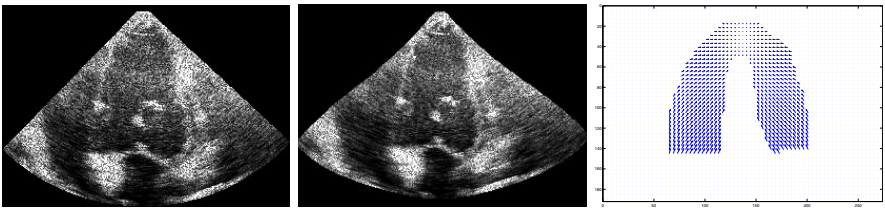

Fig. 2. The reference frame and the $6th$ frame in speckle variance 0.1 test and the displacement field (only displacement field inside a bell-shaped mask is displayed and the displacement vectors are normalized for ease of display.)

In the real dataset tests, 3D echo sequences are chosen from the STACOM challenge datasets. A sequence of 16 frames each of which is downsampled into size of $104 \times 112 \times 104$ is used for our test.

We compare the proposed method with two other diffeomorphic motion estimation methods. The first one is a B-spline method with transformation transitivity as temporal constraint. The constraint enforce that in each three consecutive frames, the composition of the transformations obtained from each two consecutive frame registration should be equal to the transformation from the first frame to the third one [14], we call this as method with transitivity constraint. The second one is a method which optimizes a spatiotemporal B-spline velocity field function by minimizing the SSD errors between the reference to each of the deformed following frames [19], referred as LDFFD method. Same regularization parameters are used for the three algorithms.

4 Result

We compare the proposed method with the other two methods by tracking the trajectories of the points in the myocardial wall during the motion process. Fig. (3) shows the 11-frame trajectories of nine tracked points in myocardium for the test of speckle noise variance 0.06. For contrast, the ground truth trajectories are overlaid for comparison. We can see generally coordinates of the points in each time step in the proposed method are closer to the ground truth position, larger errors can be seen in the right part of the trajectories in transitivity constraint method, and in LDFFD method, larger errors appear in time steps near the end of the trajectories.

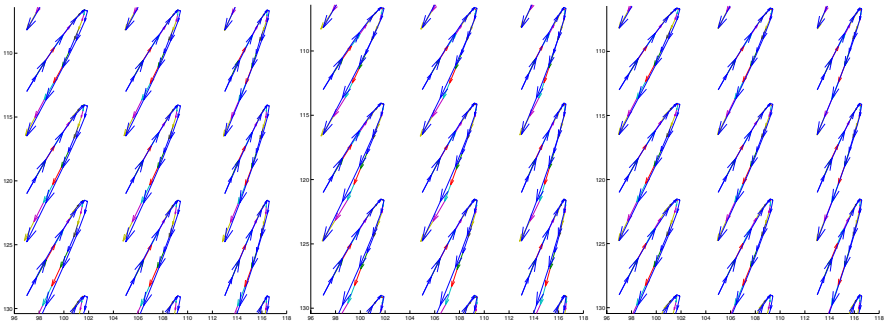

Fig. 3. Trajectories of nine points in 11 frames in transitivity constraint method, LDFFD method and the proposed method. The ground truth trajectories (blue) are overlaid with the estimated curves (multiple color) for comparison. The arrow shows the velocity at each time step.

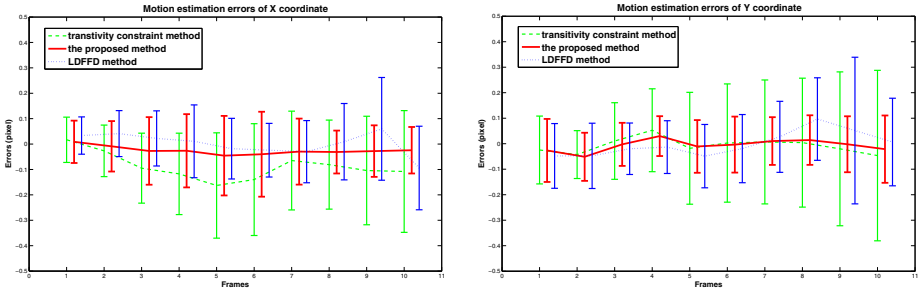

Fig. 4. The motion estimation errors (unit in pixel) in x (left) and y (right) coordinates in the transitivity constraint method (green), LDFFD method (blue) and the proposed method (red). The error bars show the mean and standard deviation of the transformation errors in each image frames.

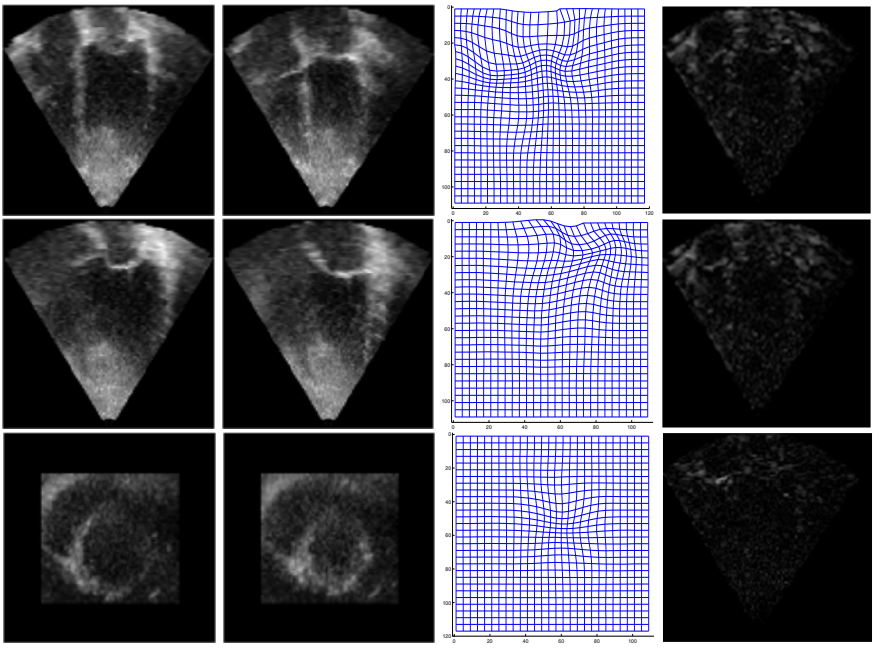

Fig. 5. Deformation estimation of a real ultrasound dataset. From left to right, the first two columns show the three center orthogonal views of the diastolic and systolic frames, the third column shows the grid deformation between the diastolic and systolic frames in three center orthogonal planes, the last column shows the axial plane alignment errors in transitivity constraint method, LDFFD method and the proposed method.

In Fig.(4) we illustrate the motion estimation errors in both x and y coordinates in noise level 0.08 dataset. The estimated transformation error of all the pixels in each frame is shown as an error bar at the frame index. We can see the mean of motion estimation errors in both x and y directions in the proposed method is smaller than the other two methods and the variance of the estimated transformation error is also smaller in the proposed method.

We calculate the mean of magnitude of transformation errors in the three noise variance levels in three registration methods. In our proposed method, the errors are 0.225, 0.267 and 0.312, while in the transitivity constraint method and the LDFFD method they are 0.329, 0.365, 0.403 and 0.314, 0.347, 0.392 respectively.

For the real dataset, we show the result in Fig.(4). The first two columns show center orthogonal views of the diastolic and systolic frames. The deformations in three center orthogonal plane from diastolic to systolic frames are shown in third column. The last column shows the error image in axial view between the diastolic and systolic frames after registration, we can see the error in the proposed method is smaller than other two methods.

5 Conclusion

We propose a diffeomorphic motion estimation method with temporal smoothness by constrain the velocity flow to have maximum transitivity consistency with local image frames. Simulation image and real dataset tests show that results in our motion estimation method are more smooth and accurate than other methods with temporal constraint. Our future work includes to develop algorithm using robust similarity measurement instead of SSD and increase the algorithm speed with the aid of parallel computing.

Acknowledgement. This paper is supported by a NIH/NHLBI grant 1R01HL102407-01 awarded to Xubo Song and David Sahn.

References

1. Buckberg, G., Hoffman, J.I.E., Mahajan, A., Saleh, S., Coghlan, C.: Cardiac Mechanics Revisited The Relationship of Cardiac Architecture to Ventricular Function. Circulation 118, 2571–2587 (2008)
2. Hung, J., Lang, R., Flachskampf, F., Shernan, S.K., McCulloch, M.L., Adams, D.B., Thomas, J., Vannan, M., Ryan, T.: 3D Echocardiograhy: A Review of the Current Status and Future Directions. JASE 20(3), 213–233 (2007)
3. Frangi, A.F., Niessen, W.J., Viergever, M.V.: Three-Dimensional Modeling for Functional Analysis of Cardiac Images: A Review. IEEE Trans. Med. Imag. 20(1), 1–25 (2001)
4. Papademetris, X., Sinusas, A.J., Dione, D.P., Duncan, J.S.: Estimation of 3D left ventricular deformation from echocardiography. Med. Imag. Anal. 5(1), 17–28 (2001)
5. Wang, Y., Georgescu, B., Houle, H., Comaniciu, D.: Volumetric Myocardial Mechanics from 3D+t Ultrasound Data with Multi-model Tracking. In: Camara, O., Pop, M., Rhode, K., Sermesant, M., Smith, N., Young, A. (eds.) STACOM 2010. LNCS, vol. 6364, pp. 184–193. Springer, Heidelberg (2010)
6. Elen, A., Choi, H.F., Loeckx, D., Gaom, H., Claus, P., Suetens, P., Maes, F., D'hooge, J.: Three-dimensional cardiac strain estimation using spatio-temporal elastic registration of ultrasound images: a feasibility study. IEEE Trans. Med. Imag. 27(11), 1580–1591 (2008)
7. Myronenko, A., Song, X., Sahn, D.J.: LV Motion Tracking from 3D Echocardiography Using Textural and Structural Information. In: Ayache, N., Ourselin, S., Maeder, A. (eds.) MICCAI 2007, Part II. LNCS, vol. 4792, pp. 428–435. Springer, Heidelberg (2007)
8. Rougon, N., Petitjean, C., Preteux, F., Cluzel, P., Grenier, P.: A non-rigid registration approach for quantifying myocardial contraction in tagged MRI using generalized information measures. Medical Image Analysis 9, 353–375 (2005)
9. Ledesma-Carbayo, M.J., Mah-Casado, P., Santos, A., Prez-David, E., GarMA, D.M.: Spatio-Temporal Nonrigid Registration for Ultrasound Cardiac Motion Estimation. IEEE Trans. Med. Imag. 24(9), 1113–1126 (2005)
10. Metz, C.T., Klein, S., Schaap, M., Walsum, T., Niessen, W.J.: Nonrigid registration of dynamic medical imaging data using nD+t B-splines and a groupwise optimization approach. Med. Imag. Anal. 15(2), 238–249 (2011)

11. Delhay, B., Clarysse, P., Magnin, I.E.: Locally Adapted Spatio-temporal Deformation Model for Dense Motion Estimation in Periodic Cardiac Image Sequences. In: Sachse, F.B., Seemann, G. (eds.) FIHM 2007. LNCS, vol. 4466, pp. 393–402. Springer, Heidelberg (2007)
12. Castillo, E., Castillo, R., Martinez, J., Shenoy, M., Guerrero, T.: Four-dimensional deformable image registration using trajectory modeling. Physics in Medicine and Biology 55, 305–327 (2010)
13. Sundar, H., Littb, H., Shen, D.G.: Estimating myocardial motion by 4D image warping. Pattern Recognition 42, 2514–2526 (2009)
14. Skrinjar, O., Bistoquet, A., Tagare, H.: Symmetric and Transitive Registration of Image Sequences. IJBI (2008)
15. Beg, M.F., Miller, M.I., Trouve, A., Younes, L.: Computing Large Deformation Metric Mappings via Geodesic Flows of Diffeomorphisms. International Journal of Computer Vision 61(2), 139–157 (2005)
16. Arsigny, V., Commowick, O., Pennec, X., Ayache, N.: A Log-Euclidean Framework for Statistics on Diffeomorphisms. In: Larsen, R., Nielsen, M., Sporring, J. (eds.) MICCAI 2006. LNCS, vol. 4190, pp. 924–931. Springer, Heidelberg (2006)
17. Ashburner, J.: A fast diffeomorphic image registration algorithm. NeuroImage 38(1), 95–113 (2007)
18. Khan, A.R., Beg, M.F.: Representation of time-varying shapes in the large deformation diffeomorphic framework. In: ISBI 2008, pp. 1521–1524 (2008)
19. De Craene, M., Camara, O., Bijnens, B.H., Frangi, A.F.: Large Diffeomorphic FFD Registration for Motion and Strain Quantification from 3D-US Sequences. In: Ayache, N., Delingette, H., Sermesant, M. (eds.) FIMH 2009. LNCS, vol. 5528, pp. 437–446. Springer, Heidelberg (2009)
20. De Craene, M., Piella, G., Duchateau, N., Silva, E., Doltra, A., Gao, H., D'hooge, J., Camara, O., Brugada, J., Sitges, M., Frangi, A.F.: Temporal Diffeomorphic Free-Form Deformation for Strain Quantification in 3D-US Images. In: Jiang, T., Navab, N., Pluim, J.P.W., Viergever, M.A. (eds.) MICCAI 2010. LNCS, vol. 6362, pp. 1–8. Springer, Heidelberg (2010)
21. Dupuis, P., Grenander, U.: Variational problems on flows of diffeomorphisms for image matching. Q. Appl. Math. 56(3), 587–600 (1998)
22. Rueckert, D., Aljabar, P., Heckemann, R.A., Hajnal, J.V., Hammers, A.: Diffeomorphic Registration Using B-Splines. In: Larsen, R., Nielsen, M., Sporring, J. (eds.) MICCAI 2006. LNCS, vol. 4191, pp. 702–709. Springer, Heidelberg (2006)
23. Meunier, J.: Tissue motion assessment from 3D echographic speckle tracking. Phys. Med. Biol. 43, 1241–1254 (1998)

Author Index